Establishing the Roles of the DNA Binding Domains of Replication Protein A (RPA)

Nilisha Pokhrel
Marquette University

ESTABLISHING THE ROLES OF THE DNA BINDING DOMAINS OF REPLICATION PROTEIN A (RPA)

By

Nilisha Pokhrel

A Dissertation submitted to the Faculty of the Graduate School,
Marquette University,
in Partial Fulfillment of the Requirements for
the Degree of Doctor of Philosophy

Milwaukee, Wisconsin
May 2020

ABSTRACT
ESTABLISHING THE ROLES OF THE DNA BINDING DOMAINS OF REPLICATION PROTEIN A (RPA)

Nilisha Pokhrel

Marquette University, 2020

During DNA metabolic processes such as replication and repair, double-stranded DNA is transiently unwound to expose single-stranded DNA (ssDNA). Such ssDNA intermediates are immediately coated by Replication Protein A (RPA), an essential single-stranded DNA binding protein present in all eukaryotes. RPA binding to ssDNA fulfills four goals: 1. The ssDNA is protected from degradation by endo- and exo-nucleases. 2. A cell-cycle checkpoint signaling cascade is triggered to indicate the presence of ssDNA. 3. RPA recruits other DNA metabolic enzymes on to the ssDNA. 4. Finally, RPA promotes the catalytic activity of the recruited enzyme. The overall objective of my thesis work focuses on deciphering how a single enzyme can coordinate multiple DNA metabolic processes in the cell to protect genomic integrity.

RPA is a multi-subunit complex composed of four DNA binding domains (DBDs-A, B, C and D) and two protein interaction domains (PIDs). The DBDs promote high affinity binding to ssDNA and the PIDs interact with more than two dozen proteins to control and coordinate various DNA metabolic processes. The DBDs and PIDs are tethered by flexible disordered linkers that enable RPA to adopt a variety of conformations. A long-standing hypothesis posits that specific RPA-conformations drive a corresponding cellular activity. My thesis work has developed experimental methodologies to visualize and capture the conformational states of RPA. Furthermore, we show how RPA-conformations are modulated by RPA-interacting proteins and post-translational modifications.

The major findings of my thesis research are: i) Establishment of DBDs A, B as the flexible unit of RPA, and DBDs C, D with RPA14 as the stable unit of RPA. ii) Existence of four distinct microscopic binding/ dissociation states of DBD-A and DBD-D in context of full-length RPA iii) DNA structures encountered by RPA affect the conformational states and arrangement of RPA-DBDs iv) RPA interacting proteins, such as Rad52, can selectively modify the DNA binding dynamics of a particular DBD. v) Cooperative binding in Rad52 selectively modulates the DNA binding states of DBD-D but not DBA-A and vi) Post-translational modification alters microscopic binding states and conformational arrangement of DBDs on DNA. This alteration can affect both assembly and stability of the RPA-DNA complex alone, or in the presence of proteins seeking to displace RPA from DNA.

In summary, this research provides a comprehensive mechanistic insight into conformational dynamicity attained by individual modules of RPA.

ACKNOWLEDGEMENTS

Nilisha Pokhrel

To,

My advisor, Dr. Edwin Antony, thank you for providing me with a platform to practice science. Your continued enthusiasm in finding something new and exciting has been the driving force behind my successful graduate school career. You have been a great teacher and an amazing guide. I am confident that the lessons I learnt under your guidance will continue to help me become a better scientist and a better person in the future.

My mom, who believes in 'never giving up'. Thank you for being so strong, first, for bringing me into this world and then shaping me to be the woman I am today. I know that you have sacrificed your joy and comfort for me, that you have always fought for my education, happiness, and my success. I cannot fathom what I would be without your continuous support and unconditional love. You have been an amazing friend, incredible mentor, and my guide in navigating life. I am honored to be your daughter and I hope I can continue to make you proud.

My husband, Mark C. Mashock, you are the absolute best husband anyone could ask for. Thank you for being so patient with me and loving me no matter how crazy the situations could get. Your smile and warmth kept me going through the hardships of graduate school. You listened to my non-stop jargon when I got excited about interesting experimental results, you held me when I cried and screamed in frustrations and above all, you decided to spend your life with me, looking beyond my imperfections. I look forward to our lives together. I love you.

My brother, thank you for loving me so much. I am excited to see the man you are becoming, and I pray for your continued progress. To my dad, thank you for letting me pursue my goals.

My late great-grandmother, Jagayama Bhattarai, thank you for raising me and loving me so much. I hope you have found eternal peace and I pray to the almighty that I can be re-joined with you in afterlife. To my grandmother, Mani Devi Bhattarai, as strong and independent you are, you taught me the meaning of responsibility and pushed me to do the absolute best I can. I have never seen anyone with a will like yours. Thank you for providing me with a solid foundation upon which I am building my life and my career. I am forever in your debt.

My lab-mates in the Antony Lab, especially, Elliot I. Corless and Emma A. Tillison, life in the lab would not be the same without you two. Thank you for making

everyday so joyous and being such amazing friends to me. I will remember all the trolls and our little talks together. They made me smile then, and will continue to do so as I revisit the memories. I will miss our hugs, and of course working together in the ‘small and mighty room’.

My committee members, Dr. Martin St. Maurice, Dr. Anita Manogaran and Dr. Edward Blumenthal, thank you for being such excellent mentors. You have guided me through difficult times, taught me to acknowledge my weaknesses and have helped me become a better learner. Thank you for all your support.

Dr. Martin St. Maurice, thank you for being an amazing teacher and a mentor. I had the privilege of being the TA for your class in the last semester of my graduate school, and doing so, I learned a lot from you. Thank you for being so patient with me, answering all my questions and finding time amidst your busy schedule.

The Mashock Family and all my friends, thank you for your continued love and support.

TABLE OF CONTENTS

LIST OF TABLES

LIST OF FIGURES

LIST OF ABBREVIATIONS

dsDNA	Double-Stranded DNA
DNA	DeoxyriboNucleic Acid
ssDNA	Single-Stranded DNA
RPA	Replication Protein A
ATM	Ataxia Telangiectasia Mutated
ATR	Ataxia Telangiectasia mutated and Rad3 related
HR	Homologous Recombination
DSB	Double Stranded DNA Break
DDR	DNA Damage Response
NHEJ	Non- Homologous End Joining
alt-EJ	Alternative End Joining
SSA	Single Strand Annealing
BRCA2	BReast CAncer Gene
ATP	Adenosine TriPhosphate
SDSA	Synthesis Dependent Strand Annealing
BIR	Break Induced Replication Repair
OB	Oligonucelotide- Oligosaccharide
DBD	DNA Binding Domain

PDB	Protein Data Bank
WH	Winged Helix
HTH	Helix Turn Helix
ADP	Adenosine Diphosphate
MMR	Mis-Match Repair
SSB	Single-Strand Binding proteins
SV40	Simian Virus 40
PID	Protein Interaction Domain
AA	Amino Acids
RIP	RPA Interacting Proteins
SBM	Sequential Binding Model
FEncAA	Fluroesence Enhancment through non-canonical Amino Acids
GFP	Green Fluroescent Protein
RFP	Red Fluorescent Protein
Nt	Nucleotides
NMR	Nuclear Magnetic Resonance
SAXS	Small Angle X-Ray Scattering
FRET	Förster Resonance Energy Transfer
SmFRET	Single molecule Förster Resonance Energy Transfer

Cryo-EM	Cryogenic Electron Microscopy
DBCO	DiBenzoCycloOctyne
PTM	Post translational modifications
SUMO	Small Ubiquitin related MOdifier
AA	Amino Acids
PIKK	Phosphatidylinositol-3-Kinase-like Kinases
Cdk	Cyclin-Dependent Kinase

CHAPTER 1: INTRODUCTION

1.1 Introduction to Replication Protein A (RPA)

"*It has not escaped our notice that the specific pairing we have postulated immediately suggests a possible copying mechanism for the genetic material*" – Watson and Crick, Nature, 1953.

The structure of double-stranded DNA (dsDNA), as noted by Watson and Crick, is an elegant structural solution to protect genomic integrity. To copy the genetic information, or to repair it, the dsDNA is unwound and single-stranded DNA (ssDNA) is transiently exposed. However, ssDNA is prone to chemical and nucleolytic attacks and can be easily damaged in the cell. In eukaryotes, the ssDNA binding protein Replication Protein A (RPA), binds to and protects the exposed ssDNA from enzymatic degradation (R. Chen & Wold, 2014b; Hass, Lam, & Wold, 2012; Zou, Liu, Wu, & Shell, 2006a).

RPA performs four essential functions in the cell: i) It binds to ssDNA with high affinity ($K_D > 10^{-10}$M) and protects it from degradation by exo- and endonucleases. ii) Formation of RPA-ssDNA complexes triggers the ATM/ATR cellular DNA damage checkpoint response. iii) RPA physically interacts with over two dozen DNA processing enzymes and recruits them to the site of DNA damage. iv) Finally, it hands-off the DNA to these enzymes and correctly positions them on complex DNA structures to facilitate their respective catalytic activity (Arunkumar, Stauffer, Bochkareva, Bochkarev, & Chazin, 2003b; Maréchal & Zou, 2015; Oakley & Patrick, 2010; Prakash & Borgstahl, 2012; Stauffer & Chazin, 2004a).

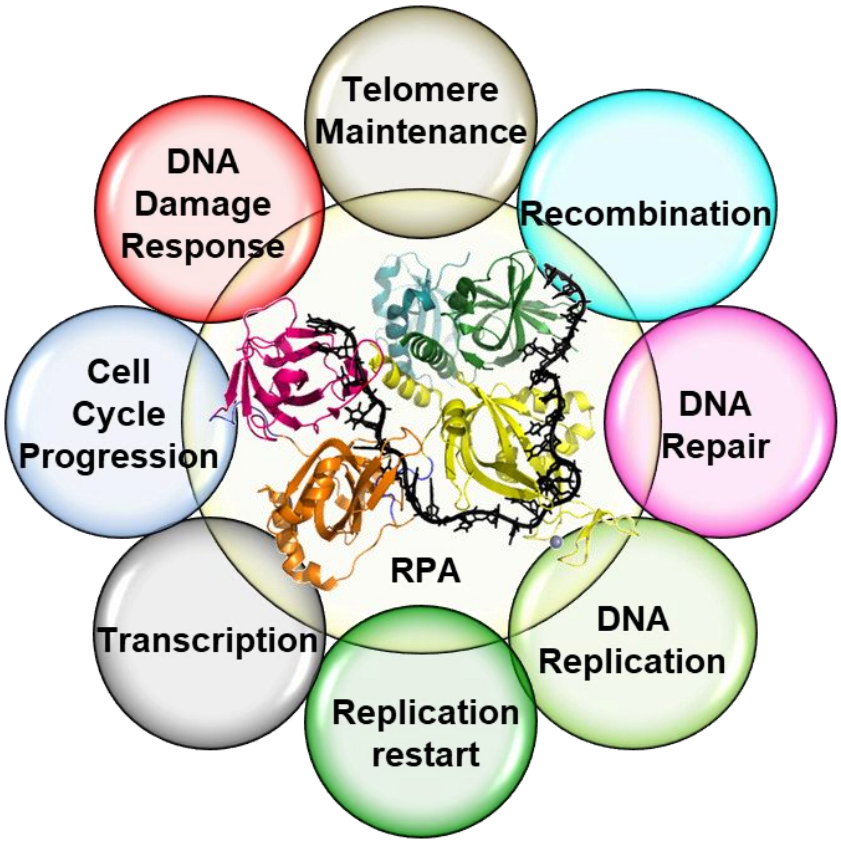

Figure 1-1: Multifaceted role of RPA in DNA metabolic processes. Schematic showing RPA as the central regulatory protein required in most DNA metabolic process with a single-stranded DNA intermediate. RPA acts a scaffold for assembly of various factors involved in DNA related transactions, such as, replication, recombination, transcription, and repair (HR, BIR, alt-EJ, MMR and NHEJ). Post-translational modification of RPA by appropriate kinases triggers DDR during replication fork stalling. In addition, RPA acts as cell-cycle checkpoint and is hyper-phosphorylated by specific kinases during DNA damage eliciting DDR in a cell-cycle dependent manner. Original diagram generated by Nilisha Pokhrel that shows the crystal structure of *U. maydis* RPA (PDB: 4GNX) solved by (Fan & Pavletich, 2012b).

The multifaceted roles of RPA and its significance is underscored by the absolute requirement of RPA in every DNA metabolic pathway that has a ssDNA intermediate: DNA replication, recombination, transcription, telomere maintenance, replication restart, and all types of DNA repair (Fig. 1-1) (Cobb et. al., 2005; Hass et. al., 2012; Maréchal & Zou, 2015; H. D. Nguyen et. al., 2017; Subramanyam, Ismail, Bhattacharya, & Spies, 2016). Such a broad cellular significance has positioned RPA as an attractive target for chemotherapeutic drug development.

The roles of RPA *in vivo* and its *in vitro* biochemical properties have been extensively studied and reported. However, one long-standing puzzle with respect to RPA has yet to be solved: RPA binds to ssDNA with very high affinity ($K_D > 10^{-10}$M) (Arunkumar, Stauffer, Bochkareva, Bochkarev, & Chazin, 2003a; Gnügge & Symington, 2017; Lao, Lee, & Wold, 1999), and the ssDNA buried under has to be handed over to incoming DNA metabolic enzyme that have DNA binding affinities that are orders of magnitude lower (Gibb et. al., 2014; Iwona M. Wyka, Kajari Dhar, Sara K. Binz, & Wold, 2003). How is this 'hand-off' mechanism orchestrated in the cell? Probing this fundamental puzzle raises other related questions:

1. Are these hand-off mechanisms unique to different RPA interacting proteins?
2. How does RPA dictate which RPA-interacting enzyme to recruit onto the ssDNA?
3. How do the cellular signaling processes communicate with and control RPA activity through post-translational modifications? How do such modifications work to alter the functional specificity of RPA?

4. How does RPA respond to the various DNA contexts it encounters, such as 3′ and 5′ ssDNA overhangs?

Answers to some of these puzzles lie in the structural and conformational complexity of RPA.

1.1.1 Structural Organization of RPA

RPA was originally discovered as a eukaryotic single strand DNA binding protein (SSBs) through *in vitro* cell-free SV40 DNA replication reactions in the presence of SV40 T antigens (Wold, 1997). RPA is a 116 kDa heterotrimeric complex made up of RPA70, RPA32 and RPA14 subunits, where the number denotes the approximate molecular weight of the respective polypeptide (Fig. 1-2 a,b). The subunits are also termed as Rfa1, Rfa2, Rfa3 in *Saccharomyces cerevisiae*; or RPA1, RPA2 and RPA3 in other organisms. A finer structural description of RPA can also be made in terms of individual sub-domains within each subunit. There are six oligonucleotide-oligosaccharide (OB) structural folds labeled A, B, C, D, E, and F. Four OB-folds (A, B, C and D) coordinate high-affinity RPA-ssDNA interactions and we term these as DNA binding domains (DBDs) (Fig. 1-2 a, b) (E Bochkareva, Belegu, Korolev, & Bochkarev, 2001; Fan & Pavletich, 2012a). The largest subunit, RPA70, harbors DBD-A, DBD-B and DBD-C. DBD-D resides within RPA32 (Fig. 1-2 a, b). RPA14, which in itself is an OB-fold (OB-E), interacts with RPA32 and DBD-C of RPA70 to form the trimerization core and is critical for the stability of RPA heterotrimer (Fan & Pavletich, 2012a).

Flexible linkers tether DBDs A, B (AB-linker) and DBDs B, C (BC-linker). Apart from the DBDs, there are two structurally well-defined protein-interaction domains

(PIDs) that mediate RPA binding to RPA-interacting proteins (RIPs) (Binz & Wold, 2008; Haring, Mason, Binz, & Wold, 2008; Oakley & Patrick, 2010; Xu et. al., 2008). PID^{70N} is located at the N-terminus of RPA70 and is connected by a long (80 aa) flexible linker (N-linker) to DBD-A. PID^{32C} is located at the C-terminus of RPA32 and is connected by a shorter (34 aa) disordered linker (C-linker) to DBD-D. In the existing literature, PID^{70N} is known as OB-F and PID^{32C} is termed the winged helix (Wh) domain. The final structural feature of RPA is the phosphorylation motif that resides at the N-terminus of RPA32 (Fig. 1-2). This 40-aa long region has multiple serine/threonine residues and is extensively phosphorylated by specific kinases in a cell-cycle dependent manner and in response to DNA damage (Binz, Sheehan, & Wold, 2004a; Elena Bochkareva et. al., 2002a; Dubois et. al., 2017; Maréchal & Zou, 2015; Oakley & Patrick, 2010). The heterotrimeric structure of RPA is stabilized by a three-helix bundle, where each subunit of RPA contributes a C-terminal α-helix towards the bundle formation to form a constitutive heterotrimer (Elena Bochkareva, Korolev, Lees-Miller, & Bochkarev, 2002b; Fan & Pavletich, 2012a).

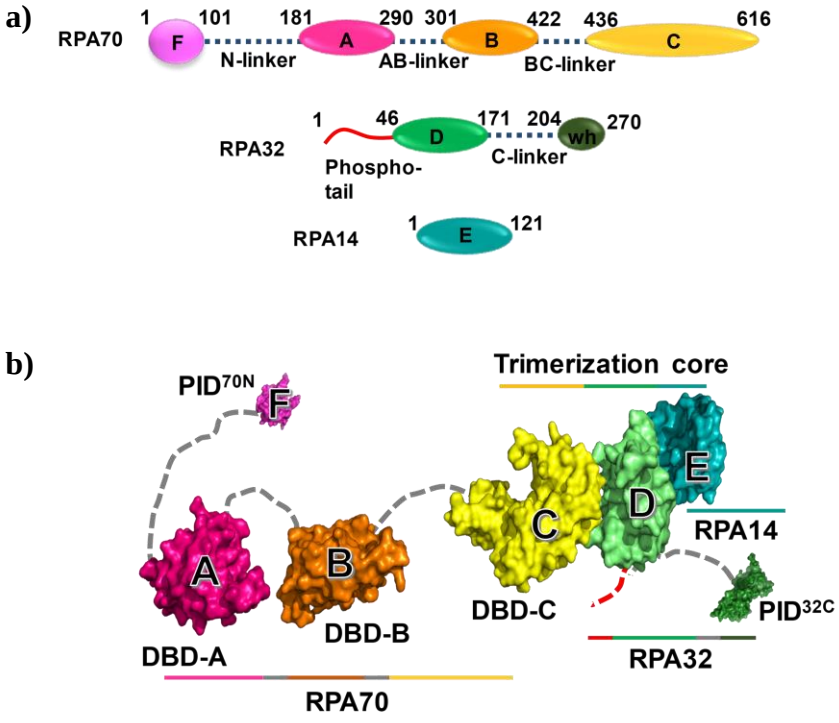

Figure 1-2: Structural organization of RPA. a) Schematics of the three subunits of RPA depicting functional domains with their residue numbers for *Sc.* RPA. The three DBDs in RPA 70 (DBD-A, DBD-B and DBD-C) are connected by flexible amino acid (aa) linkers (dashed navy-blue lines) and the fourth DBD (DBD-D) is present in RPA32. Of the two protein interaction domains, PID^{70N} and PID^{32C}, OB-F, also known as PID^{70N} is located at the N-terminus of RPA70 and connected by a long N-linker (dashed navy-blue line) to DBD-A. Winged helix domain (Wh), also known as PID^{32C} is located towards the C-terminus of RPA32 and connected by C-linker (dashed navy-blue line) to DBD-D. The N-terminus of RPA32 consist of a 34aa long phosphorylation domain, also called the phospho-tail (red line) that is phosphorylated by various kinases in a cell-cycle dependent manner to induce DDR. RPA14 itself is an OB-fold (OB-E) that does not bind to ssDNA but is required for stability of the RPA heterotrimer. **b)** Crystal structure of *U.maydis* RPA (PDB: 4GNX) shown as surface representation with DBDs and PIDs. The color scheme is same as in a), except, the aa linkers are shown as dashed lines (grey). For representation purposes, PID^{70N} and PID^{32C} were incorporated into 4GNX.

1.1.2 DNA binding properties of individual DBDs drive the conformational states of RPA

The flexible linkers allow the DBDs and PIDs to adopt a multiplex of structural configurations (Brosey et. al., 2009; J. Chen, Le, Basu, Chazin, & Yan, 2015; R. Chen, Subramanyam, Elcock, Spies, & Wold, 2016b; Chu Jian Ma, Gibb, Kwon, Sung, & Greene, 2017a; B. Nguyen et. al., 2014a). One can envision RPA as a series of interconnected Lego blocks that can be arranged and rearranged in many conformations on its own, and even more when bound on DNA. Adding to this complexity, multiple RPA molecules form cooperative nucleoprotein filaments on ssDNA (Gibb, Ye, Kwon, et. al., 2014a; Lavrik et. al., 1999). Thus, both intra-RPA and inter-RPA conformational assemblies and states can be formed. When one RPA molecule binds to ssDNA, all four DBDs or a selected subset of DBDs can engage the DNA. Specific binding modes for RPA have been defined on ssDNA (RPA does not interact with dsDNA). NaCl concentration and DNA length dependent 8-nucleotide and 30-nucleotide binding modes have been established. The models posit preferential binding of DBD-A and DBD-B on to ssDNA in the 8-nt mode and binding of all four DBDs in the 30-nt mode (Fig. 1-3 a, b) (Arunkumar et. al., 2003a; Elena Bochkareva et. al., 2002b; Iwona M. Wyka et. al., 2003; Kumaran, Kozlov, & Lohman, 2006). These findings are in line with 4-nt bound to DBD-A and DBD-B each and 32-nt bound to the entire RPA molecule (Fan & Pavletich, 2012a). These models also stem from early biochemical studies that measured the ssDNA

binding affinities of isolated DBDs. In these studies, DBDs A and B were purified separately, or together, and their ssDNA

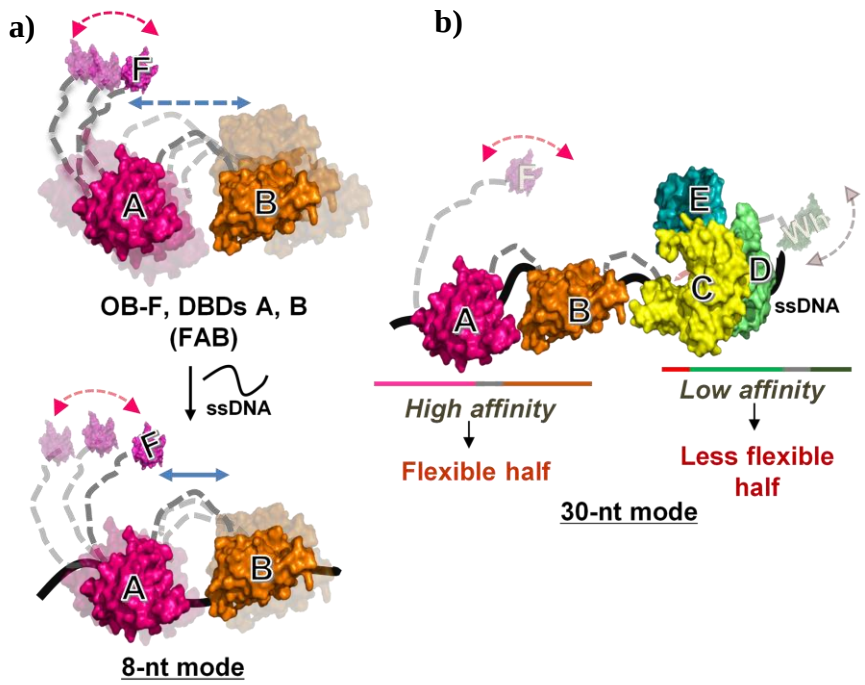

Figure 1-3: Nucleotide dependent modes of RPA-DNA binding. Surface diagram of RPA showing **a)** Independent motions of DBDs A, B (shown as reflections of two DBDs with dashed blue arrow) are coordinated (solid blue arrow) upon binding to 8-nt long DNA. OB-F adopts conformations independent of DBDs A, B (curved pink dashed arrows) with or without DNA. **b)** 30-nt mode with all the DBDs bound on ssDNA. N-linker and C-linker connecting OB-F and Wh domains, respectively, enable movement of these two PIDs independent of the DBDs. Traditionally, DBDs A, B were assigned as the high-affinty domains and DBDs C, D with RPA14 (trimerization core) were assigned as the low affinity domains (brown font). In chapter 3, our results show that DBDs A and B are the flexible half of RPA and the trimerization core makes the non-flexible half (red font).

binding constants were determined using electrophoretic mobility band shift analysis: K_a = $5x10^5$ M^{-1} (DBD-A), $5x10^4$ M^{-1} (DBD-B), $2x10^7$ M^{-1} (DBDs A+B). In comparison, full length RPA binds to ssDNA with K_a ~10^{10} M^{-1}. The trimerization core made up of DBD-C (RPA70), DBD-D (RPA32) and RPA14 is considered to have a weaker ssDNA binding affinity (K_a<10^6M^{-1}) (Arunkumar et. al., 2003a; Iwona M. Wyka et. al., 2003). Thus, the

identity of DBD-A and DBD-B as '*high-affinity*' domains and DBD-C and DBD-D as '*low-affinity*' domains has been widely established and systemically adopted in subsequent models for RPA function. Strikingly, the recently solved crystal structure of the RPA-ssDNA complex shows the trimerization core bound to 17-nts compared to 4-nt a piece by DBD-A and DBD-B (Fan & Pavletich, 2012a). This finding made us wonder if the DNA binding properties of the DBDs were different when in the context of full-length RPA. To probe this question, the DNA binding properties of each DBD has to be measured whilst keeping the heterotrimeric RPA intact. Based on the structure, we hypothesized RPA to be made of two halves: the '*flexible half*' consisting of DBD-A, B and PID^{70N}, connected by long disordered linkers, and the '*less-flexible half*' with DBD-C, D and RPA14 (trimerization core) that have extensive buried interaction interfaces and hold the RPA complex as a heterotrimer (Fig.1-8 b). It is again important to note that individual DBDs can have differential DNA binding affinities in isolation, but when tethered via linkers, as in the context of full-length RPA, they can function with a greater complexity. Furthermore, the intra- and inter-domain conformations adopted by individual DBDs could be different in context of full-length RPA and extend beyond observations made with the truncated variants. An example is the BC-linker, which appears to be uncoiled in the apo-form but forms a transient helix upon binding to 10nt or longer ssDNA and is absolutely required for high affinity DNA binding (Elena Bochkareva et. al., 2002b; Brosey et. al., 2013; Fan & Pavletich, 2012a; Walther, Gomes, Lao, Lee, & Wold, 1999). RPA-DNA engagement has also been proposed to follow a 'sequential binding model (SBM)', where the 'high-affinity' DBDs A and B, being the prime contributors for RPA-DNA interactions, bind first and help binding of the 'low-

affinity' trimerization core. Given the importance of DBDs in establishing RPA-ssDNA complexes, in my thesis research, I set out to decipher the DNA binding properties of the individual DBDs in the context of the full-length RPA. The following is a summary of my findings:

1. We developed Fluorescence Enhancement through Non-Canonical Amino Acids (FEncAA), a new tool to monitor the DNA binding dynamics of single domain in a multi-domain protein such as RPA (N. Pokhrel et. al., 2017).
2. Using FEncAA, we showed that the assignment of DBDs A and B as high affinity DNA binding domains were inaccurate. In fact, DBD-A was highly dynamic and easily displaced by the trimerization core, which was stably bound to ssDNA (Nilisha Pokhrel et. al., 2019).
3. We showed how RPA interacting proteins (Rips) can remodel a specific DBD to modulate RPA conformations on DNA (Nilisha Pokhrel et. al., 2019).
4. We showed how multiple RPA molecules arrange on DNA and how DBD-A and DBD-B binding were affected on DNA upon binding of the next RPA molecule to form cooperative complexes (Yates et. al., 2018).
5. We showed how phosphorylation of RPA altered the dynamics of specific DBDs leading to the formation of alternate RPA conformations on ssDNA (Yates et. al., 2018; Pokhrel *et. al.* unpublished)
6. Finally, we have shown how RPA can form distinct conformations on ssDNA with overhangs and gaps (Pokhrel *et. al.* unpublished).

Note: Experimental and mechanisitic interpretation of the word remodeling:

Throughout this dissertation, the word 'remodeling' is extensively used in a context-dependent manner. Mechanistically, the modular structure of RPA allows it to adopt a multitue of conformations, however, defining and capturing these conformations is experimentally challenging. We use the word 'remodeling' to describe the changes in the conformations that can be adopted by a particular RPA-DBD, and can be measured with our experimental system that uses stopped-flow or single-molecule TIRF microscope. The changes in conformations can be caused by several factors: other DBDs affecting the conformation of a DBD within an RPA heterotrimeric complex (intra-DBD) (chapter-3), change in conformations of DBDs due to interaction between two RPA molecules (inter-DBD)(chapter-6), in response to the change in the DNA topology that DBD encounters, for example, in the form of overhangs versus blocked end DNA (chapter 4), or, changes in conformations of a DBD in presence of RIP (chapter 3). In all these scenarios, the information gained from our experimental system relies on composite changes. Except for smTIRF microscopy, we cannot ascertain the information regarding the type, extent or number of conformations being affected.

1.1.3 Fluorescence Enhancement through Non-Canonical Amino Acids (FEncAA) reveals the dynamics of individual DBDs within the RPA heterotrimer.

Studying RPA poses a unique experimental challenge as it is composed of individual DNA binding domains that have distinct DNA binding properties. DBDs A and B function as a single unit and are shown to bind with high-affinity. Whereas, DBDs C, D and RPA14 function as a separate unit, and bind to ssDNA with lower affinity (Arunkumar et. al., 2003b; Brosey et. al., 2009; Iwona M. Wyka et. al., 2003). Meanwhile, these domains also cooperate with each other to form specific

conformational DNA-bound states of the RPA trimer. To gain a complete mechanistic insight into individual DBD-DNA binding in context of full-length RPA, we site-specifically incorporated non-canonical amino acids into individual DBDs of RPA and introduced fluorophores through click-chemistry. This approach enabled us to generate a DNA-binding specific read out from each DBD while maintaining the RPA trimer intact. RPA with fluorescent label on either DBD-A or DBD-D produced quantifiable changes in fluorescence signal upon binding to ssDNA. We positioned the fluorophore such that the observed changes in fluorescence directly reflects the dynamics (binding, dissociation, and/or remodeling) of a single DBD in context of full-length RPA. We termed this methodology "Fluorescent Enhancement through Non-Canonical Amino Acids (FEncAA)". In contrast to GFP or RFP based labeling, which are restricted towards the C- or N-terminus and involve addition of a sterically bulky group, fluorophores incorporated for FEncAA are relatively small in size and are less likely to cause problems due to steric hindrance. Furthermore, FEncAA allows us to track the actions of individual DBDs in a multi-protein complex making it an excellent probe to understand how DBD-DNA binding dynamics is influenced by RIPs without perturbing RPA's structure, function, and biochemical properties.

The proof-of-principle study establishing FEncAA as an experimental tool is described in Chapter 2. In chapter 3, I present the comparative analysis of two specific DBDs, their kinetics and dynamics on ssDNA. We showed that DBD-A binds faster to ssDNA than DBD-D, but is remodeled under conditions where there is not enough binding sites for all four DBDs to stably engage ssDNA. On the other hand, DBD-D forms a stable complex with DNA and does not display this remodeling phase. The

conditional remodeling of DBD-A under sub-stoichiometric concentrations of DNA or shorter lengths of ssDNA (number of nucleotides ≤ 20) is induced by its own trimerization core: a phenomenon we termed as 'intra-DBD remodeling'. Our findings contradict the long-held belief that DBDs A and B are the high affinity stable DNA binders. Our work demonstrates that DBDs A and B are flexible, more dynamic and are functionally utilized to search for free segments of ssDNA. The trimerization core, meanwhile, ensures stable engagement of the RPA complex on ssDNA.

The intra-domain remodeling in RPA highlights two key facts: first, DBD-A (and possibly DBD-B) acts as a 'sensor' for binding to ssDNA; and second, DBD-D (and possibly the trimerization core) acts as 'stabilizer' for RPA-DNA engagement. In a cellular context, upon encountering short ssDNA segments, intra-domain remodeling would allow PID^{70N} adjacent to DBD-A to recruit RIPs while the trimerization core maintains stable engagement to DNA. Alternatively, on long stretches of DNA, when all four RPA-DBDs are engaged, it would allow for functional versatility as both PID^{70N} and PID^{32C} can recruit different RIPs on DNA. As an alternative to the SBM that classifies the FAB and trimerization cores as the *high affinity* and *low affinity* domains, respectively, we propose FAB to be the '*flexible, more dynamic half*' and the trimerization core as the '*less-flexible, stable half*' of RPA. Our findings and the related unique methodologies are significant as it allows one to mechanistically probe how full-length RPA is remodeled on the ssDNA by RIPs – *a critical step in all DNA repair processes*.

1.1.4 Individual DBDs of RPA are intrinsically dynamic in DNA binding

The word ‘dynamic’ has often been used to describe the repertoire of structural and functional versatility of RPA. Although high-affinity, recently, RPA-DNA binding has been ascribed to be highly dynamic consisting of several microscopic binding and dissociation events. Several studies monitoring movement of ssDNA binding proteins are derived from the motion of bacterial SSB, and in-context of RPA, performed with human RPA. Despite being functionally homologous, both SSB and RPA diffuse on ssDNA by unique mechanisms (B. Nguyen et. al., 2014a; Roy, Kozlov, Lohman, & Ha, 2009; Zhou et. al., 2011). Homotetrameric SSB has three DNA binding modes: a 35-nucleotide (35-nt) binding mode engaging two subunits, 65-nt mode engaging all four subunits of the homotetramer, and a less characterized 56-nt intermediate mode (Bujalowski, Overman, & Lohman, 1988). Movement of SSB involves a sliding mechanism with formation of transient DNA bulges to facilitate the sliding process (Zhou et. al., 2011). Unlike SSB, RPA does not wrap the DNA. Rather, it transitions from an 8-nt mode engaging DBDs A, B to a 30-nt mode engaging all four DBDs, extending DNA structure in the processes to resolve any secondary structures. RPA also diffuses about ten times faster than SSB (one dimensional diffusion coefficient of RPA is 5000 $nt^2\ s^{-1}$ and SSB is 270 $nt^2\ s^{-1}$ for SSB) (Fanning, Klimovich, & Nager, 2006; K. S. Lee et. al., 2014; B. Nguyen et. al., 2014a). When the local concentration of RPA is high, RPA bound to ssDNA readily undergoes self-exchange with the surrounding RPA in a process also known as ‘facilitated exchange’ (Gibb, Ye, Gergoudis, et. al., 2014; Gibb, Ye, Kwon, et. al., 2014b; Chu Jian Ma, Gibb, Kwon, Sung, & Greene, 2017b). This phenomenon of facilitated exchange could be a global output of events driven by RPA diffusion. Yet, when engaged on

ssDNA, the components of RPA driving diffusion or facilitated exchange has not been fully dissected.

Movement/ diffusion/ facilitated exchange of RPA has been captured using fluorescently labeled human RPA, where, one or all three subunits have terminal fluorophores incorporated (R. Chen et. al., 2016b; Gibb, Ye, Gergoudis, et. al., 2014; B. Nguyen et. al., 2014a). Thus, information regarding the movement of the heterotrimeric complex is known but not with the resolution at the DBD-level. How individual DBDs move, the number of steps in this movement and the overall underlying mechanism at the microscopic level driving this movement is still a mystery. A major reason for this gap in understanding of what fuels diffusion or facilitated exchange of RPA is the inability to monitor each module (individual DBDs or PIDs) as they engage or disengage on DNA. This is further compounded by the heterotrimeric modular structure of RPA where individual modules can exist in a multitude of conformations independent of DNA, and then transition to several DNA dependent structural conformations. Recent studies combining NMR, SAXS, molecular tweezers and molecular dynamics simulation techniques to probe RPA-DNA binding dynamics have proposed that RPA-DNA binding has inherent nuances which could potentially translate towards tailoring its functional processivity (Brosey et. al., 2013; J. Chen et. al., 2015; R. Chen et. al., 2016b; Kemmerich et. al., 2016; B. Nguyen et. al., 2014a). These microscopic events are proposed to consist of independent or coordinated binding, dissociation, and rearrangement of individual DBDs and PIDs, while RPA as a heterotrimeric complex remains fully engaged on DNA on the macroscopic level. These microscopic events have been proposed to be the drivers for conformational changes in RPA, the diffusion of RPA

and could potentially be one of several mechanisms by which a RIP can modulate RPA-DNA binding to gain access to DNA. However, direct experimental evidence demonstrating quantitative assessment of these microscopic events and how it could be relevant to RPA's functions has been lacking.

Using smFRET and DBD specific fluorescently labeled RPA, we monitored the binding of DBD-A and DBD-D in context of full-length RPA at the resolution of a single-molecule. In chapter 3, I will present experimental evidence revealing the presence of four distinct microscopic binding- dissociation events/ states of both DBD-A and DBD-D in RPA. Furthermore, I will show that microscopic binding- dissociation states of DBD-A differ between full-length RPA and FAB (truncated RPA). This is the first known quantitative assessment showing DNA binding dynamics of RPA at the resolution of individual DBDs. Our studies show that in context of a full-length RPA, DBD-A and DBD-D can adopt maximum of four distinct binding states on DNA. Whereas, in the truncated RPA, DBD-A is able to adopt two distinct binding states on DNA. This difference in DNA binding states of DBD-A in context of full length RPA versus truncated RPA further bolsters our reasoning that truncated forms of RPAs provide partial information relating to regulation of RPA-DNA binding and individual DBDs of RPA have the potential of regulating the binding events of other DBDs.

1.1.5 RIPs can selectively modulate RPA- DBD dynamics

Extension of RPA dynamics to understand functional processing is further complicated by the array of RIPs interacting via PIDs, or RIPs interacting with DBDs or occasionally RIPs interactions involving composite of both (Elena Bochkareva et. al.,

2005; Ikegami et. al., 1998; D. Jackson, Dhar, Wahl, Wold, & Borgstahl, 2002; Matsuda et. al., 1995; Xu et. al., 2008). Usually, majority of RPA-RIPs interactions result in displacement of RPA from DNA. Active displacement of RPA by helicases or ATPases can be explained by the ATP-powered enzymatic activity of the helicase changing the DNA architecture along with displacing RPA-DBDs, which would eventually lead to complete displacement of RPA heterotrimer from DNA (Awate & Brosh, 2017; Nimonkar et. al., 2011). However, how RIPs with comparatively lower DNA binding affinities than RPA and devoid of any enzymatic activity displaces RPA from DNA (Stephen C. Kowalczykowski et. al., 1998; Sugiyama & Kowalczykowski, 2002a) is still an area of active investigation. Microdomain dynamics (binding, dissociation, and rearrangement) of DBDs, including diffusion of RPA has been proposed to open patches of DNA which could then be accessed by RIPs. Upon establishing an initial 'toehold' on DNA, RIPs could change the structure of DNA or push RPA-DBDs, eventually leading to displacement of RPA (Brosey et. al., 2013; R. Chen et. al., 2016b; Gibb, Ye, Kwon, et. al., 2014b; Kemmerich et. al., 2016; Chu Jian Ma et. al., 2017a). But do incoming RIPs selectively modify the microdomain dynamics of a particular DBD or do they equally impact the dynamics of all DBDs? If a RIP has composite interaction, for example, Rad52 which interacts with all three subunits of RPA, including PID^{70N} and PID^{32C}, how will the modulation of microdomain dynamics differ from RIPs that have a single interaction site with RPA?

To obtain answers to these questions, we implemented smFRET and monitored the DNA binding dynamics of DBD-A and DBD-D of RPA in the presence of Rad52. In chapter 3, I will present results demonstrating DBD specific modulation of DNA binding

states by Rad52. Specifically, Rad52 altered both the frequency and residence time of each DNA binding state of DBD-D but did not affect the DNA binding states of DBD-A. In chapter 5, I will present biochemical properties of Rad52 that drive selective modulation of DBD dynamics. This is the first evidence of selective modulation of DBD dynamics by a RIP that has interaction with all the DBDs of RPA and provides an explanation of what drives this selective modulation. Our findings provide a new mechanism for displacement of RPA form DNA, where an incoming RIP can selectively change the conformational state of a particular DBD, possibly weakening its overall binding, ultimately leading to displacement.

1.1.6 Flexibility of DBDs drive RPA assembly on DNA

It has been known for more than two decades that RPA binds rapidly to ssDNA and this binding is critical for controlled progression of major cellular events. But how do multiple RPAs assemble on DNA? To date, a high-resolution crystal structure of RPA depicting multiple RPAs bound on DNA with intact DBDs and PIDs has not been resolved. However, over the years an approximate mechanism underlying RPA assembly has evolved. Before the release of the *U.maydis* RPA crystal structure, a general consensus was that DBDs A, B being the high-affinity domains were absolutely required for binding to ssDNA and would sequentially bind to DNA first, obeying the 8-nt mode. This would then shift the local conformation of DNA, lowering the energy barrier and enabling the low affinity domains i.e DBDs C, D to sequentially bind to DNA attaining a 30-nt mode. Finally, DBD-D -DNA engagement would be the weakest as DBD-D made the least contacts with ssDNA and contributed least to RPA-DNA binding (Arunkumar

et. al., 2003a; Elena Bochkareva et. al., 2002b). The role of RPA14 which lacks a DBD, in RPA-DNA binding was unclear, as RPA14 did not bind to ssDNA but was required for the stability of RPA heterotrimer independent of DNA binding. By deduction, this raises a straight-forward question: if RPA14 only provides structural support to keep the RPA heterotrimer intact for the purpose of binding to DNA, why is it still present after all four DBDs are on DNA? A possible answer to this question is that, following DBDs engagement on ssDNA, RPA14 could play role in RIP recruitment. But a counter-argument to this would be that RPA14 has the least known RIP recruitment, as the majority of RIP interaction is performed by PID^{70N}, PID^{32C} or DBD surfaces (Fanning et. al., 2006). Therefore, it is conceivable that RPA14 has the potential to interact with DBDs and PIDs of its own heterotrimeric complex and the neighboring heterotrimeric complex, as well. This RPA14 mediated interaction would play a significant role in stabilizing binding of multiple RPAs on DNA. For this to occur, it is imperative that domains in the vicinity of RPA14 have enough flexibility to interact with RPA14, and this interaction is stable enough to be captured/ monitored.

The crusade of visualizing assembly/assembled multiple RPAs on DNA has involved the use powerful microscopy, such as, electron microscopy, atomic force, and cryo-electron microscopy (cryo-EM) along with biophysical and biochemical tools. This has provided structural cues ranging from beads-on-a-string to amorphous nucleoparticles forming an extended shape (J. Chen et. al., 2015; Eckerich, Fackelmayer, & Knippers, 2001; Hamon et. al., 2007). Yet, these studies provide minimal insight into domain-domain interactions involved when at least two RPAs are bound to DNA. Recently, Yates et. al., resolved cryo-EM structure showing assembly of dimeric *Sc.* RPAs on DNA. The

cryo-EM structures had a well-defined electron density of the trimerization core of both RPA molecules bound to DNA, including poorly resolved additional density which suggested interaction between two RPAs could be occurring via RPA14 (Yates et. al., 2018). By modeling (docking) the crystal structures of DBDs A, B and RPA14 in the additional density, together with measuring the binding affinity between isolated DBD-A and RPA14 core (lacking the C-terminal trimerization α- helix), Yates et. al. demonstrated that DBD-A of *Sc.* RPA could directly interact with RPA14 (Yates et. al., 2018). The cryo-EM structure showed a potentially different path for DNA binding (linear path) than the crystal structure of *U. maydis* RPA which showed DNA following a U-shaped path (Fig. 1-1 center structure). Based on the cryo-EM structure and additional biochemical analysis, Yates et. al. proposed that DNA is linearized upon engagement with multiple *Sc.* RPAs, where, the path of DNA within an RPA is guided by the action of flexible DBDs, and between RPAs is guided by the synergistic coordination of DBD motions along with RPA14 mediated interactions of two RPAs (Yates et. al., 2018).

Yates et. al, further demonstrated the significance of RPA14 in assembly of multiple RPAs by using a phosphomimetic RPA where the serine at position 178 of the N-linker was mutated to aspartate (RPA-S178D). S178 has been shown to be phosphorylated by Mec1 kinase during mitosis and in response to DNA damage (Biswas, Goto, Wang, Sung, & Sugimoto, 2019; Brush & Kelly, 2000; Brush, Morrow, Hieter, & Kelly, 1996; Majka & Burgers, 2007). Strikingly, introducing a single negative charge in between PID^{70N} and DBD-A, as in RPA-S178D, resulted in a 3-fold increase in affinity between DBD-A and the RPA14 core, independent of the 8-nt mode (Yates et. al., 2018). Compared to RPA-wt, RPA-S178D bound cooperatively but with lower affinity to longer

ssDNA (> 100-nt). In addition, of the two RPA-S178D bound to ssDNA, the cyro-EM density of the trimerization core of the first RPA was well resolved but the trimerization core of the second RPA situated closer towards the 3′ end of DNA was poorly resolved (Yates et. al., 2018). These finding suggests altered conformational assembly of RPA-S178D, particularly in longer ssDNA.

How any phosphorylation event is translated into structural and functional tailoring of RPA has been an open question. Therefore, to answer how a single-site phosphorylation event mechanistically influences assembly of multiple RPAs on DNA, I performed bulk FRET experiments and compared the assembly of wild-type RPAs (RPA-wt) and RPA-S178D as a function of increasing lengths of ssDNA (Chapter 6). Bulk FRET results showed a loss of inter-DBD remodeling for RPA-S178D, possibly due to reduced flexibility of DBD-A as it interacts strongly with RPA14. In addition, RPA-S178D complex was resistant to clearing by Srs2 helicase than RPA-wt, suggesting a direct implication of this phosphorylation event in the pre-synaptic phase of HR.

1.1.7 DNA context affects DBD dynamics

DNA processing requires RPA to bind ssDNA presented in different contexts. For example, the primer template junction encountered during replication initiation is different than the chicken-foot-structure during elongation, or the 3′ overhang following end resection in homologous recombination, which is different than the transient ssDNA encountered during transcription. When ssDNA is present in long-stretches, a subset of the RPA population will encounter the ssDNA-dsDNA junction, whereas subsequent binding by the rest of the RPA will bind to ‘normal’ ssDNA i.e. away from the ssDNA-

duplex junction. This phenomenon is further compounded when RPA loading is simultaneous with functioning of another DNA modifying enzyme. For example, during unwinding of dsDNA by DNA helicases, DNA toplogy encountered by RPA close to the helicase is different than the RPAs that occupy ssDNA space farther away from the helicase (Wouter L. de Laat et. al., 1998; Raney, Byrd, & Aarattuthodiyil, 2013). Based on the cryo-EM structure (and as mentioned in section 1.3.6), it could be hypothesized that RPA14 could be fulfilling a 'moonlighting' role in tailoring passage of DNA between RPA molecules in specific DNA contexts. But the polarity of DNA 'sensed' by individual DBDs of an incoming RPA is highly affected by the ongoing cellular processes and the DNA-context in which ssDNA is presented to RPA (for example, overhangs, junctions, forks etc.). Consequently, there has to be a mechanism in place by which RPA can coordinate ssDNA binding when ssDNA is presented in different DNA-contexts as it requires DBDs to 'sense' the polarity and optimize binding to DNA accordingly. In addition, DBD, PIDs and linkers have to regulate their intrinsic flexibility, and potentially adopt a particular conformation to be able to interact with RIPs.

Therefore, to investigate if the ssDNA encountered by RPA in various DNA contexts affects the binding of RPA-DBDs, I performed stopped flow experiments with RPA-DBD-A^f, RPA-DBD-D^f and three types of DNA structures (5′ overhang, 3′ overhang and ssDNA flanked by DNA duplexes (blocked end DNA)). In chapter 4, I will present experimental results that show trimerization core induced intra-DBD remodeling of DBD-A requires a free 5′ end of DNA. This result provides mechanistic insight into the previous observation showing the trimerization core to be sufficient for stable

engagement to a 5′ overhang DNA (R. Chen et. al., 2016b; W. L. de Laat et. al., 1998; Pestryakov, Khlimankov, Bochkareva, Bochkarev, & Lavrik, 2004).

DBD-A is situated towards the 5′ end of DNA and under the conditions of shorter lengths of DNA or scarcity of binding sites, is remodeled by the trimerization core. Therefore, any blockage at the 5′ end could exert significant steric clashes or tension in microdomain dynamics of DBD-A and possibly DBD-B, and both DBDs A, B tethered via AB-linker as a unit. Arrangement of DBDs on a particular DNA substrate, restricted conformational freedom, and modulation of existing RPA-protein interactions by an incoming RIP under these conditions could be a possible way of selectively handing over DNA to a specific RIP during a specific DNA event.

Recent technological advancements in crystallographic and biophysical tools have enabled access to structural and functional insights of megadalton complexes. In multi-domain proteins like RPA, a combination of these techniques is proving to be invaluable in understanding how these domains arrange, move, coordinate protein-DNA transactions and fundamentally behave as a ‘master of all trades’.

CHAPTER 2: MONITORING REPLICATION PROTEIN A (RPA) DYNAMICS IN HOMOLOGOUS RECOMBINATION THROUGH SITE-SPECIFIC INCORPORATION OF NON-CANONICAL AMINO ACIDS

2.1 Introduction

Enzymes that bind and function on DNA are necessary for all DNA metabolic processes such as replication, recombination, repair, and transcription. Multiple DNA binding proteins function together to catalyze these processes (Nord, 2009). Measuring the DNA binding properties of a single enzyme is relatively straightforward. However, when more than one enzyme is present in the reaction, determining the sequence of binding, and how the presence of one enzyme influences another is required to determine the overall mechanism of action. In multi-protein, steady-state experiments, the contribution of an individual enzyme is often probed by varying the concentration of the target enzyme relative to all other components (including the DNA substrate). Such experiments do not yield the microscopic rate constants of the individual steps in the reaction which are required to decipher the complete mechanism of action. Moreover, transient-kinetic tools are required to capture rapid conformational changes in proteins, and this information sheds light on how the various proteins interact with each other and the DNA template. The use of fluorescently-labeled DNA substrates serve as excellent tools to monitor overall reaction kinetics or to characterize the DNA binding/dissociation dynamics of a single protein (Anderson, Larkin, Guja, & Schildbach, 2008; Hwang & Myong, 2014; Song, Graham, & Loparo, 2016; Valuchova, Fulnecek, Petrov, Tripsianes, & Riha, 2016). For example, short oligonucleotides have been labeled with fluorophores to monitor the outcome of DNA recombination (Ragunathan, Joo, & Ha, 2011),

assembly/disassembly of Rad51 nucleoprotein filaments (Antony et. al., 2009b; Danyal et. al., 2016), track protein movement on DNA and RNA (Fischer & Lohman, 2004; Lucius et. al., 2002; Rasnik, Myong, Cheng, Lohman, & Ha, 2004), and to capture DNA unwinding (Bjornson, Amaratunga, Moore, & Lohman, 1994; Fischer, Tomko, Wu, & Lohman, 2012). Such an approach is limited by the read out from the DNA substrate and the contribution of individual enzymes cannot be interpreted when multiple proteins are present in a reaction.

To capture the sequence of binding and dynamics of each enzyme in a multi-protein reaction, one approach is to obtain a direct, quantifiable signal from a fluorescent label positioned on the individual protein that can undergo a change in fluorescence upon binding to DNA (Davenport, Harris, Origanti, & Antony, 2016; Fischer & Lohman, 2004). The changes in fluorescence help ascertain enzyme dynamics on DNA and how such dynamics are influenced by the presence of other DNA binding proteins in the reaction. Ensemble and single-molecule based fluorescence spectroscopy serve as powerful tools to investigate enzyme function on nucleic acid substrates, but are reliant on the generation of proteins tagged with genetically encoded fluorophores such as eGFP or mCherry (Collins, Ye, Duzdevich, & Greene, 2014; Gorman et. al., 2012; Redding & Greene, 2013). These tags are large in size, have positional constraints, are likely to interfere with activity (Fischer, Wooten, Tomko, & Lohman, 2010), and potentially inhibit protein-protein interactions (Lisby, Barlow, Burgess, & Rothstein, 2004). The attachment of large genetically-encoded fluorophores is particularly problematic for smaller DNA binding proteins such as Rad51, RecA or Dmc1, that function by forming cooperative nucleoprotein filaments on DNA. Finally, attachment of genetically encoded

fluorophores is often limited to the N- and C-terminal ends of the candidate proteins. Due to the positional constraints, and their size, they cannot be site-specifically introduced in internal regions of a protein, which is often necessary to capture conformational movements and for Förster Resonance Energy Transfer (FRET) studies (Hillisch, Lorenz, & Diekmann, 2001). Small, chemical fluorophores circumvent many of these issues, and can be site-specifically placed anywhere in the primary sequence of a protein.

The most commonly used approach to site-specifically attach fluorescent probes on proteins relies on maleimide-thiol chemistry to cysteine residues (Fox & Kennedy, 1965). While robust, this approach suffers from the need to generate a single cysteine bearing functional version of the target protein. This approach is not feasible in proteins where multiple cysteines are important for function or folding. In addition, screening and isolating modifiable cysteines in multi-cysteine proteins is time-intensive. This problem is circumvented using non-canonical amino acids (ncaa), an attractive strategy to engineer site-specific fluorescently labeled versions of proteins without the need to generate a single-cysteine version of a protein (C. C. Liu & Schultz, 2010; Young & Schultz, 2010). The ncaa methodology uses an amber suppressor stop codon (UAG) to mark the site of incorporation in the protein of interest. Co-expression of the TAG-construct along with a cognate pair of $tRNA^{AUG}$ and tRNA synthetase, specific to ncaa recognition and incorporation, generates the site-specific ncaa carrying protein. This methodology has been successfully used to directly incorporate fluorescent-ncaas (Chatterjee, Guo, Lee, & Schultz, 2013; H. S. Lee, Guo, Lemke, Dimla, & Schultz, 2009; Summerer et. al., 2006), or ncaas carrying functional groups that can subsequently be covalently attached to

fluorophores using click-chemistry (Blizzard et. al., 2015; Leisle, Valiyaveetil, Mehl, & Ahern, 2015; Miyake-Stoner et. al., 2009; Peeler & Mehl, 2012).

Using the ncaa approach, we sought to address the function of Replication Protein A (RPA), a key enzyme in various DNA metabolic processes (R. Chen & Wold, 2014b; Hass et. al., 2012). RPA is essential for survival and functions as a single-stranded DNA binding protein during DNA replication, replication restart, repair, recombination, transcription, and telomere maintenance (Binz et. al., 2004a). In addition, RPA has also been shown to resolve R-loop and G-quadruplex secondary structures (H. D. Nguyen et. al., 2017; Salas et. al., 2006). Binding of RPA to ssDNA in the cell also serves as a signaling cue to initiate DNA repair processes acting as a binding platform for the recruitment of various DNA processing enzymes (Zou, Liu, Wu, & Shell, 2006b). Recent evidence also points to RPA facilitating the re-establishment of chromatin structures after DNA replication and repair (S. Liu et. al., 2017). In each of these biologically important reactions, RPA functions in the presence of several other proteins capable of binding to DNA, e.g., polymerases, helicases, histones, etc.

RPA plays an indispensable role in homologous recombination (HR), a critical DNA repair pathway that corrects double stranded DNA (dsDNA) breaks in the genome (Binz et. al., 2004a; Roy et. al., 2009; Zou et. al., 2006b). Defective HR leads to genomic rearrangements and chromosomal defects often resulting in hereditary cancers and cancer-prone diseases such as Fanconi Anemia and Bloom's syndrome (Daley, Gaines, Kwon, & Sung, 2014; Daley, Kwon, Niu, & Sung, 2013). In addition to DNA repair, HR is fundamental to the maintenance of gametic diversity during meiotic crossover events. During HR, dsDNA at the site of a break is resected to yield long stretches of single

stranded DNA (ssDNA), which serve as a template for the nucleation of the Rad51 recombinase and formation of nucleoprotein filaments. Rad51 functions as the central engine in HR by performing ATP-dependent strand exchange (S C Kowalczykowski, 2000; S C Kowalczykowski, Dixon, Eggleston, Lauder, & Rehrauer, 1994). In the cell, the resected ssDNA is rapidly coated by RPA to protect it from nucleolytic degradation, and this step has been shown to activate the DNA damage response through several checkpoint kinases (Zou et. al., 2006b). To promote HR, RPA must first be displaced from the ssDNA, thus allowing formation of the Rad51 nucleoprotein filament. Pro-recombinogenic mediator proteins such as Rad52 and BRCA2 have been shown to promote Rad51 binding to ssDNA by displacing RPA (Tomko, Fischer, & Lohman, 2012; C. G. Wu, Bradford, & Lohman, 2010; Xie, Wu, Weiland, & Lohman, 2013). The Rad51 nucleoprotein filament then catalyzes strand exchange to drive homologous recombination. Similarly, in other instances where homologous recombination is inhibited, Rad51 filaments are disassembled by anti-recombinogenic mediators such as the Srs2 helicase (Antony et. al., 2009b; Krejci et. al., 2003; Seong, Colavito, Kwon, Sung, & Krejci, 2009). In Rad51 filament clearing reactions, RPA is proposed to sequester naked ssDNA once the Rad51 molecules are removed by Srs2 (Macris & Sung, 2005). While RPA has been shown to regulate several steps in HR, its precise mode of action in these events is not clearly understood.

The complexity of RPA function in multi-protein contexts necessitates the need for a site-specifically labeled fluorescent RPA probe to tease out its mechanism of action in the presence of other DNA binding proteins. The technical complexity in site-specifically labeling RPA arises from its heterotrimeric arrangement. RPA is composed

of three subunits - RPA70, RPA32 and RPA14, and contains six oligosaccharide-oligonucleotide folds (OB-folds) and four DNA-binding domains (DBD) (E Bochkareva et. al., 2001; Fan & Pavletich, 2012a). Three of the DBD's reside on the large RPA70 subunit and the fourth one lies in the RPA32 subunit (Fig. 2-2 a). The DBD's are connected by flexible linkers that enable RPA to exist in multiple conformational states on DNA (R. Chen et. al., 2016b). The individual DBD's play disparate roles in ssDNA binding and have been shown to modulate the strength of RPA-ssDNA interactions and/or its sliding/diffusion on DNA (B. Nguyen et. al., 2014b). DBD's A and B in RPA70 are the dominant contributors that cooperatively bind to ssDNA with high affinity ($K_a > 2x10^7\ M^{-1}$) (Arunkumar et. al., 2003a). The order of DBD binding and their orientation on ssDNA controls the polarity of RPA and associated activities (W. L. de Laat et. al., 1998; Iftode & Borowiec, 2000; Changsoo Kim, Paulus, & Wold, 1994). Our understanding of how RPA binds to DNA stems from elegant biophysical characterization of its kinetic and thermodynamic properties (C Kim, Snyder, & Wold, 1992; Kumaran et. al., 2006; B. Nguyen et. al., 2014b; Patrick & Turchi, 2001; Yuzhakov, Kelman, Hurwitz, & O'Donnell, 1999). How these properties are affected in the presence of other proteins such as the Rad51 recombinase or mediator proteins such as Rad52 or BRCA2 remains poorly resolved. Recent advancements in single-molecule fluorescence microscopy has enabled the study of RPA dynamics on long DNA substrates in the presence of multiple DNA binding proteins, (Gibb, Ye, Gergoudis, et. al., 2014; Gibb, Ye, Kwon, et. al., 2014a; Chu Jian Ma et. al., 2017b) but are limited by resolution of the imaging technology. Thus far, these experiments have been reliant on genetically encoded fluorophores with the limitations described above. Our ncaa

approach overcomes several of these limitations and enables the study of RPA dynamics in multi-protein reactions.

In this chapter, we describe A) the development of a *Saccharomyces cerevisiae* RPA probe (RPA^f), labeled at a single site in the heterotrimeric complex using a combination of ncaa and bio-orthogonal chemistry. This methodology circumvents the need for maleimide chemistry to covalently attach fluorophores or create a single-cysteine version of the protein, thereby leaving all Cys residues in RPA intact and rendering a fully functional protein. B) This approach also enables us to perform single molecule total internal reflection fluorescence (TIRF) microscopy-based investigation of protein dynamics without the need for genetically encoded fluorophores.C) We have identified a unique position in the RPA32 subunit which enables strategic attachment of a fluorescent reporter that does not affect RPA function, but yields a quantifiable change in fluorescence upon binding to ssDNA. D) Finally, using RPA^f, we describe the kinetics of RPA binding, dissociation, facilitated self-exchange, and facilitated exchange in the presence of Rad51 and HR-mediator proteins.

2.2 Materials and Methods

2.2.1 Materials

Standard laboratory chemicals and protease inhibitor cocktail (PIC) were purchased from Sigma-Aldrich (St. Louis, MO) and Research Products International (Mt. Prospect, IL). Q-sepharose, Heparin and S200 size exclusion chromatography columns were from GE Healthcare (Pittsburgh, PA). Ni^{2+}-NTA agarose was from Gold

Biotechnology (St. Louis, MO). Biogel-P4 resin was from Bio-Rad Laboratories (Hercules, CA). Enzymes for molecular Biology were from New England Biolabs (Ipswich, MA). Oligonucleotides were purchased from Integrated DNA Technologies (Coralville, IA). Fmoc-4-amino-phenylalanine was from Angene International Ltd. (Nanjing, China), and was used to prepare 4AZP, in collaboration with Dr. Christopher Dockendorff (Department of Chemistry, Marquette University). Commercial 4-azidophenylananine was purchased from Chem-Impex International (Wood Dale, IL). MB543 DBCO was purchased from Click Chemistry Tools (Scottsdale, AZ). Alexa Fluor 594 DIBO alkyne and BL21Ai cells were purchased from ThermoFisher Scientific (Waltham, MA).

Note: 4AZP was prepared by Dr. Disha Gandhi, a graduate student in the lab of Dr. Dockendorff at the time, and the full protocol is not mentioned in this dissertation. It is available at (N. Pokhrel et. al., 2017)

2.2.2 Plasmids for protein overexpression and ncAA incorporation

The plasmid expressing all three subunits of RPA (p11d-tscRPA) was a kind gift from Dr. Marc Wold (University of Iowa). The amber suppression stop codon (TAG) in RPA14 was substituted with an ochre stop codon (TAA), and a C-terminal 6X polyhistidine tag was incorporated in RPA32 using Q5 site directed mutagenesis (New England Biolabs, Ipswich, MA). Finally, a single TAG stop codon was introduced at position W101 in the RPA32 subunit marking the site for incorporation of p-azido-L-phenylalanine (4AZP). Plasmids for 4AZP incorporation are as described (Hammill,

Miyake-Stoner, Hazen, Jackson, & Mehl, 2007; Miyake-Stoner et. al., 2009; Peeler & Mehl, 2012).

2.2.3 Expression and purification of proteins

Wild type RPA was overexpressed in BL21Ai cells containing plasmid p11d-tscRPA and purified as described (Sibenaller, Sorensen, & Wold, 1998) with the following modifications. 4 L Luria-broth cultures were grown for each protein preparation. Cells were induced with 0.4 mM IPTG and 0.05 % (w/v) L-arabinose when they reached OD_{600} = 0.6, and grown for an additional 3 hours at 37 ºC. Harvested cells were resuspended in 120 ml cell resuspension buffer (30 mM Hepes, pH 7.8, 300 mM KCl, 0.1 mM EDTA, protease inhibitor cocktail, 1 mM PMSF, 10 % v/v glycerol and 10 mM imidazole). Cells were lysed using 400 μg/ml lysozyme followed by sonication. Clarified lysates were fractionated on a Ni^{2+}-NTA agarose column. Protein was eluted using cell resuspension buffer containing 400 mM imidazole. Fractions containing RPA were pooled and diluted three-fold with buffer H^0 (30 mM Hepes, pH 7.8, 0.1 mM EDTA, pH 8.0, 1 mM DTT, and 10 % v/v glycerol). The diluted protein sample was then fractionated over a Q-sepharose column equilibrated with buffer H^{100} (buffer H^0 with 100 mM KCl). Protein was eluted with a linear gradient H^{100} – H^{400} (superscript denotes final KCl concentration in the buffer). Fractions containing RPA were pooled and diluted with H^0 buffer to match the conductivity of buffer H^{100}, and further fractionated over a 10ml Heparin column. Protein was eluted using a linear gradient H^{100}-H^{1000}, and fractions containing RPA were pooled and concentrated using an Amicon spin concentrator (30 kDa molecular weight cut-off). RPA was dialyzed into storage buffer (30 mM Hepes, pH

7.8, 30 mM KCl, 2 mM DTT, and 10 % v/v glycerol), flash frozen using liquid nitrogen, and stored at -80 °C. RPA concentration was measured spectroscopically using ε_{280} = 98,500 $M^{-1}cm^{-1}$.

To obtain RPA carrying 4AZP, the p11d-tscRPA-TAG32-101 plasmid, which contains the TAG at position 101 in the RPA32 subunit, was cotransformed into BL21Ai cells with the plasmid pDule2-pCNF containing the orthogonal $tRNA^{UAG}$ and tRNA synthetase for 4AZP (Fig 2-2 a) (Miyake-Stoner et. al., 2009; Peeler & Mehl, 2012). Cotransformants were selected using both ampicillin (100 μg/ml) and spectinomycin (50 μg/ml). An overnight culture (50 ml) from a single colony was grown in LB media containing ampicillin and spectinomycin. 10 ml of the overnight culture was added to 1 L of minimal media. The minimal media for ncaa incorporation was prepared as previously described (Hammill et. al., 2007), but lactose was excluded. Cells were grown at 37 °C until the OD_{600} reached 2.0 and then induced with 0.4 mM IPTG and 0.05 % L-arabinose along with 1 mM 4AZP. The 4AZP solution was prepared by first dissolving 206 mg in 250 μl of 5 M NaOH, vortexed extensively, and then adjusted to 8 ml with H_2O, and the entire mixture was added to 1 L of media to achieve a 1 mM final concentration. Induction was carried out at 37 ºC for 3 hours. Cells were resuspended in cell resuspension buffer and purified as described above for wild type RPA. Care should be taken not to add DTT during purification of RPA^{4AZP} as it interferes with downstream click chemistry reactions. RPA^{4AZP} was flash frozen and stored at -80 °C. Srs2 and Rad51 were purified as described (Antony et. al., 2009b). Escherichia coli SSB was purified as described (Lohman, Green, & Beyer, 1986).

Note: We have made subtle changes to the purification process of both wild-type RPA and fluorescently labeled RPA, which are described in chapter 3. Except for this chapter, all the chapters requiring purification of wild-type RPA, RPA with mutations, and fluorescent RPA variants were conducted by following the protocol described in chapter 3.

2.2.4 Bio-orthogonal labeling of RPA

~2.5 ml of 20 μM RPA^{4AZP} was incubated with 1.5 molar excess (30 μM) of DBCO-MB543 (an alkyne derivatized fluorophore) in labeling buffer (30 mM Hepes, pH 7.8, 300 mM KCl, and 10 % v/v glycerol) for 1 hour at 4 ºC temp. Labeled RPA (RPA^{f}) was separated from excess dye using Biogel-P4 gel filtration (50 cm x 2 cm bed volume), in storage buffer (30 mM Hepes, pH 7.8, 30 mM KCl, and 10 % v/v glycerol). Labeling efficiency was calculated using absorption values at 280 nm and 550 nm and ε_{280} = 98,500 and ε_{550} = 105,000 for RPA and MB543 fluorophore, respectively. When measuring the concentration of RPA^{f}, a correction factor of 0.127 was applied to the protein absorbance value at 280 nm to correct for the contribution of MB543 dye absorbance at 280 nm. See appendix II (section 9.1-9.4) for detailed procedure.

2.2.5 Fluorescence measurements

Fluorescence spectra were obtained using a PTI QM40 instrument (Horiba Scientific, Edison, NJ, USA). 100 nM of ssDNA [$(dT)_{97}$] or plasmid dsDNA (100 nM nucleotides) were added to quartz cuvettes containing 2 ml solutions of 100 nM RPA^{f} in

reaction buffer (30 mM HEPES, pH 7.8, 100 mM KCl, 5 mM $MgCl_2$, 1 mM β-mercaptoethanol and 6% (v/v) glycerol). Samples were excited at 535 nm and emission spectra (555–580 nm) were recorded. All experiments were performed at 25 °C.

2.2.6 DNA binding

The DNA binding activity of RPA^f was measured using electromobility band shift analysis. To generate a 5′ ^{32}P-$(dT)_{35}$, *in vitro* Polynucleotide kinase reaction (PNK) with 1μM $(dT)_{35}$ in presence of $\gamma^{32}P$-ATP was performed. Briefly, to prepare 100μl of 1μM $\gamma^{32}P$- $(dT)_{35}$, in a 1.5ml microfuge tubes, 10μl of 10X PNK buffer (NEB, Ipswich, MA), 10μl of 10μM $(dT)_{35}$, 2μl of stock PNK enzyme (NEB, Ipswich, MA), 5μl of 250μCi $\gamma^{32}P$-ATP (commercial stock) and 73 μl of MilliQ water were added, vortex gently to ensure proper mixing, spun down for ~10 sec using a table- top centrifuge and incubated at 37^{o}C for 2 hours. Excess $\gamma^{32}P$-ATP was separated from ^{32}P- $(dT)_{35}$ using Microspin™ G-25 columns (GE) as per the manufacturer's protocol. To ensure complete separation, 25 μl of the radiolabeled reaction was loaded per column. Thus, in total, 4 columns were used for separation of ^{32}P- $(dT)_{35}$ from residual $\gamma^{32}P$-ATP and the clarified ^{32}P-$(dT)_{35}$ was pooled in a single 1.5ml microfuge tube. For a total reaction volume of 20μl, 50 nM of ^{32}P-$(dT)_{35}$ oligonucleotide was incubated with increasing concentrations of RPA or RPA^f (0 – 1 μM) in reaction buffer for 10 minutes at 4 ºC. 1 μl of DNA loading dye (50 % v/v glycerol and 0.2 % w/v bromophenol blue in 1 X TBE) was added to the reaction and mixed thoroughly, following which 20ul samples were resolved using an 8 % TBE-acrylamide gel at 110 volts for 45 minutes (composition per gel: 2ml of 10x TBE, 1ml of

40% bis- acrylamide, 100µl of 10% APS, 20 µl of TEMED, 6.9ml of MilliQ H_2O, polymerized at room temperature). Gels were exposed overnight onto a phosphorimaging screen and scanned using a STORM scanner (GE Healthcare, Pittsburgh, PA). Bound and unbound DNA signals were quantitated using ImageQuant software and the fraction ssDNA bound to RPA was calculated using the equation:

((bound ^{32}P signal)/(bound ^{32}P signal + unbound ^{32}P signal))*[ssDNA] (Eq. 1)

2.2.7 Stopped-Flow assays of RPA binding

All stopped-flow experiments described below to monitor RPA^f dynamics were performed on an Applied Photophysics SX20 instrument (Surrey, UK) in reaction buffer (30 mM Hepes, pH 7.8, 100 mM KCl, 5 mM $MgCl_2$, 1 mM β-mercaptoethanol and 6 % v/v glycerol) at 25 °C. Samples were excited at 535 nm and emission was monitored using a 555 nm cut-off filter (Newport corp., Irvine, CA).

2.2.8 RPA^f-ssDNA binding kinetics

To quantitate RPA^f binding to ssDNA, 100 nM RPA^f was rapidly mixed with 30 nm $(dT)_{97}$ oligonucleotide (post-mixing concentrations). Assuming a binding site size of 18-20 nt for RPA (Kumaran et. al., 2006), we expect 4-5 molecules to occupy each $(dT)_{97}$ oligonucleotide in our experiment. Data were fit to a single exponential plus linear equation to obtain observed rate constants:

$$\Delta F = A\,(1 - e^{-k_1 t}) + k_2 t \qquad \text{(Eq. 2)}$$

Where, ΔF is change in RPA^f fluorescence, *A* and k_1 are the amplitude and observed rate of the exponential phase, k_2 is the steady state rate and *t* is time. To measure non-specific changes in RPA^f fluorescence in the presence of other proteins, 100 nM RPA^f was mixed with Rad51 (0.97 μM) or Srs2 (200 nM). No change in fluorescence was observed. The concentrations of proteins mentioned are post-mixing concentrations in the stopped flow instrument.

2.2.9 RPA^f facilitated exchange kinetics

RPA^f-$(dT)_{97}$ complexes were preformed using 200 nM RPA^f and 60 nM $(dT)_{97}$ in one syringe and rapidly mixed with increasing concentrations of RPA^{WT} from the second syringe (100–1000 nM) and the change in RPA^f fluorescence was monitored. Facilitated exchange experiments with *Escherichia coli* SSB were assayed similarly, where preformed RPA^f-$(dT)_{97}$ complexes were challenged with SSB (40–200 nM). Both data were analysed using Eq. 2 to obtain observed rate constants. $k_{obs,1}$ was plotted against [RPA] and a linear fit was used to generate a rate for the facilitated exchange processes.

2.2.10 RPA^f kinetics during homologous recombination

To quantitate the dynamics of RPA^f in the presence of Rad51, RPA^f-$(dT)_{97}$ complexes were performed as described above and challenged with Rad51 (0.97 μM; post-mixing concentration) in the absence or presence of ATP (5 mM). Assuming a binding site size of 3.3 nt/Rad51, there are ~30 Rad51 binding sites per $(dT)_{97}$ substrate. To saturate ~900 nM Rad51 binding sites we used 970 nM Rad51 in our experiments.

Rad51 displaces RPA^f in the presence of ATP (Fig 2-12 b) and the change in fluorescence was fit using a double exponential equation:

$$[\Delta F = A_1(1 - e^{-k_1 t}) + A_2(1 - e^{-k_2 t})] \qquad \text{(Eq. 3)}$$

The analysis yields two observed rate constants. Similarly, displacement of RPA^f by Srs2 was measured by challenging RPA^f-$(dT)_{97}$ complexes with increasing concentrations of Srs2 (100 or 200 nM; post-mixing). Data were well described by Eq. 2 and yielded observed rate constants for the process. Finally, the ability of RPA^f to disrupt Rad51-ssDNA nucleoprotein filaments in the presence or absence of Srs2 was investigated by premixing Rad51 (1.94 μM) with $(dT)_{97}$ (60 nM) in one syringe and challenging the complex with RPA^f (200 nM) in the absence or presence of Srs2 (200 nM) [all concentrations pre-mixing]. 5 mM ATP was present in both reactions. The filament clearing data in the presence of Srs2 is described by Eq. 2.

2.2.11 Tryptophan quenching experiments to obtain RPA–ssDNA binding kinetics

Intrinsic tryptophan fluorescence was used to capture RPA binding to ssDNA in reaction buffer. 100 nM RPA^{WT} or RPA^f was rapidly mixed with 30 nM $(dT)_{97}$ oligonucleotide and the change in Trp fluorescence was monitored by exciting the sample at 290 nm and measuring emission with a 350 nm cut-off filter. To obtain the association rates for RPA^{WT} and RPA^f, similar intrinsic tryptophan quenching stopped-flow experiments were performed with 100 nM RPA^{WT} or RPA^f (post-mixing concentrations) and increasing concentrations of $(dT)_{35}$. All tryptophan quenching stopped-flow data were fit using Eq. 2 to obtain the observed rate constants for RPA–DNA binding.

2.2.12 Single molecule DNA curtain assays to monitor RPA facilitated exchange

ssDNA curtains were prepared and visualized by total internal reflection fluorescence microscopy (TIRFM), as previously described, with the exception that GFP-RPA was replaced with RPA^f (C.J. Ma, Steinfeld, & Greene, 2017; Chu Jian Ma et. al., 2017b). Briefly, a lipid bilayer is built upon a glass support with nanofabricated chromium barriers and pedestals inside a microfluidic flowcell that allows for buffer exchange. Long ssDNA were generated using rolling circle replication with Phi29 DNA polymerase from a circular ssDNA template (M13mp18) primed with a 5′-biotinylated oligonucleotide. ssDNA is then tethered to the lipid bilayer through a biotin-streptavidin-biotin linkage and pushed against the nanofabricated barrier with hydrodynamic force. Flowing HR buffer (30mM Tris-acetate, pH 7.5, 100 mM KCl, 5 mM $Mg(OAc)_2$, 1 mM DTT, 2 mM ATP and 0.2 mg/ml BSA) containing 100 pM RPA^f allows for visualization of ssDNA and a second attachment point is made through non-specific interaction of the 3′ end of ssDNA to a chromium pedestal to keep the ssDNA in the evanescent TIRF field. Presynaptic complex assembly was initiated by injecting 2 μM Rad51 in HR buffer lacking RPA^f. Disassembly of the presynaptic complex was initiated by flushing the sample chamber with HR buffer with 100 pM RPA^f lacking ATP as previously described (C.J. Ma et. al., 2017; Chu Jian Ma et. al., 2017b).

2.3 Results

2.3.1 Generation of fluorescent RPA^{f} using non-canonical amino acids and bio-orthogonal chemistry

A fluorescent version of RPA that produces a change in signal upon binding to ssDNA would facilitate investigation of its binding dynamics in the presence of multiple DNA binding proteins. To obtain a fluorescent version of RPA (RPA^{f}) that does not contain a large protein-based fluorophore, we used a combination of ncaa incorporation and bio-orthogonal chemistry. RPA is composed of three subunits – RPA70, RPA32 and RPA14, where the number corresponds to their respective molecular weights. There are 14 total cysteine residues in *Saccharomyces cerevisiae* RPA and the ncaa methodology circumvents the need to generate a cysteine-free version of the protein for site-specific labeling. We used the crystal structure of *Ustilago maydis* RPA as a guide for the positioning of the ncaa (Fig 2-1 a) (Fan & Pavletich, 2012a), and selected a position that resides close to the DNA binding interface in the RPA32 subunit. Both the RPA70 and RPA32 subunits interact with DNA through conserved DNA binding domains, and a greater degree of contacts reside in the larger RPA70 subunit (Fig 2-1 a). We chose to insert the ncaa at position W101 in RPA32 due to its proximity to DNA in the crystal structure. Strong sequence conservation in this region is also observed (Fig 2-1 b) suggesting that this region might be responsive to conformational changes upon binding to ssDNA. In addition, the region is situated away from terminal portions of RPA70 and RPA32, which are known to mediate protein–protein interactions (R. Chen & Wold, 2014a).

We used *p*-azido-L-phenylalanine (4AZP) as the ncaa as it can be readily coupled to commercially available alkyne-fluorophores using click chemistry. A C-terminal polyhistidine tag was engineered into RPA32 to separate out 4AZP carrying RPA from prematurely truncated protein that is formed when the UAG is read as a stop codon during protein expression. The RPA plasmid was coexpressed with a cognate pair of amber suppressor tRNA and amino-acyl tRNA synthetase specific for the incorporation of 4AZP. RPA^{4AZP} purified as a single complex (Fig 2-2 a, b) and similar to the wild type

RPA protein sedimented as a single species in sedimentation velocity experiments with apparent molecular weights consistent with a heterotrimer (Fig 2-3).

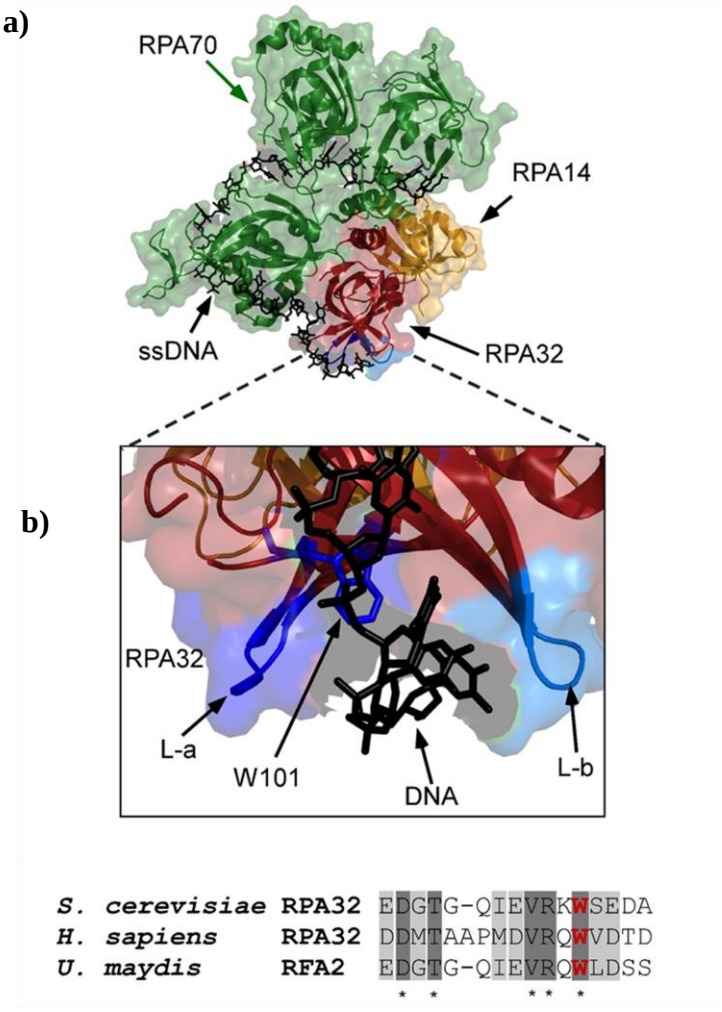

Figure 2-1: Position of non-canonical amino acid insertion in RPA. a) Crystal structure of Ustilago maydis RPA bound to ssDNA is shown (PDB ID: 4GNX) with RPA70, RPA32 and RPA14 colored green, red and yellow, respectively. The zoomed-in image shows two loops, L-a and L-b, flanking the ssDNA (black sticks) and Trp-101 is shown as stick representation in blue. **b)** Conservation of amino acid sequence in the region where Trp-101 resides in RPA32. W101 is highlighted in bold (red).

Site specific incorporation of 4AZP at position W101 in RPA32 was confirmed by subjecting the protein to LC-MS analysis after tryptic digestion. Further MS-MS fragment analysis obtained using a linear ion trap generate spectra confirming the

presence of peptides corresponding to RPA32 carrying 4AZP at position 101 (Fig 2-4). The peptide contains amino acids RK right before the site of 4AZP incorporation. Since trypsin cuts after both R and K, we observe both the shortest peptide, with the K cut off, and a missed cleavage fragment, starting with K. The data also confirm the presence of peptides with 4AZP at position 101 and no tryptophan containing peptide (at 101) was observed. Peptides containing 4-aminophenylalanine at position 101 were also detected. Laser-induced degradation of azide ($–N_3$) to amine ($–NH_2$) occurs during MS analysis (Y. Li, Hoskins, Sreerama, & Grayson, 2010) and such chemical conversions do not occur during cell growth, as established for 4AZP incorporation in other systems (W. Liu, Brock, Chen, Chen, & Schultz, 2007; Nehring, Budisa, & Wiltschi, 2012; Shao, Singh, Slade, Jones, & Balasubramanian, 2015).

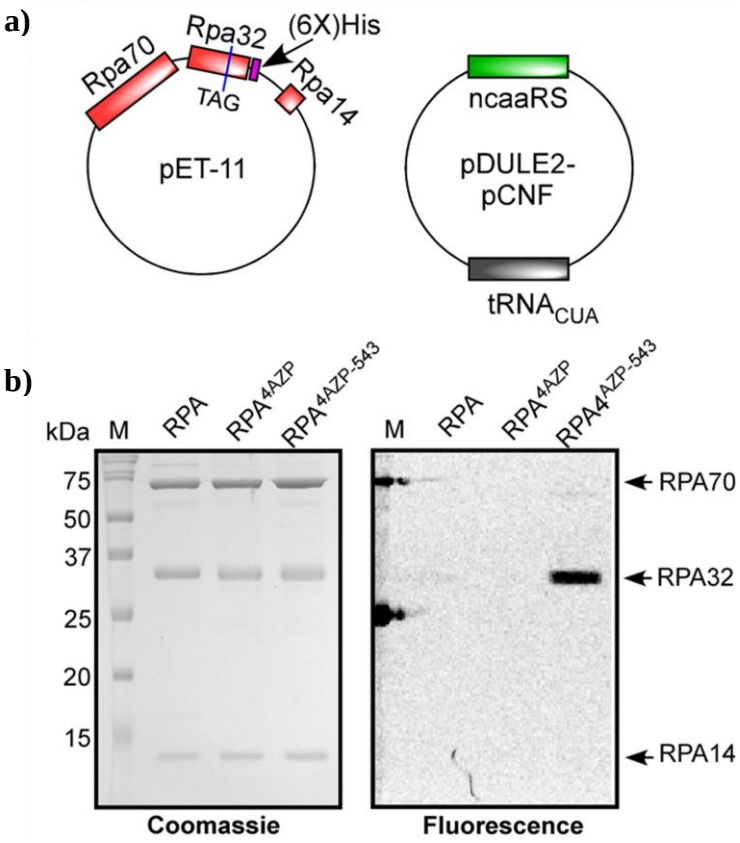

Figure 2-2: Insertion of ncAA and bio-orthogonal labeling of RPA. a) Plasmids used for the overexpression of RPA and ncaa components. The three subunits of RPA are cloned into a pET vector and the RPA32 subunit is engineered to carry a C-terminal polyhistidine tag and a TAG inserted for the incorporation of 4AZP. The genes for the tRNA that recognizes the amber suppressor codon and inserts 4AZP ($tRNA_{CUA}$) and its corresponding tRNA synthetase are engineered into the pDULE2-pCNF plasmid. **b)** SDS-PAGE analysis of RPA^{WT}, RPA^{4ZAP} and the MB543-labeled RPA (RPA^{f})proteins are shown after coommassie staining (left) or fluorescence imaging (right). Site-specific fluorescence labeling of the RPA32 subunit is observed.

Fluorescent RPA (RPA^{f}) was generated by incubating RPA^{4AZP} with dibenzocyclooctyne (DBCO) functionalized MB543 fluorescent dye, which covalently tethered the fluorophore onto the protein through strain-promoted azide-alkyne

cycloaddition. Site-specific fluorescent labeling of RPA^{f} was confirmed by analyzing the protein on SDS-PAGE, where only the RPA32 subunit is detected upon fluorescence imaging (Fig 2-2 b). RPA70 and RPA 14 serve as internal negative control and cannot be detected in fluorescence imaging. RPA^{f} sediments as a stable trimer in sedimentation velocity experiments suggesting that fluorescence labeling does not alter the overall structure of the protein complex (Fig 2-3). The copper-free coupling reaction yielded ~50-65% labeling efficiencies and had no deleterious effects on the integrity of the protein, as evaluated by SDS-PAGE analysis (Fig 2-2 b).

In reactions where copper-based click chemistry was attempted with 5-FAM-alkyne in the presence of 0.1 mM $CuSO_4$, 0.5 mM Tris(3-hydroxypropyltriazolylmethyl)amine, 5 mM sodium ascorbate and 5 mM amino guanidine, no labeling of RPA^{4AZP} was achieved and RPA^{4AZP} showed severe degree of degradation over time in our reaction conditions (data not shown). For *Saccharomyces cerevisiae* RPA^{4AZP}, DBCO functionalized fluorophores appear to be ideally suited under our reaction conditions because we do not observe non-specific labeling (Fig 2-2 b).

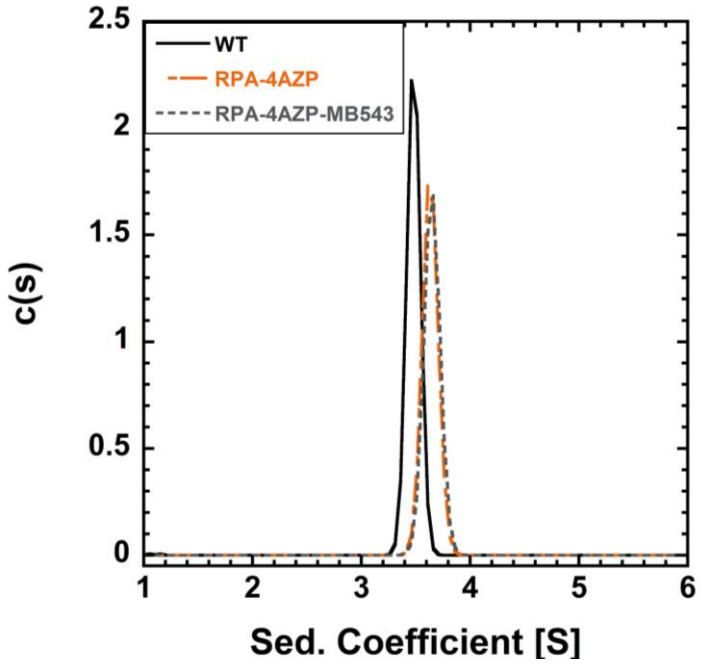

Figure 2-3: Sedimentation velocity analysis of RPA[f]. Analytical ultracentrifugation analysis of RPA, RPA with 4AZP incorporated, and RPA samples bio-orthogonally labeled with MB543 show the presence of a single heteromeric species with predicted molecular weights – 114 kDa, 116.4 kDa and 117 kDa, respectively. AUC experiments were performed with 3 μM RPA at 25 °C.

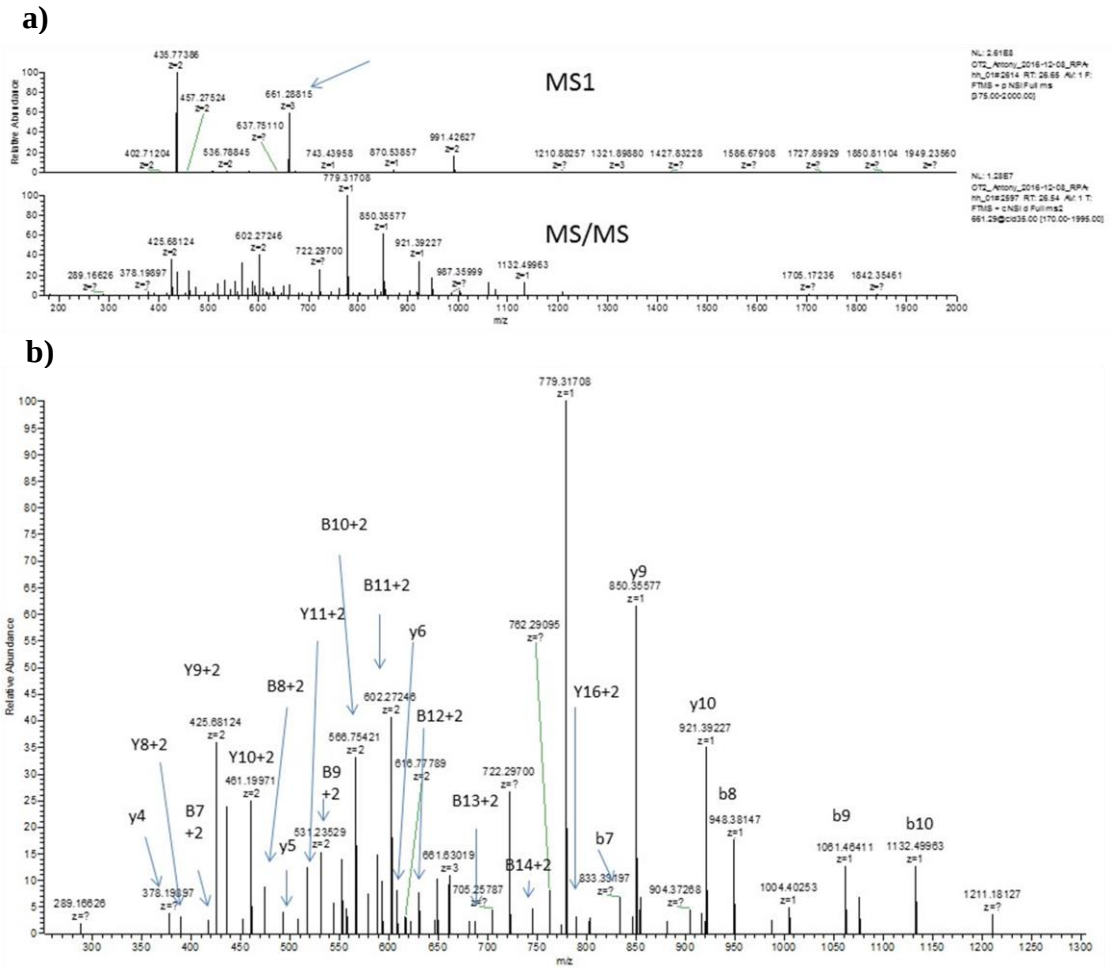

Figure 2-4: Mass spectrometric analysis of RPA^{4AZP}. Wild type RPA and RPA^{4AZP} were separated on a 12 % SDS-PAGE gel and bands corresponding to RPA32 were excised, extracted, digested with trypsin, and analysed using electrospray orbitrap MS and MS/MS sequencing. a) Data from the orbitrap analysis shows the presence of the peptide carrying the 4AZP replacement at position 101. The predicted mass of the peptide [K(4AZP)SEDANDLAAGNDDSSGK] with the 4AZP modification is 661.28. The spectra show the presence of the $(M+3H)^{3+}$ species with mass of 661.28 (denoted by the arrow). b) A zoomed version of the MS/MS spectra and analysis of the peptide show excellent coverage and high resolution of the species corresponding to the expected peptide and position of 4AZP.

2.3.2 ssDNA binding properties of RPA^f

We next examined the spectral properties of RPA^f to determine whether a change in fluorescence is observed upon binding to ssDNA. The excitation–emission spectra of RPA^f show maximal fluorescence excitation and emission at 555 nm (λ_{ex}) and 566 nm (λ_{em}), respectively (Fig 2-5 a). RPA binds ssDNA selectively, rapidly, and with high affinity; and RPA^f binding to ssDNA produces a ~5% enhancement in total fluorescence (Fig 2-5 b). No change in fluorescence is observed in the presence of dsDNA due to the lack of RPA binding. Next, to assess whether the positioning of the fluorophore interfered with the ssDNA binding properties of RPA, we compared the DNA binding affinities of RPA^{WT} and RPA^f using electrophoretic mobility shift analysis. Titration of increasing amounts of RPA^{WT} or RPA^f with a ^{32}P-labeled $(dT)_{35}$ oligonucleotide generated a RPA–ssDNA complex visible as a slower migrating band in the gel (Fig 2-5 c). Quantitation of the bandshifts show that both proteins bind stoichiometrically to the $(dT)_{35}$ ssDNA substrate (Fig 2-5 d). RPA carrying the incorporated 4AZP (RPA^{4AZP}) also binds to $(dT)_{35}$ with similar affinity (Fig 2-6). Therefore, positioning of the fluorophore at position 101 in the RPA32 subunit does not interfere with ssDNA binding affinity.

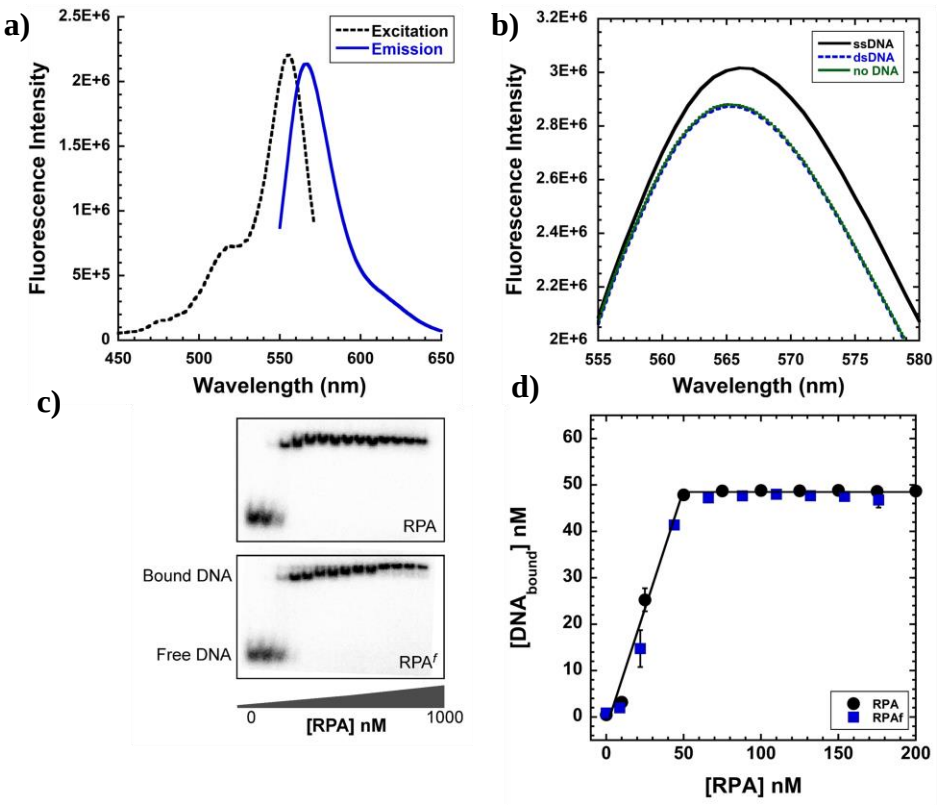

Figure 2-5: ssDNA binding properties of RPA^{f}. a) Excitation and emission spectra of RPA^{f} show maximum values at 555 nm (λex) and 566 nm (λem). **b)** RPA^{f} was excited at 535 nm and emission spectra were recorded in the absence or presence of ssDNA [$(dT)_{97}$] or plasmid dsDNA. A ~5% increase in fluorescence signal is observed when ssDNA is present in the reaction**. c)** Electromobility band shift analysis (EMSA) of RPA^{WT} (top) and RPA^{f} (bottom) binding to 50 nM ^{32}P-labeled $(dT)_{35}$ oligonucleotides show bound and unbound complexes and **d)** quantitation of the EMSA data show stoichiometric binding to ssDNA for both RPA and RPA^{f}.

RPA binds rapidly to ssDNA, and on longer ssDNA substrates multiple RPA molecules bind and form a protein coated filament. Occluded ssDNA binding site sizes of 18–20 nt and 25–26 nt at low (0.02 M) versus high (1.5 M) NaCl concentrations have been reported for yeast RPA (Kumaran et. al., 2006). Our reactions are performed at 100

mM KCl, where a 18–20 nt site size is expected. Thus, on a $(dT)_{97}$ oligonucleotide, ~4–5 RPA molecules could bind. To observe the kinetics of RPA^{f} binding to ssDNA, we performed a stopped-flow fluorescence experiment by rapidly mixing RPA^{f} with a $(dT)_{97}$ oligonucleotide (Fig 2-7 a). The reaction was excited at 535 nm and emission monitored using a 555 nm long pass filter. The data displays rapid ($k_{obs,1}$ = 23 ± 1.2 s^{-1}) and slow phases ($k_{obs,2}$ = 0.003 ± 0.0006 s^{-1}) of change in fluorescence signal upon binding to ssDNA (Fig 2-7 b, c). To compare the ssDNA binding kinetics of RPA^{f} with the RPA^{WT} protein, we monitored changes in intrinsic tryptophan fluorescence of RPA^{WT} and RPA^{f} (Fig 2-7 d, e). Both RPA proteins bind rapidly to $(dT)_{97}$, and two binding phases are observed. The rapid phase shows $k_{obs,1}$ = 28 ± 1.8 s^{-1} and 32 ± 3.8 for RPA^{WT} and RPA^{f}, respectively (Fig 2-7 d, e). The slower phase shows $k_{obs,2}$ = 0.014 ± 0.004 s^{-1} and 0.008 ± 0.003 for RPA^{WT} and RPA^{f}, respectively (Fig 2-7 d, e).

To test if the second phase reflected reorganization of multiple RPA molecules on the $(dT)_{97}$ substrate, we performed these experiments on a shorter DNA substrate $(dT)_{35}$. Given the occluded site-size of RPA (18–20 nt/RPA), less than two RPA molecules will bind to a $(dT)_{35}$ oligonucleotide. If $k_{obs,2}$ reports on Trp fluorescence changes associated with rearrangement of multiple RPA molecules on the $(dT)_{97}$ substrate, then on a $(dT)_{35}$ substrate $k_{obs,2}$ should be significantly slower. We determined the association rate of RPA^{WT} and RPA^{f} by monitoring the change in Trp fluorescence as a function of increasing $(dT)_{35}$ oligonucleotide concentration (Fig 2-8). Under these conditions, $k_{obs,2}$ is slower (0.002–0.006 s^{-1}) compared to our observations on $(dT)_{97}$ (0.014 and 0.008 s^{-1}; Fig 2-7). More importantly, these rates do not change with increasing DNA concentration. The data also yield association rates for RPA^{WT} and RPA^{f}, and the values

are very similar for both proteins: $5.2 \pm 0.3 \times 10^{-10}$ $M^{-1}s^{-1}$ versus $5.6 \pm 0.5 \times 10^{-10}$ $M^{-1}s^{-1}$ for RPA^{WT} and RPA^{f}, respectively (Fig 2-8). These data suggest that the ssDNA binding kinetics are similar between RPA^{WT} and RPA^{f} protein. It should be noted that in the experiments with RPA^{f} where fluorescence changes are monitored at 555 nm (Fig 2-7 b, c), only conformational changes in RPA32, close to the single fluorophore, are observed upon binding to ssDNA; whereas, in the Trp-quenching experiments, global conformational changes in both RPA70 and RPA32 are captured. The smallest RPA14 subunit is not thought to interact with DNA (Fan & Pavletich, 2012a). These experimental differences might account for the small variations in the two observed rate constants.

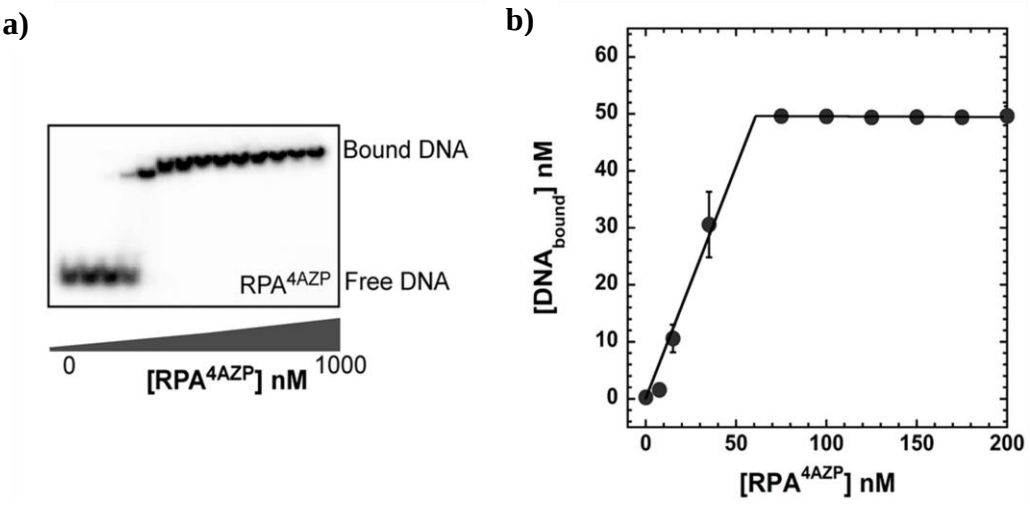

Figure 2-6: Electrophoretic mobility band shift analysis of RPA^{4AZP} DNA interaction. a) 50 nM ^{32}P-end labeled $(dT)_{35}$ was incubated with increasing concentration of RPA^{4AZP} and the band shift was assessed as described in the methods. **b)** Quantitation of the band shifts in panel A show stoichiometric binding of RPA^{4AZP} to $(dT)_{35}$.

To test whether RPA^{f} fluorescence is influenced by other proteins, we mixed it with Rad51 or Srs2 and monitored the change in fluorescence. We observe no change in the fluorescence signal when Rad51 or Srs2 is present in the reaction (Fig 2-7 f). Rad51 and RPA have been shown to interact in the absence of DNA (Nehring et. al., 2012),

whereas no physical interactions have been reported between RPA and Srs2, but are known to work together in Rad51 clearing reactions (Seong et. al., 2009). Both RPA^{WT} and RPA^{f} physically interact with Rad51 (Fig 2-9). These experiments suggest that RPA^{f} is fully functional, retains the ability to interact with Rad51, and can be used to investigate RPA–DNA binding dynamics in multi-protein reactions.

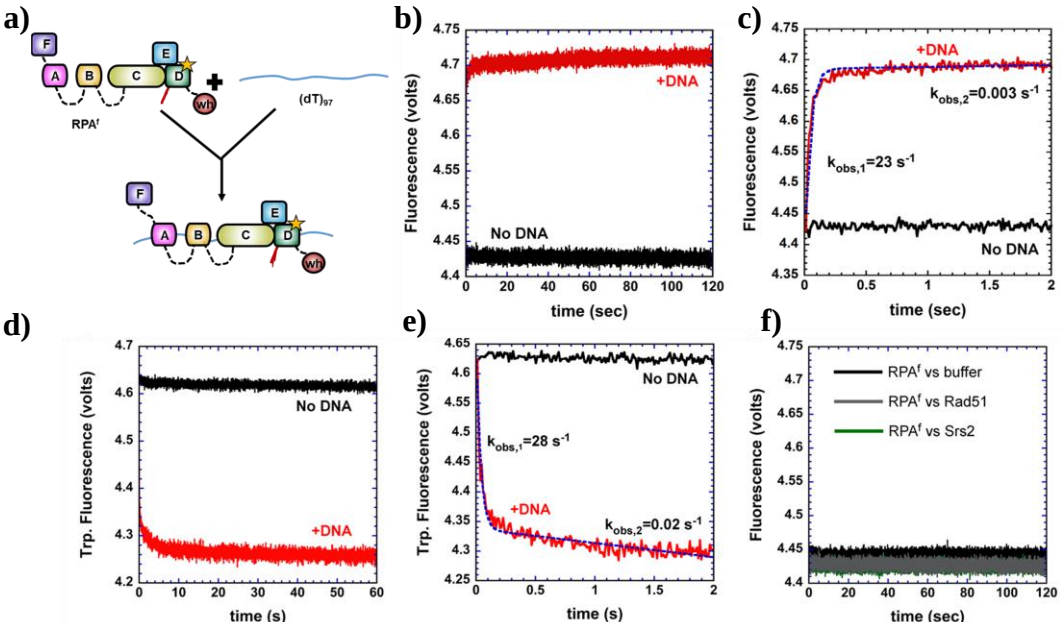

Figure 2-7: Kinetics of RPA binding to ssDNA. a) Schematic of stopped-flow experiment to capture RPA–ssDNA binding kinetics. **b)** A rapid change in RPA^f fluorescence is observed upon binding to a $(dT)_{97}$ ssDNA oligonucleotide (red trace), whereas no change in fluorescence is observed in the absence of DNA (black trace). **c**) Fit of the stopped-flow data (dashed blue line) show the presence of a rapid ($k_{obs,1}$ = 23 ± 1.2 s^{-1}) and slow phase ($k_{obs,2}$ = 0.003 ± 0.0006 s^{-1}) for ssDNA dependent changes in RPA^f fluorescence. Intrinsic tryptophan fluorescence changes in **d)** RPA^{WT} and **e)** RPA^f upon binding to ssDNA reveal rapid changes in fluorescence and fit of the data yield $k_{obs,1}$ = 28 ± 1.8 s^{-1}, $k_{obs,2}$ = 0.014 ± 0.004 s^{-1} for RPA^{WT}, and $k_{obs,1}$ = 32 ± 3.8 s^{-1}, $k_{obs,2}$ = 0.008 ± 0.003 s^{-1} for RPA^f, respectively. **f)** Free Rad51 or Srs2 in the reaction do not affect the basal fluorescence of RPA^f.

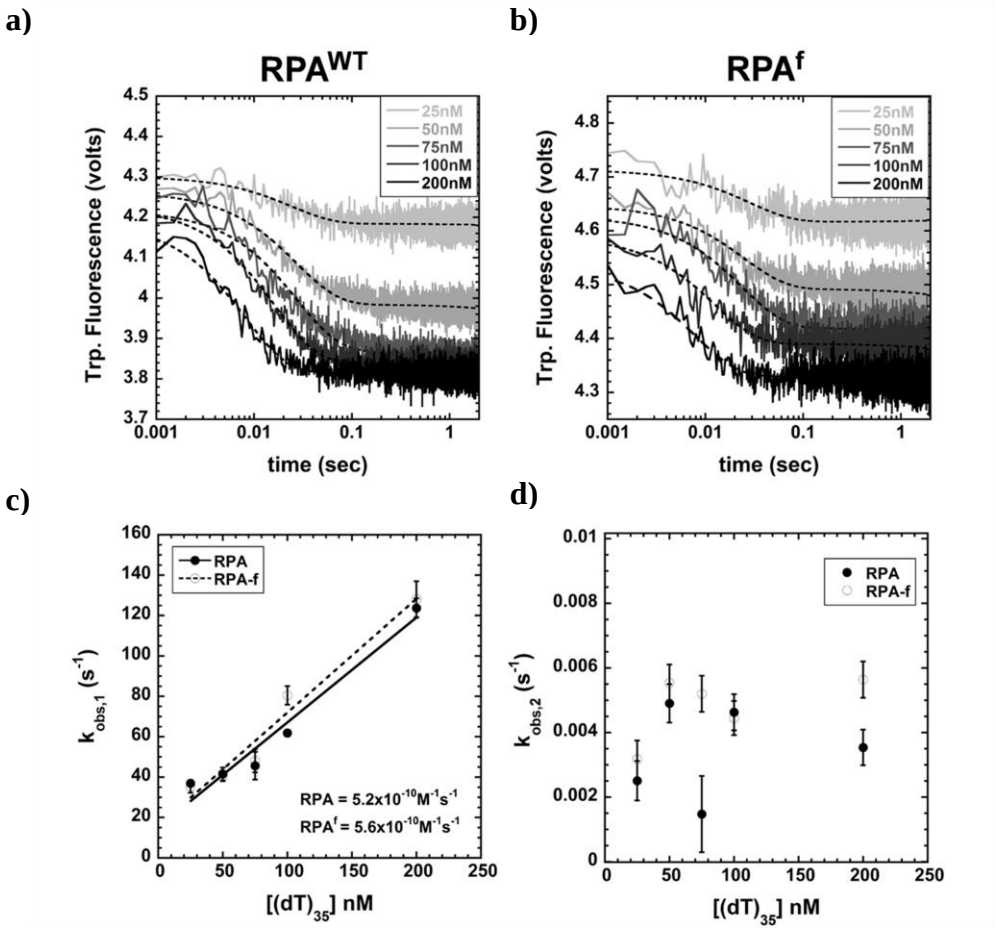

Figure 2-8: Intrinsic tryptophan-based measurement of RPA-$(dT)_{35}$ kinetics. Increasing concentrations of $(dT)_{35}$ was rapidly mixed with 100 nM **a)** RPA^{WT} or **b)** RPA^{f} [post-mixing concentrations], and the change in intrinsic tryptophan fluorescence was measured. Data were fit to a single exponential + linear fit (Eq.2) and two observed rate constants were obtained. $k_{obs,1}$ and $k_{obs,2}$ describe the exponential and linear phases, respectively. **c)** Plot of $k_{obs,1}$ as a function of $[(dT)_{35}]$ yields association constants of $5.2\pm0.3\text{x}10^{-10}\text{M}^{-1}\text{s}^{-1}$ versus $5.6\pm0.5\text{x}10^{-10}\text{M}^{-1}\text{s}^{-1}$ for RPA and RPA^{f}, respectively. **d)** $k_{obs,2}$ does not change appreciably for either RPA^{WT} or RPA^{f}.

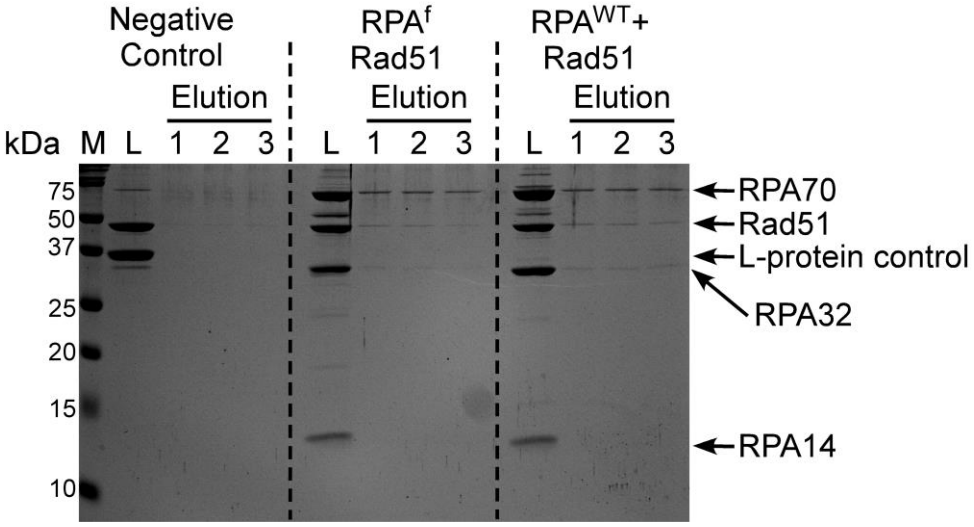

Figure 2-9: RPA-Rad51 interactions. 3 μM of His-RPA^{WT}, His-RPA^{f} or a non-specific protein (L-protein, an unrelated oxidoreductase protein) were bound to Ni^{2+}-NTA beads in the presence of Rad51 (3 μM), washed and then sequentially eluted with increasing concentrations of imidazole (100, 200 and 400 mM – elutions 1, 2 and 3). Rad51 forms a complex with RPA^{WT} and RPA^{f}, and is found in the elution samples. There is no Rad51 binding to the non-specific control protein. Lanes represent: M = protein marker, L = total Load, 1, 2, 3 = serial imidazole elutions.

2.3.3 Facilitated exchange of RPA^{f} by RPA and SSB

RPA bound on ssDNA has been shown to undergo facilitated exchange with free RPA in the reaction (Gibb, Ye, Gergoudis, et. al., 2014). To test whether RPA^{f} can be utilized to capture such dynamics on ssDNA we performed stopped-flow experiments where preformed RPA^{f}–ssDNA filaments were challenged with increasing concentrations of RPA^{WT} or Rad51. In the first series of experiments, RPA^{f} -$(dT)_{97}$ complexes were pre-formed by incubating RPA^{f} and $(dT)_{97}$ oligonucleotides and rapidly mixed with increasing concentrations of RPA^{WT} (unlabeled). The resulting change in fluorescence shows a rapid drop in fluorescence and both the observed rate constant and amplitude of the signal change increases with free RPA concentration (Fig 2-10 a, b). A plot of

the k_{obs} versus free RPA concentration yields an apparent rate for the facilitated exchange process ($0.7 \pm 0.1 \times 10^{12}$ M^{-1} s^{-1}; Fig 2-10 c). A hypothetical model has been proposed for facilitated exchange where the four OB-folds of RPA can be remodelled individually, while allowing the complex to remain on the ssDNA (Gibb, Ye, Gergoudis, et. al., 2014). The precise mechanism of how this self-propagated facilitated exchange occurs is poorly understood. *Escherichia coli* SSB, the functional homolog of RPA in prokaryotes, can also catalyze facilitated exchange of RPA (Gibb, Ye, Gergoudis, et. al., 2014). In fact, we observe faster and effective displacement of RPA^f by *E. coli* SSB with an apparent facilitated exchange rate of $47.3 \pm 1.7 \times 10^{12}$ M^{-1} s^{-1} (Fig 2-10 d-f). While both RPA and SSB are homologs, they are structurally unrelated and bind to DNA using different mechanisms (Ferrari, Bujalowski, & Lohman, 1994). The differences between SSB-induced versus facilitated self-exchange of RPA remain to be explored.

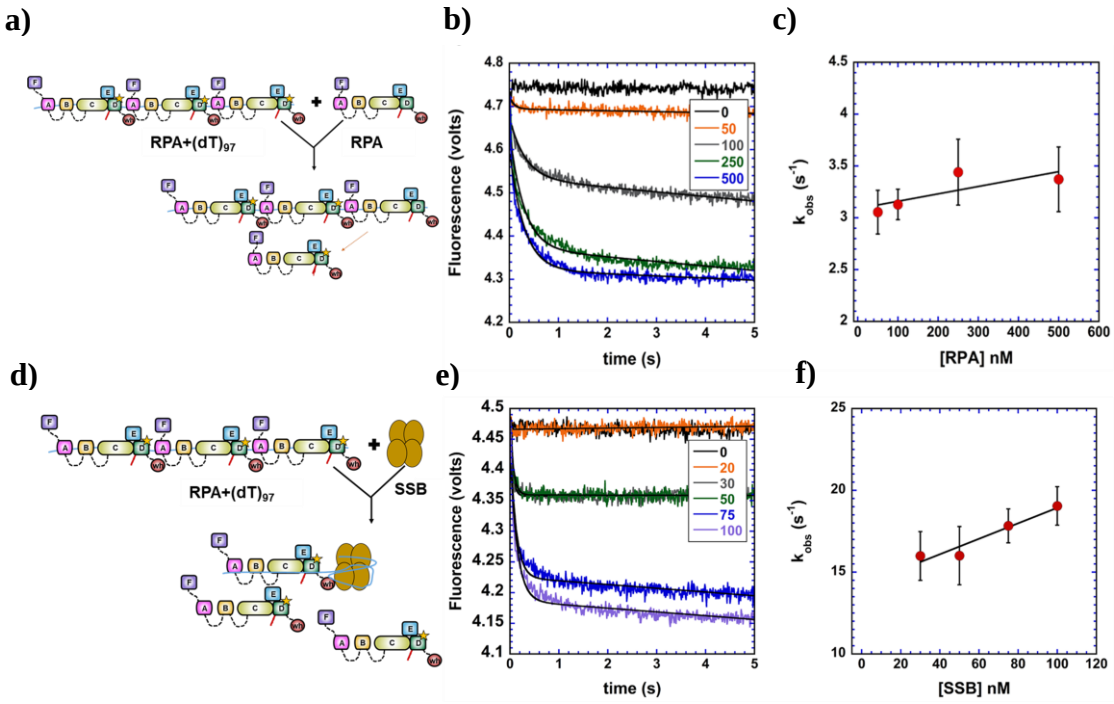

Figure 2-10: Facilitated exchange of RPA^{f} on ssDNA by RPA and SSB. a) Schematic of stopped-flow experiments to capture facilitated exchange of RPA^{f} by unlabeled RPA^{WT}. **b)** Pre-formed RPA^{f}-ssDNA complexes formed on $(dT)_{97}$ ssDNA substrates are effectively displaced by unlabeled RPA^{WT}. The rate of exchange increases with concentration of unlabeled RPA^{WT}, and **c)** yields an apparent observed rate of $0.7 \pm 0.1 \times 10^{12}$ M^{-1} s^{-1} for facilitated exchange. **d)** Schematic of facilitated exchange experiments with *E. coli* SSB, which **e)** displaces or exchanges with RPA^{f} more effectively than RPA^{WT} with **f)** an apparent observed rate of $47.3 \pm 1.7 \times 10^{12}$ M^{-1} s^{-1}.

2.3.4 Dynamics of RPA^{f} during homologous recombination events

RPA-coated ssDNA serve as the foundation for the nucleation and growth of Rad51 presynaptic filaments in homologous recombination. Rad52 is a mediator protein that functions to promote the exchange of RPA for Rad51 on the DNA (Xie et. al., 2013). However, in single molecule DNA curtain experiments, Rad51 displaces RPA in the absence of Rad52 (Gibb, Ye, Kwon, et. al., 2014a). Rad51 binds to ssDNA in the presence of ATP and forms stable complexes (Antony et. al., 2009b). Rad51 binding to a Cy3-labeled DNA substrate results in an increase in fluorescence. Using this assay, we first measured the rate of Rad51 binding to free 5′-Cy3-$(dT)_{79}$ oligonucleotide ($k_{obs,1}$ = 1.3 ± 0.3 s^{-1}; and $k_{obs,2}$ = 0.008 ± 0.001 s^{-1}; Fig 2-11). To investigate RPA^{f} dynamics during Rad51 nucleoprotein filament formation, we preformed RPA^{f}-$(dT)_{97}$ complexes and challenged them with Rad51 in the absence or presence of ATP (Fig 2-12 a). In the absence of ATP, there is no change in the fluorescence signal, as yeast Rad51 does not form a complex with ssDNA in the absence of ATP and hence no nucleoprotein filament formation is expected, thus is not able to displace RPA^{f} (Fig 2-12 b). In the presence of ATP, Rad51 displaces RPA^{f} as it forms a filament on the ssDNA substrate. The change in fluorescence signal shows RPA^{f} being dissociated in two distinct steps with $k_{obs,1}$ = 0.26 ± 0.08 s^{-1} and $k_{obs,2}$ = 0.02 ± 0.004 s^{-1} (Fig 2-12 b). Whether the two rate constants reflect Rad51 nucleation and growth, respectively, remains to be established. In the absence of other mediator proteins such as Rad52, our data show that Rad51 can form a stable nucleoprotein filament with rapid kinetics on RPA-coated ssDNA.

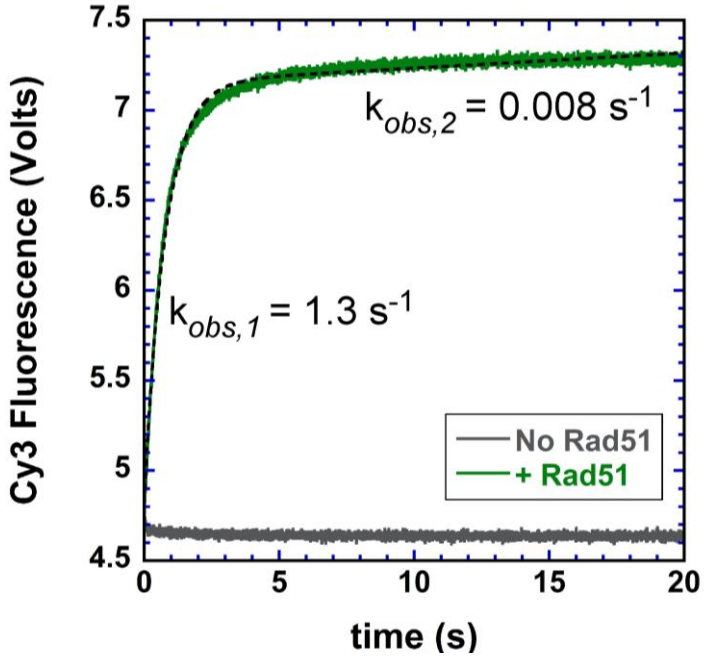

Figure 2-11: Kinetics of Rad51 binding to 5′ Cy3-$(dT)_{79}$ ssDNA. Stopped flow analysis of Rad51 (1.5 μM) binding to 5′ Cy3-$(dT)_{79}$ ssDNA oligonucleotide (40 nM) in reaction buffer (50 mM Tris-HCl, pH 7.6, 50 mM NaCl, 10 mM $MgCl_2$, 1 mM DTT, 5 mM ATP and 6 % v/v glycerol) at 25 °C. Cy3 fluorescence was measured by exciting the sample at 515 nm and emission was monitored using a 555 nm long-pass filter. Data were fit to a single-exponential plus linear equation to obtain observed rate constants: $\Delta F = A(1 - e^{-k_1 t}) + k_2 t$. k_1 and k_2 are the two observed rate constants and A is the amplitude of Cy3 fluorescence change. A rapid and slow phase with observed rate constants of 1.3 ± 0.3s^{-1} and 0.008 ± .001 s^{-1} were captured.

The Srs2 helicase/translocase is an anti-HR mediator and functions by disassembling Rad51 nucleoprotein filaments (Krejci et. al., 2003). Srs2 is a motor protein in yeast and uses ATP to translocate along ssDNA substrate and capable of unwinding dsDNA(Antony et. al., 2009b; Davenport et. al., 2016; Lytle et. al., 2014; Qiu et. al., 2013). Single stranded DNA binding proteins such as SSB and RPA can diffuse along ssDNA substrates and other DNA binding proteins have been shown to modulate this sliding behavior to displace SSB/RPA from DNA (B. Nguyen et. al., 2014b; Rasnik et. al., 2004). We tested if a translocase such as Srs2 would be able to displace RPA^f from ssDNA. When preformed RPA^f-$(dT)_{97}$ complexes are rapidly mixed with Srs2 and ATP, an initial drop in fluorescence is observed followed by signal stabilization (Fig 2-12 c, d). When the concentration of Srs2 is doubled in the reaction to 200 nM (post-mixing), the fluorescence signal does not appreciably change as in experiments with 100 nM Srs2. The early exponential drop in signal yields $k_{obs} = 8.3 \pm 1.2\ s^{-1}$ and $8.5 \pm 0.8\ s^{-1}$ for 100 and 200 nM Srs2 in the reaction, respectively (Fig 2-12 d). These data suggest that there is displacement of RPA^f by Srs2. However, Srs2 is either rapidly outcompeted on ssDNA by the dissociated RPA^f, or RPA^f rapidly rebinds the DNA after it's removed by Srs2.

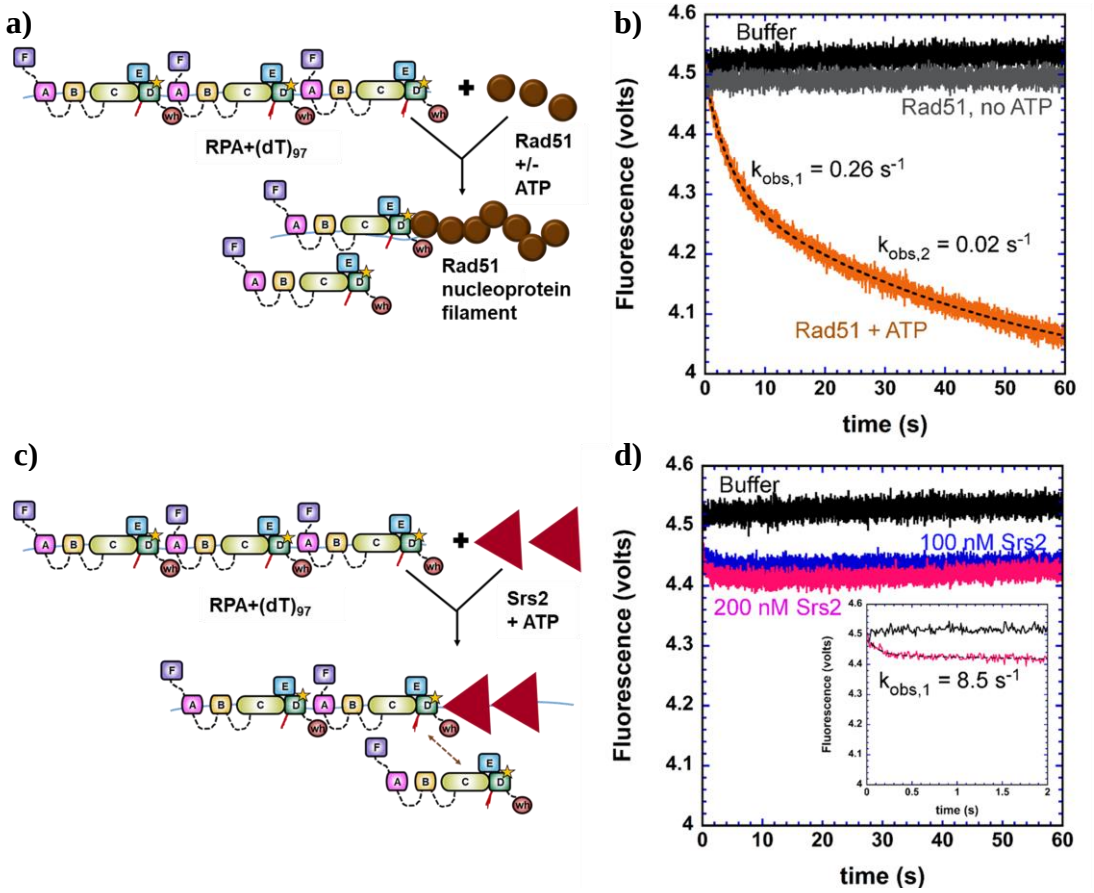

Figure 2-12: Dynamics of RPA^f during pre- synapsis stages of homologous recombination. a) Schematic of Rad51 binding to RPA^f–ssDNA complexes. **b)** Preformed RPA^f–ssDNA complexes are not disrupted by Rad51 in the absence of ATP (gray trace), but effectively displaced in the presence of ATP (orange trace). The data is well described by a double exponential fit yielding $k_{obs,1}$ = 0.26 ± 0.08 s−1 and $k_{obs,2}$ = 0.02 ± 0.004 s−1. **c)** Schematic of stopped-flow experiments to observe the effect of Srs2 on RPA^f–ssDNA complex stability. The brown arrow depicts potential rebinding of RPA^f in the reaction. **d)** Increasing concentrations of Srs2 show a small change in the fluorescence signal, but no significant change in overall fluorescence is observed. Insert shows an exponential phase with an observed rate constant of 8.5 ± 0.8 s−1**.**

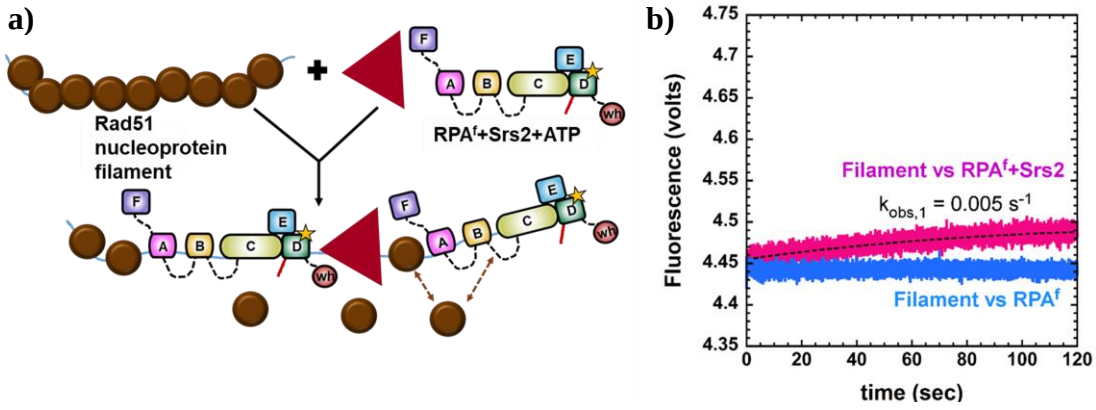

Figure 2-13: Srs2 regulates Rad51 filament disassembly and RPA exchange. a) Schematic of events during filament disassembly. The brown arrows denote removal of RPA^f upon Rad51 rebinding. **b)** In filament clearing experiments, a preformed Rad51 filament prevents RPA^f from binding to ssDNA (blue trace), however, when Srs2 is present in the reaction, a gradual increase in fluorescence is observed (pink trace) highlighting clearing of Rad51 molecules from ssDNA by Srs2 followed by RPA^f binding to ssDNA. The data displays a single exponential profile (dotted line) with $k_{obs} = 0.005 \pm 0.001\ s^{-1}$.

RPA has been shown to promote Rad51 filament disassembly by Srs2 and is proposed to sequester the ssDNA substrate following Rad51 dissociation (Krejci et. al., 2003). To test this model, we preformed Rad51 nucleoprotein filaments on a $(dT)_{97}$ substrate and rapidly mixed it with RPA^f in the absence or presence of Srs2 (Fig 2-2 e). In the absence of Srs2, no RPA^f binding is observed. However, when Srs2 is present in the reaction, an increase in fluorescence is observed ($k_{obs} = 0.005 \pm 0.002\ s^{-1}$; Fig 2-13 b). These data suggest that Srs2 displaces Rad51 and enables binding of RPA^f to the free ssDNA. However, it should be noted that Rad51 displaces RPA (Fig 2-12 b), hence the apparent rate for filament clearing would also be severely influenced by RPA^f removal by Rad51. The presence of mediator proteins during homologous recombination might enable stabilization of RPA on the ssDNA.

2.3.5 Single molecule DNA curtain analysis of RPA^{f} dynamics in HR

Using ncaa to generate fluorescent DNA binding proteins will be useful in single molecule analysis of enzyme reactions because it overcomes the need to attach genetically encoded fluorophores. This approach is vital to studying proteins such as Rad51 and RecA, which are rendered inactive when GFP is tethered to the termini (Fischer et. al., 2010). We have previously shown that GFP- or mCherry-tagged RPA can be used for preparing and visualizing ssDNA curtains for single molecule studies of HR intermediates (Gibb, Ye, Kwon, et. al., 2014a). As a proof of principle, we next sought to determine whether RPA^{f} could also be used in double-tethered ssDNA curtain measurements to visualize the RPA^{f}-ssDNA complexes and monitor assembly of the Rad51 presynaptic complex (Fig 2-14 a, b). For these experiments, long ssDNA substrates (~50 knt) were loaded into a sample chamber and tethered to a lipid bilayer through a biotin–streptavidin linkage that also serves to prevent non-specific protein binding to the surface of the flowcell. Flushing the chamber with buffer containing 100 pM RPA^{f} revealed ssDNA-RPA^{f} complexes when visualized by total internal reflection fluorescence microscopy (TIRFM; Fig 2-14 b). To further establish if these are bonafide ssDNA–RPA^{f} complexes, we next tested whether Rad51 is able to displace RPA^{f}. Injection of 2 μM wild type Rad51 (dark/unlabeled) in the presence of 2 mM ATP resulted in the rapid loss of fluorescence signal as RPA^{f} is displaced from the ssDNA (Fig 2-14 d). Consistent with previous findings, (Gibb, Ye, Kwon, et. al., 2014a) these presynaptic Rad51 filaments remained stable on the ssDNA, even after flushing unbound Rad51 and introducing 100 pM free RPA^{f} into solution for 30 min. Switching to a buffer that is identical except that it lacks ATP shows rapid return of RPA^{f} signal as the Rad51-

ADP dissociates and is replaced by RPA^f (Fig 2-14 d). These experiments highlight the utility of RPA^f for use in single molecule experiments of recombination intermediates where large genetically-encoded fluorescent tags could potentially confound measurements or affect protein function.

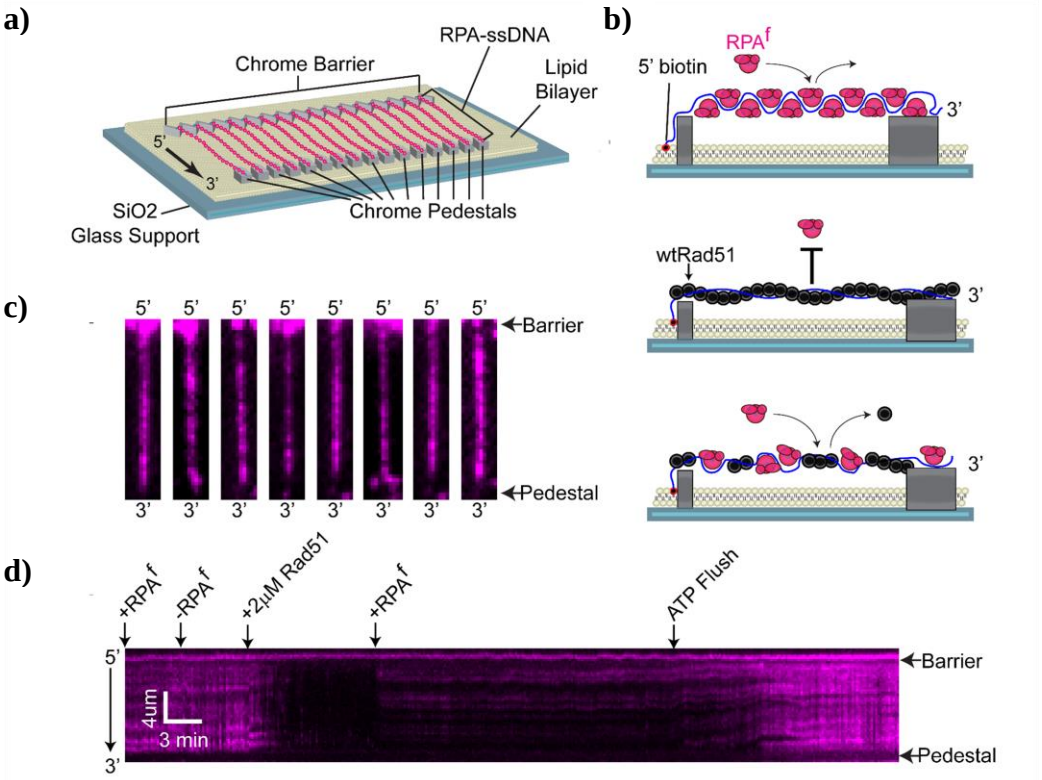

Figure 2-14: ssDNA curtains to visualize RPA^f. a) Schematic of a RPA-coated double-tethered ssDNA curtain. **b)** Representative examples of individual ssDNA molecules bound by RPAf (shown in magenta). The 5′-biotin tether is oriented at the top of each window that are all 2.7 × 13.5 μm. **c)** Schematic showing the ssDNA curtain experiment time course beginning in the top panel with an RPA-coated ssDNA molecule. Injecting 2 μM Rad51 displaces RPA^f from the ssDNA to form the pre-synaptic filament that is resistant to rebinding of RPA^f in the middle panel. Flushing ATP from the system results in spontaneous Rad51 dissociation and the re-binding of RPAf. **d)** A representative kymograph of a ssDNA molecule through time. At the start, ssDNA is already coated by RPA^f and buffer containing 100 pM RPA^f is flowing through the chamber at 0.2 ml/min. Switching to a buffer lacking RPA^f shows that bound RPA^f remains stable until the introduction of 2 μM wild type Rad51 when flow is stopped. The loss of RPA^f signal is evidence that Rad51 outcompetes the bound RPA^f to form a pre-synaptic filament. Resuming flow with buffer containing 100 pM RPA^f and 2 mM ATP shows the ssDNA remains dark as RPAf cannot displace Rad51. However, switching to buffer with 100 pM RPA^f and no ATP shows assembly and disassembly of a wild type Rad51 filament on an RPA^f-coated ssDNA molecule.

2.4 Discussion

Multiple DNA binding proteins function together during all DNA metabolic process such as replication and repair. To investigate the mechanism of action of a single enzyme that functions in a multi-protein context, a quantifiable experimental signal from the enzyme of interest is required. In this study, we generated a fluorescent version of RPA (RPA^{f}) utilizing the ncaa methodology. 4AZP was used as the ncaa and inserted at position 101 in the RPA32 subunit. W101 in one of two aromatic residues in RPA32 proposed to interact with DNA. However, mutation of both aromatic residues does not affect DNA replication as the mutant cells show normal growth rates (Dickson, Krasikova, Pestryakov, Lavrik, & Wold, 2009). A slight sensitivity to UV damage is observed in the double mutant (Brill & Bastin-Shanower, 1998; Rosenkranz et. al., 2006). The MB543 fluorescent dye was covalently attached to RPA^{4AZP} using strain-promoted azide–alkyne cycloaddition. Upon binding to ssDNA, RPA^{f} generates a robust and quantifiable change in florescence, and the DNA binding properties of RPA^{f} are similar to RPA^{WT} including stoichiometric and rapid binding to ssDNA (Fig 2-5, 2-7 and 2-8). This approach leaves all the cysteine residues intact and generates functional RPA complexes. This methodology is an attractive alternative to using genetically-encoded fluorophores which are large, interfere with function, and have positional limitations for attachment.

RPA is a unique protein that functions as a control hub to recruit various proteins, thereby coordinating almost all DNA metabolic processes in the cell (Sugitani & Chazin, 2015). By monitoring the change in fluorescence signal in RPA^{f} we can selectively investigate its dynamics in multi-protein reactions such as HR. Here, we have captured

the kinetics of RPA binding, dissociation, and facilitated exchange during HR in in the presence of the Rad51 recombinase and Srs2, an anti-recombination mediator. Multiple DNA binding proteins are required to orchestrate HR and are present together during various steps in the reaction. The 5′ ends flanking a dsDNA break are nucleolytically cleaved during resection to yield ssDNA overhangs that are sequestered by RPA (Mazón et. al., 2010; Mimitou & Symington, 2009). We show that RPA^f binds rapidly to free ssDNA (k_{obs} = 23 ± 1.2 s^{-1}; Fig 2-7 c) and self-exchanges at a 6–7-fold slower rate (k_{obs} = 3–4 s^{-1}; Fig 2-10 c). These data show that RPA bound to ssDNA are stable, as described previously (Niedziela-Majka, Chesnik, Tomko, & Lohman, 2007). During pre-synapsis, RPA bound to ssDNA needs to be displaced for Rad51 to bind and form the nucleoprotein filament. Pro-recombination mediator proteins such as Rad52 and BRCA2 are known to promote the binding of Rad51 on RPA-coated ssDNA (Tomko et. al., 2012; C. G. Wu et. al., 2010; Xie et. al., 2013). RPA interacts with both Rad52 and BRCA2 and assembly of Rad51 on RPA-coated ssDNA is regulated through post-translational modifications (Kozlov, Cox, & Lohman, 2010; Tomko, Fischer, & Lohman, 2010). The observed rate of Rad51 binding and filament formation on naked ssDNA is ∼1.3 s^{-1} (Fig 2-11), whereas on RPA^f coated DNA, Rad51 binds and displaces RPA^f at ∼0.26 s^{-1} (Fig 2-12 b). These data suggest that Rad51 displaces RPA at ∼15-fold slower rate compared to the RPA facilitated self-exchange process. The difference in rate constants suggest that the mechanism of Rad51 binding to an RPA-coated ssDNA is different compared to facilitated self-exchange. The four OB-folds of RPA bind to ssDNA with different affinities and can be individually remodeled by other proteins to gain access to ssDNA (R. Chen et. al., 2016b; Gibb, Ye, Gergoudis, et. al., 2014). Such differences in DNA

binding affinities within the OB-folds allow RPA to be tightly bound on the ssDNA, while allowing access to other DNA binding proteins that they recruit during various DNA metabolic processes. However, for complete RPA displacement, all four OB-folds will have to dissociate from ssDNA.

During facilitated self-exchange, RPA^{f} could dissociate from the ends or internal regions and the vacant ssDNA binding site can now be occupied by unlabeled RPA. On the other hand, RPA has also been shown to diffuse on ssDNA (B. Nguyen et. al., 2014b) and could be pushed off by free RPA or other proteins (Chu Jian Ma et. al., 2017b). Our data suggests that an active sliding-pushing off mechanism might be more applicable as we observe different observed rate constants for facilitated-self exchange ($\sim$3.5 s^{-1}; Fig 2-10 c), facilitated exchange with SSB ($\sim$17 s^{-1}: Fig 2-10 f), and displacement by Rad51 (0.26 s^{-1}; Fig 2-12 b). However, a passive mechanism, where the individual DNA binding domains of RPA dissociates followed by replacement with another DNA binding protein, cannot be ruled out. In our experiments, a $(dT)_{97}$ ssDNA substrate is used where both ends of the DNA are free. Whether RPA can be removed effectively by other proteins in cases where the ends are blocked, as in a replication fork or dsDNA bound by histones, remains to be investigated. Sliding and diffusion models of RPA movement on ssDNA have been suggested and how these models fit into mechanisms of facilitated self-exchange versus Rad51-mediated displacement remain to be explored (Gibb, Ye, Gergoudis, et. al., 2014; B. Nguyen et. al., 2014b). While *in vitro* assays show that mediators such as Rad52 are not required to displace RPA from ssDNA, (Chu Jian Ma et. al., 2017b) mediators can enhance the rate of Rad51 nucleation and growth in HR reactions where other DNA structures and proteins are present.

Rad51 nucleoprotein filaments promote the search for homology and catalyze strand-exchange (synapsis) in HR followed by replication and strand resolution. The dynamics between Rad51 and RPA during pre-synapsis is of immense interest as mutations in Rad51, RPA, BRCA2 and Rad52 have all been linked to various cancerous states (P. A. Jeggo & Lobrich, 2015; Penny A. Jeggo, Pearl, & Carr, 2016). To capture the kinetics of Rad51 nucleation and filament growth in the presence of RPA and mediator proteins, we are currently developing ncaa-based fluorescent Rad51 to directly investigate its dynamics in HR. In other scenarios, Rad51 filaments are displaced by anti-HR mediator proteins such as the Srs2 helicase. In the presence of ATP, Rad51 forms a stable nucleoprotein filament on ssDNA substrates that is refractory to RPA rebinding (Fig 2-14 c, d). Previous studies have shown that Srs2 displaces Rad51 by stimulating ATP hydrolysis within the nucleoprotein filament and the reaction is enhanced in the presence of RPA (Antony et. al., 2009b; Qiu et. al., 2013; Van Komen, Reddy, Krejci, Klein, & Sung, 2003). Based on these studies, current models posit RPA sequestering the ssDNA behind the Srs2 helicase as it clears Rad51 molecules (Macris & Sung, 2005). We have measured the binding of RPA^f behind the Srs2 helicase during Rad51 filament clearing (Fig 2-13 a). RPA^f binding in this context occurs at $k_{obs} = 0.005\ s^{-1}$, much slower than the rates of Srs2 filament clearing previously reported (Antony et. al., 2009b; Davenport et. al., 2016). Since Rad51 can displace RPA^f in our experiments (Fig 2-12 b), RPA^f molecules that bind behind the Srs2 helicase will be exchanged by free Rad51 in the reaction. Thus, how RPA is stabilized during filament clearing remains to be established. One possibility is the contribution of a mediator protein that might stabilize RPA binding to DNA or post-translational modifications of Rad51 could prevent its

rebinding or exchanging RPA. Interestingly, our results suggest that a motor protein such as Srs2 is capable of displacing RPA^f from ssDNA. RPA^f–ssDNA complexes challenged with Srs2 show a small, but rapid initial drop in RPA^f fluorescence (k_{obs} = 8.5 ± 0.8 s^{-1}; Fig 2-12 d) followed by a plateauing of the signal. This suggests that RPA^f being displaced is either rapidly able to compete off Srs2 from ssDNA or binds to the free ssDNA behind the Srs2 helicase, causing the stabilization in fluorescence signal (Fig 2-12 c, d). Single molecule fluorescence experiments will be required to better understand these mechanisms and the ncaa methodology can be applied to generate fluorescently labeled proteins.

We show the application of RPA^f in single molecule DNA curtain assays where dynamics of RPA on long ~50 knt substrates are captured (Fig 2-14) Assembly of RPA^f molecules can be visualized and its displacement during facilitated self-exchange can be quantitated. Flowing in Rad51 with ATP displaces RPA^f and formation of the nucleoprotein filament is observed. When ATP is washed out of the reaction, Rad51 dissociates and binding of RPA^f is clearly visualized. The development of fluorescent Rad51 and mediator proteins will be applicable to monitoring their individual dynamics during HR and other DNA metabolic processes.

In summary, we have used RPA^f to describe its dynamics during HR. Since RPA coordinates several DNA metabolic processes, this approach now presents a powerful experimental tool to investigate its dynamics in DNA replication, replication restart, nucleotide excision repair, dynamics on telomeric ends, and other such processes on DNA. The use of ncaa to generate fluorescently-labeled proteins should be broadly applicable to investigating other processes in multi-protein systems. In addition, this

methodology enables click chemistry based attachment of dyes that will enable us to investigate conformational changes in this region using EPR and NMR specific probes.

CHAPTER 3: DYNAMICS AND SELECTIVE REMODELING OF DNA BINDING DOMAINS OF RPA

3.1 Introduction

In eukaryotic cells, RPA binds to transiently exposed ssDNA and serves as a hub protein to coordinate DNA replication, recombination, repair, and telomere maintenance(R. Chen & Wold, 2014a; Wold, 1997). Cellular functions of RPA rely on its high ssDNA binding affinity, ability to physically interact with over two dozen DNA processing enzymes, and to correctly position these enzymes on complex DNA structures. The precise mechanisms by which RPA functions in many contexts and how RPA differentiates between multiple DNA metabolic events is a long-standing puzzle (R. Chen & Wold, 2014a; Fanning et. al., 2006; Wold, 1997). RPA is heterotrimeric, flexible, and modular in structure. It is composed of three subunits: RPA70, RPA32 and RPA14 (Fig. 3-1 a, b), which harbor six oligonucleotide/oligosaccharide binding folds (OB-folds; labeled A through F). We refer to the DNA binding OB-folds as DNA binding domains (DBDs; Fig. 3-1 b). RPA binds to ssDNA with sub-nanomolar affinity but can be displaced by DNA binding proteins with much lower DNA binding affinity. Recent studies have suggested that the RPA-ssDNA complex is relatively dynamic (R. Chen et. al., 2016b; Gibb, Ye, Gergoudis, et. al., 2014; B. Nguyen et. al., 2014b) positing a selective dissociative mechanism where not all DBDs are stably bound to the DNA, whereas, microscopic dissociation of individual DNA binding domains occurs.

In all existing models for RPA function, DBDs A and B are assigned as high affinity binding domains. Purified DBD-A, DBD-B and DBD-A/DBD-B constructs bind ssDNA with K_d values of 2 μM, 20 μM and 50 nM, respectively (Arunkumar, Stauffer,

Bochkareva, Bochkarev, & Chazin, 2003; Bochkareva, Korolev, Lees-Miller, & Bochkarev, 2002; Iwona M. Wyka, Kajari Dhar, Sara K. Binz, & Wold, 2003). The trimerization core made up of DBD-C, DBD-D and DBD-E is considered to have a weaker ssDNA binding affinity (K_d> 5 μM) (Elena Bochkareva, Frappier, Edwards, & Bochkarev, 1998). Additionally, mutational analysis of individual aromatic residues that interact with the ssDNA in either DBD-C or DBD-D show minimal perturbations on ssDNA binding affinity (R. Chen et. al., 2016b). Paradoxically, in the crystal structure of the RPA-ssDNA complex (Fig. 3-1 b), the ssDNA interactions of all four DBDs are similar, with DBD-C having more contacts with ssDNA bases than DBD-A, DBD-B or DBD-D (Fan & Pavletich, 2012a). Thus, the exact nature of the contributions from each DBD to RPA function is likely complicated and may be influenced by the dynamics of DBD-ssDNA interaction.

Both the N-terminus of RPA70 and the C-terminus of RPA32 interact with distinct sets of RPA-interacting proteins (RIPs). During DNA processing, RIPs must displace RPA from ssDNA. Displacement may be achieved by modulating the DNA binding activity of specific DBDs within RPA. In such a model, a protein that exchanges for RPA does not dissociate all DBDs at once but displaces individual DBDs after gaining access to DNA that is transiently exposed by dissociation of a DBD. Moreover, if the RPA-ssDNA complex were to be considered as a sequential, linear assembly of DBDs as seen in the crystal structure, then depending on the DBD first displaced, a

downstream DNA binding protein could be positioned at the 5′ or 3′ end of the RPA-occluded ssDNA.

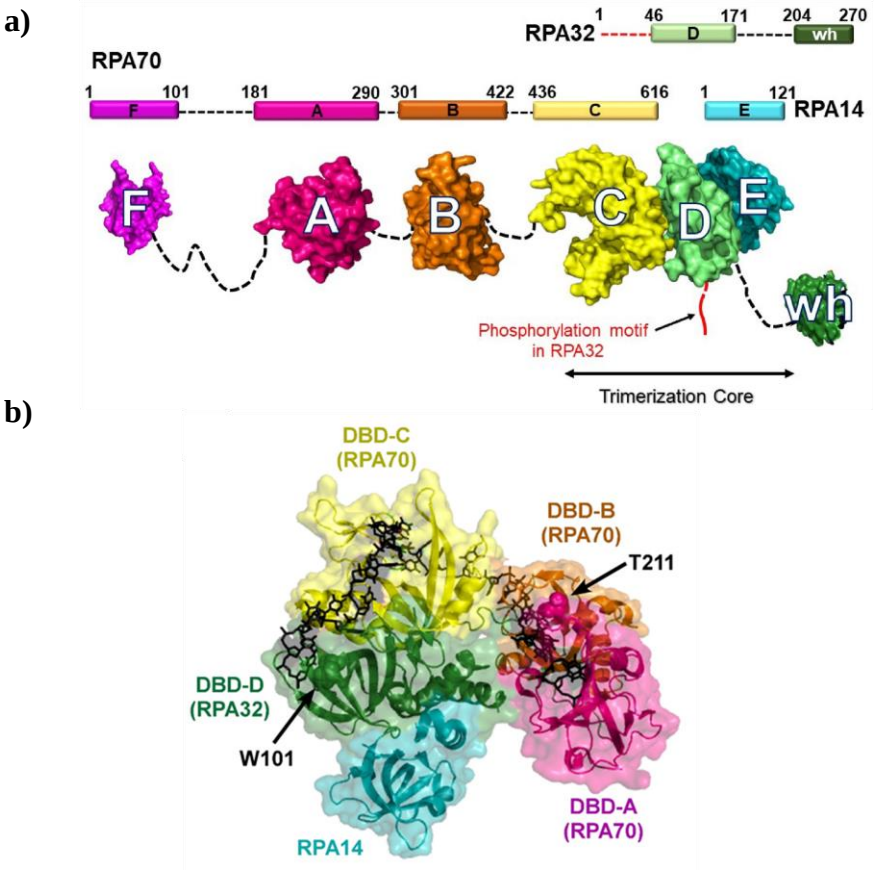

Figure 3-1: Non-canonical amino acid-based fluorescent RPAs report on individual DBD dynamics. a) The residue numbers for the three RPA subunits and their respective DNA binding domains (DBDs A-F) are denoted. The winged-helix (wh) domain in RPA32 and DBD-F in RPA70 mediate interactions with RPA-interacting proteins (RIPs). The N-terminus of RPA32 that is phosphorylated is shown in red. Crystal structures of the ordered domains are shown as surface representations with intervening disordered linkers as dotted lines (black). DBD-C, DBD-D and RPA14 interact to form the trimerization core. **b)** Crystal structure of the DNA binding domains of U. maydis RPA bound to ssDNA (PDB ID:4GNX). Residues T211 in DBD-A and W101 in DBD-D are sites where 4-azidophenylalanine (4AZP) is incorporated (residue numbering in Saccharomyces cerevisiae RPA). The bound ssDNA is shown as sticks (black).

The recombination mediator Rad52 is one example of a RIP. It belongs to a group of proteins that orchestrate homologous recombination (HR) and homology directed DNA repair. *S. cerevisiae* Rad52 regulates recombination by facilitating replacement of

RPA on ssDNA with the Rad51 nucleoprotein filament, an active species in homology search and DNA strand exchange (Benson, Baumann, & West, 1998; New, Sugiyama, Zaitseva, & Kowalczykowski, 1998; Akira Shinohara & Ogawa, 1998; Sung, 1997). Nucleation of the Rad51 filament is a slow and tightly controlled process as Rad51 fails to compete for binding to ssDNA with RPA (Sugiyama & Kowalczykowski, 2002b). Thus, Rad52 must physically interact with both RPA and Rad51 to promote Rad51 filament nucleation. The mechanism by which Rad52 loads Rad51 on the ssDNA is unclear except that Rad51 filament formation is simultaneous with displacement of RPA from ssDNA and likely proceeds through a Rad52-RPA-ssDNA intermediate (Sugiyama & Kowalczykowski, 2002b). Within this complex, Rad52 was shown to stabilize the RPA-ssDNA interaction (Gibb, Ye, Kwon, et. al., 2014a), further mystifying its assigned mechanism of action as a recombination mediator to displace RPA (Gibb, Ye, Kwon, et. al., 2014a).

To determine how individual DBDs work in the context of the full-length protein and investigate how proteins such as Rad52 modulate RPA binding, we generated fluorescent forms of RPA containing a non-canonical amino acid (ncAA) that is labeled with the fluorescent dye MB543 in either DBD A or D. When positioned near the DNA-binding site, MB543 produces a change in fluorescence intensity upon binding to ssDNA. Using direct measurements of full-length RPA carrying a fluorescently-labeled DBD binding to, and dissociating from ssDNA, we show that both DBD-A and DBD-D are highly dynamic, frequently binding to and dissociating from ssDNA. We also show that RPA-ssDNA complexes exist in at least 4 distinct conformational states offering differential access to the ssDNA within this complex. Rad52 interacts with the RPA-

ssDNA complex and selectively modulates the dynamics of DBD-D preventing its full engagement to ssDNA and thereby opening the 3′ end of the RPA-occluded sequence.

3.2 Materials and methods

3.2.1 Chemicals and reagents

Chemical reagents were purchased from Sigma-Aldrich (St. Louis, MO, USA) and Research Products International (Mt. Prospect, IL, USA). Resins used for protein purification were from the following vendors: Q-sepharose, Heparin and S200 from GE Healthcare (Pittsburgh, PA, USA); Ni^{2+}-NTA agarose form Gold Biotechnology (St. Louis, MO), and Biogel-P4 from Bio-Rad Laboratories (Hercules, CA, USA). Enzymes used for cloning and the Q5- quick change mutagenesis kit were purchased from New England Biolabs (Ipswich, MA, USA). 4-Azidophenylalanine (4AZP) was prepared from Fmoc-4-amino-phenylalanine (Angene Inc., Nanjing, China) as described . All fluorophores used to generate fluorescently labeled proteins were purchased from Click Chemistry Tools (Scottsdale, AZ, USA). BL21Ai and BL21 Rosetta pLysS cells were purchased from Thermo Fisher Scientific (Waltham, MA, USA).

3.2.2 DNA

Cy3-labeled, biotinylated and unmodified oligonucleotides were purchased form Integrated DNA Technologies (Coralville, IA).

3.2.3 Plasmids for Protein Expression

Plasmid plld_tscRPA carrying the open reading frames for all three RPA subunits from *S. cerevisiae* (Sibenaller et. al., 1998) was the template used to construct the wild type RPA plasmid (EANP-scRPA-70-32-14) by substituting the two original TAG stop codons with TAA stop codons using Q5 site-directed mutagenesis. This plasmid was used as the template to generate all further constructs described in this study. Q5 site-directed mutagenesis was used to insert the following polyhistidine (his^6) affinity tags and mutations: To generate fluorescent RPA-DBD-A, a his^6 tag was first introduced at the C-terminal end of RPA70 using the following primers – 5′ CACCATCACTAATGGATCTCGATCCCG 3′ and 5′ GTGATGATGAGCTAACAAAGCCTTGGATAAC 3′ to generate plasmid EANP-scRPA-70^{his6}-32-14. An amber suppression codon ‘TAG’ was introduced at the position corresponding to T 211 using the following primers - 5′AGAAATTAAATAGTGGCACAATCAAAGAG 3′ and 5′ CCCTTGTAGGAAACTCTTG 3′ (EANP-scRPA-$70^{his6\text{-}T211TAG}$-32-14). Generation of the plasmid for fluorescent RPA-DBD-D (EANP-scRPA-70-32 $^{his6\text{-}W101TAG}$ -14) was previously described (section 2.2.2) (N. Pokhrel et. al., 2017). To generate RPA-FAB, the open reading frame encompassing the N-terminus (DBD-F), DBD-A and DBD-B of *S. cerevisiae* RPA70 (amino acids 1-422) was amplified from plasmid EANP-scRPA-70-32-14 and a his^6 tag was inserted at the end of DBD-B using primers 5′GGAGATATACCATGGGCAGTGTTCAACTTTCGAGGGG 3′ and 5′ATAAAATAGGATCCTTAGTGGTGATGATGGTGATGGTTTGCGTTGCGGCCC 3′. This was subsequently sub-cloned into a pRSFDuet-1 vector using *Nco*I and *Bam*HI

restriction sites (EANP-scRPA-F-A-B^{his6}). A TAG codon was introduced at position T211 in DBD-A (EANP-scRPA-F-$A^{T211TAG}$ -B^{his6}) to incorporate non-canonical amino acids during protein purification. The plasmid to purify CBD tagged *S. cerevisiae* Rad52 was a kind gift from Dr. Eric Greene (Columbia University, NY) (Described in detail in chapter 5, section 5.2.1 and 5.2.2).

3.2.4 Proteins

4AZP (4-azidophenylalanine) incorporated RPA were purified as described (chapter 2, section 2.2.3- 2.2.4) with the following modifications. Stock 4AZP solutions for a 1 L culture were prepared by dissolving 206 mg of 4AZP in 2 ml of 100% methanol and then diluted with 3 ml of ddH_2O and added to the culture (1 mM final concentration) during induction of protein expression with IPTG and arabinose. Wild-type RPA (RPA^{wt}) was purified as described with the addition of a final ssDNA cellulose separation as described (chapter 2, section 2.2.3). RPA^{4AZP} was purified as described in methods section of chapter 2, section 2.2.3), with the following modifications: The protein eluates containing RPA^{4AZP} from the Ni^{2+}-NTA column was diluted with buffer H^0 (30 mM HEPES, pH 7.8, 0.1 mM EDTA, 10% glycerol (v/v)) to match the conductivity of H^{100} (superscript denotes concentration of KCl in mM) and fractionated over a 10 ml heparin column equilibrated with buffer H^{100}. RPA^{4AZP} was eluted with a linear gradient of H^{100}-H^{1000}. Fractions containing RPA^{4AZP} were pooled, diluted with buffer H^0 to a conductivity equivalent to H^{100} and applied on to a 25 ml (bed volume) ssDNA column. The column was sequentially washed with 200 ml of buffer H^{300} followed by 150 ml of H^{500}. RPA^{4AZP} was step eluted with H^{2000}. Fractions containing RPA^{4AZP} were dialyzed in storage buffer

(30 mM Hepes, pH 7.8, 100 mM KCl, 10% glycerol (v/v)) and subjected to labeling with fluorophore or flash frozen in liquid nitrogen and stored at -80^{o}C. Site-specific Incorporation of 4AZP was confirmed using mass spectrometry. We did not see difference in activity of RPA^{4AZP} with or without the use of ssDNA column in the purification process. RPA-FAB and RPA-FAB^{4AZP} proteins were generated by co-transforming the respective plasmids and pDULE2-CNF in Rossetta (DE3)pLysS cells, expressed, and purified as described above for the full length RPA^{4ZP} versions, with the following modifications. Eluates containing RPA-FAB from the Ni^{2+}-NTA chromatography step were pooled and diluted with buffer H^{0} to match the conductivity of buffer H^{100} and applied on to a 10 ml Q-sepharose column equilibrated with buffer H^{100}. FAB^{4AZP} does not bind to the Q-sepharose column and comes out in the flow-through. The Q-sepharose column was further washed with 100 ml of buffer H^{100}. The flow-through and wash fractions from the Q-sepharose column were combined and fractioned over a 10 ml Heparin column equilibrated with H^{100} buffer. Protein was eluted using a linear gradient of H^{100}-H^{2000}. Fractions containing FAB^{4AZP} were pooled, concentrated using an Amicon spin concentrator (30 kDa molecular weight cut-off), and subjected to labeling with fluorophores.

S. cerevisiae Rad52 was purified as described in (Gibb, Ye, Kwon, et. al., 2014a) with the following modifications. Rad52 was fractionated using a 20 ml chitin sepharose column and fractions containing Rad52 were pooled and diluted with buffer R (50 mM Tris-HCl, pH 7.5, 1 mM EDTA, pH 8.0, 1X protease inhibitor cocktail, 10% glycerol (v/v)) to a conductivity equivalent to buffer R^{200} (subscript denotes concentration of NaCl in mM) and applied on to a 10 ml heparin column equilibrated with buffer R^{200}. Rad52 was eluted with a linear gradient of R^{200}-R^{1000}. Fractions containing Rad52 were pooled, diluted with

buffer R to a conductivity equivalent to R^{100} and purified further over a 25 ml ssDNA cellulose column using a linear gradient of R^{100}-R^{1500}. Fractions containing Rad52 were pooled, concentrated using a Amicon spin concentrator (30 kDa molecular weight cut-off) and dialyzed in storage buffer (20 mM Tris-HCl, pH 8.0. 200 mM NaCl, 0.2 mM EDTA, pH 8.0, 10% glycerol (v/v)). Rad52 was flash frozen with liquid nitrogen and stored at -80^{o}C. **A detailed procedure is mentioned in section 5.2.2 of chapter 5.**

3.2.5 Generation of fluorescently labeled RPA variants

RPA variants carrying 4AZP were labeled with MB543, Cy3 or Cy5 as described in the section 2.2.4 of chapter 2, with the following modifications. Briefly, ~ 3 ml of RPA^{4AZP} (10 μM) was incubated on a rocker with 1.5-fold molar excess (15 μM) of either DBCO-MB543, DBCO-Cy3 or DBCO-Cy5 for 2 hours at 4 ^{o}C. Labeled RPA variants were separated from excess dye using a Biogel- P4 gel filtration column (65 ml bed volume) using storage buffer (30 mM HEPES, pH 7.8, 100 mM KCl and 10% (v/v) glycerol). Fractions containing labeled RPA were pooled, concentrated using a 30 kDa cut-off spin concentrator and flash frozen using liquid nitrogen. Fluorescent RPA were stored at -80 ^{o}C. Labeling efficiency was calculated using absorption values measured at 280 nm and ε_{280}= 98500 $M^{-1}cm^{-1}$for RPA, at 550 nm with ε_{550}= 105,000 $M^{-1}cm^{-1}$for DBCO-MB543, at 555 nm with ε_{555}= 150,000 $M^{-1}cm^{-1}$for DBCO-Cy3, and at 650 nm with ε_{650}= 250,000 $M^{-1}cm^{-1}$ for DBCO-Cy5 fluorophores. A correction factor was applied to the final concentration of labeled protein (See appendix II (section 9.1-9.4) for detailed procedure). We obtain 45 ± 17 % and 40 ± 25 % labeling efficiencies for the RPA-DBD-A^{MB543} and RPA-DBD-D^{MB543} versions, respectively.

3.2.6 Fluorescence measurements

Fluorescence spectra were obtained using a PTI QM40 instrument (Horiba Scientific, Edison, NJ). For RPA-DBD-A^{MB543}, RPA-DBD-A^{Cy5} and RPA-DBD-A^{Cy3} slit widths were set at 1.25 nm for excitation and 3 nm for emission. For RPA-DBD-D^{Cy3} and RPA-DBD-D^{Cy5} slit widths were set at 0.5 nm for excitation and 2 nm for emission. For RPA-DBD-A^{MB543}, 2 ml of 50 nM RPA-A^{MB543} in reaction buffer (30 mM Hepes, pH 7.8, 100 mM KCl, 5 mM $MgCl_2$, 1 mM β-mercaptoethanol and 6 % v/v glycerol) was added to a quartz cuvette, and the spectra were collected in the absence or presence of 50 nM ssDNA [$(dT)_{45}$] or ds plasmid DNA (100 nM nucleotides) with constant stirring. Samples were excited at 535 nm and emission spectra (555 – 600 nm) were recorded. A similar experimental setup was used to obtain fluorescence spectra for 50 nM RPA-FAB^{MB543} upon addition of 100 nM $(dT)_{45}$. For RPA-DBD-D^{Cy3} and RPA-DBD-A^{Cy3}, 2 ml of 100 nM protein was used and 100nM of $(dT)_{45}$ was added with constant stirring. The samples were excited at 559 nm and emission spectra (539 nm- 579 nm) were recorded. Similarly, for RPA-DBD-A^{Cy5} and RPA-DBD-D^{Cy5}, 2 ml of 100 nM proteins were used and 100 nM of $(dT)_{45}$ were added to the reaction. Samples were excited at 690 nm and emission spectra (640- 700 nm) were recorded. All experiments were performed at 25 °C.

3.2.7 Site-size measurement

The total number of nucleotides occupied by RPA variants (RPA-wt, RPA-DBD-A^{MB543} and RPA-DBD-D^{MB543}) in reaction buffer was determined as previously described using poly(dT) ssDNA (Kumaran et. al., 2006). Briefly, 1.95ml of 100nM RPA in

reaction buffer (30mM HEPES, pH 7.8, 5mM $MgCl_2$, 6% glycerol (v/v), 1 mM βME, 100 mM KCl) was added to a 2ml quartz cuvette. First, to determine the fixed emission wavelength to be used in the experiment, using a fluorometer, RPA was excited at 290nm and emission spectra (300-350) collected. The peak emission wavelength ($\lambda_{emi\ (max)}$) was noted, and used for rest of the experimentation.

For rest of the experiment, RPA was excited at λ_{exci}: 290nm and emission collected at $\lambda_{emi\ (max)}$, for a total of 10 seconds (time-based setting in the fluorometer). 100nM RPA was titrated with increasing concentrations of Poly(dT) (0.5 μM to 12 μM), and decrease in tryptophan fluorescence recorded. (Note: Each titrant (aliquot) consisted of 2μl 495μM Poly(dT). In total, 24 aliquots were added and addition of each aliquot increased the concentration of Poly(dT) in the cuvette by 0.5μM.). Following addition of each aliquot of Poly(dT), samples in the cuvette were mixed thoroughly by stirring for a minute, and emission collected for 10 seconds. The resulting data was analyzed using the tabulation worksheet from Timothy Lohman's Lab, Department of Biochemistry and Molecular Biophysics, Washington University School of Medicine, St. Louis, MO, USA, and plotted to determine the site-size.

3.2.8 DNA Binding

The DNA binding activity of unlabeled and fluorescent RPA was measured using electromobility band shift analysis. 50 nM of ^{32}P-labeled $(dT)_{30}$ oligonucleotide was incubated with increasing concentrations of RPA-wt or RPA-DBD-A^{MB543} or RPA-DBD-D^{MB543} (0 – 1 μM) in reaction buffer for 10 minutes at 4 ºC. 1 ml of DNA loading dye (50

% v/v glycerol and 0.2 % w/v bromophenol blue in 1 X TBE) was added to the samples and resolved using an 8 % TBE-acrylamide gel (110 volts, 25 °C). Gels were exposed overnight onto a phosphorimaging screen and scanned using a STORM scanner (GE Healthcare, Pittsburgh, PA). Bound and unbound DNA signals were quantitated using ImageQuant software and the fraction ssDNA bound to RPA was calculated using the equation:

((bound ^{32}P signal)/(bound ^{32}P signal + unbound ^{32}P signal))*[ssDNA] (Eq. 1)

Detailed procedure for radiolabeling nucleotide and preparation of 8% TBE gel is described in section 2.2.6 of chapter 2.

3.2.9 Stopped flow analysis of RPA-DNA interactions

Stopped-flow experiments described below to monitor RPA – ssDNA dynamics were performed using an Applied Photophysics SX20 instrument (Surrey, UK) in reaction buffer (30 mM Hepes, pH 7.8, 100 mM KCl, 5 mM $MgCl_2$, 1 mM β-mercaptoethanol and 6 % v/v glycerol) at 25 °C. All the concentrations mentioned in the methods are ‘pre-mixing’ concentrations which are reduced to half upon mixing the samples to provide final ‘post- mixing’ concentrations. RPA labeled with MB543 were excited at 535 nm and emission was monitored using a 555 nm cut-off filter (Newport corp., Irvine, CA). Changes in tryptophan fluorescence were monitored by exciting the samples at 290 nm and emission was measured using a 350 nm cut-off filter. For the FRET experiments, the Cy5-labeled RPA and Cy3-labeled DNA samples were mixed and excited at 555 nm and changes in Cy5 fluorescence was monitored with a 645 nm cut-off emission filter.

3.2.10 RPA-DBD-A^{MB543}, RPA-DBD-D^{MB543} and RPA-FAB^{MB543} ssDNA binding kinetics

To quantitate RPA-DBD-A^{MB543}, RPA-DBD-D^{MB543} or RPA binding to ssDNA, 200 nM of the respective protein was rapidly mixed with 200 nm of $(dT)_{25}$ oligonucleotide, and the change in MB543 fluorescence was captured. All the data were fitted using either Kaleidagraph or Kintek Explorer to obtain the appropriate rate constants. For RPA-DBD-A^{MB543}, the data were fit to a two-step model:

$$\Delta f = A_1(1-e^{-k1*t}) + A_2(1-e^{-k_2*t}) + k_3*t \qquad \text{(Eq. 2)}$$

Where, Δf is the change in fluorescence signal, A_1 and A_2 are the amplitude of fluorescence change, and k_1, k_2, and k_3 are the observed rate constants and t is time. For RPA-DBD-D^{MB543} and RPA-FAB^{MB543}, the data were well described by a single step binding model defined phenomenologically by a single exponential plus linear equation.

$$\Delta f = A_1(1-e^{-k1*t}) + k_2*t \qquad \text{(Eq. 3)}$$

3.2.11 RPA-DBD-A^{MB543}, RPA-DBD-D^{MB543}, and RPA- FAB^{MB543} association kinetics

To obtain the rate of association for DBD-A binding to ssDNA, 200 nM RPA-A^{MB543} in one syringe was rapidly mixed with increasing concentrations (50- 400 nM) of $(dT)_{35}$ oligonucleotide from the second syringe and the change in fluorescence of RPA-DBD-A^{MB543} was monitored. All the data obtained were analyzed using Eq.2 to obtain observed rate constants. $k_{obs,1}$ was plotted against $[(dT)_{35}]$ and a linear fit was used to generate a rate for DBD-A binding to ssDNA. Similarly, to measure DBD-D binding to ssDNA, 200nM RPA-DBD-D^{MB543} in one syringe was rapidly mixed with increasing

concentrations (50- 400 nM) of $(dT)_{35}$ oligonucleotide from the second syringe and the change in fluorescence of RPA-D^{MB543} was monitored. Finally, to obtain the rate of association of FAB binding to ssDNA, 300 nM of FAB^{MB543} in one syringe was rapidly mixed with increasing concentration of $(dT)_{30}$ oligonucleotide (100-1000 nM) from the second syringe and the change in fluorescence of FAB^{MB543} was monitored. For RPA-DBD-D^{MB543} and RPA-FAB^{MB543}, all the data obtained were analyzed using Eq.3 to obtain observed rate constants. $k_{obs,1}$ was plotted against $[(dT)_{35}]$ and against $[(dT)_{30}]$ for RPA-DBD-D^{MB543} and RPA-FAB^{MB543} respectively. A linear fit was used to generate a rate for DBD-D and FAB binding to ssDNA.

3.2.12 RPA-A^{MB543} and RPA-D^{MB543} length dependent association kinetics

To measure the oligonucleotide length dependent rate of association for DBD-A, 200 nM RPA-DBD-A^{MB543} was rapidly mixed with 200 nM $(dT)_8$, $(dT)_{10,}$ $(dT)_{15,}$ $(dT)_{20,}$ $(dT)_{25,}$ $(dT)_{30}$ or $(dT)_{35}$ and change in fluorescence was monitored. All the data obtained were analyzed using Eq.2 to obtain the observed rates. $k_{obs,1}$ was plotted against $(dT)_n$ to determine the rate for oligonucleotide length dependent association of DBD-A. Using the same concentration of reactants, similar experiments were performed with RPA-DBD-D^{MB543} and RPA-FAB^{MB543} to measure the oligonucleotide length dependent rate of association for DBD-D. All the data obtained were analyzed using Eq.3 to obtain the observed rates. $k_{obs,1}$ was plotted against $(dT)_n$ to determine the rate for oligonucleotide length dependent association of FAB and DBD-D.

3.2.13 RPA-DBD-A^{Cy5} and RPA-DBD-D^{Cy5} polarity for DNA binding

For all FRET experiments, samples (Cy3) were excited at 555 nm and Cy5 fluorescence emission was monitored with a 645 nm long-pass emission filter. 5′ or 3′ Cy3-labeled DNA (100 nM) was mixed with the appropriate Cy5-labeled RPA protein and the change in Cy5 fluorescence was captured. Data were fit to Eq. 3 to obtain observed rate constants for the resulting change in fluorescence.

3.2.14 RPA-DBD-A^{MB543} and RPA-DBD-D^{MB543} facilitated exchange kinetics

200 nM of either RPA-DBD-A^{MB543} or RPA-DBD-A^{MB543} was premixed with 200 nM $(dT)_{25}$ in one syringe to form the RPA-DNA complex and rapidly mixed with increasing concentrations of RPA-wt from the second syringe (100 – 500 nM). The change in MB543 fluorescence was monitored, and the data were analyzed using Eq.3 to obtain observed rate constants. $k_{obs,1}$ was plotted against [RPA-wt] and a linear fit was used to generate a rate for the facilitated exchange processes.

3.2.15 RPA-FAB^{MB543} facilitated exchange kinetics

To measure the facilitated exchange kinetics of FAB^{MB543}, FAB^{MB543}- $(dT)_{30}$ complexes were pre-formed using 375 nM FAB^{MB543} and 100 nM $(dT)_{30}$ in one syringe. FAB^{MB543}- $(dT)_{30}$ complexes were rapidly mixed with increasing concentrations of RPA-wt from the second syringe (100 – 500 nM) and the change in fluorescence of FAB^{MB543} was monitored. All the data obtained were analyzed using Eq.3 to obtain observed rate

constants. $k_{obs,1}$ was plotted against [RPA-wt] and a linear fit was used to generate a rate for the facilitated exchange processes.

3.2.16 Tryptophan binding kinetics

Intrinsic tryptophan fluorescence was used to capture the binding of unlabeled and fluorescently labeled RPA variants to ssDNA in reaction buffer. 200 nM RPA (RPA-wt or RPA-DBD-A^{MB543} or RPA-DBD-D^{MB543}) was rapidly mixed with increasing concentrations (50- 400 nM) of $(dT)_{35}$ oligonucleotide and the change in Trp fluorescence was monitored by exciting the sample at 290 nm and measuring emission with a 350 nm cut-off filter. Data were fit using Eq.3 and $k_{obs,1}$ was plotted against [$(dT)_{35}$]. A linear fit was used to obtain the observed rate constants for RPA-DNA binding.

3.2.17 Single Molecule Experiments and Data analysis

All the experimental procedures for single-molecule imaging, data collection and analysis is described in (Nilisha Pokhrel et. al., 2019) and was carried by Colleen Caldwell in Dr. Maria Spies laboratory, University of Iowa, Iowa.

3.3 Results

3.3.1 Direct read out of DBD dynamics using non-canonical amino acids and fluorescence

Directly monitoring the dynamics (*binding, dissociation, or remodeling*) of a single enzyme in multi-protein reactions remains technically challenging. To decipher

how the DBDs of RPA function in the context of the heterotrimeric RPA complex, we labeled DBD-A or DBD-D (in RPA70 and RPA32, respectively; Fig. 3-2 a, b) of *S. cerevisiae* RPA (N. Pokhrel et. al., 2017) with MB543, an environmentally sensitive fluorophore. To confirm that labeling of RPA did not affect function, DNA binding properties of all fluorescent versions of RPA were extensively characterized and compared to the activity of wild type RPA. To compare DNA binding, stopped flow experiments were performed by mixing unlabeled or fluorescent RPA (RPA-A^{MB543} or RPA-D^{MB543}) with increasing concentrations of ssDNA [$(dT)_{35}$], and the change in intrinsic tryptophan fluorescence was measured (Fig 3-3 a-c). Unlike RPA labeled at individual DBDs with MB543, tryptophan signal changes reflect ssDNA binding and conformational changes within all DBDs of RPA. The data were fit as described in the Methods section and yielded observed rate constants (Fig. 3-3 d-f) for the two phases. Both rate constants, and their dependence on [DNA] were similar between unlabeled and fluorescent RPA, suggesting that fluorescent RPA have DNA binding activity similar to wild type RPA (Fig 3-3 f). We next performed electromobility band shift analysis (EMSA) to monitor RPA-ssDNA binding using radiolabeled $(dT)_{30}$. Fluorescent and wild-type RPA (50 nM) bound stoichiometrically to ssDNA (50 nM $(dT)_{30}$) (Fig. 3-4 a), again suggesting similar DNA binding properties. Finally, since each DBD binds to a distinct number of DNA bases (Fan & Pavletich, 2012a), we measured the occluded site-size of fluorescent and wild-type RPA using poly(dT) ssDNA and measured the change in intrinsic tryptophan fluorescence (Fig 3-4 b). Site-sizes for *S. cerevisiae* have been shown to vary between 18 – 27 nt (Kumaran et. al., 2006). Under our reaction conditions, wild type RPA occludes 20 nt/RPA and both RPA-DBD-A^{MB543} and RPA-DBD-D^{MB543}

occlude 20 nt/RPA (Fig. 3-4 b). These DNA binding experiments suggest that the activity of the fluorescent RPAs are similar to wild type RPA. RPA labeled at domain A (RPA-DBD-A^{MB543}) and domain D (RPA-DBD-D^{MB543}) produce enhanced fluorescence upon binding to ssDNA (Fig. 3-5 a, b) (N. Pokhrel et. al., 2017).

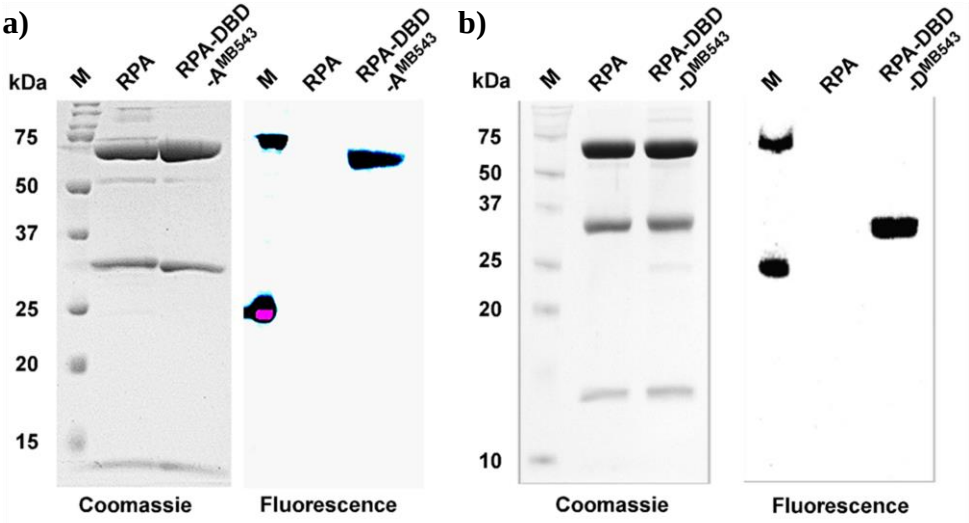

Figure 3-2: 12% SDS-PAGE gel showing site-specifically labeled DBD-A and DBD-D. a), b) left, Coomassie stained gel image showing all three subunits of RPA, while only a) right, RPA70, harboring DBD-A is visible in fluorescence scan and **b)** right, RPA32, harboring DBD-D, is visible in fluorescence scan.

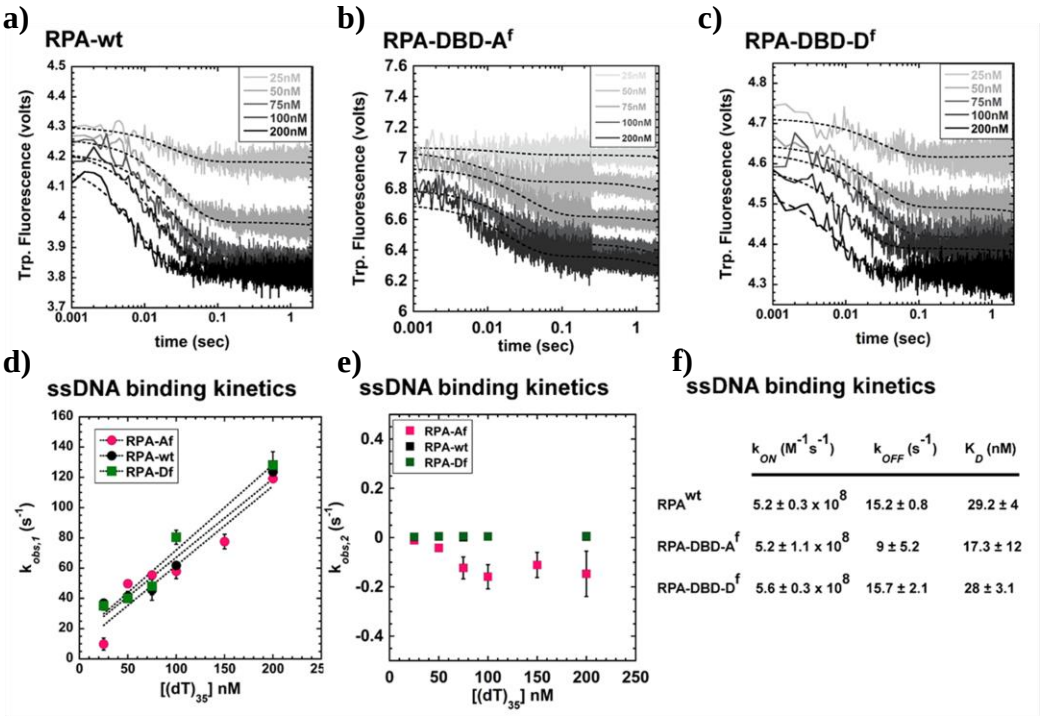

Figure 3-3: DNA binding properties of fluorescent RPA. Stopped flow experiments were performed by mixing 100nM **a)** RPA-wt, **b)** RPA-DBD-A^{MB543} or **c)** RPA-DBD-D^{MB543} with increasing concentrations of ssDNA [$(dT)_{35}$], and the change in intrinsic tryptophan fluorescence was recorded. **d) -f)** Data were fit as described in *methods* to obtain k_{off} and k_{on} values, and the apparent K_d values were calculated.

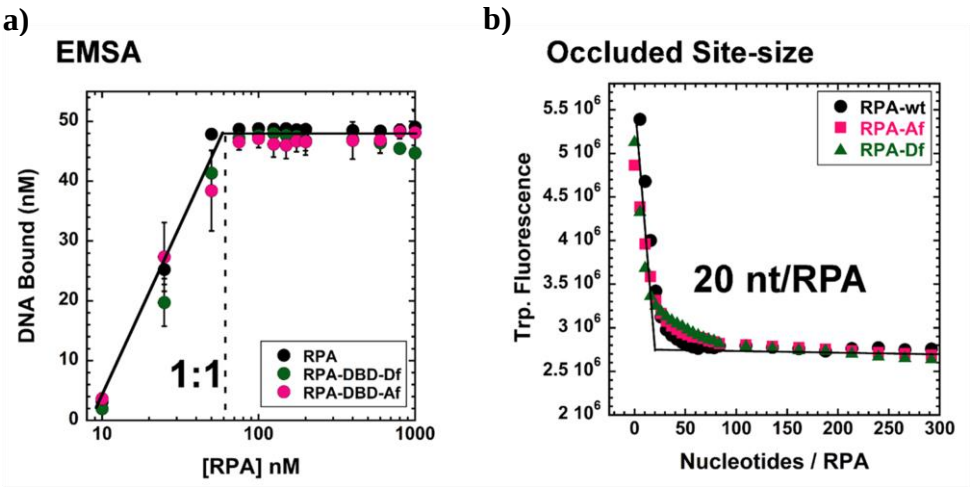

Figure 3-4: DNA occupancy of fluorescently labeled RPA. a) Stoichiometric binding of unlabeled or labeled versions of RPA to ^{32}P-labeled [$(dT)_{30}$] oligonucleotide (50 nM) is observed in EMSA experiments. **b)** Occluded site-size measurements were performed by adding increasing concentrations of poly(dT) ssDNA to RPA (0.2 μM) and monitoring the change in tryptophan fluorescence. All versions of RPA occlude ~20±2 nt/RPA in our reaction conditions (30 mM Hepes, pH 7.8, 100 mM KCl, 5 mM $MgCl_2$, 1 mM β-mercaptoethanol and 6 % v/v glycerol). These experiments show that the DNA binding properties of the labeled RPA are similar to the unlabeled wild type RPA complex.

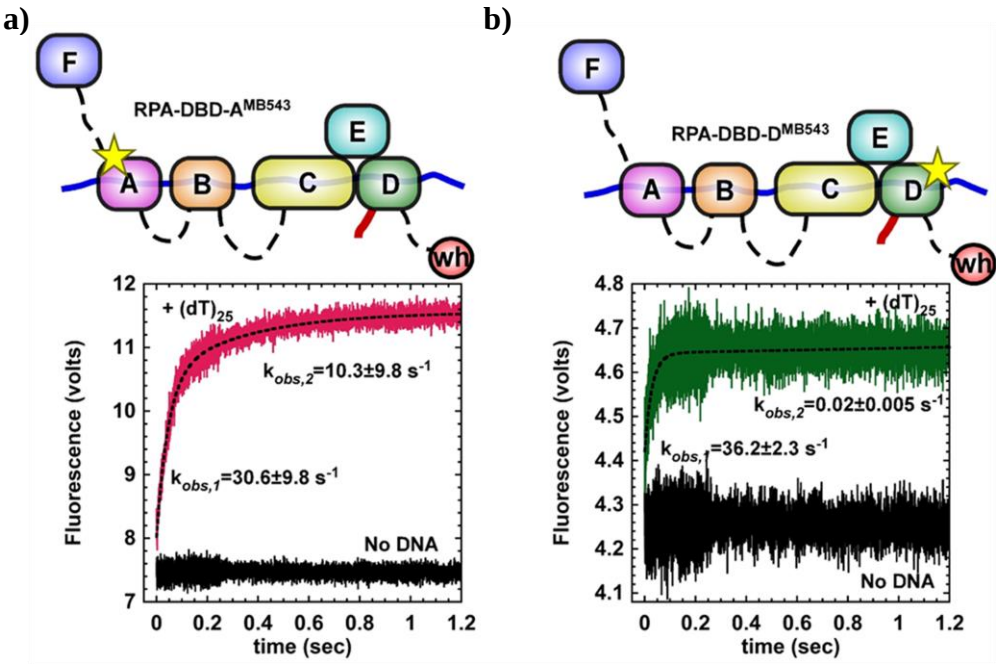

Figure 3-5: Fluorescently labeled RPA-DBD- A and RPA-DBD-D are responsive to DNA binding. A robust change in MB543 is observed upon **a)** RPA-A^{MB543} **b)** RPA-D^{MB543} binding to DNA. The observed change in fluorescence signal is specific for engagement of that particular DBD on DNA and directly reports DBD dynamics. Raw traces for each DBD-DNA engagement were fit according to the kinetic equations described in the methods section.

RPA binding to ssDNA is a paradigm for reactions where multiple DNA binding enzymes function together on a single DNA template. Knowledge of where, how, and when each enzyme gains access to the DNA in this multi-enzyme milieu is fundamental to deciphering when and how specific DNA repair/recombination processes are orchestrated. Site-specific labeling with MB543 allows us to monitor the dynamics of individual DBDs in the context of the full-length RPA heterotrimer and in multi-protein reactions. We measured the DNA binding kinetics for RPA-DBD-A^{MB543} and RPA-DBD-D^{MB543} providing direct read outs of each domain's engagement with ssDNA in the

context of full-length RPA. RPA-DBD-A^{MB543}or RPA-DBD-D^{MB543} were rapidly mixed with ssDNA [$(dT)_{25}$], and the change in fluorescence was measured (Fig. 3-5 a, b). Upon binding to ssDNA, both RPA-DBD-A^{MB543} and RPA-DBD-D^{MB543} produce a robust change in fluorescence intensity (Fig 3-5 a-b, 3-6 b, c), which is not seen for binding to double-stranded DNA (Fig 3-6 d) or in case of RPA-A^{Cy5}, when excited at 535nm and emission spectra monitored (Fig 3-6 e). The data for RPA-DBD-A^{MB543} is best described by a two-step model ($k_{obs,1}$ =30.6±9.8 s^{-1} and $k_{obs,2}$ = 10.3±9.8 s^{-1}), whereas intensity changes associated with RPA-DBD-D^{MB543} best fits a single-step DNA binding model (k_{obs} = 36.2±2.3 s^{-1}). The first step in both models is similar and reflects the initial interaction of RPA with ssDNA. The second step for RPA-DBD-A^{MB543} possibly reflects a rearrangement of DBD-A, as has been observed in structural studies (Brosey et. al., 2015a, 2013). To probe the nature of these differences further, we performed these binding experiments as a function of increasing DNA concentration using $(dT)_{35}$, which provides enough space for engagement of all the DBDs of RPA (Fig. 3-7 a-f). While measurements of RPA-ssDNA interaction footprints under our buffer conditions yield occluded site sizes of ~20 nt/RPA (Fig. 3-4 b), the modularity of the DBDs have been shown to produce occluded site-sizes between 18–28 nt (Kumaran et. al., 2006).

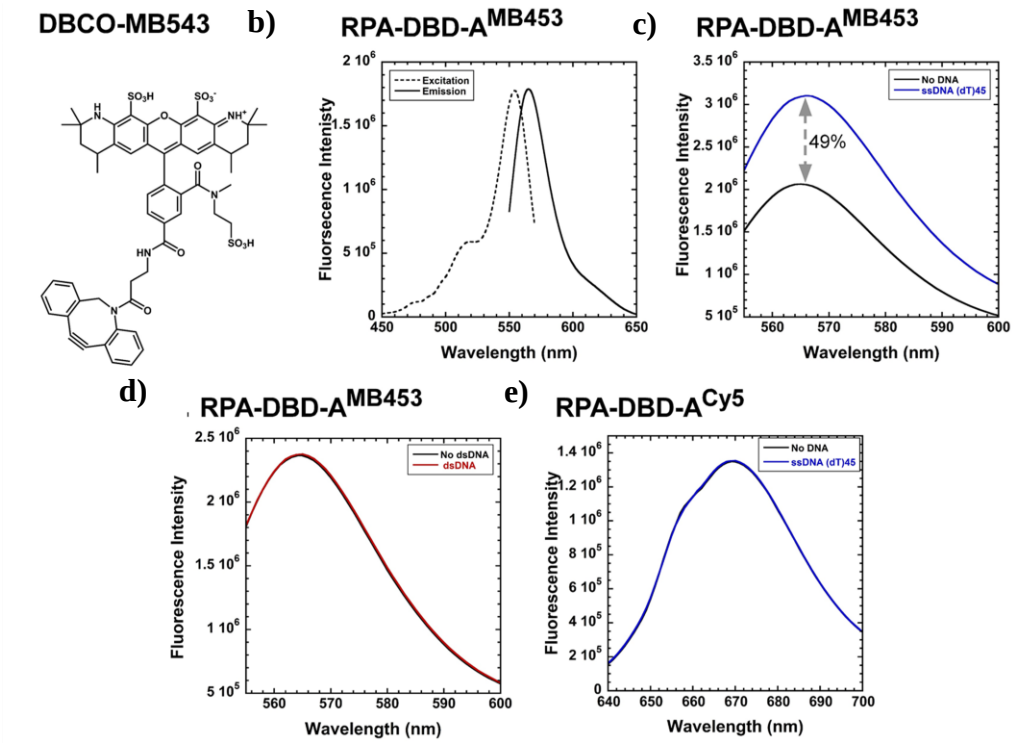

Figure 3-6: Spectral properties of fluorescent RPA. a) Structure of DBCO-MB543 used to fluorescently label RPA in this study. **b)** Excitation and emission spectra of RPA-DBD-A^{MB543} in solution. **c)** Percent change in fluorescence enhancement was measured for RPA-DBD-A^{MB543} in the absence or presence of ssDNA or **d)** dsDNA. The change in fluorescence is specific for ssDNA interactions with RPA. **e)** No change in fluorescence is observed for RPA-DBD-A^{Cy5} upon binding to ssDNA. Similar analysis for RPA-DBD-D^{MB543} is shown in Chapter 2, figure 2-5 a, b.

The observed rate for the first association step for both RPA-DBD-A^{MB543} and RPA-DBD-D^{MB543} increases as a function of DNA concentration yielding bimolecular k_{ON} values ($1.1\pm0.6 \times 10^{8} M^{-1}s^{-1}$ and $2.1\pm0.4\times10^{8} M^{-1}s^{-1}$, respectively; Fig. 3-7 c, f). The second step, observed only for RPA-DBD-A^{MB543}, is not linear (Fig. 3-7 c). This is consistent with a conformational rearrangement of DBD-A after the complex with ssDNA has been established and depends on the protein to DNA ratio in the reaction. Under conditions where RPA is present in excess over ssDNA, we clearly observe biphasic binding and dissociation/rearrangement phases for RPA-DBD-A^{MB543} (orange and pink traces in Fig. 3-7 b; 3-8 b), but not for RPA-DBD-D^{MB543} (Fig. 3-7 e, 3-8 e). These data suggest that the dynamics of individual DBDs are not identical, possibly reflecting different functional roles; as shown in our single-molecule studies.

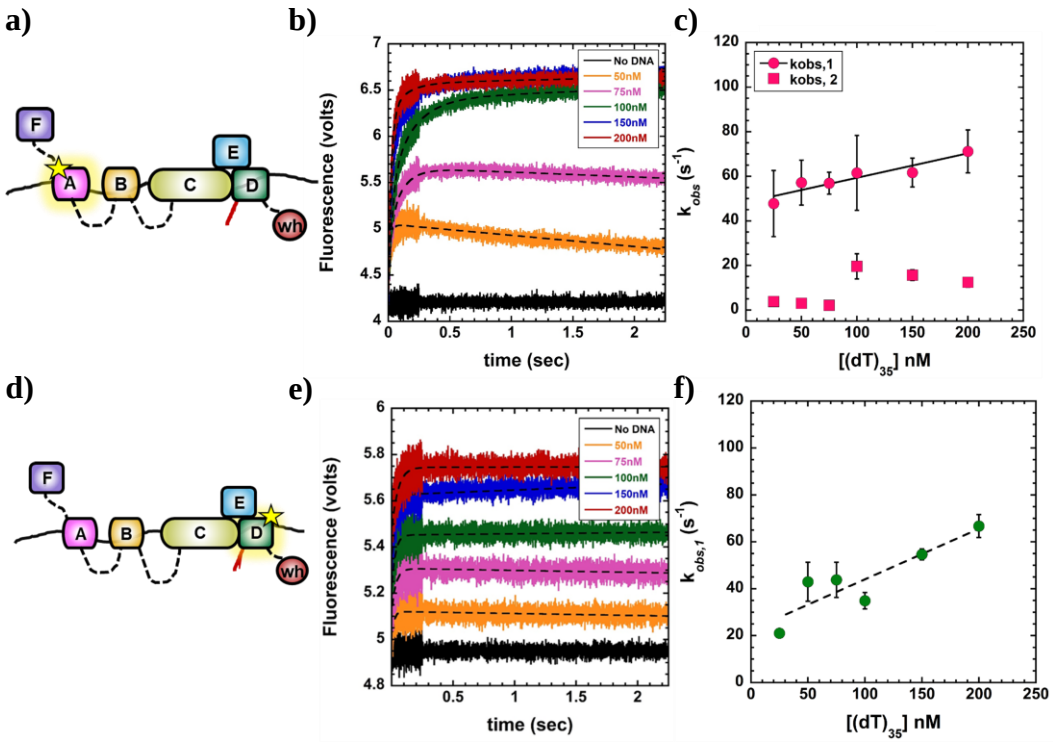

Figure 3-7: ssDNA concentration dependent binding of RPA-DBD-A and RPA-DBD-D. a), d) Diagrammatic representation of RPA-DBD-A^{MB543} or RPA-DBD-D^{MB543} binding to ssDNA and producing a change in fluorescence. Stopped flow experiments done with **b)** 100nM RPA-DBD-A^{MB543} **e)** 100nM RPA-DBD-D^{MB543} with increasing concentrations of [(dT)$_{35}$] ssDNA shows the observed rates in fluorescence change for **c)** RPA-DBD-A^{MB543} and **f)** RPA-DBD-D^{MB543}. The data for RPA-DBD-A^{MB543} are best fit using a two-step model whereas the data for RPA-DBD-D^{MB543} fit to a one-step process, suggesting distinct DNA context dependent changes in their dynamics.

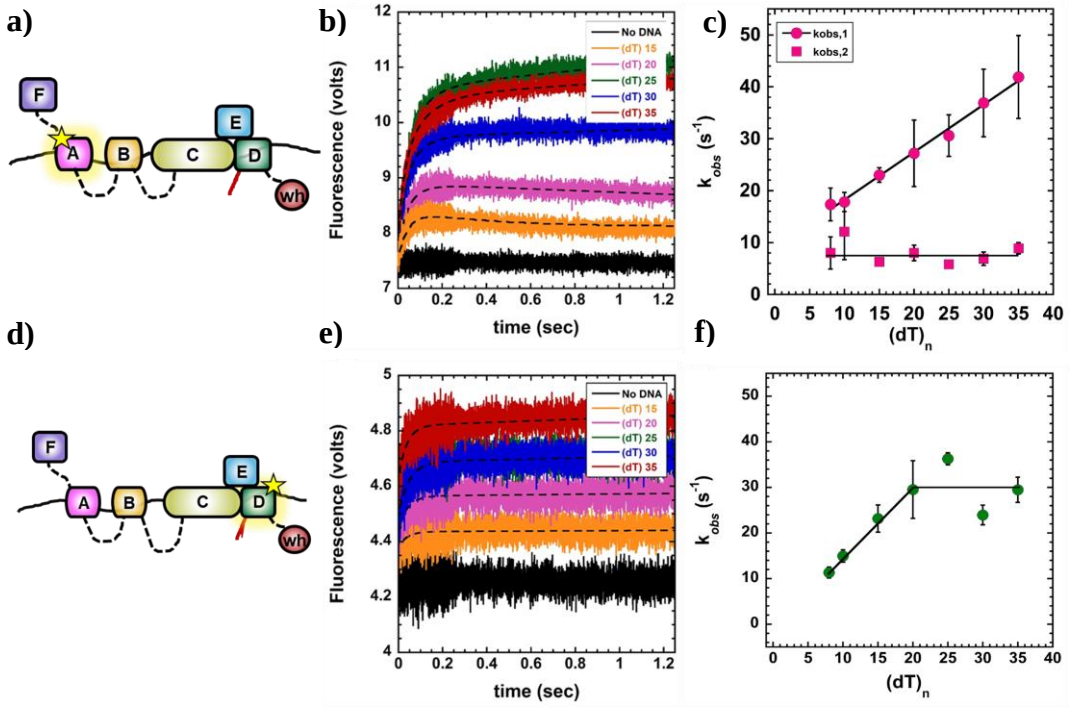

Figure 3-8: ssDNA length dependent binding of RPA-DBD-A and RPA-DBD-D. a), d) Cartoon diagram of RPA-DBD-A^{MB543} or RPA-DBD-D^{MB543} binding to increasing lengths of ssDNA and producing a change in fluorescence. Stopped flow experiments done with **b)** 100nM RPA-A^{MB543} **e)** 100nM RPA-D^{MB543} rapidly with increasing lengths (dT)n (where n= 8,10,15,20,25,30,35) shows the observed rates in fluorescence change for **c)** RPA-DBD-A^{MB543} and **f)** RPA-D^{MB543}. The data for RPA-DBD-A^{MB543} are best fit using a two-step model whereas the data for RPA-DBD-D^{MB543} fit to a one-step process. Pink and oranges traces in RPA-A^{MB543} show remodeling of DBD-A when the ssDNA is short and not enough for all DBDs to engage. This is absent in RPA-D^{MB543} suggesting distinct DBD binding dynamics.

3.3.2 FRET analysis confirms primary assessments of DBD-ssDNA dynamics

In the experiments described above, the change in fluorescence intensity arises from local environmental changes of the fluorophore upon binding to the ssDNA. We suggest that changes in the MB543 fluorescence reflect changes in the electrostatic environment of the dye (Fig 3-9 a-d). To reaffirm that the accuracy of the dynamics we measure for each fluorescent DBD reflects ssDNA interactions, we used Förster Resonance Energy Transfer (FRET) to capture DBD-ssDNA binding kinetics. RPA binds to ssDNA with specific polarity where DBD-A is positioned closer to the 5′ end of the ssDNA (Fan & Pavletich, 2012a; Kolpashchikov et. al., 2001). Similar to the MB543-labeled proteins, we generated Cy5-labeled RPAs where either DBD-A or DBD-D was labeled with Cy5. We next performed FRET experiments with either 5′ or 3′ Cy3-end-labeled DNA [$(dT)_{34}$]. On 5′Cy3 DNA, a high FRET signal is observed for RPA-DBD-A^{Cy5}, and a medium FRET state is captured for RPA-DBD-D^{Cy5} (Fig. 3-10 a, b). In the corollary experiment with 3′Cy3 DNA, a low FRET state for RPA-DBD-A^{Cy5} and a high FRET state for RPA-DBD-D^{Cy5} are observed (Fig. 3-10 c, d). These experiments are consistent with the expected 5′ to 3′ polarity of RPA binding. Strikingly, the observed rate for the appearance of the RPA-DBD-D^{Cy5} high FRET state (36±2s−1; Fig. 3-10 d) agrees with the rate for change in fluorescence intensity of RPA-DBD-D^{MB543} upon binding to ssDNA (36.2±2s−1; Fig. 3-5 b). Similarly, the observed rate of 21±1s^{-1} for the appearance of the RPA-DBD-A^{Cy5} high FRET state (Fig. 3-10 b) is likely a composite of the two observed phases captured in fluorescence intensity changes of the RPA-DBD-A^{MB543} ssDNA complex ($k_{obs,1}$ =30s^{-1} and $k_{obs,2}$=10s^{-1}; Fig. 3-5 a). The FRET data affirm

that the ssDNA binding responsive fluorescence intensity enhancements reflect specific DBD-ssDNA interactions.

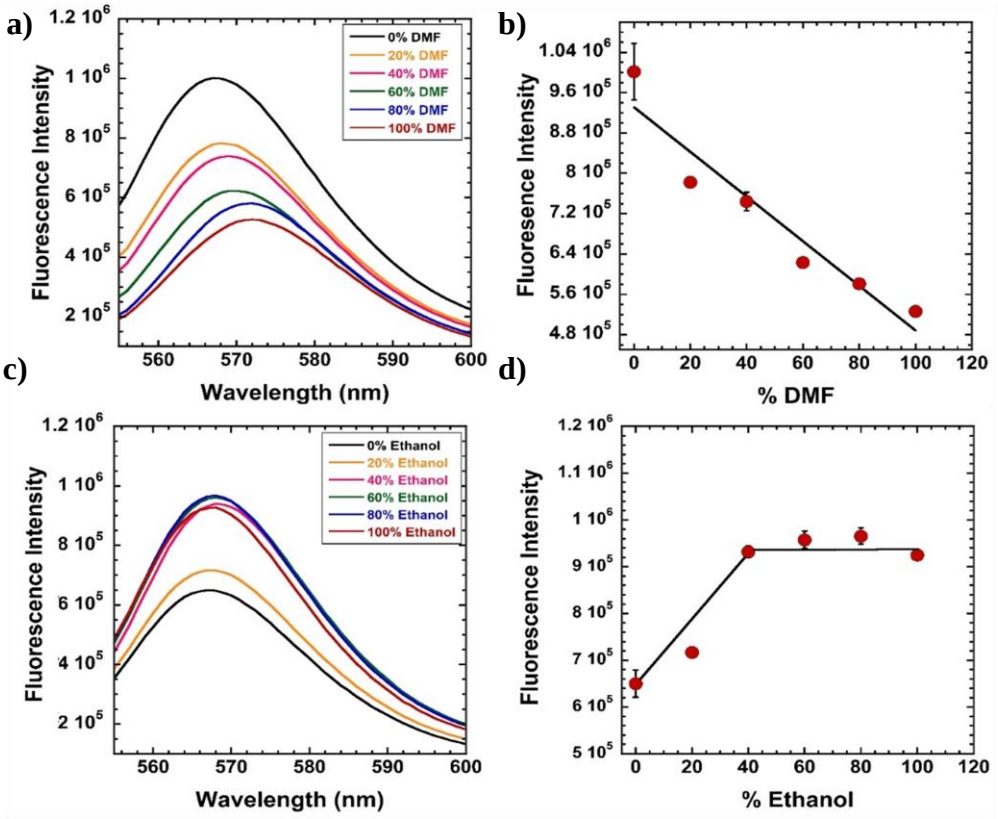

Figure 3-9: Changes in MB543 fluorescence reflect conformational changes associated with electrostatic interactions. The change in MB543 fluorescence was measured as a function of increasing concentrations of **a)** dimethyl formamide (DMF) or **c)** ethanol, and **b)** & **d)** the respective change in fluorescence was plotted. The solvent dependent changes in emission spectra are suggestive of electrostatic changes around the fluorophore.

a)

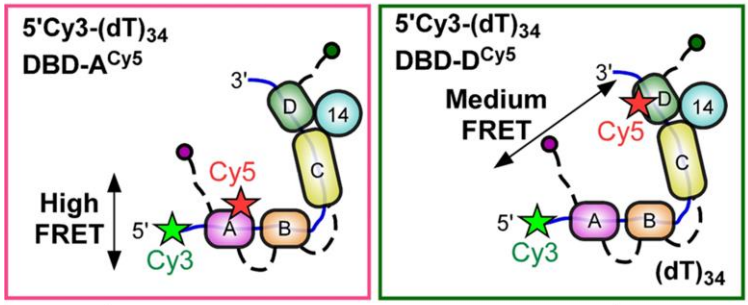
5'Cy3-(dT)34
DBD-ACy5
3'
D
14
C
Cy5
High
FRET
5'
Cy3
A
B
5'Cy3-(dT)34
DBD-DCy5
Medium
FRET
3'
D
14
Cy5
C
5'
Cy3
A
B
(dT)34

b)

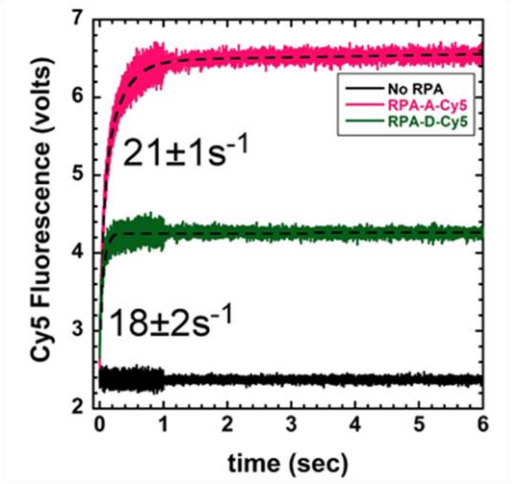
Cy5 Fluorescence (volts)
time (sec)
No RPA
RPA-A-Cy5
RPA-D-Cy5
21±1s-1
18±2s-1

c)

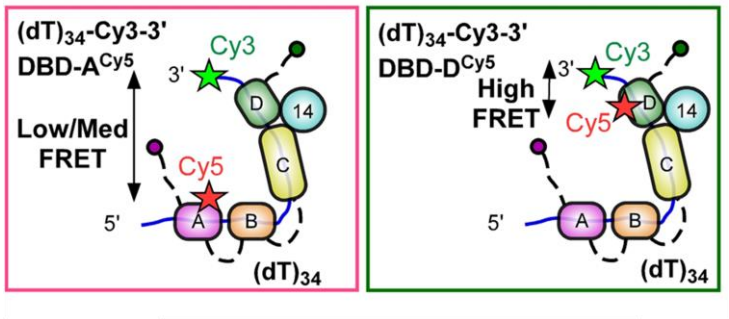
(dT)34-Cy3-3'
DBD-ACy5
Cy3
3'
D
14
Low/Med
FRET
C
Cy5
5'
A
B
(dT)34
(dT)34-Cy3-3'
DBD-DCy5
Cy3
3'
High
FRET
D
14
Cy5
C
5'
A
B
(dT)34

d)

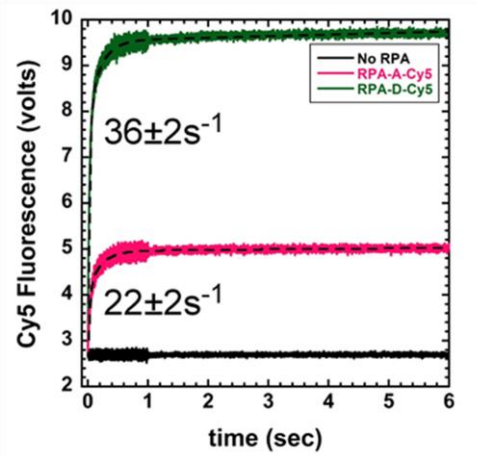
Cy5 Fluorescence (volts)
time (sec)
No RPA
RPA-A-Cy5
RPA-D-Cy5
36±2s-1
22±2s-1

Figure 3-10: FRET experiments capture the polarity of RPA binding on ssDNA. a), c) Models of the expected FRET states and the polarity of the Cy5-DBD with respect to the Cy3-DNA. Boxes are color coded to match the traces in the data. Stopped flow experiments were performed by rapidly mixing either RPA-DBD-A^{Cy5} or RPA-DBD-D^{Cy5} with ssDNA labeled at the **b**) 5′ end or **d)** 3′ end with Cy3. Cy3 was excited and change in Cy5 emission was measured. The proximity of the Cy3 and Cy5 fluorophores dictate the observed FRET efficiency and results in the enhancement of Cy5 emission. Since RPA binds to ssDNA with a 5′ -> 3′ polarity, when RPA-DBD-A^{Cy5} resides close to the 5′Cy3 on DNA, a high FRET state is observed. Similarly, when RPA-DBD-D^{Cy5} binds close to the 3′Cy3, a high FRET signal is captured. kobs values for change in FRET were obtained by fitting the data to a single exponential plus linear equation. Black traces are DNA only (no RPA). Pink and Green traces are experiments with RPA-DBD-A^{Cy5} and RPA-DBD-D^{Cy5}, respectively. The measured rates match well to the rates observed for RPA labeled with MB543 (Fig. 3-5 a, b) suggesting that the ssDNA dependent changes in RPA-MB543 intensity reflect specific DBD-ssDNA interactions.

3.3.3 Differential effects of ssDNA length on DBD conformations

Since each DBD has varying footprints on ssDNA (Fan & Pavletich, 2012a) we measured the DBD dynamics as a function of ssDNA length and found that the $k_{obs,1}$ increases as a function of ssDNA length for RPA-DBD-A^{MB543} (Fig. 3-8 a-c), whereas the same parameter saturated for RPA-DBD-D^{MB543} at ~20 nt (Fig. 3-8 d-f). On shorter DNA lengths, both binding and dissociation phases are clearly observed for RPA-DBD-A^{MB543} (Fig. 3-8 b: $(dT)_{15}$ and $(dT)_{20}$ traces); however, only a single binding phase for RPA-DBD-D^{MB543} is observed with all ssDNA lengths (Fig. 3-8 e). Since ssDNA and RPA are in molar equivalents in these experiments, the dissociation from shorter DNA probably occurs from intra-subunit competition between the four DBDs of RPA. DBDs F, A and B are considered the conformationally flexible half (Brosey et. al., 2009). In contrast, DBDs C, D and E constitutively interact to form the trimerization core and are more conformationally rigid. We considered the possibility that the trimerization core might be outcompeting the more dynamic DBD-A (and possibly DBD-B) under conditions of excess RPA or when the length of the DNA is too short to accommodate all

the DBDs. To test this scenario, we generated the RPA-FAB fragment containing DBDs F, A and B and labeled it with MB543 in DBD-A (RPA-FAB-A^{MB543}). RPA-FAB-A^{MB543} bound to ssDNA [$(dT)_{45}$] and produced an 89% enhancement in fluorescence (Fig. 3-11 a). Stopped flow measurement of DNA binding kinetics of RPA-FAB-A^{MB543} yield k_{on}=1.0±0.1×$10^8 M^{-1}s^{-1}$ (Fig.3-11 b-d), which is similar to that measured for RPA-DBD-A^{MB543} (1.1±0.6×10^8 $M^{-1}s^{-1}$; Fig. 3-7 b, c), suggesting that DBD-A has intrinsically distinct DNA binding capacity compared to DBD-D, and possibly other DBDs as well. Interestingly, RPA-FAB-A^{MB543} binds to ssDNA with monophasic kinetics under both conditions of excess protein or shorter DNA lengths (Fig.3-11 b, c). We do not observe the second phase where a decrease in fluorescence signal (Fig. 3-11 b, c) as observed for RPA-DBD-A^{MB543} (Fig. 3-7 b, 3-8 b; orange trace). These data show that the second rearrangement phase observed for RPA-DBD-A^{MB543} is due to competition from either DBD-C and/or D) and rearrangements between the DBDs within full length RPA when the binding sites on ssDNA are limiting. Free RPA in solution can displace ssDNA-bound RPA through a mechanism called ‘facilitated exchange’ (Gibb, Ye, Gergoudis, et. al., 2014). ssDNA-bound RPA-FAB-A^{MB543} is exchanged at two orders of magnitude faster than either RPA-DBD-A^{MB543} or RPA-DBD-D^{MB543} (Fig. 3-12 a-c, h), suggesting that the presence of all the DBDs enhance the stability of RPA on ssDNA. Interestingly, RPA-DBD-A^{MB543} and RPA-DBD-D^{MB543} are exchanged at similar rates suggesting that unlabeled RPA can efficiently compete for either DBD (Fig. 3-12 d-h). We propose that when only a short segment of ssDNA ($(dT)_{15}$ or $(dT)_{20}$) is available, DBD-A rapidly binds and dissociates, whereas DBD-D (and possibly the trimerization core) forms more stable, longer-lived complexes with ssDNA, thus outcompeting DBD-A from short

ssDNA substrates. These data also suggest that the interactions of each DBD and resulting conformations of the RPA-ssDNA complex are sensitive to the context of DNA encountered during various DNA metabolic processes in the cell (Discussed in detail in chapter 4).

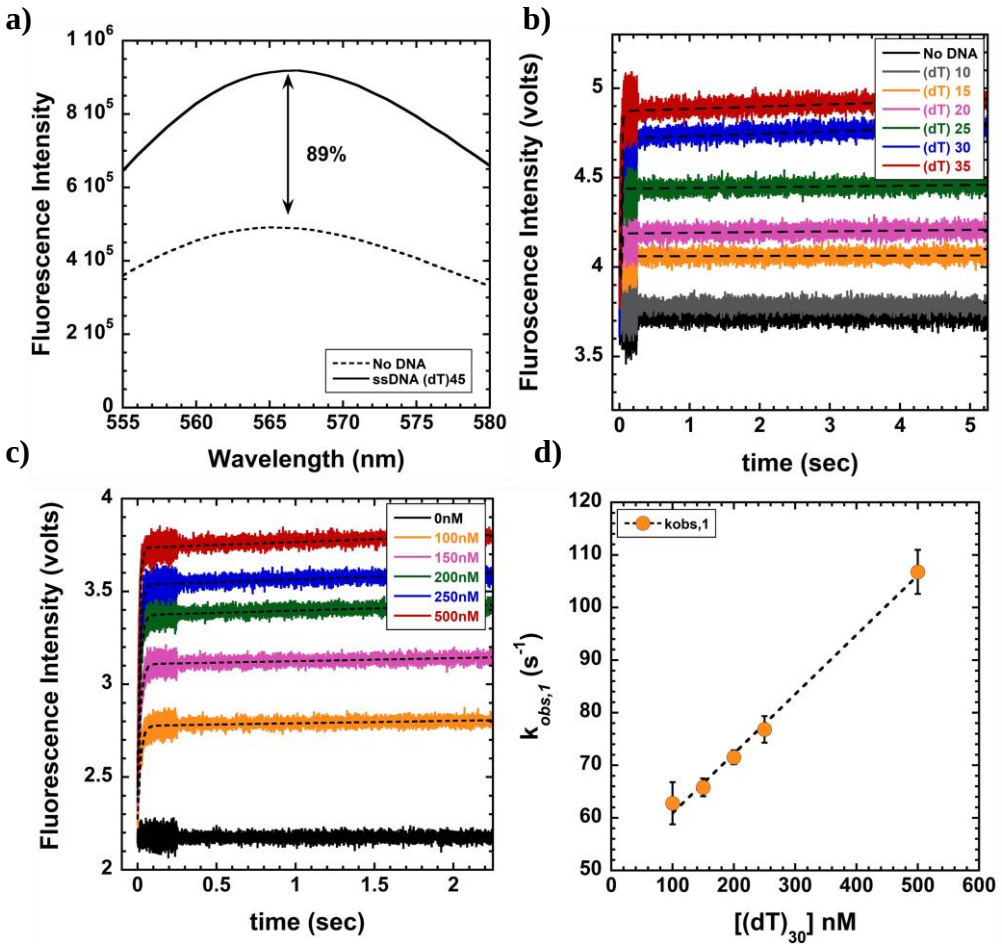

Figure 3-11: The RPA fragment comprised of FAB domains displays rapid and monophasic binding to ssDNA. The FAB region of RPA (DBDs F, A and B) was purified and labeled with MB543 at DBD-A (RPA-FAB-A^{MB543}), and **a)** produces a robust change in fluorescence upon binding to ssDNA. **b)** Stopped flow analysis shows rapid binding of RPA-FAB-A ^{MB543} (100 nM) to 100 nM of ssDNA of increasing lengths $(dT)_n$. A minimum of 15 nt is required to observe binding. **c)** RPA-FAB-A^{f} binding dynamics on ssDNA were measured by monitoring the change in fluorescence upon binding to increasing concentrations of $[(dT)_{30}]$ ssDNA. **d)** Measurement of DNA binding kinetics reveal k_{on} ($1.1\pm0.1 \times 10^8\ M^{-1}s^{-1}$). The RPA-FAB-A^{MB543} binding data were fit to a single exponential plus linear equation to obtain $k_{obs,1}$.

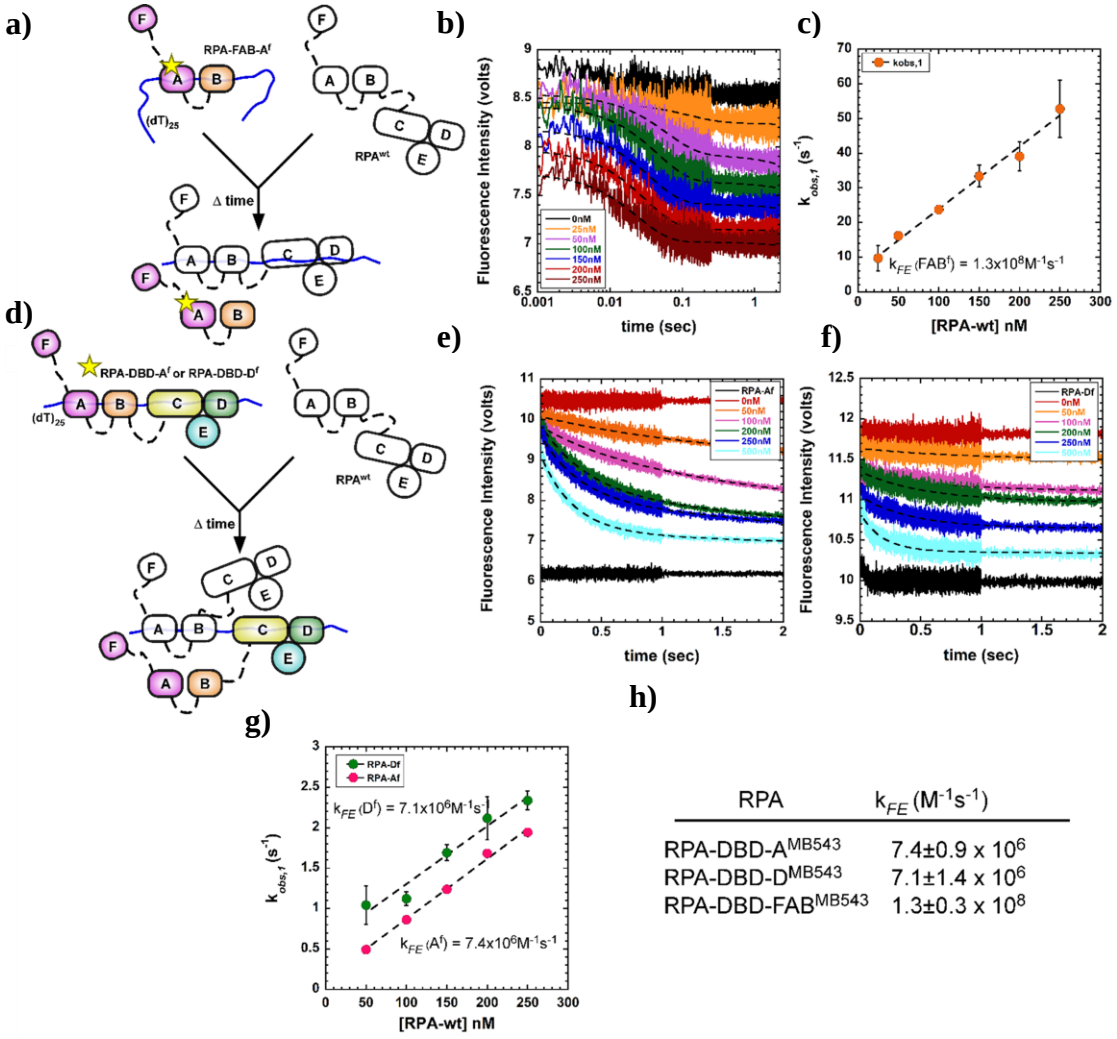

Figure 3-12: RPA-FAB is exchanged more readily on ssDNA compared to the full-length RPA. a)-c) Preformed RPA-FAB-A^{MB543}:$(dT)_{25}$ complexes were challenged with increasing concentrations of unlabeled RPA-wt and the rate of exchange was measured by monitoring the decrease in fluorescence intensity. RPA-FAB-A^{MB543} was cleared at an apparent rate of ($1.3\pm0.3x10^8$ $M^{-1}s^{-1}$). In comparison, **d)-h)** the rates of exchange of RPA-DBD-A^{MB543} or RPA-DBD-D^{MB543} by RPA-wt was two orders of magnitude slower.

3.3.4 Single-molecule analysis reveals the presence of multiple conformational states involving DBD-D and DBD-A

Ensemble stopped flow experiments described above suggest that the terminal DBDs of RPA associate with ssDNA with different rates and that, upon binding to ssDNA, RPA commences a complex and dynamic rearrangement of its DBDs. Single-molecule total internal reflection microscopy (smTIRFM) was used to directly observe RPA-DBD-A^{MB543} and RPA-DBD-D^{MB543} binding to and dissociation from surface-tethered ssDNA in the context of the RPA heterotrimer. In the smTIRFM experiments, biotinylated ssDNA (66 nt) was tethered to the surface of the TIRFM flow cell (see Methods and (Nilisha Pokhrel et. al., 2019) for details). The surface was illuminated with a 532 nm laser to excite the MB543 dye on fluorescent-RPA molecules entering the evanescent field (Fig. 3-13 a, b). Binding of a MB543-labeled RPA to surface-tethered ssDNA molecules generates a fluorescence signal at a particular location of the flow cell surface. This signal persists until RPA dissociates, transitions to a dark-state and then dissociates, or until the dye photobleaches.

Several hundred molecules are observed in the field of view, each yielding a fluorescence trajectory (i.e. change in fluorescence in a particular location on the slide as a function of time) (Boehm, Subramanyam, Ghoneim, Washington, & Spies, 2016). The trajectories allow measurement of binding and dissociation of individual RPA molecules. Moreover, fluorescence changes of the dye in the trajectory can also report on the presence of conformational states in the dye-decorated protein (Ghoneim & Spies, 2014). The experiments were carried out in three stages: first, the surface was observed for 30 seconds to confirm the absence of the non-protein derived fluorescence spots; second,

RPA-DBD-A^{MB543} or RPA-DBD-D^{MB543} was injected into the flow cell; finally, at 120 seconds, protein-containing solution was replaced with the buffer (Fig. 3-13 a, b). The last step ensured that the observed changes in fluorescence can be attributed to single RPA molecules. Fluorescence trajectories were extracted from the recorded movies and were normalized (see (Nilisha Pokhrel et. al., 2019) for more details). Resultant trajectories showed dynamics within the RPA-ssDNA complex (Fig. 3-13 c, d). Moreover, transitions between different fluorescence states persisted during the last segment of the experiment suggesting that they truly reflect the conformational dynamics of individual RPA-ssDNA complexes. Global analysis of normalized trajectories for the ssDNA-bound RPA-DBD-A^{MB543} and RPA-DBD-D^{MB543} was performed with ebFRET (Subramanyam, Kinz-Thompson, Gonzalez, Spies, & Spies, 2018; van de Meent, Bronson, Wiggins, Gonzalez, & Jr., 2014). This analysis revealed that the fluorescence derived from both proteins best fit a 4-state model, with state 1 corresponding to very low fluorescence and states 2–4 corresponding to increasing fluorescence enhancement (Fig. 3-13 c, d). Segments of the trajectories between 120 and 210 seconds, which can be attributed to the dynamics of a single bound RPA, were used in the quantification of the lifetimes and visitation frequencies for all states.

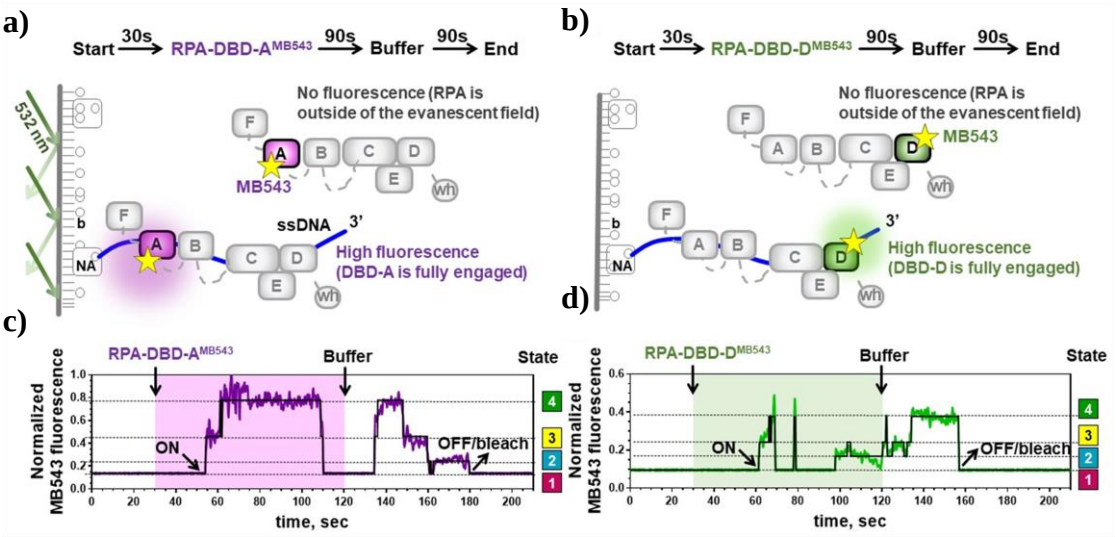

Data collected by Colleen Caldwell and Maria Spies, University of Iowa

Figure 3-13: Single molecule analysis to capture the conformational dynamics of DBDs. a), b) Experimental scheme for visualizing conformational dynamics of DBD-A and DBD-D. Binding of fluorescently labeled RPA to a surface-tethered ssDNA (purple line) brings the MB543 fluorophore within the evanescent field of TIRFM. NA – neutravidin, b – biotin. **c), d)** Representative fluorescence trajectories for individual RPA-DBD-A^{MB543} and RPA-DBD-D^{MB543} molecules, (purple and green lines, respectively). Black lines are the results of ebFRET fitting.

We attribute state 4 in each case to the RPA conformation where the labeled domain is potentially fully engaging the ssDNA; because in bulk experiments, we observed the ssDNA-dependent fluorescence increase in the full-length RPA carrying the fluorophore, and RPA-FAB-A^{MB543} (containing only DBD-A and DBD-B). To rule out that the lowest fluorescence state (state 1) followed by the reappearance of the fluorescence during the last 90 seconds of the experiment is due to the RPA dissociation and rebinding, we substituted the buffer wash with the buffer supplemented with high concentration of ssDNA. In the absence of additional RPA in the solution, ssDNA competitor cannot strip the bound RPA from the DNA but can sequester all dissociated RPA molecules (Gibb, Ye, Gergoudis, et. al., 2014). As expected, the addition of ssDNA into the reaction chamber had no effect on the RPA fluorescence states (Fig. 3-14 a-d). The four fluorescence states and their dwell times were consistent between independent experiments suggesting that the normalization scheme we developed yields reproducible results (Fig. 3-15 a-d, 3-16 a-d). For both RPA-DBD-A^{MB543} and RPA-DBD-D^{MB543}, states 1 and 4 were the most stable with average dwell times around 1 second compared to states 2 and 3 whose average dwell times were between 300 and 500 ms. As evident from the representative trajectories (Fig. 3-13 c, d), RPA spends significant periods of time in states where DBD-A or DBD-D are not fully engaged, providing a window of binding opportunity for lower affinity proteins.

In addition, we found that the collective DNA binding affinities of all DBDs produce stable RPA-ssDNA complexes. DBDs A and B have been canonically assigned as responsible for high affinity DNA binding of the RPA complex. By carrying out single-molecule experiments with the RPA-FAB-A^{MB543} we found that it forms a less

stable complex on ssDNA and readily dissociates (Fig. 3-17 a-d). These findings agree with the results from bulk stopped flow experiments (Fig. 3-11 a-d, 3-12 h). Fluorescence trajectories recorded for RPA-FAB-A^{MB543} were best fit with the three-state model (Fig. 3-17 a, c). State 1 corresponded to free ssDNA and its lifetime displayed a linear dependence on the RPA-FAB-A^{MB543} concentration (Fig. 3-17 d). States, 2 and 3 were present in the bound state of RPA-FAB-A^{MB543} whose two DBDs had been suggested to form a dynamic complex on the ssDNA (Pretto et. al., 2010). The presence of only two fluorescence states in the RPA-FAB-A^{MB543} further confirms that the four states observed for the full-length RPA are not photophysical states inherent to the MB543 dye.

In ensemble experiments, where several thousands of molecules are monitored, the composite fluorescence data obtained for DBD-A is fitted with a double-exponential+ a linear phase model, while, data for DBD-D is fitted with a single-exponential + a linear phase model (Fig. 3-5, 3-6, 3-7, 3-8). In such cases, the double exponential suggests that are two likely phases/ steps in DBD-A binding to DNA. Similarly, a single exponential phase suggests that there is one step in DBD-D binding to DNA, till an equilibrium is reached. Each of these steps can have number of association- dissociation within but when observed with stopped flow instrument, they are collected a composite signal from thousands of molecules. This is different from the smTIRF data that monitors one molecule of RPA-DBD-A or RPA_DBD-D bound on DNA at a time and shows presence of four distinct states of binding.

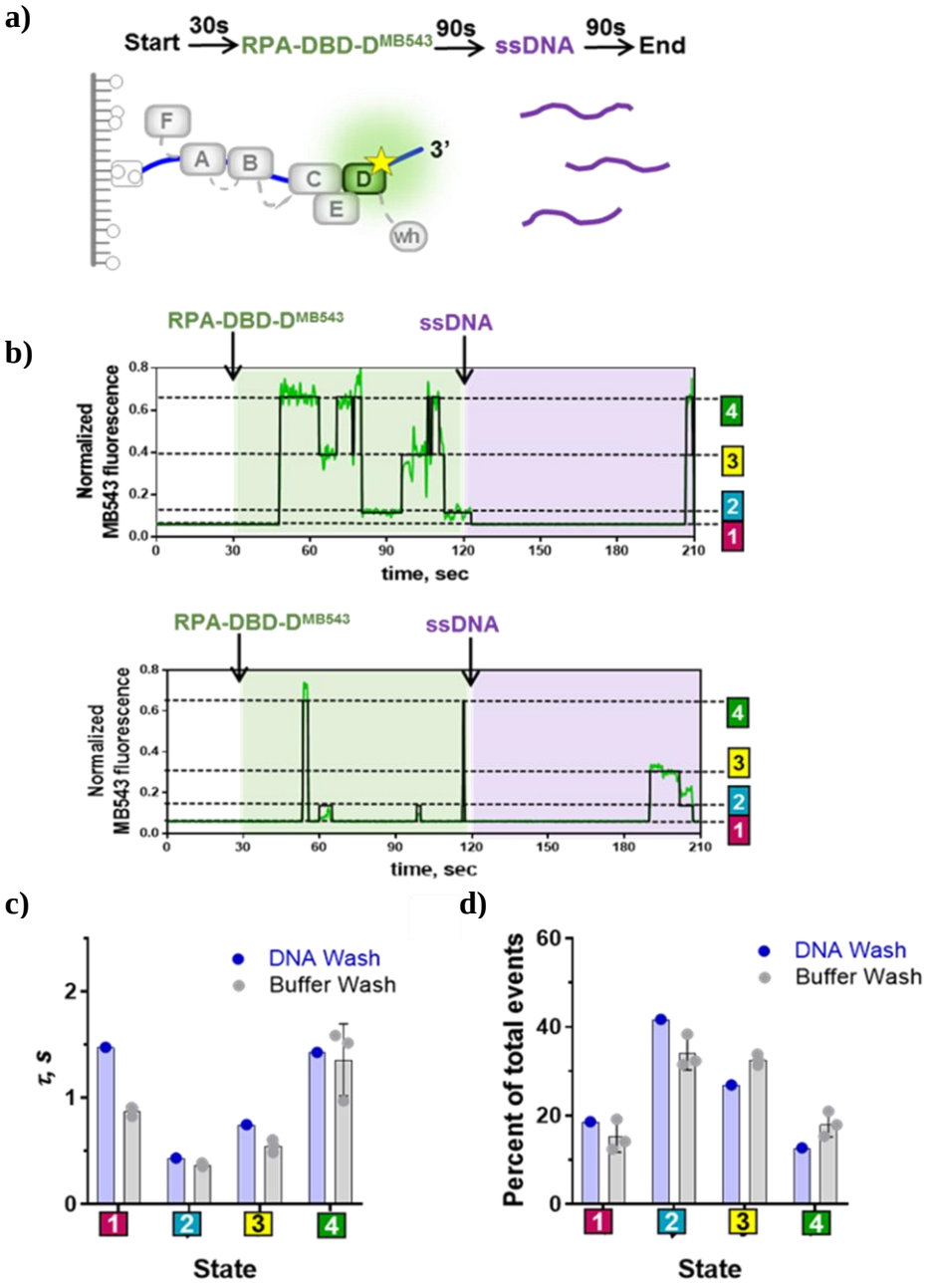

Data collected by Colleen Caldwell and Maria Spies, University of Iowa

Figure 3-14: Scavenger ssDNA in the buffer wash step confirms that RPA-DBD-A^{MB543} remains bound to ssDNA in observed dark state events. a) Experimental scheme for visualization of the effect of excess ssDNA on the RPA-DBD-D^{MB543} dynamics and association with DNA. Binding of the RPA-DBD-D^{MB543} (100pM) to the surface-tethered ssDNA (blue line) brings the MB543 fluorophore within the evanescent field and its excitation. 1nM ssDNA (42nt) was added at 90s when excess RPA was washed away. NA – neutravidin, b – biotin. **b)** Representative fluorescence trajectories depicting the conformational dynamics of the individual RPA-DBD-D^{MB543} molecules. After replacement of RPA in the reaction chamber with 1nM ssDNA, the same four conformational states are observed in the RPA-DBD-D^{MB543} trajectories. As seen in experiments where excess RPA was washed away with Reaction buffer, reappearance of higher fluorescence states are observed after visitation of the dark state (state 1) in the presence of excess ssDNA. RPA that dissociated would have been bound by the excess free DNA, thus indicating that the reappearance of higher fluorescence states (2,3,4) is due to RPA remaining bound while in the dark state (1). **c)** Comparison of the stability of each state available to RPA-DBD-D^{MB543} when excess RPA is washed away with reaction buffer (grey) or reaction buffer containing 1nM ssDNA (blue). The data on Y axis are the lifetimes calculated from the respective dwell time distributions. Data for each independent experiment is plotted separately. **d)** Comparison of the fractional visitation to each state available RPA-DBD-D^{MB543} when excess RPA is washed away with reaction buffer (grey) or reaction buffer containing 1nM ssDNA (blue).

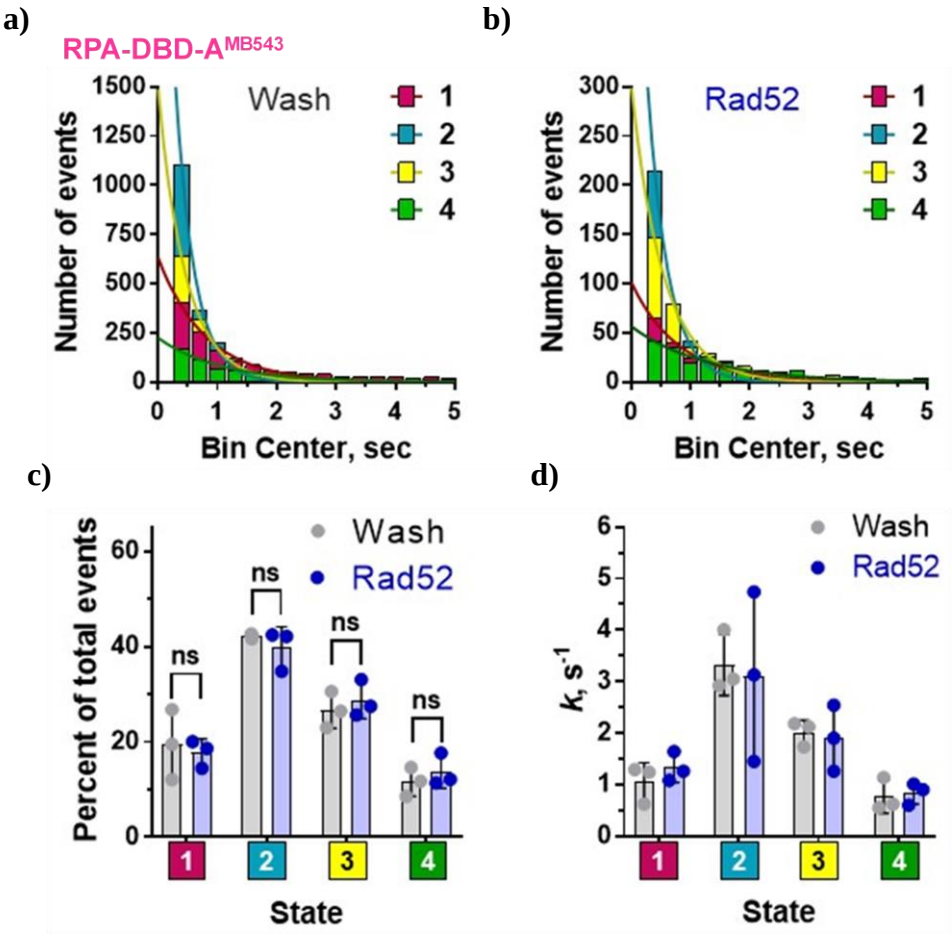

Data collected by Colleen Caldwell and Maria Spies, University of Iowa

Figure 3-15: Quantification ebFRET to confirm DBD-A domain dynamics in RPA-DBD-A^{MB543}. Dwell time histograms for the four fluorescent states obtained by the ebFRET fitting of RPA-DBD-A^{MB543} trajectories from three independent experiments **a)** after buffer wash, and **b)** Rad52 wash. **c)** Fractional visitation to each state available to RPA-DBD-A^{MB543} alone (grey) and in the presence of Rad52 (blue). **d)** Stability of each state available to RPA-DBD-A^{MB543} alone (grey) and in the presence of Rad52 (blue). The data on Y axis are the lifetimes for the respective dwell time distributions.

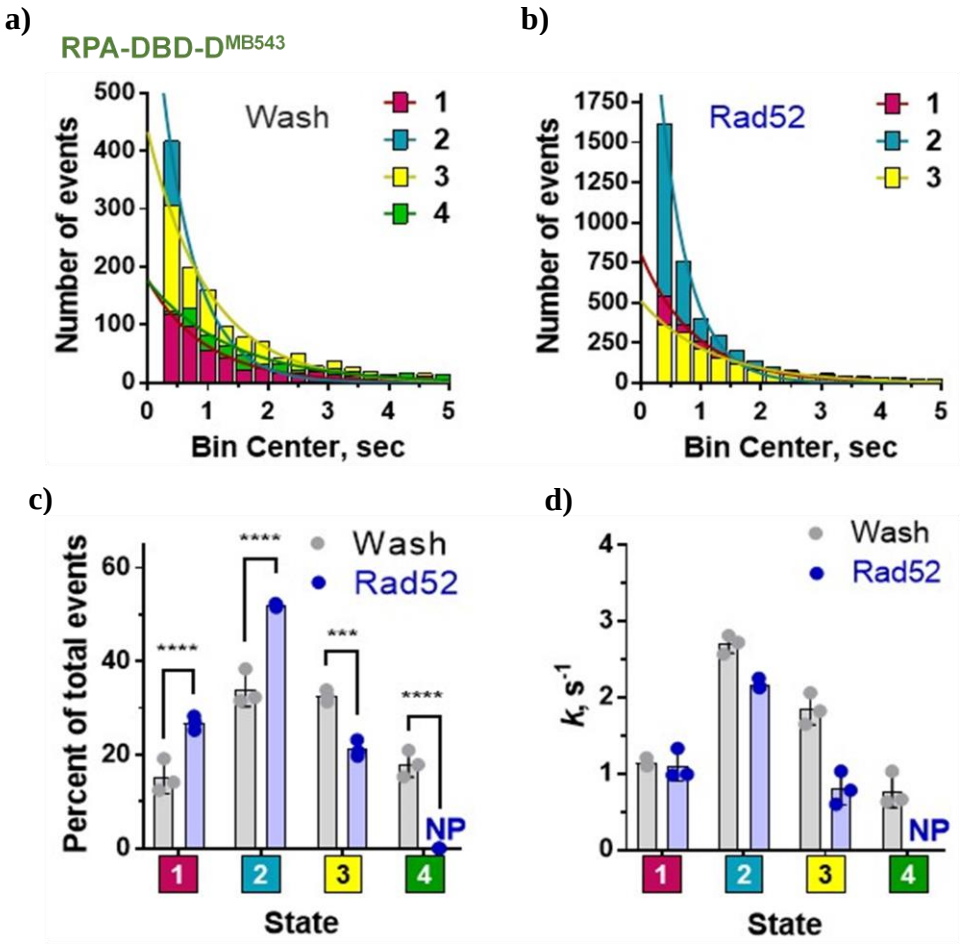

Data collected by Colleen Caldwell and Maria Spies, University of Iowa

Figure 3-16: Quantification ebFRET to confirm DBD-D domain dynamics in RPA-DBD-D^{MB543}. Dwell time histograms for the four fluorescent states obtained by the ebFRET fitting of RPA-DBD-D^{MB543} trajectories from three independent experiments **a)** after buffer wash, and **b)** Rad52 wash. **c)** Fractional visitation to each state available to RPA-DBD-A^{MB543} alone (grey) and in the presence of Rad52 (blue). **d)** Stability of each state available to RPA-DBD-D^{MB543} alone (grey) and in the presence of Rad52 (blue). The data on Y axis are the lifetimes for the respective dwell time distributions.

a)

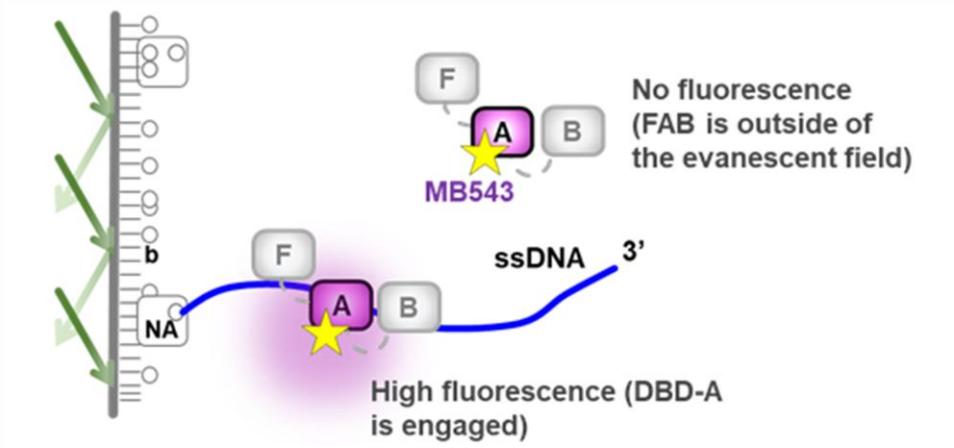

b)

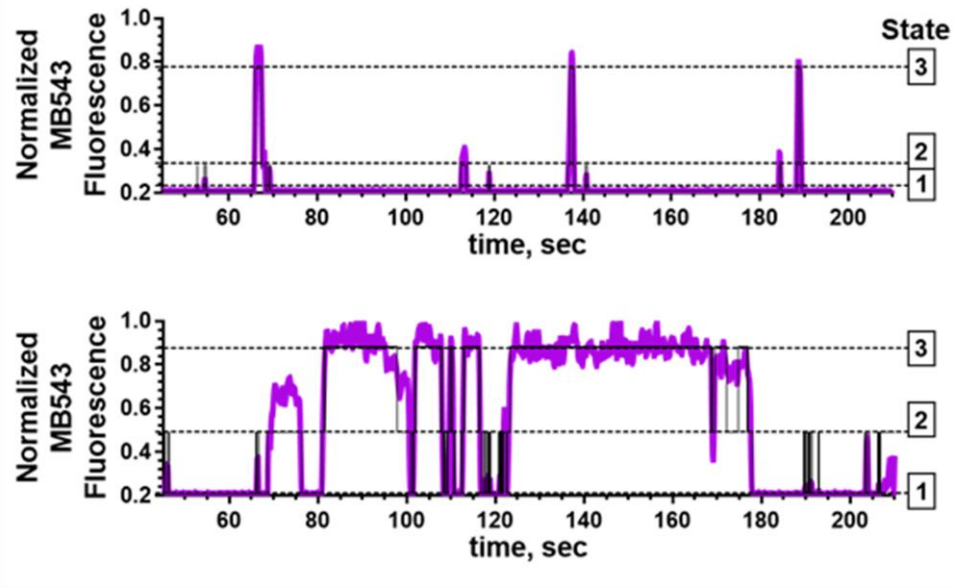

Data collected by Colleen Caldwell and Maria Spies, University of Iowa

Figure 3-17: Single-molecule analysis of RPA-FAB-A^{MB543}-ssDNA interaction. a) Experimental scheme for visualization of the binding and conformational dynamics of FAB. Binding of the fluorescently labeled FAB to ssDNA (blue line) tethered to the surface of TIRFM flow cell (grey line) brings the MB543 fluorophore within the evanescent field and its excitation. NA – neutravidin, b – biotin. **b)** Representative fluorescence trajectories depicting binding (appearance and disappearance of the signal) and conformational dynamics (change in fluorescence without FAB dissociation) of the individual RPA-FAB-A^{MB543} molecules. Purple lines represent normalized fluorescence, black lines represent the results of ebFRET fitting of the experimental data to the three-state model (where state 1 is the off state, while states 2 and 3 are the two bound states with different fluorescent intensities). The levels for the respective states are indicated by dashed lines. (Top) Representative trajectory of the most commonly observed short binding events and rare transitions between fluorescence states. (Bottom) At each RPA-FAB-A^{MB543} concentration, several trajectories displaying long binding events can be observed.

3.3.5 Rad52 selectively modulates DBD-D dynamics

To determine the mechanism by which the recombination mediator Rad52 remodels the RPA-ssDNA complex, RPA-DBD-A^{MB543} or RPA-DBD-D^{MB543} bound to the surface-tethered ssDNA in the smTIRFM experiments were challenged with Rad52 (Fig. 3-18 a-d). The last 90 second portions of the resulting trajectories were normalized and globally analyzed using ebFRET. Dwell times for each state were binned and fit to an exponential decay (Fig. 3-15 a, b, 3-16 a, b). RPA-DBD-A^{MB543} trajectories after buffer wash or after Rad52 addition fit best to a 4-state model with the same distribution of states and the same dwell times (Fig. 3-15 a-d). The trajectories collected for RPA-DBD-D^{MB543} after Rad52 addition instead best fit a 3-state model (Fig. 3-16, a-d). Attempts to fit these trajectories with a 4-state model resulted in overfitting and overlapping states. Intensities of the 3-states of RPA-DBD-D^{MB543} after Rad52 addition correspond to the 3 lowest states seen after the buffer wash with the highest state absent when Rad52 was present (Fig. 3-18 d, blue shaded area). With RPA-DBD-D^{MB543} occupancy at state 4 lost after Rad52 addition, state 3 occupancy decreases, whereas state 1 and 2 occupancy increases (Fig. 3-16 c). This suggests that Rad52 selectively modulates conformational dynamics of the RPA-ssDNA complex: reducing the engagement of DBD-D from ssDNA, providing access to the 3′ end of the occluded ssDNA.

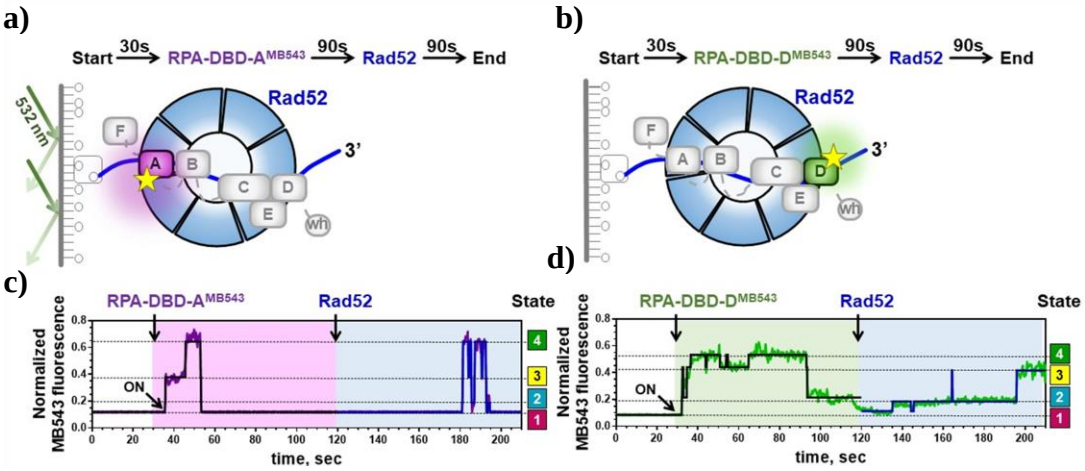

Data collected by Colleen Caldwell and Maria Spies, University of Iowa

Figure 3-18: Rad52 selectively modulates the conformation of DBD-D on DNA. Experimental scheme for visualizing the effect of Rad52 on the conformational dynamics of a) DBD-A and **b)** DBD-D. Representative fluorescence trajectories depicting conformational dynamics of the individual **c)** RPA-DBD-$A^{MB543}$and **d)** RPA-DBD-D^{MB543} molecules upon addition of Rad52. All the details pertaining to schematic representation in a) and b), except for addition of Rad52 is the same as figure 3-13.

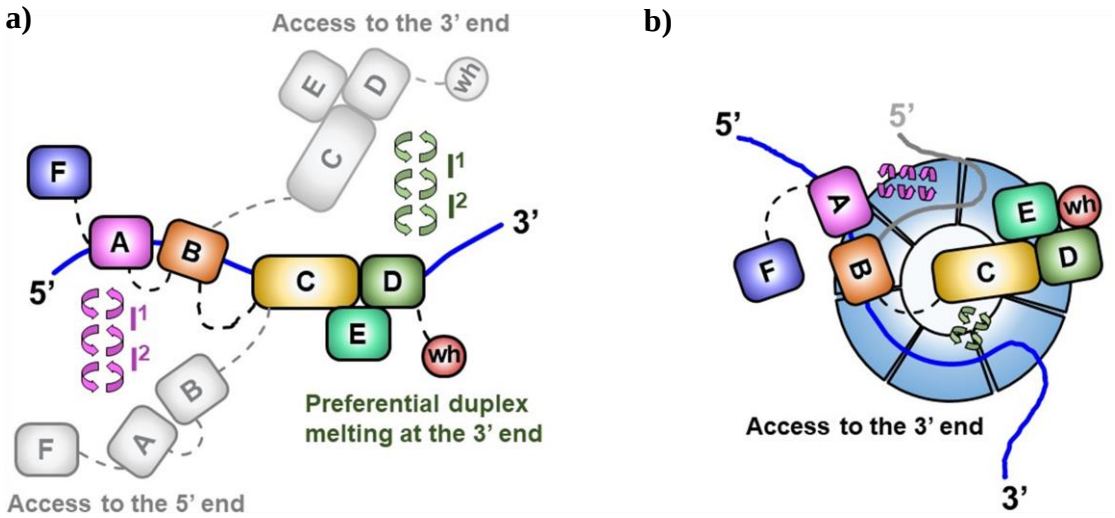

Figure 3-19: Dynamics of RPA DBDs and modulation by Rad52. a) Sequential and directional arrangement of the DBDs allows RPA to occlude 20–30 nt of ssDNA (~20 nt under our experimental conditions; Fig. 3-4 b). When RPA is in a stoichiometric complex with ssDNA, or when the ssDNA is in excess, the individual DBDs of RPA exist in a variety of distinct dynamic conformational DNA bound states. Such conformational flexibility allows access to either the 5′ or the 3′ segment of the DNA to other proteins that function in downstream processes. The circular arrows represent the transitions between multiple fluorescence states we observe in the single molecule experiments and which are implied by the bulk stopped flow experiments. Note that while we illustrate the changes in the conformation of the RPA-ssDNA complex as movement of the DBDs, the same microscopically bound states may arise from ssDNA dissociating and moving away from the respective DBDs. **b)** The DBDs are also selectively modulated by RPA-interacting proteins (RIPs) such as Rad52. In this case, only the DNA binding dynamics of DBD-D, and possibly the trimerization core, is influenced by Rad52. In the ternary RPA-ssDNA-Rad52 complex, the ssDNA is shared by RPA and Rad52, which also interact with one another. The ability of the DBD-D and other RPA elements contacting the ssDNA near the 3′ end of the occluded sequence is constrained. Such selective DBD modulation may promote loading of Rad51 onto the 3′ end of the ssDNA during homologous recombination.

3.4 Discussion

Prior RPA binding models have been based on analysis of subcomplexes or mutations. In contrast, we have analyzed the dynamics of individual domains in the context of the full RPA-ssDNA complex. This analysis demonstrates that rather than

being composed of “high” and “low” affinity domains, all DNA binding domains transiently engage ssDNA with high affinity, but with differential dynamics. We also observe interplay between the flexible half of RPA (DBDs-F, A and B) and the trimerization core. Thus, the RPA-ssDNA complex consists of an ensemble of domains that dynamically interact with ssDNA. This suggests that integration of these interactions results in overall high affinity to ssDNA while facilitating diverse functions of RPA. Our data also suggest that assembly of DBDs on ssDNA is not sequential but rather the result of dynamic, independent interactions between connected DBDs and DNA.

RPA forms a complex with the recombination mediator Rad52 (M. S. Park, Ludwig, Stigger, & Lee, 1996). RPA is in dynamic equilibrium on ssDNA and Rad52 has been shown to increase the residence time of RPA on ssDNA (Gibb, Ye, Kwon, et. al., 2014a). Formation of “early Rad52-bound” RPA and “late Rad52-bound” RPA are proposed to play distinct roles during Rad51 filament formation and second-strand capture during HR (Gibb, Ye, Kwon, et. al., 2014a). The ability to observe the individual RPA DBDs binding to, and dissociating from, the ssDNA in real time permits a mechanistic description of RPA-ssDNA-Rad52 interactions. The RPA heterotrimer and the heptameric Rad52 ring have similar ssDNA binding sites. Each Rad52 monomer contains an RPA binding site and RPA has two Rad52 binding sites per heterotrimer. Rad52 is believed to interact with the ssDNA backbone, while the DBDs of RPA, especially within the trimerization core, engage the bases. Stabilization of RPA by Rad52 is a result of both their physical interactions and their individual interactions with DNA (Nilisha Pokhrel et. al., 2019). We therefore envision a ternary complex where Rad52 and RPA interact with one another while both proteins are simultaneously bound to ssDNA.

Selective modulation of DBD-D ssDNA engagement by Rad52 provides space for Rad52 to interact with ssDNA and stabilize the ternary complex, which then makes more extensive contacts with the ssDNA than RPA does on its own. By redistributing the ssDNA between RPA and Rad52, and by reducing the contacts between RPA and ssDNA, such selective change in binding states of a particular DBD by Rad52 may provide Rad51 recombinase access to the 3′ end of RPA-occluded ssDNA, while maintaining its interaction with RPA (Fig. 3-19). Each Rad51 monomer binds to one monomer of Rad52 and to three nucleotides of ssDNA. Six Rad51 monomers are required to achieve a stable nucleation cluster (Qiu et. al., 2013), which amounts to 18 nucleotides of open ssDNA. This cannot be achieved without the help of a recombination mediator. When Rad52 binds to ssDNA-bound RPA, it modifies the dynamics of the DBD-D engagement. This provides a stretch of ssDNA with sufficient length to initiate Rad51 filament nucleation. We predict that recombination mediators in other species, including human BRCA2 may operate by a similar mechanism. The details of this mechanism, however, will depend on the intrinsic differences in nucleoprotein filament formation by human RAD51, which nucleates on ssDNA through dynamic association of RAD51 dimers (Subramanyam et. al., 2016) and grows from heterogeneous nuclei ranging in size from dimers to oligomers (Candelli et. al., 2014).

The myriad roles of RPA in DNA replication, repair, and recombination is also a paradigm for reactions where multiple DNA binding enzymes function together on a single DNA template. Knowledge of where, how, and when each enzyme gains access to DNA in this multi-enzyme milieu is fundamental to deciphering when and how specific DNA repair and recombination processes are established and used. RPA-ssDNA

complexes serve as binding targets for recruitment of appropriate enzymes during various DNA metabolic processes, and physical interactions between RPA and more than two dozen enzymes have been identified. Upon recruitment, the bound ssDNA must be handed over from RPA or remodeled in such a way that the DNA is accessible to the incoming enzyme while RPA remains at the site. Microscopic binding and dissociation of the RPA DBDs is likely to enable the persistent residence of RPA at the site of repair as well as its ability to coordinate access to the DNA by helicases and nucleases. Such a mechanism might also be applicable to RPA-like proteins that also carry a multi-OB fold architecture, such as the CST complex associated with telomerase (Chan, Wang, & Feigon, 2017).

CHAPTER 4: DNA CONTEXT DEPENDENT RPA- DNA BINDING AND ITS MODULATION BY RPA CHAPERONE RTT105

4.1 Introduction

The double- helical structure of DNA can adopt a variety of contours and shapes while maintaining Watson- Crick base pairing. The myriad of ongoing cellular processes can further change the local structure of DNA and generate unusual structural intermediates in DNA. For example, the process of DNA replication generates fork like structures or flaps, transcription generates bubbles and recombination generates overhangs or joint-molecule structures (Fig 4-1). In several cases, DNA interacting proteins recognize the particular structural perturbance and act on the DNA substrate to reinstate the double helical conformation (Cooper, 2000; Wittschieben, Iwai, & Wood, 2005). Replication Protein A (RPA) is a ubiquitous single-stranded DNA (ssDNA) binding protein present in all eukaryotes and plays a vital role in coordinating crucial DNA processes. It stabilizes the replication fork upon replication stalling and initiates replication checkpoint to restore replication fork integrity (Liao, Ji, Helleday, & Ying, 2018). It acts as a sensor for R-loops during transcription and stimulates the activity of RNAse H1 enzyme to degrade the RNA present in R-loops (H. D. Nguyen et. al., 2017). It melts the G-quadruplex structures which are abundant at telomeres (Salas et. al., 2006), and it coats the 3′ overhang ssDNA generated during homologous recombination to allow nucleation of Rad51 recombinase (Hass et. al., 2012). In each of these DNA-related events, the context in which ssDNA is presented to RPA is different. Therefore, depending on the ongoing cellular event, the ssDNA substrate encountered by RPA could distinctly affect the arrangement of RPA-DBDs on ssDNA (Fig 4-2). Since RPA also

plays a key role in coordinating simultaneous DNA-protein and protein-protein interactions, the type of DNA encounterd by RPA could directly affect RIP recruitment and access to ssDNA.

RPA-DNA binding is coordinated by the flexible half, i.e. DBDs A, B and the less-flexible half, i.e DBDs C. D and RPA14. RPA-DNA binding is dynamic in nature and several factors could be contributing to this dynamicity. First, RPA-DBDs bind sequentially onto ssDNA with a polarity of 5′ -3′, with DBD-A situated closer to 5′ and DBD-D towards 3′ (W. L. de Laat et. al., 1998; Nilisha Pokhrel et. al., 2019). Second, RPA is able to 'sense' the ssDNA substate which is documented by the finding that RPA prefers to bind to an undamaged DNA, over DNA with adducts (Krasikova, Rechkunova, Maltseva, & Lavrik, 2018). Third, it has a preferential binding to ssDNA than ssDNA with a nearby dsDNA structure (R. Chen et. al., 2016b). To elaborate, using EMSA experiments, studies have shown that RPA has comparatively higher binding affinity to ssDNA alone, than when ssDNA is presented in form of a bubble substrate, or in DNA with gaps (R. Chen et. al., 2016b). Fourth, RPA is able to diffuse on ssDNA (B. Nguyen et. al., 2014b), and finally, RPA-DNA interactions can be manipulated by changing the force applied on a particular DNA substrate (Kemmerich et. al., 2016). The presence of multiple ssDNA interacting domains that are connected by flexible linkers allows RPA to adopt a plethora of conformations, alone and on ssDNA (Elena Bochkareva et. al., 2002a; Fan & Pavletich, 2012a; Fanning et. al., 2006). This is highlighted by the number of nucleotides an RPA molecule can associate with. The first two DBDs of RPA have been shown to associate with 8-nucleotide long ssDNA, whereas all the DBDs require 22-30 nucleotides to stably engage on ssDNA (A Bochkarev, Bochkareva, Frappier, &

Edwards, 1999; Elena Bochkareva et. al., 2002a; Fanning et. al., 2006). This ssDNA footprint further changes with increasing salt concentrations, where and RPA has been shown to occupy around 18-20 nucleotides in low salt concentrations (~100mM), compared with up to 26-28 nucleotides at high salt concentrations (1.5M NaCl) (Kumaran et. al., 2006; B. Nguyen et. al., 2014b). In addition to these attributes, which are derived primarily by monitoring the interaction of a complete RPA-heterotrimer with a particular DNA substrate under controlled conditions, there are dynamic motions in play within the DNA binding domains. These dynamic motions have been termed 'micro-arrangements' of RPA where, while an entire RPA is bound to ssDNA, individual DBDs are in a constant state of association, dissociation, and rearrangement (Arunkumar et. al., 2003a; Brosey et. al., 2015a; R. Chen et. al., 2016b; Fanning et. al., 2006). Molecular dynamics simulations of these micro-arrangements depicted that DBDs of RPA could adopt distinct conformations based on the type of DNA substrates they encounter (R. Chen et. al., 2016b). These subtleties inherent to RPA-DNA engagement can play a significant role in how RPA-DBDs assemble on ssDNA with nearby dsDNA-ssDNA

junctions, or ssDNA with more complex structures, such as G-quadruplexes and RNA-DNA hybrids.

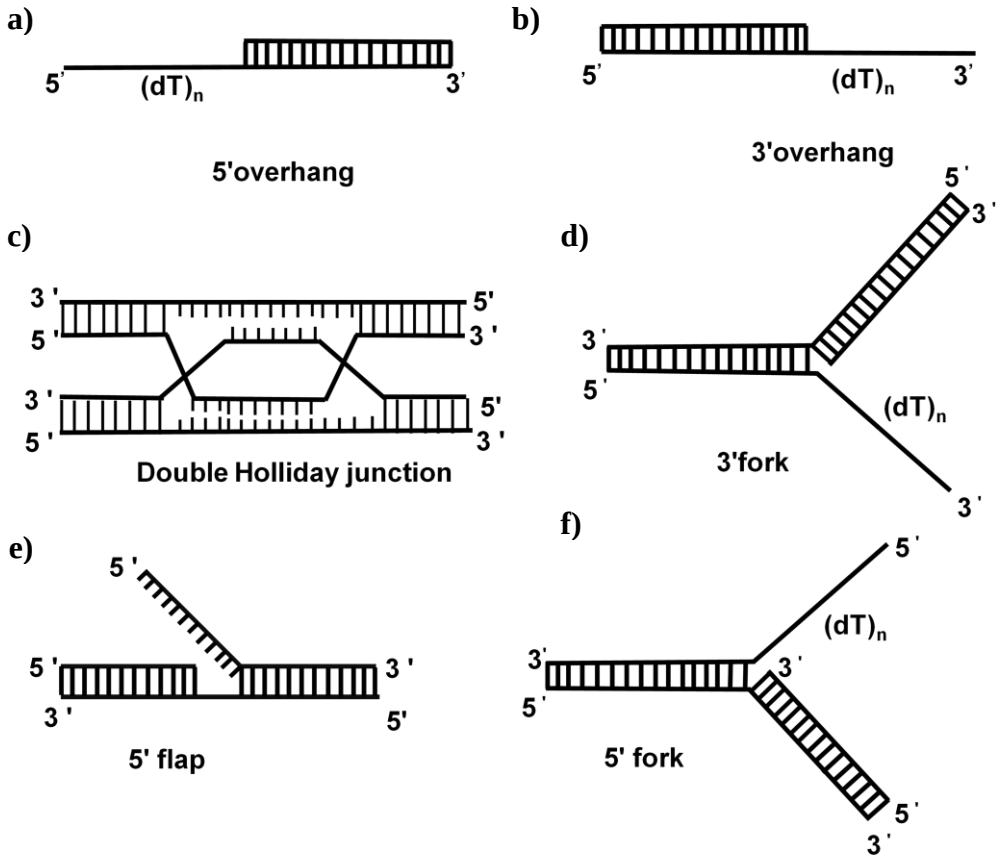

Figure 4-1: Modified structures of DNA-double helix during canonical cellular processes. a) 5′ overhang **b)** 3′ overhang DNA substrates are generated as a consequence of exonuclease and endonuclease enzymatic activity. **c)** Representation of the double Holliday junction structure generated during homologous recombination **d)** Schematics of the replication fork with 3′ overhang or **e)** 5′ flaps and **f)** 5′ overhangs that are generated during replication, or replication break induced replication repair (BIR).

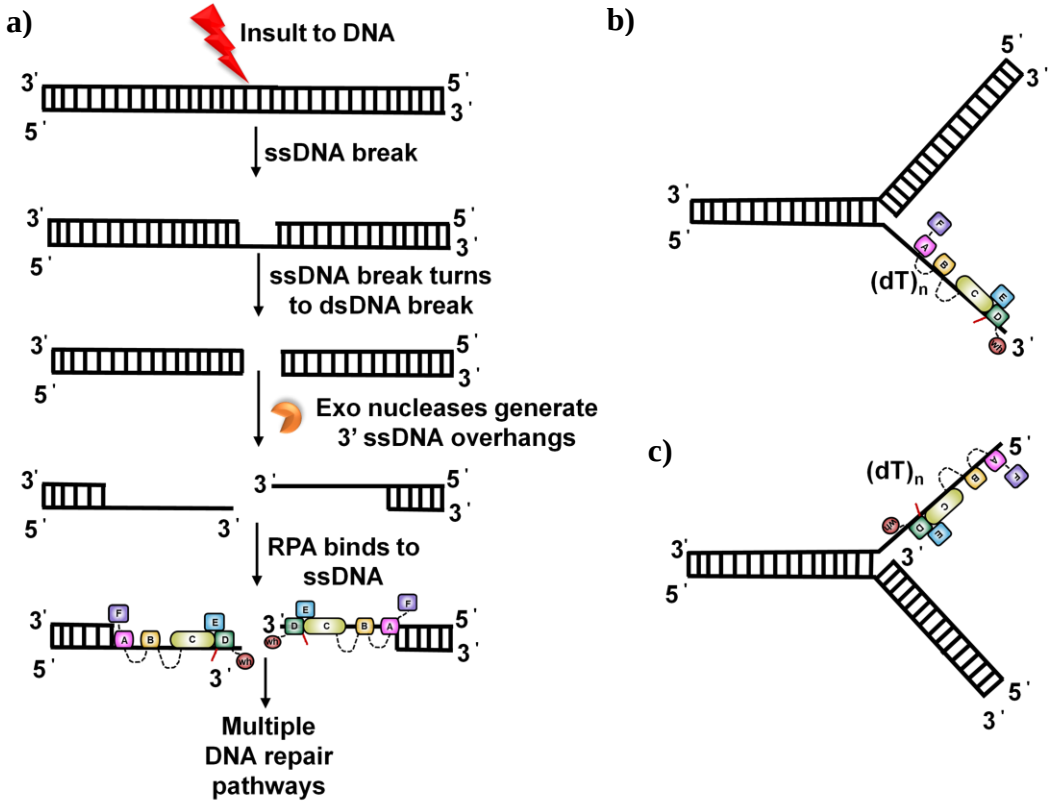

Figure 4-2: ssDNA encountered by RPA in different DNA contexts. a) Pictorial representation of initiation of DNA repair. Multiple DNA damaging agents can cause ssDNA breaks, whose accumulation lead to dsDNA break. In HR pathway, the broken ends are degraded by Exonucleases (ExoI) to generated 3′ overhangs. These overhangs are coated by RPA to allow progression of DNA repair. ssDNA is presented to RPA either as **b)** 3′ ssDNA substrate during recombination or **c)** 5′ ssDNA substrate during BIR. Both processes distinctly affect the arrangement of DBDs on the ssDNA substrate.

The majority of findings regarding how RPA behaves in a particular DNA context have been made either using full-length RPA or through computer simulations and modeling, with limited resolution at the DBD-level. These studies provide critical insights regarding properties of RPA-engagement in different DNA structure situations (such as, bubbles, overhangs and replication forks), yet, most of the models derived from

these studies have a major caveat. Until recently, studies conducted with RPA and different DNA structures have regarded DBD-A and DBD-B as high-affinity domains and the trimerization core as the low affinity domains (Bhat, Bétous, & Cortez, 2015; Iwona M. Wyka, Kajari Dhar, Sara K. Binz, & Wold, 2003). In chapter 3, I demonstrated that the so called 'high-affinity domains' are in fact more flexible, prone to dissociation and easily remodeled by the trimerization core. The 'low-affinity domains' are the stable binders on DNA. Therefore, DBD-A, DBD-B along with OB-F bind to ssDNA first, followed by the engagement of the trimerization core that stabilizes RPA-DNA binding (Nilisha Pokhrel et. al., 2019; Yates et. al., 2018). This has shifted the paradigm of how we envision the processes of RPA binding on DNA and demands a re-assessment of several RPA-DNA structural interaction models that were based on the notion of DBD-A and DBD-B being the high affinity domains. This, in turn, requires a comprehensive investigation of the ongoing mechanisms at the molecular level of DBDs.

Our findings regarding how RPA interacting proteins can selectively modulate the binding dynamics of particular DBDs has been key in further exploring the "Domain-specific sequential displacement" hypothesis. According to this hypothesis, a protein with comparatively lower binding affinity to ssDNA, modulates the binding dynamics of one or more selective DBDs. This causes a ripple effect, weakening the overall RPA binding to ssDNA and resulting in RPA displacement. While this hypothesis is being rigorously tested, the recent discovery of RPA-stabilizing protein or RPA-chaperone, i.e, Rtt105 has been of key interest, particularly because it is the first known RPA chaperone that 'stabilizes' RPA-DNA binding (S. Li et. al., 2018). Similar to DBD-specific modulation

and subsequent displacement of RPA, a DBD-specific mechanism for stabilizing RPA on DNA could one of several ways by which Rtt105 stabilizes RPA engagement on DNA.

Regulators of Ty1 transposition genes (*RTT* genes) were discovered during a genetic screen to identify genes that would otherwise inhibit or downregulate incorporation of Ty1 elements into the host genome. Rtt105 was one of the 8 genes with previously unknown characteristics, and recently has been shown to interact directly with RPA both *in vitro* and *in vivo* (Mularoni et. al., 2012; Scholes, Banerjee, Bowen, & Curcio, 2001). Using a combination of genetic and biochemical approaches *Li et. al., 2018,* demonstrated Rtt105 to function as a stabilizer of RPA-DNA interactions, and an essential factor required to maintain RPA levels in cells with hydroxyurea (HU) induced DNA replication stress (S. Li et. al., 2018). While Rtt105 itself did not bind to DNA and was not present in a 'post-formed' RPA-DNA complex, it functioned as a chaperone to stabilize the RPA-DNA interactions that were in the process of being formed. Finally, using single-molecule DNA curtain assays, *Li et. al., 2018,* showed increased DNA stretching by RPA in the presence of Rtt105, suggesting that Rtt105 affected the binding mode of RPA (S. Li et. al., 2018). These results clearly demonstrate that Rtt105 influences RPA-DNA interactions, yet the mechanisms underlying it are not fully dissected. A number of questions remain to be investigated: does Rtt105 interact with all DBDs of RPA? Does it selectively influence binding dynamics of a particular DBD? Is DNA required for interaction between Rtt105 and RPA-DBD? Is the 'chaperoning' activity of Rtt105 during RPA-DNA interactions different in various DNA structures?. RPA binds to DNA with sub-nanomolar affinity. In this chapter, we sought to understand

Rtt105-RPA interactions at the DBD-level, both in presence and absence of these of DNA substrates.

RPA is of the central proteins involved in majority of the DNA- related processes that involves transiently arising ssDNA intermediates. Delineating how RPA coordinates its DBD binding in different DNA structures could provide be instrumental in dissecting approaches underlying RIP recruitment, positioning and DNA hand-over by RPA. In this chapter, we have investigated how the DNA binding dynamics, in particular the association and remodeling of RPA-DBDs, can be affected when ssDNA has an adjacent dsDNAstructure (Fig 4-3). Using RPA-A^f and RPA-D^f as molecular probes for detecting DBD-specific response on these DNA substrates, and accounting for the fact that DBDs A, B are the flexible half of RPA, we investigated behavior of these DBDs on dsDNA with a 5′ ssDNA overhang (5′ overhang), 3′ ssDNA overhang (3′ overhang) or ssDNA flanked by a duplex end (blocked ends DNA) on either side (Fig 4-3).

Our results show that remodeling of DBD-A requires a free 5′ open end of DNA and this remodeling is not observed for DNA substrates with 3′ overhang or blocked end DNA substrates. Stopped-flow reactions monitoring DBD-D association show a linear increase in the rate of association with increasing lengths of overhangs or length of gaps in the blocked end DNA substrate. This is different from binding of DBD-D with increasing lengths of ssDNA in absence of nearby dsDNA structure. Finally, using a combination of bulk FRET stopped-flow experiments, followed by kinetic fitting of the observed change in fluorescence, we show that Rtt105 specifically interacts with DBD-D. Rtt105-RPA-DBD-D interaction doesnot require ssDNA. Finally, Rtt105 affects RPA-DBD-D DNA binding dynamics on a 5′ or 3′ overhang DNA substrates.

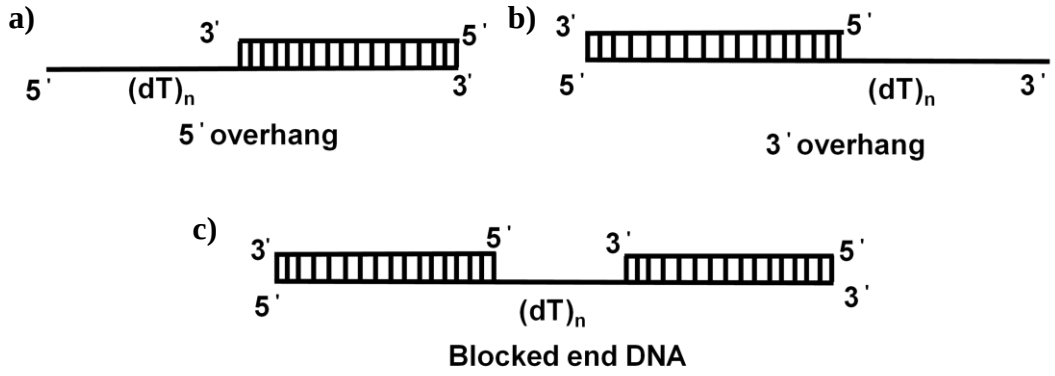

Figure 4-3: DNA substrates to delineate context dependent RPA-DBD engagement on ssDNA used in this study. Individual ssDNA substrates that have an adjacent DNA duplex region. ssDNA is presented as **a)** 5′ overhang, **b)** 3′ overhang and **c)** blocked end DNA to understand effects on RPA-DBD dynamics. The two overhangs and the ssDNA gap in the blocked end DNA consist of varying numbers of polythymidine residues $(dT)_n$. Since RPA binds with a polarity of 5′ -3′, with DBD-A close to 5′, each of the DNA substrate used in this study will allow to understand the effects of nearby duplex region on particular DBD-ssDNA engagement dynamics.

4.2 Materials and Methods

4.2.1 Purification of Rtt105

Rtt105-his plasmid with (6x-histidine amino acid at C-terminus of the protein) was a kind gift from Dr. Xiaolan Zhao (Memorial Sloan Kettering Cancer Center, Sloan Kettering Institute, New York). Approximately 300ng plasmid was transformed into standard Rosstta-2 PlysS protein expression cell line, plated in ampicillin resistant agar plates and incubated overnight at 37^{o}C. Next day, colonies on the agar plates were suspended in total 10ml of Lb, from which 3ml was inoculated in individual 2.8l baffle flask containing 1l autoclaved Lb, supplemented with 100 μg/ml ampicillin. The total growth volume was 2l. The flask was agitated at 250 rpm at 37^{o}C until the growth reached an OD_{600} of 0.6-0.8. At an OD_{600} 0.6-0.8, for each 1l growth, the culture was induced by adding 1ml of 1M IPTG (1mM final concentration), shifted to 18^{o}C and allowed to grow overnight with 150rpm agitation. Note: All the steps from here on were performed at 4^{o}C or on ice.

Cells were pelleted by centrifugation at 5000rpm for 30 mins and resuspended in 100ml cell lysis buffer (30mM Hepes, pH 7.8; 300mM KCl; 1mM TECEP-HCL; 0.02% Tween-20;, 10% glycerol; 2XPIC). Cells were first lysed with 0.02g lysozyme with stirring at 4^{o}C for 1 hour. Further lysis was performed by sonication using the following settings: 1minute pulse followed by 1 minute off, pause for additional one-minute. This was repeated twice. The culture was stirred during the 1-minute pause to ensure proper mixing. Amplitude of sonication was set to 50%. Cell lysate was collected by centrifugation at 17000 rpm for 1 hour. This was then applied to 10ml Ni^{2+}-NTA (Gold

Bio) equilibrated with 200ml of cell lysis buffer. The lysate was allowed to incubate with Ni^{2+}-NTA column for a minimum of 3 hours.

Note: Due to elevated levels of expression and subsequent Rtt105 in the cell lysate, the cell lysate tends to clump the Ni^{2+}-NTA resins and turn them brownish in color. This may slow the flow-rate of the column, particularly if it is driven by gravity.

After 3 hours, flow-through was collected and the unbound Rtt105 was sequentially washed with 100mls of cell lysis buffer + 10mM Imidazole, 100ml of cell lysis buffer + 10mM Imidazole +2M KCl (instead of 300mM KCl) and finally with 100ml of cell lysis buffer + 10mM Imidazole + 100mM KCl. The 2M KCl containing buffer helps to remove possible DNA contamination that could arise during purification. Bound protein was batch eluted with Ni^{2+}-NTA elution buffer (cell lysis buffer+100mM KCl+400mM Imidazole). For batch elution, Ni^{2+}-NTA resins were incubated with 20 ml of Ni^{2+}-NTA elution buffer for 10 minutes to ensure all the resins contacted the elution buffer. The was repeated 6 times to collect a total 120ml elution. Ni^{2+}-NTA eluates were analyzed by 10% SDS-PAGE and Rtt105 containing eluates were pooled and applied to 10ml Q-sepharose col equilibrated with buffer H^{100}, where, buffer H^0 is: 30mM Hepes, pH 7.8; 0.2 mM EDTA, pH 8.0; 0.02% Tween-20; 1mM TECEP-HCl; 10% glycerol (v/v), 2X PIC. The superscript in H^{100} denotes concentration of KCl in mM. Unbound Rtt105 was washed with 100ml of H^{100} and bound protein was eluted with a 100ml gradient elution of H^{100}-H^{1500}, and collected as 1.5ml fractions. Fractions were analyzed on 10% SDS-PAGE, following which fractions containing Rtt105 were pooled and diluted with buffer H^0 to match the conductivity of H^{100} and applied to 10ml heparin column equilibrated with H^{100}. The heparin column was washed with 100ml H^{100} and a

total of 100ml gradient elution (H^{100}-H^{1500}), with individual 1.5ml volume fractions was collected. Surprisingly, Rtt105 does not bind to heparin column and almost 80% of the protein was present in flow-through and wash of heparin column. Hence, we recommend proceeding to size-exclusion column after Q-column.

In our case, to rescue Rtt105 purification, the flow-though, wash and all the fractions with Rtt105 from heparin column were pooled, diluted to a conductivity of cell-lysis buffer, and re-applied to 10ml Ni^{2+}-NTA column equilibrated with cell lysis buffer. Ni^{2+}-NTA column was processed as mentioned above. These eluates from Ni^{2+}-NTA column were analyzed on 10% SDS-PAGE and fractions containing Rtt105 were pooled and concentrated using a 10KDa cut-off spin-concentrator to a volume less than 5ml and applied on HiLoad 16/600 200 Superdex- 200pg size exclusion column equilibrated with Rtt105 storage buffer (30mM Hepes, pH 7.8; 200mM KCl; 5mM TECEP-HCl; 0.25mM EDTA, pH 8.0; 0.01% Tween-20; 10% glycerol). A total of 320ml elution that includes 100ml void volume was collected as 1.7ml fractions. These fractions were analyzed on 10% SDS-PAGE gel, pooled, and concentrated using 10KDa cut of spin-concentrator. Concentration of Rtt105 was determined by Bradford assay and protein was stored as 100µl aliquots at -80^{o}C, after flash-freezing in liquid nitrogen.

4.2.2 Fluorescent Labeling of Rtt105

Rtt105 has two consecutive cysteine residues at position 11 and 12 towards the N-terminus. Such a positioning of cysteine residues could be one reason for higher order Rtt105 complexes which can be visualized in 10% SDS-PAGE gel. To label Rtt105 with Cy5 Maleimide (Click chemistry tools), about ~5ml of 172µM Rtt105 was thawed and

dialyzed extensively in storage buffer that does not contain TECEP-HCl. About 4 buffer exchanges, with an interval of 12 hours between individual exchange was conducted. Rtt105 precipitates in the absence of a reducing agent. Therefore, the clear protein was separated from the precipitate by centrifugation at 2000rpm for 2minutes. Concentration of Rtt105 in the supernatant was calculated by Bradford assay as 86.8μM. To label Rtt105 with Cy5, 1.5-fold molar excess Cy5 Malemide dye (83.3 μl of 6mM Cy5, 10μl at a time) was added to 3.85ml of 86.6μM Rtt105 and the dye containing protein was incubated at 4^{o}C, with gentle rocking for 3 hours. Excess dye was separated from the protein using a Biogel-P4 column. 1ml fraction each, for a total of 60ml elution was collected and the fractions were analyzed on 10% SDS-PAGE gel. The concentration of labeled Rtt105 was determined by Bradford assay and Cy5 present in the protein via spectroscopic measurements using the equation:

[Cy5] M = [{$\lambda_{abs\ (max\ @\ 640nm)}$- $\lambda_{abs\ (correction\ @750nm)}$}* dilution factor]÷ Cy5$_{\varepsilon}$, where

ε= 250,000 $M^{-1}cm^{-1}$, Labeling efficiency was ~20%

As a control, we conducted Bradford assays with Cy5 to determine if it affected absorption at 595nm and found it did not affect absorption reading at 595nm.

4.2.3 Purification of RPA-A^{MB543} and RPA-D^{MB543}

RPA-A^{MB543}, RPA-D^{MB543} and RPA-FAB^{MB543} were prepared as mentioned in methods section of chapter 3.

4.2.4 Annealing Oligos

All the oligos were purchased from IDT (Coralville, Iowa). For all annealing, in a 1.5ml microfuge tubes, equal molar concentrations (M) of respective DNA substrates were prepared in a buffer with 20mM Tris-Cl, pH 7.5, 100mM NaCl (annealing buffer). The microfuge tube was incubated in boiling water for 5 minutes (temperature of 100^{o}C was confirmed using a thermometer), following which the samples were allowed to eventually cool down to room temperature. We generally prepared 200µl of 10µM annealed substrates for all our reactions.

For 5′ overhang, equal concentrations of 5′ $(dT)_n$ CTG GGG CTC GAG CCG ACT CG 3′ and 5′ CGA GTC GGC TCG AGC CCC AG 3′ 20 base mixed sequence were annealed. $(dT)_n$ represents the number of thymidine nucleotides that were varied, and the underlined region represents 20 base pair mixed sequence that was kept consistent through all 5′ overhang substates and formed a complementary base pair with 5′ CGA GTC GGC TCG AGC CCC AG 3′. For example, to anneal 5′ $(dT)_{10}$ overhang, equal concentration of 5′ TTTTTTTTTTCTG GGG CTC GAG CCG ACT CG 3′ and 5′ CGA GTC GGC TCG AGC CCC AG 3′ were prepared in annealing buffer, incubated in boiling water for 5 minutes and allowed to cool down.

To prepare a 3′ overhang $(dT)_n$, equal concentrations of 5′ ACC GCT GCC GTC GCT CCG GG $(dT)_n$ 3′ and 20 base mixed sequence 5′ CCC GGA GCG ACG GCA GCG GT 3′ were annealed. $(dT)_n$ represents the number of thymidine nucleotides that were varied, and the underlined region represents 20 base pair mixed sequence that was kept consistent through all 3′ overhang substates and formed a complementary base pair

with 5′ CCC GGA GCG ACG GCA GCG GT 3′. For example, to generate 3′ $(dT)_{10}$ overhang, equal concentration of 5′ ACC GCT GCC GTC GCT CCG GG TTTTTTTTTT 3′ and 5′ CCC GGA GCG ACG GCA GCG GT 3 ′ were annealed.

To prepare blocked end $(dT)_n$ substrates, equal concentrations of 5′ ACC GCT GCC GTC GCT CCG GG 3′; 5′ CGA GTC GGC TCG AGC CCC AG 3′ and 5′ CTG GGG CTC GAG CCG ACT CG $(dT)_n$ CCC GGA GCG ACG GCA GCG GT 3′ were annealed. $(dT)_n$ represents the number of thymidine nucleotides that were varied, and the underlined region represents 20 base pair mixed sequence that was kept consistent through all blocked ends overhang substates and formed a complementary base pair with the two distinct 20-mer mixed base sequences. For example, to generate blocked end $(dT)_{10}$ overhang, equal concentrations of 5′ ACC GCT GCC GTC GCT CCG GG 3′; 5′ CGA GTC GGC TCG AGC CCC AG 3′ and 5′ CTG GGG CTC GAG CCG ACT CGTTTTTTTTTTCCC GGA GCG ACG GCA GCG GT 3′ were annealed.

4.2.5 Stopped flow measurements

All stopped-flow measurements were carried out with an Applied Photophysics SX20 instrument (Surrey, UK) at 25^{o}C. Reactions were performed in buffer (30 mM Hepes, pH 7.8, 100 mM KCl, 5 mM $MgCl_2$, 1 mM β-mercaptoethanol and 6 % v/v glycerol). All concentrations mentioned are post-mixing concentrations.

For all the DNA context dependent reactions with MB543 labeled RPA (RPA-A^{MB543} and RPA-D^{MB543}), were performed 100nM protein and 100nM individual DNA substrates. Samples were excited at 535nm and emission monitored at 555nm. Resulting

stopped flow data for RPA-A^{MB543} were fit with double-exponential + linear phase model i.e

$$\Delta F = A_1(1 - e^{-k_1 t}) + A_2(1 - e^{-k_2 t}) + k_3 t \qquad \text{(Eq. 1)}$$

Where, ΔF is change in fluorescence of A^{MB543}, A_1 and k_1 are the amplitude and observed rate of the first exponential phase, A_2 and k_2 are the amplitude and observed rate of the second exponential phase, k_3 is the steady state rate and t is time.

and the data for RPA-D^{MB543} were fit with single-exponential + linear phase model i.e

$$\Delta F = A_1 (1 - e^{-k_1 t}) + k_2 t \qquad \text{(Eq. 2)}$$

Where, ΔF is change in MB543 fluorescence in presence of DNA, A_1 and k_1 are the amplitude and observed rate of the exponential phase, k_2 is the steady state rate and t is time.

For all the experiments with RPA-A^{MB543}, RPA-D^{MB543} and unlabeled Rtt105, excitation emission parameters as mentioned above (for MB543) were used. RPA-Rtt105 reactions in $(dT)_{30}$ required rapid mixing of either 100nM RPA-A^{MB543} or 100nM RPA-D^{MB543} with increasing concentrations of Rtt105 (25, 50, 100, 200, 300) in one syringe, with 100nM $(dT)_{30}$ in another syringe. Binding reactions with 100nM 5′ $(dT)_{30}$ overhang and 100nM 3′ $(dT)_{30}$ overhang was performed by rapid mixing with 100nM RPA-A^{MB543} or 100nM RPA-D^{MB543} in presence or absence of 200nM Rtt105. Similar rapid-mixing reactions were performed with 100nM RPA-FAB^{MB543} with increasing concentrations of Rtt105 (50, 100, 200, 300 nM) in one syringe with100nM $(dT)_{30}$ in another syringe. All the data obtained for RPA-A^{MB543} binding to $(dT)_{30}$, 5′ $(dT)_{30}$ overhang and 3′ $(dT)_{30}$

overhang in presence or absence of Rtt105 were fit with equation Eq.1. Similar data for RPA-D^{MB543} and RPA-FAB^{MB543} were fit with Eq.2.

4.2.6 FRET analysis to monitor interaction between Rtt105 and RPA-DBDs

For all FRET experiments, samples were excited at 555nm and FRET was monitored with a 645nm cut-off emission filter. For FRET experiments, RPA-A^{cy3} or RPA-D^{Cy3} was the FRET donor and Rtt105^{Cy5}was the FRET acceptor. To monitor DBD specific interaction, 100nM RPA-A^{Cy3} or 100nM RPA-D^{Cy3} was rapidly mixed with 100nM Rtt105^{Cy5} and FRET monitored. Resulting FRET between RPA-D^{Cy3} and Rtt105^{Cy5} was analyzed using Eq. 1.

FRET in presence of ssDNA was conducted with either 100nM RPA-A^{cy3}/ 100nM RPA-D^{Cy3} and 100nM $(dT)_{35}$, and rapidly mixed with 100nM Rtt105^{cy5}. Alternatively, 100nM Rtt105^{Cy5} and 100nM $(dT)_{35}$ in one syringe were rapidly mixed with RPA-A^{cy3}/ RPA-D^{Cy3} in another syringe. The resulting FRET between RPA-D^{Cy3} and Rtt105^{Cy5} in presence of $(dT)_{35}$ was analyzed with Eq. 2.

Finally, FRET complex challenging experiments were performed with 100nM FRET complex (100nM RPA-A^{cy3} or 100nM RPA-D^{Cy3} and Rtt105^{cy5}) and 100nM $(dT)_{35}$ in another syringe. The resulting decrease in FRET for RPA-D^{cy3} was analyzed using Eq.2. FRET-DNA complex was formed between 100nM FRET complex and 100nM $(dT)_{35}$ and challenged with 1X reaction buffer. No change in FRET for both RPA-A^{Cy3} and RPA-D^{Cy3} was observed.

4.3 Results

4.3.1 DNA context dependent remodeling of DBD-A

RPA forms a stable complex with DNA, yet, RPA-DNA engagement is plastic at the microscopic level (Kemmerich et. al., 2016; B. Nguyen et. al., 2014b). In chapter 2, using fluorescently labeled RPA, we demonstrated the phenomenon of 'intra-DBD remodeling', where DBD-A is remodeled by RPA's trimerization core under conditions of low concentration of ssDNA or shorter lengths of ssDNA. To investigate if trimerization core mediated intra-DBD remodeling could occur in different DNA structures, similar experiments were performed with 5′ $(dT)_n$ overhang, 3′ $(dT)_n$ overhang or blocked ends $(dT)_n$ (where (dT) is flanked by a DNA duplex on both sides; n= number of thymidine nucleotides, ranging from 6 to 30 nucleotides) (Fig 4-3). The duplex region in all DNA substrates consists of the same 20 base pairs of complementary sequences. Stopped flow experiments performed with 100nM RPA-A^{MB543} and structurally distinct DNA substrates (5′ overhang, 3′ overhang and blocked ends) as a functions of increasing $(dT)_n$ produced a robust and quantifiable change in fluorescence which was quantified using a double exponential followed by a linear state model for all the substrates. Consistent with previously published results monitoring RPA-A^{MB543} binding with increasing lengths of single- stranded DNA (explained in chapter 2), the initial rate of binding ($k_{obs,1}$) was directly proportional to increasing lengths of 5′ $(dT)_n$ and 3′ $(dT)_n$ overhangs (Fig 4-4 b, 4-5 c, 4-6 c). However, the $k_{obs,1}$ measurement for RPA-A^{MB543}

binding with blocked ends $(dT)_n$ did not follow this linear-trend and remained relatively unchanged (Fig 4-7 c). Surprisingly, trimerization core mediated remodeling of DBD-A (seen as decrease in signal after initial robust binding) was observed only with 5′ $(dT)_{10}$ (light grey trace) and 5′ $(dT)_{12}$ (navy blue trace) overhang substates (Fig 4-8). This decrease in signal was not present in 3′ $(dT)_n$ overhang and blocked ends $(dT)_n$ substrates even when the lengths of overhang were kept same (Compare light grey and navy-blue traces in Fig 4-8). This is particularly interesting as RPA binds to DNA with a polarity of 5′ -3′, such that DBD-A resides close to 5′ end of DNA. Blocking the 5′ end, as in the case for 3′ overhang and blocked end substrate could pose steric hindrance for DBD-A movement, thereby, changing the number of conformations it can adopt on DNA. This is more severe for the blocked end substrates which could be one of the many explanations for loss of increase in the $k_{obs,1}$ value as a function of increasing the ssDNA gap sandwiched between two dsDNA.

All the data sets for RPA-A^{MB543} engagement can best be described by a two- step model. Depending on the DNA substrate encountered by DBD-A, there are subtle changes in the mechanisms of remodeling/ rearrangement in 5′ overhang and 3′ overhang DNA substrate. This effect is more prfound for blocked ends DNA substrates. This suggets that the type of DNA structures encountered by DBD-A could influence its mechanism for engaging with ssDNA. There was a negligible change in the rate of the linear phase ($k_{obs,3}$) for all DNA substrates (Fig. 4-4 d, 4-5 e, 4-6 e, 4-7 e) and no significant conclsuions can be drawn from $k_{obs,2}$ values given the low signal to noise ratio (Fig. 4-4 c, 4-5 d, 4-6 d, 4-7 d).

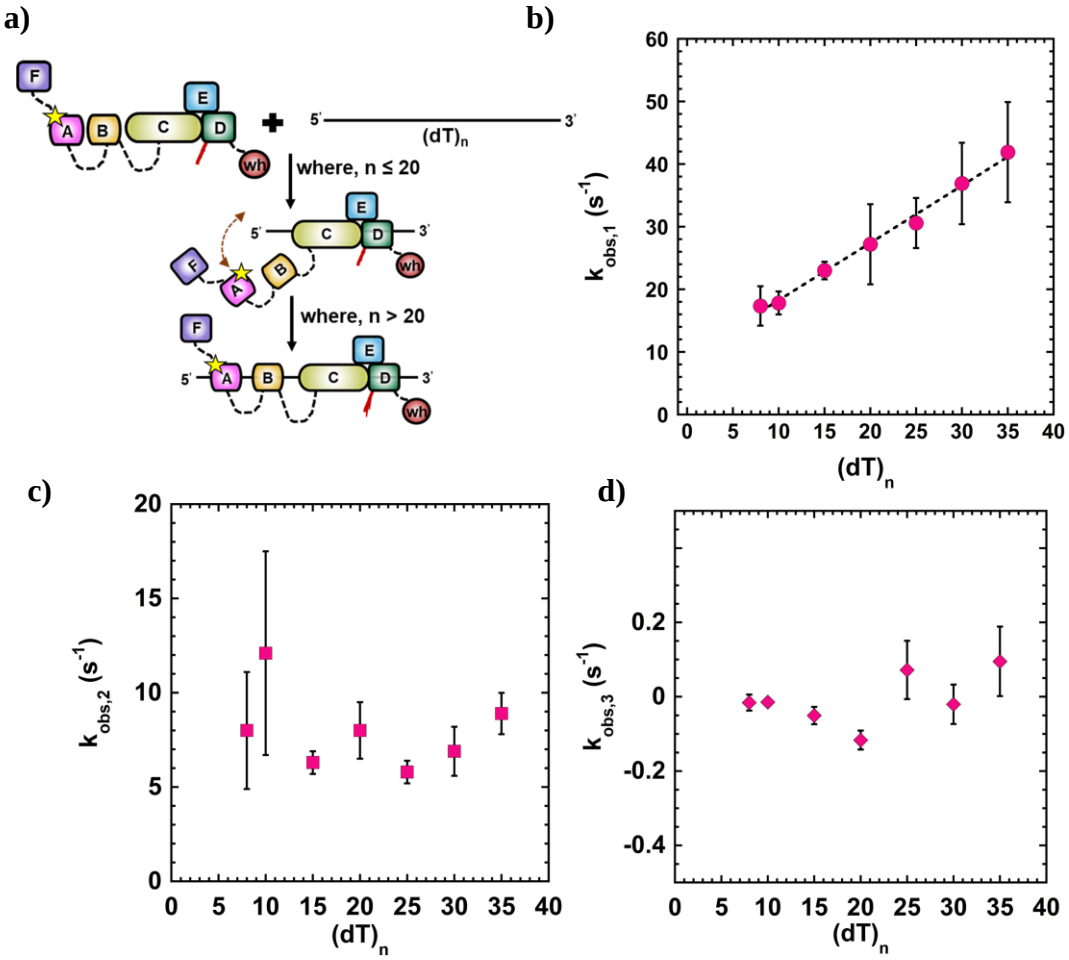

Figure 4-4: DNA binding dynamics of DBD-A with increasing lengths of ssDNA. a) Graphic representation of the stopped-flow mixing scheme, where RPA-A^{MB543} is rapidly reacted with stoichiometric concentrations of increasing lengths of (dT) oligonucleotides. Arrow represent conformational arrangement of DBD-A as a function of increasing lengths of (dT) oligonucleotides. Fitting the raw traces with two-step kinetic model yields **b)** plot of observed initial rate of engagement ($k_{obs,1}$), which follows a linear trend, **c)** rate of remodeling/ rearrangement ($k_{obs,2}$), **d)** steady-state rate ($k_{obs,3}$).

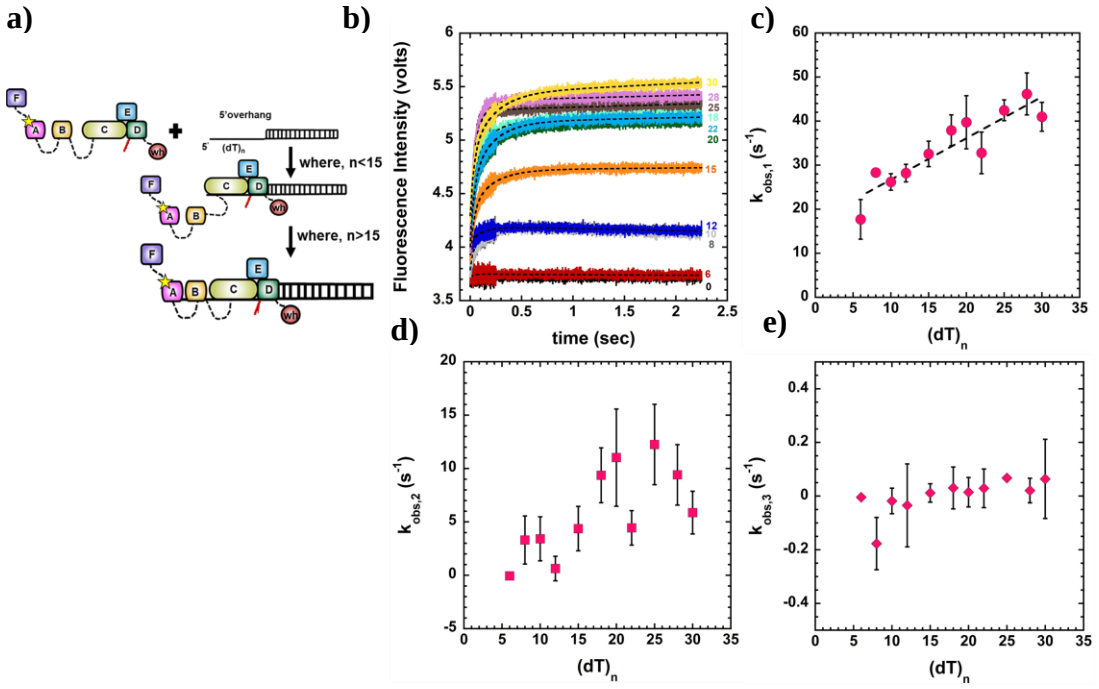

Figure 4-5: DNA binding dynamics of DBD-A with increasing 5′ (dT)$_n$ overhang DNA. a) Diagrammatic representation of the stopped-flow reaction where RPA-A^{MB543} is rapidly reacted with stoichiometric concentrations of increasing lengths of 5′ (dT)$_n$ overhang DNA substrates. **b)** Stopped-flow traces show robust increase in MB543 fluorescence as RPA-A^{MB543} binds to increasing lengths of 5′ (dT)$_n$ overhang DNA substrates. Remodeling of DBD-A can be observed with shorter overhangs which are usually less than 15 nucleotides in length. Fitting the raw traces with a two-step binding followed by steady- state model yields **c)** plot of observed initial rate of engagement ($k_{obs,1}$), which follows a linear trend, **d)** rate of remodeling/ rearrangement ($k_{obs,2}$) and **e)** steady-state rate ($k_{obs,3}$).

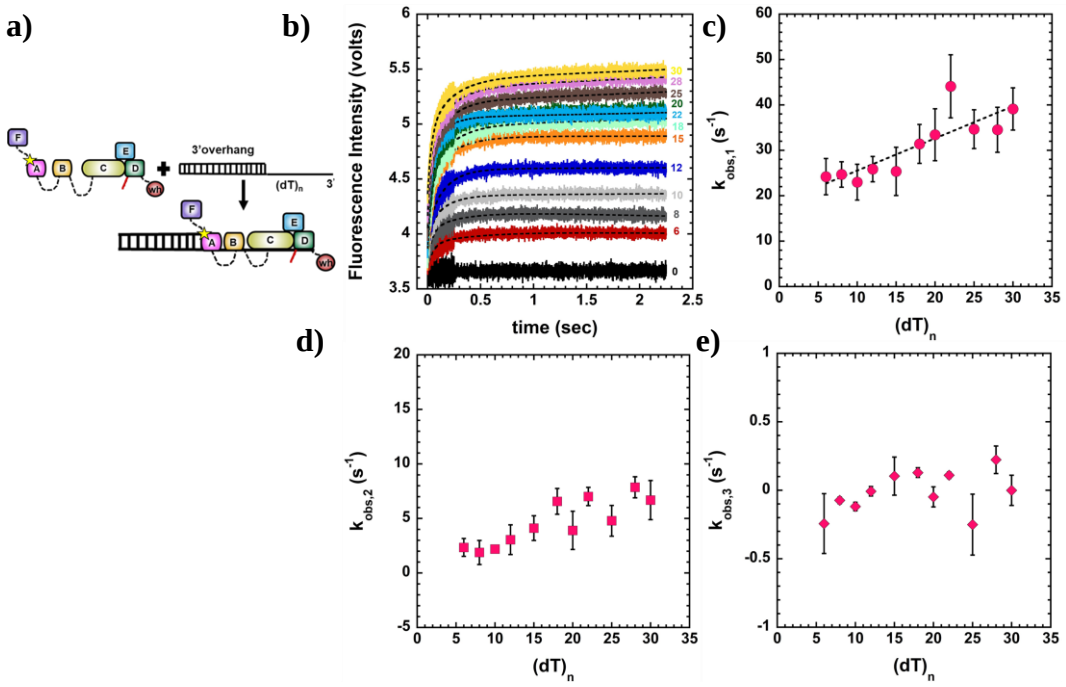

Figure 4-6: DNA binding dynamics of DBD-A with increasing 3′ $(dT)_n$ overhang DNA. a) Diagrammatic representation of the stopped-flow reaction where RPA-A^{MB543} is rapidly reacted with stoichiometric concentrations of increasing lengths of 3′ $(dT)_n$ overhang DNA substrates. **b)** Plot of raw stopped-flow traces show a robust increase in MB543 fluorescence as RPA-A^{MB543} binds to increasing lengths of 3′ $(dT)_n$ overhang DNA substrates. Fitting the raw traces with a two-step binding followed by steady-state model as a function of increasing lengths of 3′ $(dT)_n$ overhang yields **c)** plot of observed initial rate of engagement ($k_{obs,1}$), which follows a linear trend, **d)** rate of remodeling/ rearrangement ($k_{obs,2}$), showing a slightly cooperative behavior **e)** steady-state rate ($k_{obs,3}$) with negligible change in the observed values.

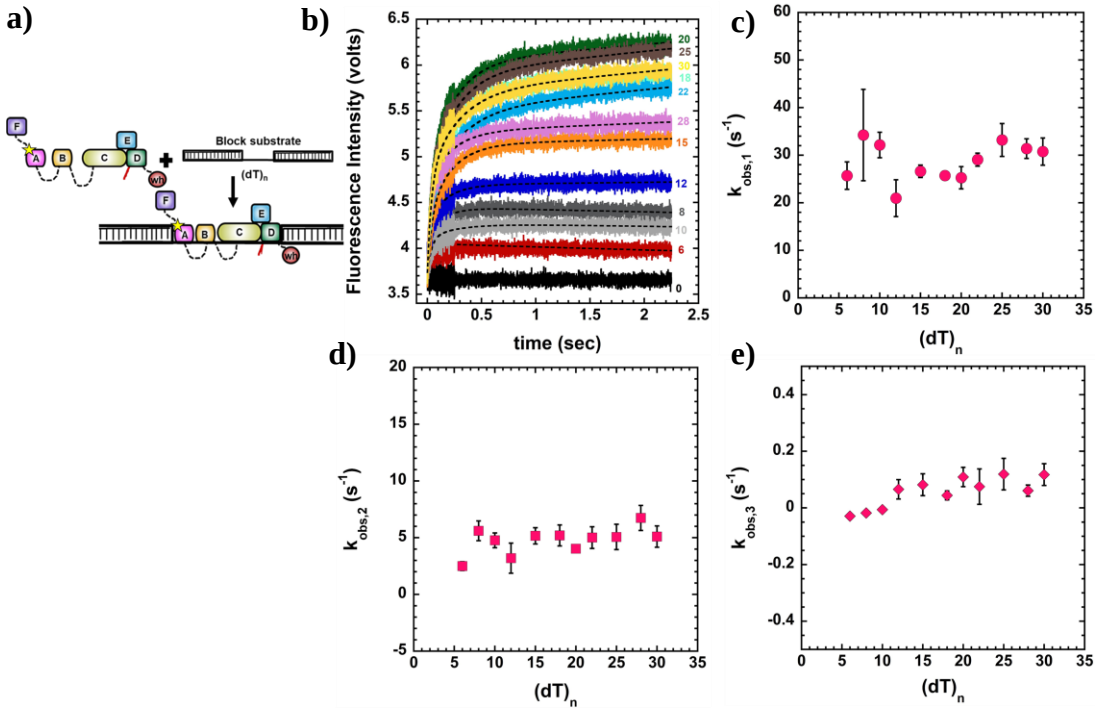

Figure 4-7: DNA binding dynamics of DBD-A with increasing blocked ends $(dT)_n$ DNA substrate. a) Diagrammatic representation of the stopped-flow reaction where RPA-A^{MB543} is rapidly reacted with stoichiometric concentrations of increasing lengths of blocked ends $(dT)_n$ DNA substrates. Blocked end DNA substrate consist of a single-stranded $(dT)_n$ region flanked by 20 base-pair (bp)DNA duplex on both ends. The length of $(dT)_n$ region is varied while keeping the 20bp duplex region constant. **b)** Stopped-flow traces show a robust increase in MB543 fluorescence as RPA-A^{MB543} binds to increasing lengths of blocked end DNA substrates. Fitting the raw traces with a two-step binding followed by steady-state model as a function of increasing lengths of $(dT)_n$ yields **c)** plot of observed initial rate of engagement ($k_{obs,1}$), **d)** rate of remodeling/ rearrangement ($k_{obs,2}$) and **e)** steady-state rate ($k_{obs,3}$).

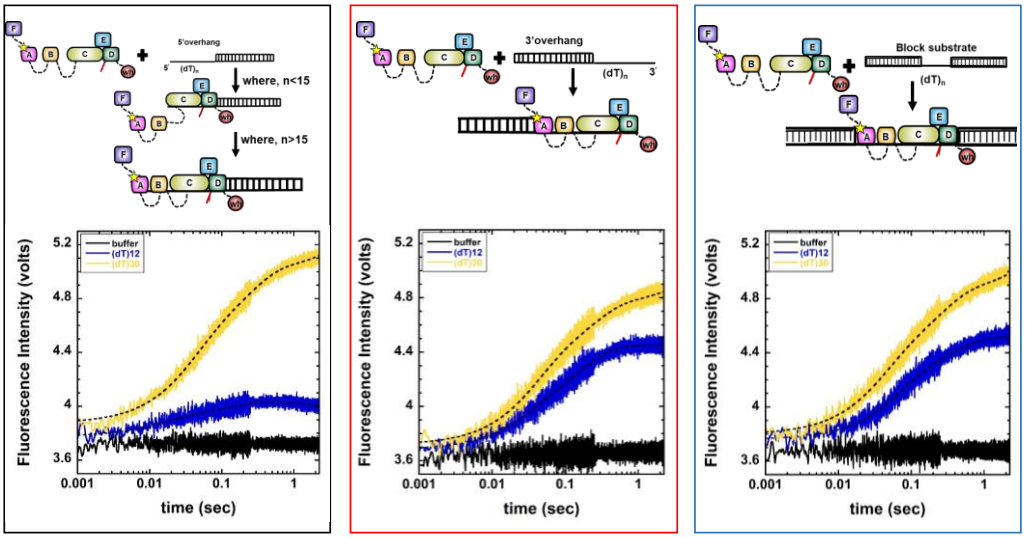

Figure 4-8: Summary figure showing DNA context dependent DBD-A ssDNA binding dynamics. Black, red, and blue boxes highlight reactions with 100nM RPA-A^{MB543} vs 5′ $(dT)_n$ overhang, 3′ $(dT)_n$ overhang and blocked end DNA substrates, respectively. Navy blue traces represent reactions with short ssDNA region available for binding i.e $(dT)_{12}$ and yellow traces represent comparatively longer DNA substrate i.e $(dT)_{30}$ that is enough DNA binding space for all DBDs to stably engage on ssDNA. Dashed lines in the center of each traces represents curve fitting with two-step + linear phase binding model equation. Following excitation of MB543 fluorophore, for both lengths of ssDNA available i.e $(dT)_{12}$ and $(dT)_{30}$, robust increase in fluorescence can be observed upon monitoring emission at 555nm. However, the remodeling-phase of DBD-A, which is characterized by decrease in signal, can be seen only for 5′ $(dT)_{12}$ DNA, suggesting DNA context affects the trimerization core mediated remodeling of DBD-A.

4.3.2 DNA context dependent remodeling of DBD-D

We next wanted to understand if there were any effects on DBD-D ssDNA engagement when the ssDNA DNA was presented in the form of 5′ $(dT)_n$, 3′ $(dT)_n$ or blocked end $(dT)_n$ substrates. DNA substrates that were used to monitor DNA-context dependent remodeling of DBD-A were also used to monitor DBD-D dynamics in these different DNA structure scenarios. RPA-D^{MB543} was rapidly mixed with either 5′ $(dT)_n$ 3′ $(dT)_n$ and blocked end $(dT)_n$ DNA substrates and change in MB543 fluorescence was recorded (Fig 4-10 a, 4-11 a, 4-12 a). All the data sets obtained were fit with single exponential followed by a linear phase model. For all three contextual DNA substrates, no RPA-D^{MB543} engagement was observed when the available ssDNA was $(dT)_6$ and $(dT)_8$ (Fig 4-10 b, c; 4-11 b, c). This was more severe for blocked ends DNA substrates, where no binding event could be observed until a length of $(dT)_{10}$, including $(dT)_6$ and $(dT)_8$ (Fig 4-12 b, c). This is different from RPA-D^{MB543} engagement on ssDNA that lacks any other structural complexity, where, binding events could be monitored at $(dT)_8$ (Fig 4-9 b). In addition, there are kinetic differences in DBD-D engagement as a function of increasing lengths of single- stranded DNA when presented with an adjacent dsDNA region. RPA-D^{MB543} showed an increase in rate of binding ($k_{obs,1}$) with increasing lengths of $(dT)_n$ region in 5′ overhang, 3′ overhang and blocked ends DNA substates (Fig 4-10 c, 4-11 c, 4-12 c). This is distinct from binding observed with only ssDNA that lacks adjacent dsDNA region, where, the rate of binding increased with increasing lengths of ssDNA until $(dT)_{20}$, following which it saturated (Fig 4-9 b). Under our experimental conditions, one RPA has a binding site of 20 ±2 nucleotides and saturation of $k_{obs,1}$ value at $(dT)_{20}$ suggested formation of stable trimerization core-DNA complex. However, the

linear increase in $k_{obs,1}$ value when ssDNA is presented with a dsDNA region suggests DBD-D can sense the dsDNA region and perhaps destabilize the helix to open up new binding sites (Lao et. al., 1999).

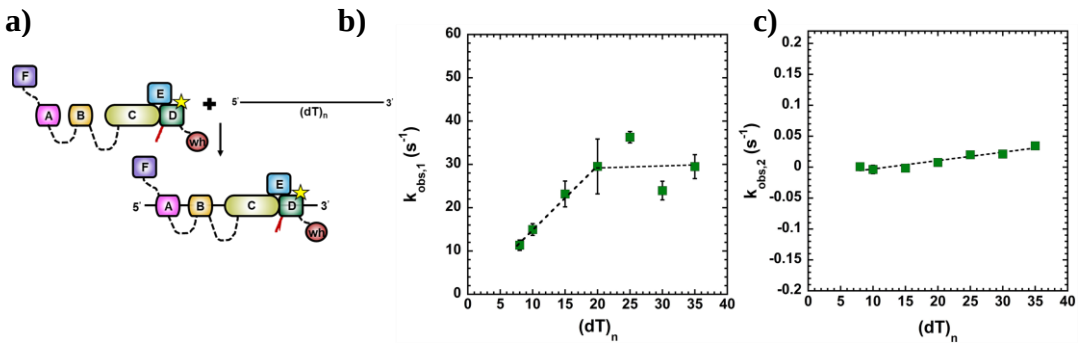

Figure 4-9: DNA binding dynamics of DBD-D with increasing lengths of ssDNA. a) Graphic representation of the stopped-flow mixing scheme, where RPA-D^{MB543} is rapidly reacted with stoichiometric concentrations of increasing lengths of (dT) oligonucleotides. A stable RPA-DBD-D complex is formed. Fitting the raw traces with a single-step followed by linear phase kinetic model yields **b)** plot of observed initial rate of engagement ($k_{obs,1}$), which increases linearly until $(dT)_{20}$ following which it saturates, **c)** steady-state rate ($k_{obs,2}$) with increasing lengths of ssDNA $(dT)_n$ plotted on X-axis.

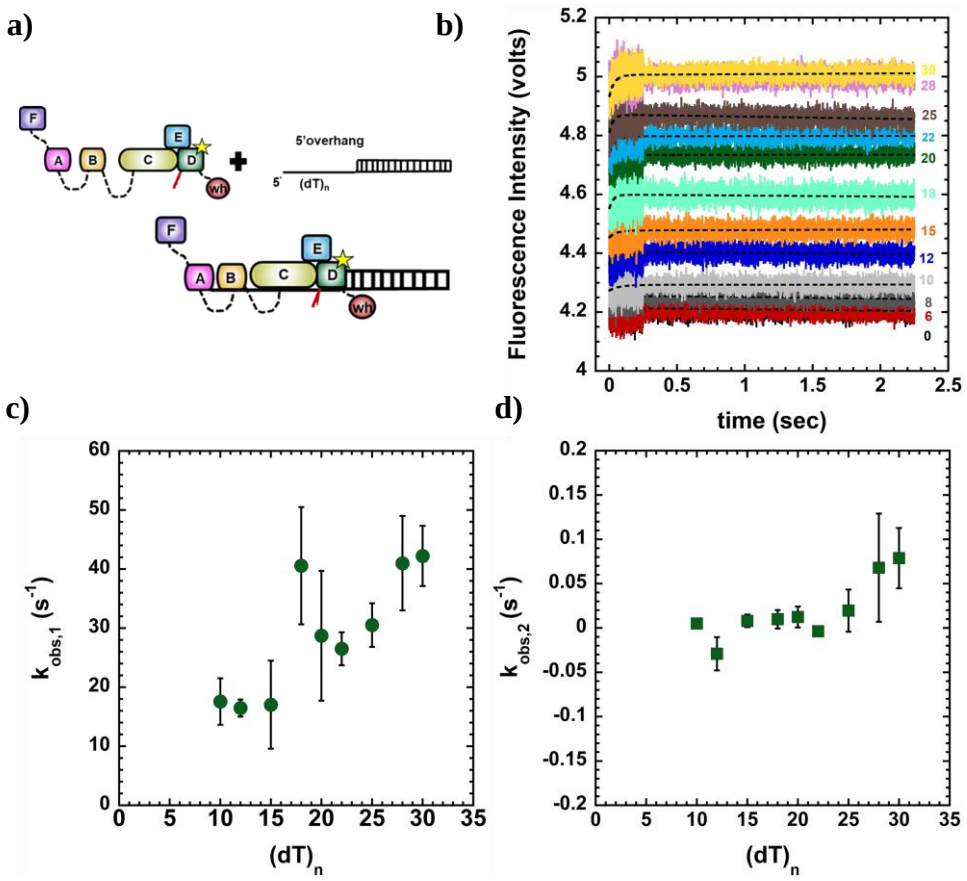

Figure 4-10: DNA binding dynamics of DBD-D with increasing 5′ $(dT)_n$ overhang DNA. a) Diagrammatic representation of the stopped-flow reaction where RPA-D^{MB543} is rapidly reacted with stoichiometric concentrations of increasing lengths of 5′ $(dT)_n$ overhang DNA. MB543 labeled DBD-D produces a robust change in fluorescence upon binding to overhangs longer than 8 thymidine nucleotides in length. **b)** Representative traces from stopped-flow reaction when fit with one-step binding followed by linear phase model yields **c)** plot of observed initial rate of engagement ($k_{obs,1}$), which follows a linear trend, **d)** and plot of steady-state rate ($k_{obs,2}$).

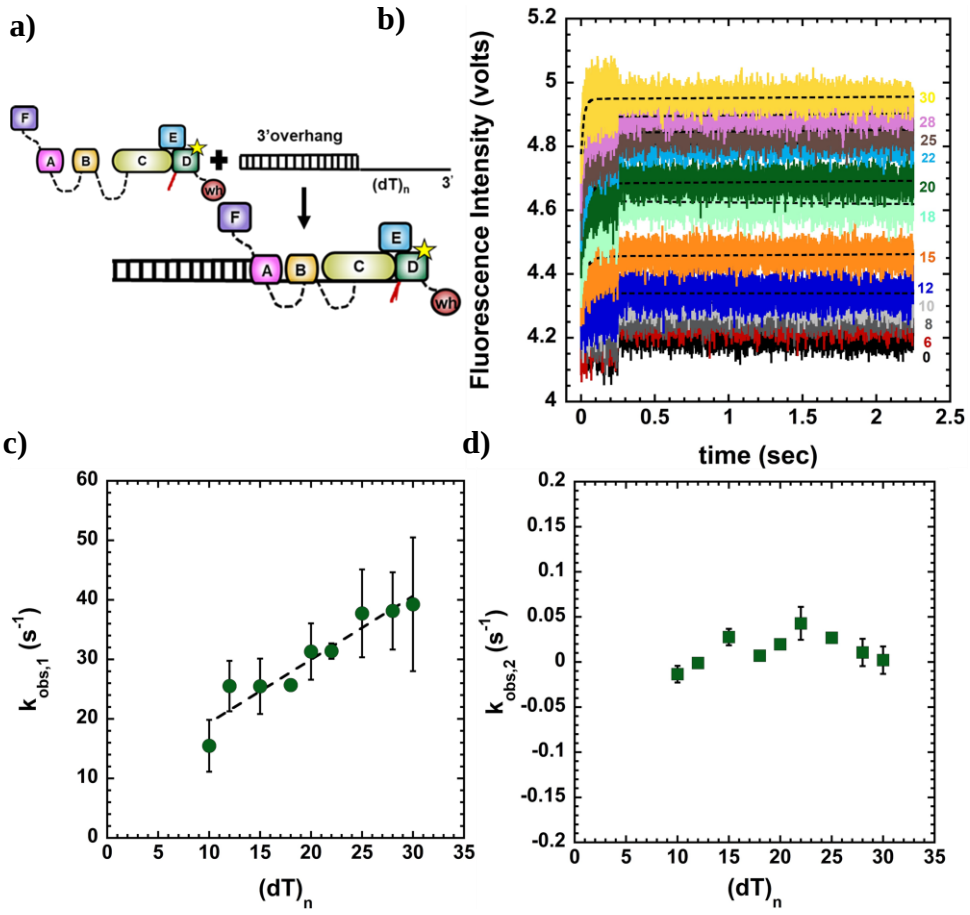

Figure 4-11: DNA binding dynamics of DBD-D with increasing 3′ $(dT)_n$ overhang DNA. a) Pictorial representation of the stopped-flow reaction where RPA-D^{MB543} is rapidly reacted with stoichiometric concentrations of increasing lengths of 3′ $(dT)_n$ overhang DNA. MB543 labeled DBD-D produces a robust change in fluorescence upon binding to overhangs longer than 8 thymidine nucleotides in length. **b)** Representative traces from stopped-flow reaction when fit with one-step binding followed by linear phase model yields **c)** plot of observed initial rate of engagement ($k_{obs,1}$), which follows a linear trend, **d)** and plot of steady-state rate ($k_{obs,2}$).

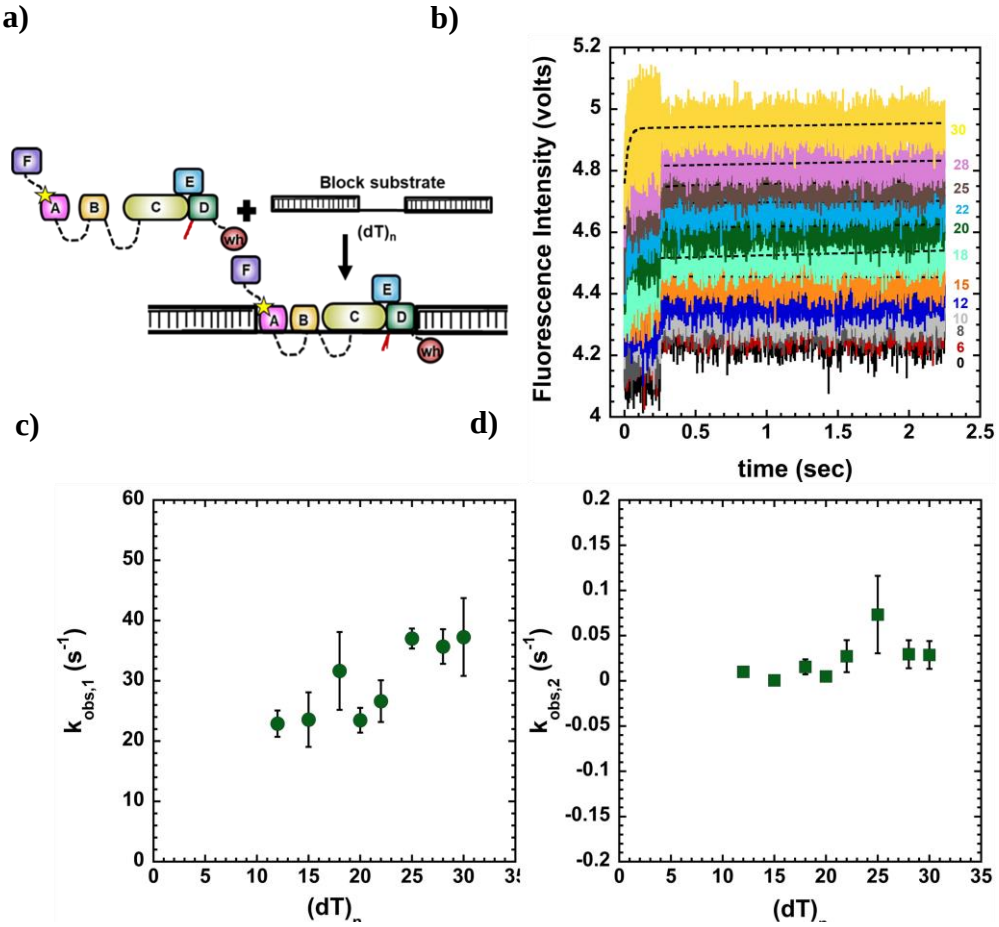

Figure 4-12: DNA binding dynamics of DBD-D with increasing blocked end $(dT)_n$ DNA substrates. a) Illustrative representation of the stopped-flow reaction where RPA-D^{MB543} is rapidly reacted with stoichiometric concentrations of increasing lengths of blocked ends DNA. MB543 labeled DBD-D produces a robust change in fluorescence upon binding to overhangs longer than 10 thymidine nucleotides in length. **b)** Representative traces from stopped-flow reaction when fit with one-step binding model followed by linear phase yields **c)** plot of observed initial rate of engagement ($k_{obs,1}$), which follows a linear trend, **d)** and plot of steady-state rate ($k_{obs,2}$).

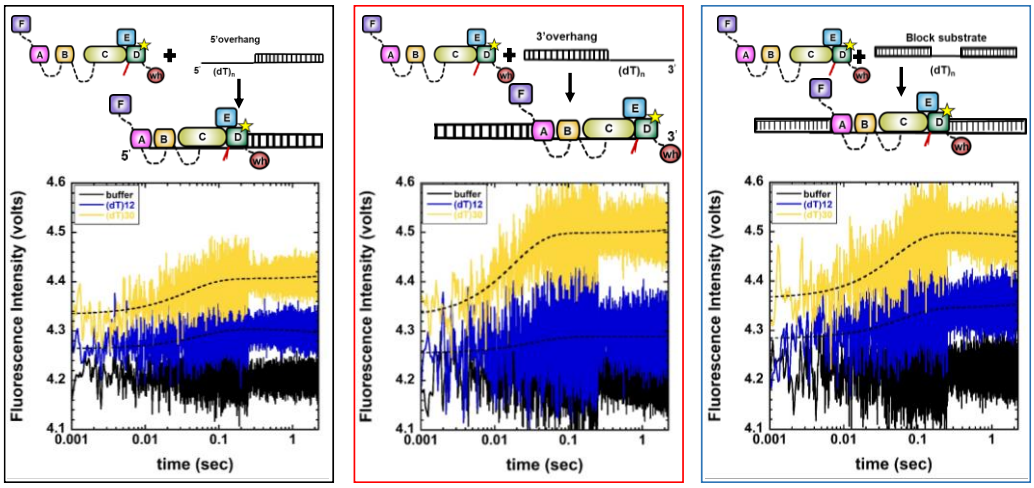

Figure 4-13: Summary figure showing DNA context dependent DBD-D ssDNA binding dynamics. Black, red, and blue boxes highlight reactions with 100nM RPA-D^{MB543} vs 5′ $(dT)_n$ overhang, 3′ $(dT)_n$ overhang and blocked end DNA substrates, respectively. Navy blue traces represent reactions with short ssDNA regions available for binding i.e $(dT)_{12}$ and yellow traces represent comparatively longer ssDNA substrate i.e $(dT)_{30}$ that is enough DNA binding space for all DBDs to stably engage on ssDNA. Dashed lines in the center of each traces represents curve fitting with one-step+ linear phase binding model equation. Following excitation of MB543 fluorophore, for both lengths of ssDNA available i.e $(dT)_{12}$ and $(dT)_{30}$, robust increase in fluorescence can be observed upon monitoring emission at 555nm. Although there are DNA context dependent differences in DBD-D interaction with DNA, DBD-D still forms a stable complex with DNA, as there are no decease in signal suggesting no dsDNA-ssDNA junction mediated remodeling of DBD-D.

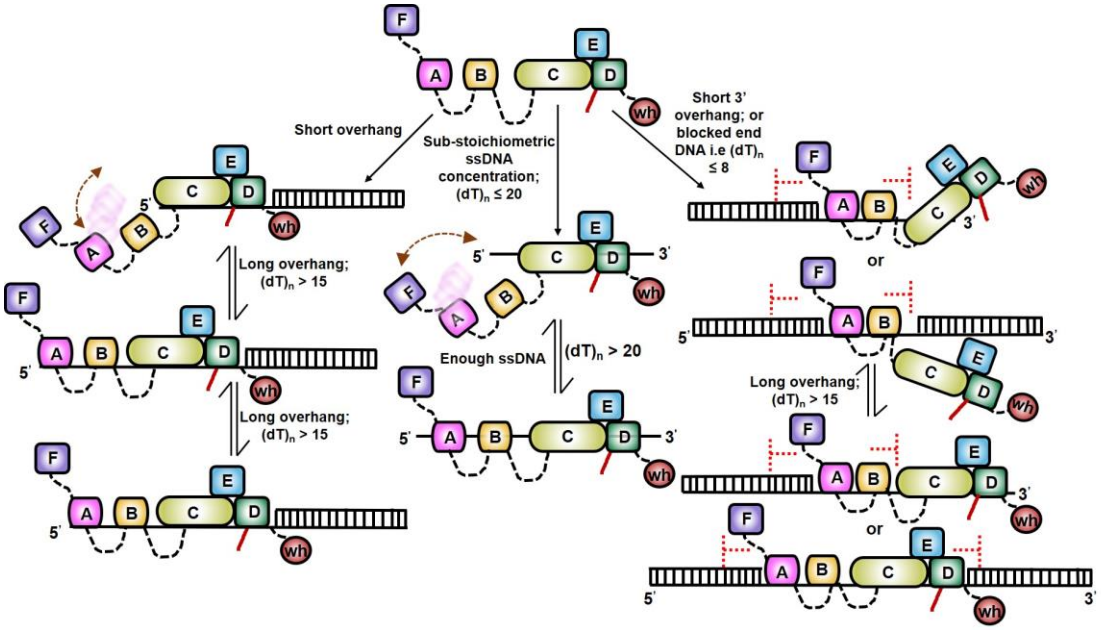

Figure 4-14: Model- DNA context depending effects on RPA-DBD engagement on ssDNA. Upon encountering a ssDNA, the flexible half of RPA is remodeled by its trimerization core (stable half), under conditions of sub-stoichiometric concentrations of ssDNA or shorter lengths of ssDNA. This remodeling requires a free 5′ end in the DNA, possibly to allow the conformational freedom for DBD-A to undergo several association-dissociation steps on ssDNA and OB-F to interact with appropriate RIPs. No DBD-A remodeling is observed for 3′ overhang or blocked end DNA substrate (represented by dotted red lines). Since DBD-A is situated close to these junctions in 3′ overhang and blocked end DNA substrates, it is possible that the nearby dsDNA-ssDNA junction poses a steric hindrance when the trimerization core is remodeling DBD-A. In addition, it is also possible that these junctions affect the association- dissociation events (microdissociation evets) of DBD-A. In conditions where DBD-D is close to duplex and there is no free 5′ end to remodel DBD-A, binding of DBD-D and possibly the trimerization core is affected, perhaps due to altered conformation of either DBD-C or DBD-D on DNA. The effect is most profound on blocked-end DNA with highest potential to conformationally constrain both DBD-A and DBD-D.

4.3.3 Rtt105 selectively interacts with DBD-D

RPA-DNA interaction is required to stabilize and protect ssDNA intermediates, yet, RPA has to be displaced by an incoming DNA binding protein. Mechanistically, how RPA hands over ssDNA space to an incoming protein is still poorly understood. This situation is further complicated by the dynamic binding of individual DBDs, while the RPA heterotrimeric complex simultaneously maintains a high-affinity DNA binding. There is a plethora of DNA binding enzymes that can displace RPA from ssDNA, however, due to the sub-nanomolar binding affinity characteristics of RPA-ssDNA engagement, there are no reported instances of factors that stabilize RPA-DNA binding itself. Recently, Rtt105 has been shown to stabilize RPA-DNA interactions in replication fork and regulate RPA localization in the replicating genome (S. Li et. al., 2018). We wanted to systematically understand if this stabilization was a result of protein-protein interaction, where Rtt105 affected the conformation of RPA during the ongoing binding event to DNA, or if this was due to Rtt105 induced conformation after RPA-DNA binding had occurred. To this extent, first, we investigated if Rtt105 could interact with both DBDs A and D of RPA. Since DBD-A is situated towards 5′ and DBD-D is situated towards 3′, Rtt105 interaction with both the DBDs would suggest that Rtt105 could be distributed throughout RPA-DBDs to stabilize RPA-DNA interaction. Thus, we generated a Cy5 labeled Rtt105 ($Rtt105^{Cy5}$) and performed stopped-flow bulk FRET experiments with Cy3 labeled RPA-DBD-A ($RPA\text{-}A^{Cy3}$) or RPA-DBD-D ($RPA\text{-}D^{Cy3}$) in presence or absence of single-stranded DNA $(dT)_{30}$. Bulk-FRET assays showed that Rtt105 preferentially interacted with DBD-D, and not DBD-A, independent of ssDNA (Fig 4-15, 4-16, 4-17). In absence of ssDNA, increase in Cy5 fluorescence was observed

only with RPA-D^{Cy3} as a FRET donor (Fig 4-15 b), suggesting that Rtt105 associated with DBD-D positioned towards 3′ end of DNA. Interaction between Rtt105 and DBD-D could be explained with a two-step binding model, with an initial rate of interaction ($k_{obs,1}$) of 9.2 ± 0.6 s^{-1}. It has been shown that Rtt105 is not present in an RPA-DNA 'formed' complex (S. Li et. al., 2018). To further investigate how Rtt105 could affect DBD-D dynamics during its engagement with ssDNA, we conducted FRET experiments with RPA-D^{Cy3}-ssDNA complex and Rtt105^{Cy5} and monitored Cy5 emission (Fig 4-16, a). Alternatively, we performed FRET between Rtt105^{Cy5} with DNA in one reaction syringe, and RPA-D^{cy3} in another syringe and monitored Cy5 emission (Fig 4-16, a). FRET occurring (as denoted by the intensity of Cy5 fluorescence after exciting cy3) was higher when RPA-D^{Cy3} was not bound to ssDNA than RPA-D^{Cy3}-$(dT)_{35}$ complex (compare navy blue trace and light grey trace). Interestingly, FRET between Rtt105^{Cy5}-$(dT)_{35}$, and RPA-D^{Cy3} could be explained with single-step binding model, where, the rate of engagement ($k_{obs,1}$) of 51.2 s^{-1} is almost equivalent to the sum of rates of interaction between DBD-D and ssDNA, and DBD-D and Rtt105 i.e (k_{obs1} for 100nM RPA-D^{MB543}vs 100nM $(dT)_{35}$ is 36.2±2.3 and $k_{obs,1}$ for 100nM RPA-D^{cy3} vs 100nM Rtt105^{Cy5} :100nM $(dT)_{35}$ complex is 9.2 ± 0.6 s^{-1}). RPA-A^{Cy3} did not produce a FRET signal with Rtt105^{Cy5} both in presence and absence of ssDNA (Fig. 4-15 a, 4-16. a), suggesting that Rtt105 did not interact directly with DBD-A. Finally, a slow decrease in Cy5 fluorescence at a rate of 2.4s^{-1} was monitored when preformed RPA-D^{cy3} and Rtt105^{Cy5} FRET complex was mixed rapidly with $(dT)_{35}$ (Fig 4-17 d) suggesting Rtt105 remodeled DBD-D dynamics as it engages on ssDNA. No decrease in Cy5 fluorescence was detected upon performing similar experiments with RPA-A^{Cy3} (Fig 4-17 a, c). Taken together, these results suggest

that Rtt105 stabilizes engagement of DBD-D as it is binding with DNA and does not affect DBD-D dynamics once a stable complex with ssDNA has been formed.

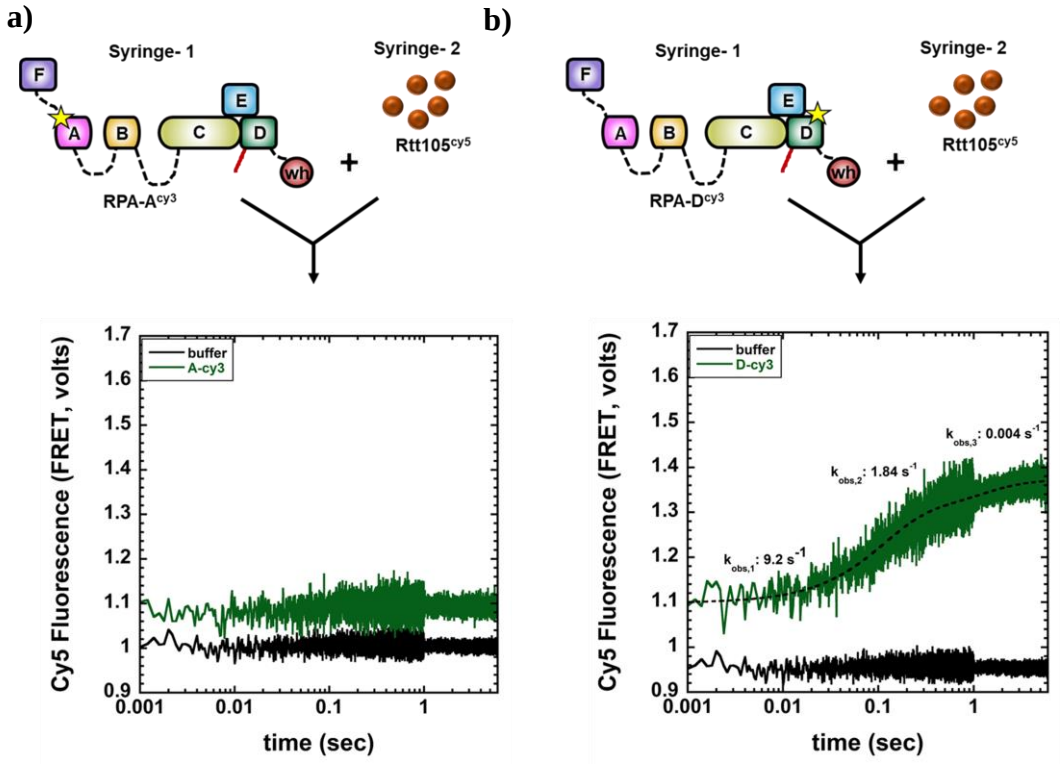

Figure 4-15: Rtt105 selectively interacts with DBD-D independent of ssDNA. For **a)** (Top) Graphic illustration of stopped-mixing scheme with FRET donor (RPA-A^{Cy3}) on one syringe and FRET acceptor ($Rtt105^{Cy5}$) in another syringe. The FRET donor was excited at 555nm and Cy5 emission monitored at 645nm. (Bottom) Green trace shows, no FRET is observed between RPA-A^{Cy3} and $Rtt105^{Cy5}$. **b)** (Top) Similar mixing scheme but with RPA-D^{cy3} as a FRET donor. (Bottom) A robust increase in Cy5 fluorescence (green trace) is monitored between RPA-D^{cy3} and $Rtt105^{Cy5}$ which can be best described with a two-step kinetic binding model. For both the experiments, buffer represents reaction between FRET donor and reaction buffer, with excitation-emission parameter as mentioned above.

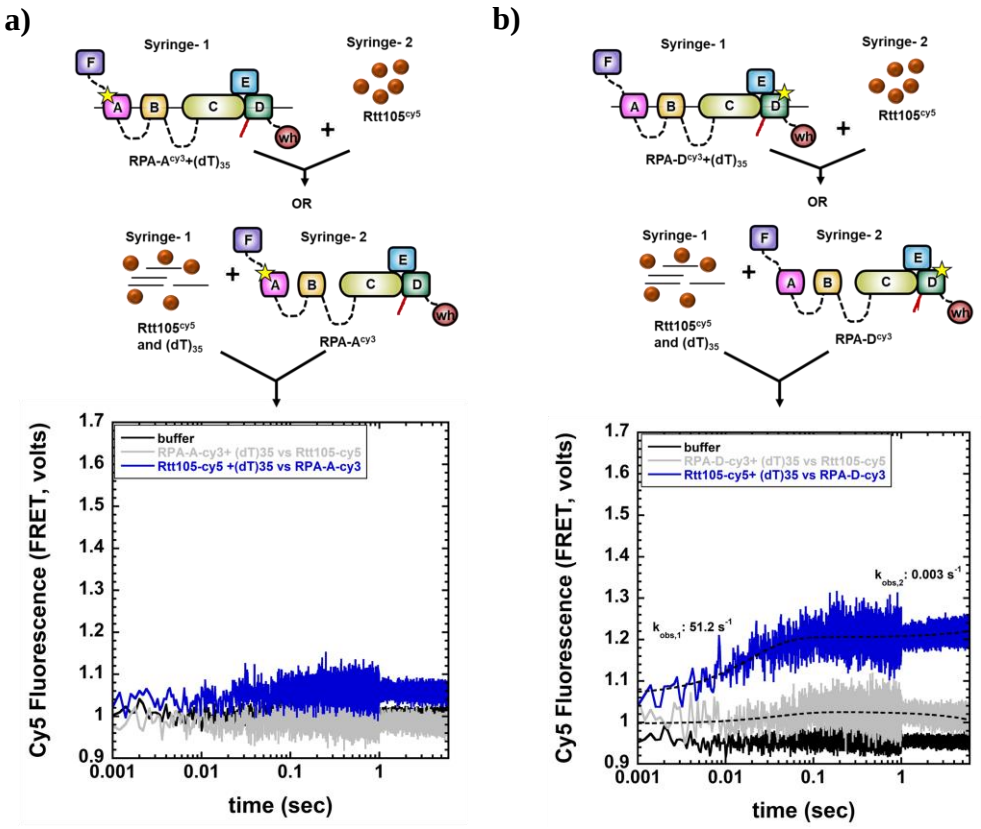

Figure 4-16: Rtt105 selectively modulates DBD-D binding to ssDNA. a) Top, stopped-flow mixing scheme where, either RPA-A^{Cy3}-ssDNA complex is mixed with $Rtt105^{Cy5}$, or, $Rtt105^{Cy5}$ and $(dT)_{35}$ in one syringe is mixed with RPA-A^{Cy3} in another syringe. **(**Bottom) Stopped-flow traces show no FRET occurs between RPA-A^{Cy3} and $Rtt105^{Cy5}$ in presence of $(dT)_{35}$ oligonucleotide. **b)** (Top) Similar mixing scheme but with RPA-D^{Cy3} as FRET donor. **(**Bottom) A robust increase in Cy5 fluorescence (navy blue trace) is observed when $Rtt105^{Cy5}$:$(dT)_{35}$ complex in one syringe are mixed with RPA-D^{Cy3} in another syringe.Similar experiments with preformed RPA-D^{Cy3}-$(dT)_{30}$ complex in one syringe when mixed with $Rtt105^{Cy5}$ in another syringe (grey trace) show comparatively lower amplitude of Cy5 fluorescence.This suggests Rtt105 affects DBD-D dynamics as DBD-D is engaging on ssDNA and doesn't affect DBD dynamics when it has completed forming a complex with DNA.

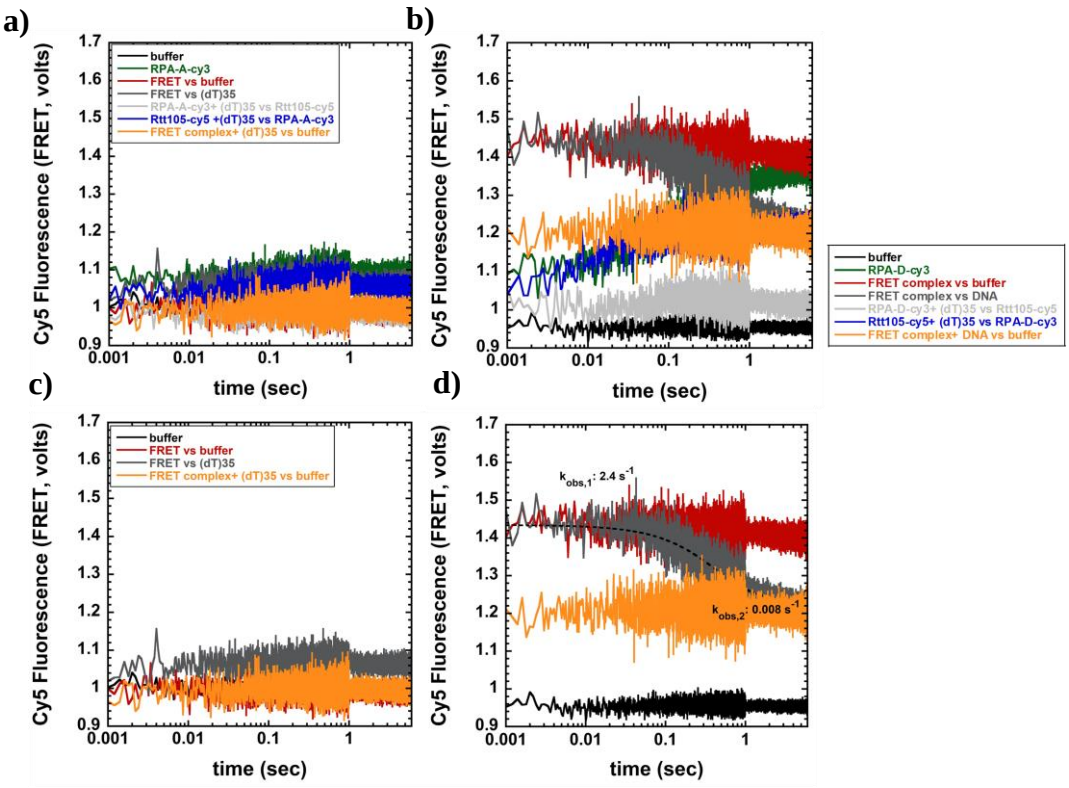

Figure 4-17: FRET experiments show Rtt105 selectively affects DBD-D-DNA interaction. a), b) Complete set of experiments performed between **a)** RPA-A^{Cy3} **b)** RPA-D^{Cy3}, and Rtt105^{Cy5} that were shown as individual data panels in figures 4-15 and 4-16. Experiments with preformed Cy3 labeled **c)** RPA-A^{Cy3} or **d)**RPA-D^{Cy3} and Rtt105^{Cy5} FRET complex, shows no change in Cy5 fluorescence for DBD-A but a slight decrease in fluorescence when RPA-D^{Cy3}-Rtt105^{Cy5} FRET complex is reacted with $(dT)_{35}$. This decrease in fluorescence (dark grey trace in **d)**) was fit with a single-exponential+ linear binding model and shows an initial rate of decrease ($k_{obs,1}$) of 2.4s^{-1}.

To confirm this was not a fluorophore induced interaction artifact, we investigated effects of increasing concentrations of Rtt105 on binding of MB543 labeled RPA-DBD-A (RPA-A^{MB543}) and RPA-DBD-D (RPA-D^{MB543}) in presence of $(dT)_{30}$ oligonucleotide. Since Rtt105 does not require ssDNA to interact with RPA, stopped-flow measurements were conducted with preformed 100nM RPA-A^{MB543} or RPA-D^{MB543} and Rtt105 complex and were rapidly mixed with 100nM $(dT)_{30}$. Samples were excited at 535nm and MB543 emission was monitored at 555nm. Reactions with RPA-D^{MB543} showed a gradual moderate decrease in the initial rate of engagement ($k_{obs,1}$) with increasing concentrations of Rtt105, until 1:1 molar stoichiometric concentration (Fig 4-18, d), following which it saturated (Fig 4-18, d). This effect was opposite in case of RPA-A^{MB543}. There was no change in $k_{obs,1}$ value until the stoichiometric concentration of Rtt105, following which a gradual decease was monitored (Fig 4-18, c). Similarly, there was no change in $k_{obs,1}$ value when similar experiments were performed with RPA-FAB^{MB543} that lacks the trimerization core (Fig 4-19). It is important to note that DBD-A engagement is comparatively faster than DBD-D for individual concentrations of Rtt105. Since, all the FRET experiments were performed with stoichiometric concentration of RPA and Rtt105 (i.e) 100nM, results from MB543 labeled RPA variants confirm that Rtt105 performs DBD specific interaction and modulation of DBD-D dynamics.

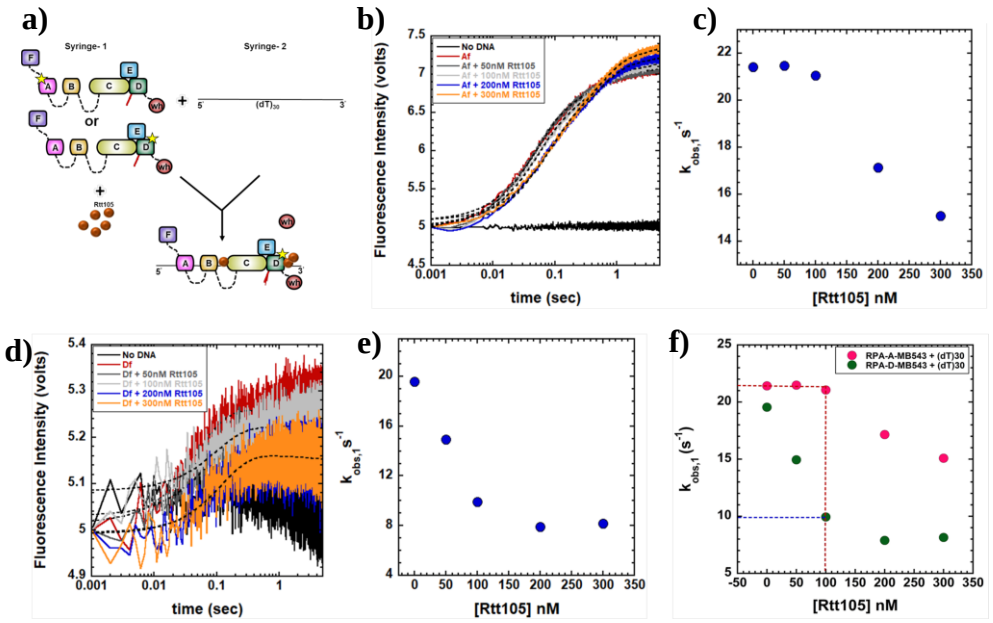

Figure 4-18: Effects of Rtt105 on MB543 labeled RPA-A^{MB543} and RPA-D^{MB543} binding to ssDNA. a) Schematic representation of the stopped-flow reaction showing the mixing scheme. Either RPA-A^{MB543} or RPA-D^{MB543}, and Rtt105 in one syringe was mixed with $(dT)_{30}$ oligonucleotide in another syringe. Representative raw traces obtained from stopped flow experiments for **b)** RPA-A^{MB543} and **d)** RPA-D^{MB543}, respectively. Quantified traces showing the rate of initial engagement ($k_{obs,1}$) as a function of increasing concentrations of Rtt105 for **c)** RPA-A^{MB543} and **e)** RPA-D^{MB543}, respectively. **f)** $k_{obs,1}$ value for RPA-A^{MB543} (pink dots) and RPA-D^{MB543}(green dots) engagement with $(dT)_{30}$, as a function of increasing concentrations of Rtt105, when plotted in a single graph. Red and blue dashed lines represent the stoichiometric concentration (i.e 100nM) of RPA, Rtt105 and $(dT)_{30}$, and the point until which $k_{obs,1}$ value decrease for RPA-D^{MB543} but not RPA-A^{MB543}, suggesting a DBD specific modulation of ssDNA binding by Rtt105.

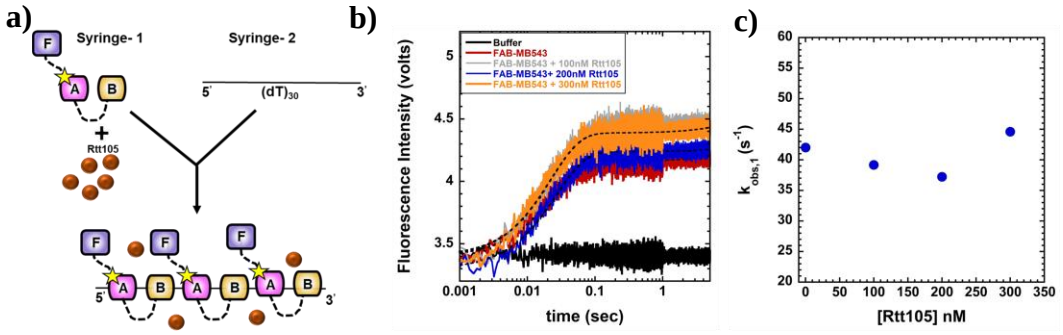

Figure 4-19: Effects of Rtt105 on RPA-FAB^{MB543} binding to ssDNA. a) Schematic representation of the stopped-flow reaction showing the mixing scheme. RPA-FAB^{MB543} with increasing concentrations of Rtt105 in one syringe was mixed with $(dT)_{30}$ oligonucleotide in another syringe. **b)** Representative raw traces obtained from stopped flow experiments. **c)** Quantified traces showing the rate of initial engagement ($k_{obs,1}$) of RPA-FAB^{MB543} in presence of increasing concentrations of Rtt105 with $(dT)_{30}$.

4.3.4 Effects of Rtt105 on DBD engagement in various structures of DNA.

The replication fork structure consists of dsDNAregions with single-stranded extension. To understand how Rtt105 could impact DBD dynamics when presented with DNA that has duplex regions, we performed stopped flow experiments with 5′ $(dT)_{30}$ overhang or 3′ $(dT)_{30}$ overhang harboring a 20 base-pair dsDNA duplex region adjacent to the ssDNA overhang. Based on our results obtained with ssDNA $(dT)_{30}$, in our experiments, we used 200nM Rtt105 complexed with 100nM RPA-A^{MB543} or RPA-D^{MB543} and reacted it against 100nM of 5′ $(dT)_{30}$ or 3′ $(dT)_{30}$ DNA (Figure 4-20 a, 4-21 a). Preliminary results with 5′ $(dT)_{30}$ overhang DNA show no kinetic differences in engagement of DBD-A with 5′ $(dT)_{30}$ and 3′ $(dT)_{30}$ overhang DNA in presence of Rtt105, although a slight decrease in the net amplitude of MB543 fluorescence is

observed (Fig 4-20 b, 4-21-b). Similarly, there is slight decrease in the net amplitude of RPA-D^{MB543} fluorescence in presence of Rtt105, with negligible effects in the rate of engagement of DBD-D (Fig 4-20, c). However, similar experiments performed with 3′ $(dT)_{30}$ overhang showed a significant decrease in the rate of initial engagement of DBD-D on DNA (Fig 4-21 c). This suggests interaction between DBD-D and Rtt105 could potentially affect the conformation of DBD-D as it is engaging on ssDNA with a nearby dsDNA.

Trimerization core induced remodeling of DBD-A requires a free 5′ end of DNA (Fig 4-5, 4-8 (black box)) and Rtt105 does not interact with DBD-A (Fig 4-15, 4-16, 4-17). However, Rtt105 significantly decreases the rate of DBD engagement when presented with a 3′ ssDNA overhang with an adjacent dsDNA region. Our results monitoring the DBD-A and DBD-D dynamics with 3′ $(dT)_n$ overhang substrates that has a dsDNA region revealed loss of trimerization core mediated DBD-A dynamics and significant changes in the nature of binding of DBD-D than bindig with ssDNA lacking the dsDNA region (Fig 4-8, 4-9, 4-11). Taken together, these results suggest that Rtt105 can selectively affect the DNA binding dynamics DBD-D which is a constituent of the less-flexible half of RPA.

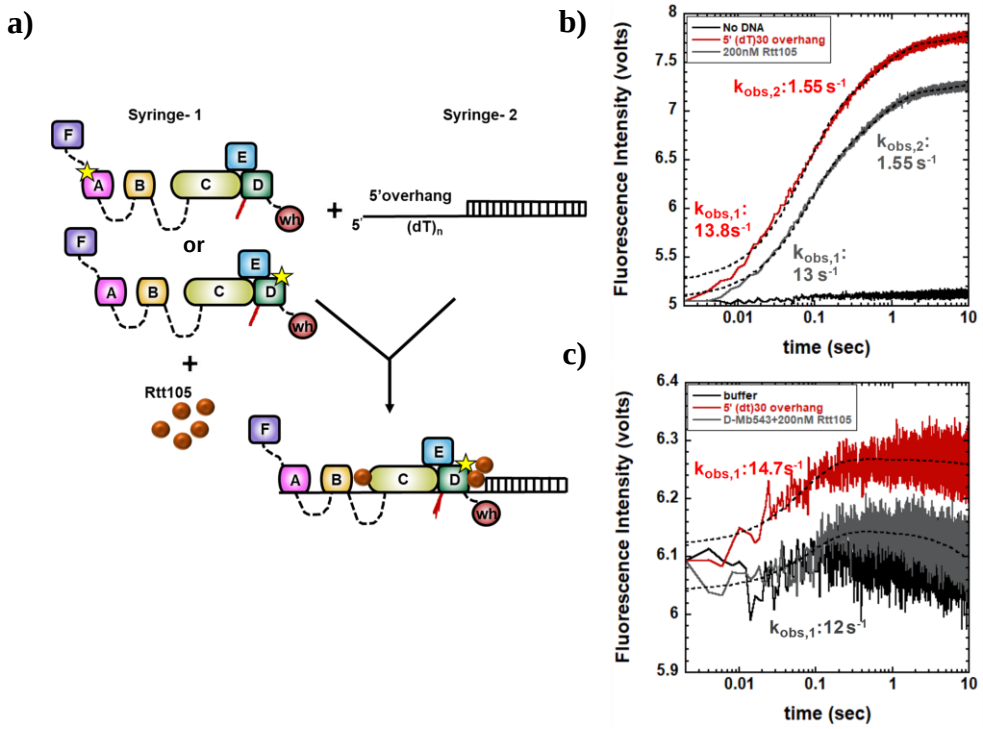

Figure 4-20: Effects of Rtt105 on RPA-A^{MB543} and RPA-D^{MB543} binding to 5′ (dT)$_{30}$ overhang DNA substrate. a) Graphic representation of the stopped-flow reaction showing the mixing scheme. Either RPA-A^{MB543} or RPA-D^{MB543}, and Rtt105 in one syringe was mixed with 5′ (dT)$_{30}$ overhang DNA substrate in another syringe. Traces obtained from stopped flow experiments for **b)** RPA-A^{MB543} and **c)** RPA-D^{MB543}, respectively. Obtained data traces were quantified with appropriate kinetic models, as mentioned in *methods*, to yield the observed rates of binding (k_{obs}). Trace-fitting is shown as dashed black lines.

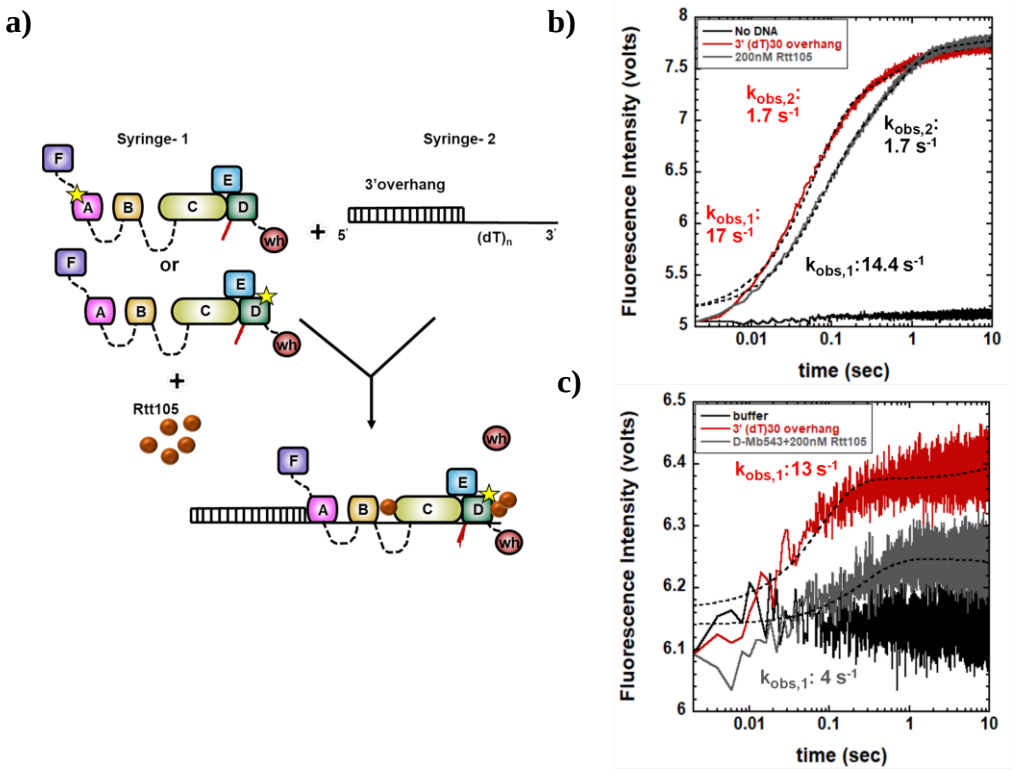

Figure 4-21: Effects of Rtt105 on RPA-A^{MB543} and RPA-D^{MB543} binding to 3′(dT)$_{30}$ overhang DNA substrate. a) Graphic representation of the stopped-flow reaction showing the mixing scheme. Either RPA-A^{MB543} or RPA-D^{MB543}, and Rtt105 in one syringe was mixed with 3′ (dT)$_{30}$ overhang DNA substrate in another syringe. **T**races obtained from stopped flow experiments for **b)** RPA-A^{MB543} and **c)** RPA-D^{MB543}, respectively. Red traces represent binding of **b)** RPA-A^{MB543} or **c)** RPA-D^{MB543} with 3′ (dT)$_{30}$ alone and grey traces represent binding in presence of 200nM Rtt105. Raw traces were quantified with appropriate kinetic models, as mentioned in *methods*, to yield the observed rates of binding (k_{obs}). Trace-fitting is shown as dashed black lines.

4.4 Discussion

RPA acts as a center for regulating processes that have a common goal of maintaining genomic integrity. To perform its functions, RPA binds to transiently exposed ssDNA with a nanomolar binding affinity, yet, this binding is very dynamic. Several studies have shown 'facilitated-exchange' of RPA, where, if present in excess, an RPA bound on DNA can be displaced by RPA present in the surrounding (Gibb et. al., 2014; N. Pokhrel et. al., 2017; Pokhrel et. al., 2019). Micro-dissociation of RPA-DBDs on DNA has been proposed as one mechanism by which an incoming protein is able to overcome high affinity RPA-DNA binding to occupy the existing DNA space. In chapter 3, we showed that DBD-A of RPA is more dynamic and its binding can be remodeled by its own trimerization core under restrictive conditions (intra-DBD remodeling). In addition, using smFRET microscopy, we showed that DBD-A and DBD-D, each had four states of binding on ssDNA, and an RPA interacting protein, Rad52, selectively modulated the binding state of DBD-D.

In this study, first, we investigated the DNA binding dynamics of DBD-A and DBD-D when ssDNA is presented with a nearby dsDNA (i.e 5′ overhang, 3′ overhang and blocked end DNA). We then investigated how DBD dynamics are affected by Rtt105, a protein known to chaperone RPA-DNA binding and stabilize RPA-DNA interactions. We show that remodeling of DBD-A requires a free 5′ end of DNA and this is not observed if DBD-A is situated close to a DNA duplex region (Fig 4-14). This remodeling could arise from trimerization core affecting the binding of DBD-A, as observed on ssDNA (chapter 3). Additional control experiments monitoring RPA-

FAB^{MB543} binding with 5′ $(dT)_n$, 3′ $(dT)_n$ and blocked-end DNA susbtrates need to be perfomed to verify this scenario.

Single molecule studies with human RPA have shown that RPA is able to diffuse freely along single-stranded DNA (B. Nguyen et. al., 2014b), while maintaining its DNA binding polarity with DBD-A being close to 5′ end of DNA (Pokhrel et. al., 2019). This diffusion of RPA continues on ssDNA, until it reaches an equilibrium, all the while RPA still forms a high-affinity complex with ssDNA. Since, DBD-A is more dynamic than DBD-D, presence of duplex region towards the 5′ end of DNA can pose as a steric hindrance and inhibit DBD-A from moving freely even when trimerization core is trying to remodel DBD-A. Therefore, different DNA contexts can further affect conformations that can be adopted by DBD-A on DNA (Fig 4-14). This is reflected in teh the $k_{obs,1}$ values of DBD-A engagement with increasing lengths of blocked ends DNA. This phenomenon can be particularly important when RPA is bound on DNA that is a substrate for an incoming DNA modifying enzyme (W. L. de Laat et. al., 1998).

Surprisingly, the DNA binding dynamics for DBD-D in all three DNA contexts were different than in ssDNA (Fig 4-13, 4-14). DBD-D is one of the constituents of the trimerization core and forms a stable complex on DNA (Fanning, Klimovich, & Nager, 2006; Pokhrel et. al., 2019; Yates et. al., 2018). RPA has been observed to transiently destabilize DNA duplexes, particularly at low ionic concentrations (Lao et. al., 1999); and occupy more nucleotides at high ionic concentrations (Kumaran et. al., 2006). Our reactions are performed with 100mM KCl and have a binding-site of approximately 20 nucleotides for one RPA. Thus, one explanation for increase in $k_{obs,1}$ value of DBD-D with increasing lengths of ssDNA available in all three DNA context could be transient

destabilization of DNA duplex, further resulting in more ssDNA for DBD-D to bind. DBD-A interaction with 3′ overhang and blocked ends DNA could have similar effects and could also explain loss of remodeling phase (Fig 4-14). Indeed, a detailed analysis of RPA-DBD engagement in these DNA substrates have to be performed at single-molecule level to understand the core mechanism underlying the observation made by bulk stopped flow experiments.

Finally, using a combination of bulk FRET and fluorescence enhancement approaches, our results show that Rtt105 specifically interacts with DBD-D and affects the ongoing event of DBD-D's interaction with ssDNA (Fig 4-15 b, 4-16 b, 4-17 b). Rtt105 does not bind to DNA and has no effect in binding of DBD-A to ssDNA (Fig 4-17 a, 4-20 b, 4-21 b). Rtt105 has been shown to be important for RPA import and localization in cells under replication stress (S. Li et. al., 2018). To better understand how Rtt105 affects DBD-D engagement on ssDNA, further studies have to be conducted on a replication fork and blocked ends DNA. It would be revealing to know if Rtt105-DBD-D interaction required winged helix domain present in RPA32 to better understand the importance of change in Rtt105 induced DNA binding behavior of DBD-D. Our studies provide the first documented event of DNA context specific change in DNA binding dynamics of DBD-A and DBD-D, and DBD-D specific interaction of Rttt105. Future implications could include potential role of Rtt105 in stabilizing a particular conformation/ DNA binding state of DBD-D in a particular DNA related process.

CHAPTER 5: DOMAIN SPECIFIC REMODELING OF RPA-DBDS IS DRIVEN BY COOPERATIVITY IN RAD52

5.1 Introduction

In yeast, proteins in the Rad52 epistasis group, which include Rad50, Rad51, Rad52, Rad54, Rdh54- TID1, Rad55, Rad57, Rad59, MRE11 and XRS2) are critical for repairing ionization radiation induced DNA damage. Meanwhile several of these proteins also play a critical role in the DNA replication and DNA damage response pathways (Game & Mortimer, 1974; Ranatunga et. al., 2001; Sotiriou et. al., 2016; Stein, Kalifa, & Sia, 2015). Of the proteins in the Rad52 epistasis group, Rad52 is critical for the pre-synaptic phase of homologous recombination (HR) (Sugiyama & Kowalczykowski, 2002b). During pre-synapsis, the sites of initial double stranded breaks are processed by 5′→ 3′ Exo-1 and Sgs1 nucleases resulting in formation of 3′ ssDNA overhangs which are immediately bound and protected by RPA (L. S. Symington et. al., 2014). RPA-ssDNA complexes are stable for prolonged periods both *in vitro* and *in vivo* and serve as a scaffold for recruitment of other HR proteins (Gibb, Ye, Gergoudis, et. al., 2014; Glover, Marques, Suska, & Horn, 2019). However, for the pre-synapsis phase to proceed towards synapsis during HR, Rad51 needs to nucleate and form a nucleoprotein filament on ssDNA. Rad51 filament formation appears to have a 3′ - 5′ polarity. To overcome the high-affinity binding of RPA on DNA, mediator proteins like Rad52 facilitate Rad51 recruitment and enable effective displacement of RPA from ssDNA (Sugiyama & Kowalczykowski, 2002b). The Rad51-nucleoprotein filament initiates homology search and promotes strand invasion once homology region has been established (Qi et. al., 2015).

Independent of Rad51 related functions, Rad52 has been shown to perform single-strand annealing (SSA) and micro-homology mediated DNA repair which serve a critical role in telomeric maintenance (Bhowmick, Minocherhomji, & Hickson, 2016; Verma et. al., 2019). It also plays a key role in break induced replication repair to ensure proper DNA replication and preserve replication fork integrity (Hengel et. al., 2016). The importance of Rad52 is underscored by its existence throughout eukaryotes and marked sequence conservation in its DNA binding domain located towards the N-terminal region of the protein. Several studies have shown structural and functional similarity between *Saccharomyces cerevisiae* Rad52 (*Sc.* Rad52) and human Rad52 (hRad52) with mutations in *Sc.* Rad52 severely affecting cell viability and mutations in hRad52 along with the main mediator protein BRCA2 being synthetically lethal in human cells (Feng et. al., 2011; Krogh & Symington, 2004). In addition, a key similarity between Rad52 from both the species is that it functions in-concert with RPA.

During HR, the RPA-ssDNA complex serves as a platform for Rad52 recruitment, and during SSA, RPA bound DNA are annealed by Rad52 (Ceccaldi et. al., 2016; Hanamshet, Mazina, & Mazin, 2016; Verma & Greenberg, 2016). Similarly, in break induced replication repair, the attributes of high-affinity ssDNA binding and relative abundance of RPA results in ssDNA being first occupied by RPA, then processed by Rad52. Two contrasting models exist for the interplay between RPA and Rad52 on DNA: The first (older model) suggests the displacement of RPA by Rad52 and concurrent promotion of Rad51 nucleation through physical interactions between Rad52 and Rad51. The second (newer model), primarily derived from single molecule DNA curtain experiments suggest formation of a co-complex between RPA and Rad52, which then

serves as a handle for Rad51 nucleation and growth. In support of the newer model, several *in vivo* studies have shown colocalization of Rad52 with RPA on mitotic and meiotic double-stranded DNA breaks, and during DNA replication preceding meiosis and at telomeres (Gasior, Wong, Kora, Shinohara, & Bishop, 1998; Miyazaki, Bressan, Shinohara, Haber, & Shinohara, 2004; Zhang, Yadav, Ouyang, Lan, & Zou, 2019). Furthermore, colocalization of RPA-Rad52-Rad51 on ssDNA has been captured by *in vitro* single-molecule fluorescence studies (Gibb, Ye, Kwon, et. al., 2014a; Kaniecki et. al., 2017; Chu Jian Ma et. al., 2017b). Our data on RPA remodeling by Rad52 also shows a co-complex between the two proteins on ssDNA and selective remodeling of just one DBD (DBD-D) in RPA (Chapter 3).

RPA physically interacts with Rad52 via multiple interaction sites that lie primarily in the RPA70 and RPA32 subunits. The smallest subunit, RPA14 also interacts with Rad52, albeit with weaker affinity (Hays, Firmenich, Massey, Banerjee, & Berg, 1998a; M. S. Park et. al., 1996). In addition to physical interactions, both RPA and Rad52 bind ssDNA (Lao et. al., 1999; A Shinohara, Shinohara, Ohta, Matsuda, & Ogawa, 1998). Thus, in situations where RPA and Rad52 function together, how RPA and Rad52 coordinate ssDNA occupancy is still not well understood. The model is further complicated by the oligomeric properties of Rad52. In yeast, Rad52 functions as a heptamer, and human RAD52 functions either as a decameric (10 subunit) or undecameric (11 subunit) ring-like complex. Oligomerization creates multiple RPA-binding subunits and DNA engagement points within Rad52. Furthermore, Rad52 can also bind to dsDNA. Since multiple DNA binding regions in Rad52 have been identified, investigating the mechanistic details underlying coordination of ssDNA binding between

RPA and Rad52 is exceedingly challenging (Saotome et. al., 2018; Akira Shinohara & Ogawa, 1998).

To better establish the interplay between Rad52 and RPA we investigated the DNA binding properties of Rad52 from *Saccharomyces cerevisiae* and the assembly of the Rad52-RPA complex on different DNA structures encountered during DNA metabolism. Using intrinsic tryptophan quenching and Protein Induced Fluorescence Enhancement (PIFE), as reproters for ssDNA interaction we demonstrate cooperative assembly of Rad52 at the 5′ end of DNA, where cooperativity exists between the inner and outer DNA binding sites (Fig. 5-1 a-c). Mutating key amino acid residues in the inner or outer binding site perturbs cooperativity but does not have a significant effect on overall ssDNA binding. Furthermore, we show that cooperativity in Rad52 is required for modulating RPA-DBD-D dynamics, specifically on a 5′ overhang DNA substrate. Using FRET, we show that Rad52 is unable to position itself in between multiple RPA molecules. Our studies provide key insights into RPA-DBD-Rad52 assembly, especially in situations mimicking recombination or replication, where ssDNA is presented as a structure flanked by dsDNA.

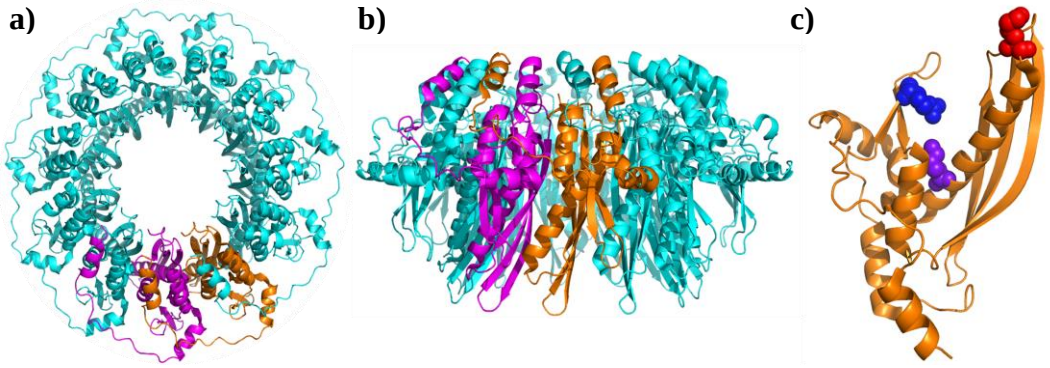

Figure 5-1: Crystal structure of hRad52$_{1-212}$. a) Crystal structure of hRad52 (residues 1-212) (PDB: 1KNO) lacking the C-terminal domain. The oligomeric structure shows an undecamer with 11 protomers. Two subunits are shown in magenta and orange, respectively to highlight the disordered loop reaching over the the neighboring subunit. **b)** Same as in a) but showing the side view. **c)** Single protomer of hRad52 (1-212) showing critical amino acids required for DNA binding in the outer site (K133, shown as red sphere), inner site (K152, shown as purple sphere) and transition site (R55, shown as navy blue sphere).

5.2 Materials and Methods

5.2.1 Generating plasmids for protein purification

Plasmid carrying Rad52-wt with a N-terminal poly-histidine and C-terminal chitin binding domain (CBD) tags (a gift from Dr. Eric Greene, Columbia University) was used as a template for cloning. We first removed the poly-histidine tag from the N-terminus using Q5 site directed mutagenesis and the following primers: forward primer (F)- 5′ ATG AAT GAA ATT ATG GAT ATGG 3′, and reverse primer (R)- 5′ ATG TAT ATC TCC TTC TTA TAC TTA AC 3′. The annealing temperature of PCR reaction was 63^{o}C. The Rad52-wt-CBD plasmid was used as template to generate Rad52 mutants by Q5-site directed mutagenesis. The following primers and PCR conditions were used:

<u>Rad52-R37A</u>

F: 5′ TAT CTC CAA GGC AGT TGG GTT TG 3′ T_m: 56^{o}C

R: 5′ TAC TCA GGT CCT AAT TTC 3′

<u>Rad52-R115A</u>

F: 5′ GGA GAA CGA AGC ACG GAA ACC TG 3′ T_m: 60^{o}C

R: 5′ ACG GTA CCA TAC CCA ATA TC 3′

<u>Rad52-K134A</u>

F: 5′ GGA TGC CTT GGC AAG ATC TTT GAG 3′ T_m: 58^{o}C

R: 5′ GTA ACG GCA GAT TTC TTG 3′

Plasmid carrying Rad52-R37A-CBD was used as template to generate Rad52-R37A K134A double mutant using the same primers that were used to generate Rad52-K134A.

Note: All the constructs have a C-terminal CBD-tag which is cleaved during protein purification by incubation with DTT to generate untagged Rad52-wt or Rad52 mutants.

5.2.2 Purification of Rad52-wt and Rad52 mutants

Rad52-wt-CBD or Rad52 mutant plasmids were transformed into Rosstta-2 PlysS cells, plated on agar plates (with 100 μg/ml ampicillin) and incubated overnight at 37^{o}C. Next day, a single colony was inoculated in a 50ml LB starter culture supplemented with 100 μg/ml ampicillin and incubated overnight at 250 rpm at 37^{o}C. A larger growth was started by adding 10 ml of overnight culture to each 2.8 l baffle flask with 1 l autoclaved LB supplemented with 100 μg/ml ampicillin. The flask was agitated at 250 rpm at 37^{o}C until the growth reached an OD_{600} of 0.6. At OD_{600} 0.6-0.8, for each 1l growth, the culture was induced by adding 500μl of 1M IPTG (0.5mM final concentration). Following induction, the culture was incubated overnight at 150rpm, 18^{o}C. Note: All the steps from here on were performed at 4^{o}C or on ice. Cells were pelleted by centrifugation at 5000rpm for 30 mins and resuspended in 200ml cell lysis buffer (50mM Tris-HCl, pH 7.5; 600mM NaCl; 1mM EDTA, pH 8.0; 2X PIC). Cells were lysed by sonication using the following settings: 2 sec pulse followed by 2 sec off for 60 seconds, pause for additional one-minute. This was repeated twice. The culture was stirred during the 1-minute pause to ensure proper mixing. Amplitude of sonication was set to 50%. Cell lysate was collected by centrifugation at 17000 rpm for 1 hour. The clarified supernatant

was then batch-bound for 3 hours on to 20ml chitin resin (NEB, Ipswich, MA) equilibrated with 200ml of cell lysis buffer. After 3 hours, flow-through was collected and the resin was sequentially washed with 100mls of cell lysis buffer, 100ml of cell lysis buffer+1.5M NaCl and again with 100ml of cell lysis buffer. Bound Rad52 protein was batch eluted with CBD elution buffer (cell lysis buffer+50mM DTT). For batch elution, CBD column was incubated with 20 mls of CBD elution buffer ensuring all the CBD resins contact the elution buffer. The batch elution was collected every 6 hours, for a total of 6 batches, each time using fresh DTT resulting in 120 ml total CBD elution volume. Chitin column eluates were analyzed by 10% SDS-PAGE and eluates containing Rad52 were pooled, diluted with R_0 (50mM Tris-HCl pH 7.5, 1mM EDTA pH 8.0, 2mM βME, 10% glycerol, 2X PIC) to a final conductivity of R_{200} and applied on to a10ml heparin column pre-washed with 2M NaCl and equilibrated with R_{200} (the subscript denotes concentration of NaCl in mM). Unbound Rad52 was washed with 100ml of buffer R_{200} and Rad52 was fractioned using a linear gradient of R_{200}-R_{1000}. The eluted fractions were analyzed by 10% SDS-PAGE, and fractions containing Rad52 were pooled, concentrated with a 30kDa cut-off spin concentrator to a volume less than 5ml and applied on to a HiLoad 16/600 200 Superdex-200pg size exclusion column equilibrated with Rad52 storage buffer (50 mM Tris-HCl, pH 7.5, 200mM NaCl, 2mM βme, 0.2 mM EDTA, pH 8.0, 10% glycerol (v/v)). S200 fractions were further analyzed by 10% SDS-PAGE and those containing Rad52 were pooled, concentrated with a 30kDa cut-off spin concentrator and stored at -80^{o}C as small aliquots after flash freezing with liquid nitrogen. Before flash freezing, concentration of Rad52 was determined spectroscopically using $\lambda_{abs\,(280)}$,

correction at $\lambda_{abs\ (350)}$ and extinction coefficient (ε) 24000$M^{-1}cm^{-1}$. The equation used was:

Concentration in Molar = ($\lambda_{abs\ (280)}$- $\lambda_{abs\ (350)}$)*dilution factor / ε

The dilution factor is 1 if no serial dilutions were made.

Rad52-R37A, Rad52-R115A, Rad52-K134A and Rad52-R37A K134A were purified similar to Rad52-wt-CBD

5.2.3 Purification of fluorescently labeled RPA-DBD-A and RPA-DBD-D

Non-fluorescent RPA-DBD-A or RPA-DBD-D carrying 4-Azidophenylalanine (4AZP) in DBD-A and DBD-D, respectively was purified and labelled with MB543, Cy3 or Cy5 as described in the Methods section of Chapter 3.

5.2.4 DNA oligonucleotides

Non-fluorescent and fluorescent oligodeoxynucleotides were synthesized by IDT (Coraville, IA). Poly(dT) was purchased form Midland Certified Reagent Co (Midland, TX). DNA annealing procedures for obtaining 5′ $(dT)_{30}$ overhang, 3′ $(dT)_{30}$ overhang, and blocked end $(dT)_{30}$ substrates are described in the Methods section of Chapter 4.

Note: *Saccharomyces cerevisiae* Rad52 predominantly behaves as a heptamer in solution. Therefore, in the subsequent sections, we denote the heptametic concentration of Rad52: i.e., a molar equivalent of Rad52 = 7 molar equivalents of monomeric Rad52.

5.2.5 Fluorescence measurements

5.2.5.1 Excitation-Emission scans

Fluorescence spectra were obtained using a QM40 fluorometer Photon Technologies Inc (Edison, NJ). For Rad52-wt and Rad52 mutants slit widths were set at 1.25 nm for excitation and 3 nm for emission. 2 ml of 100nM Rad52-wt in reaction buffer (30 mM Hepes, pH 7.8, 100 mM KCl, 5 mM $MgCl_2$, 2 mM β-mercaptoethanol and 6 % v/v glycerol) was added to a quartz cuvette, and the excitation spectra (240-330 nm) recorded at fixed emission of 350nm. To collect emission scans, samples was excited at 290nm and emission spectra recorded at 310-360nm. To this reaction, 100nM of $(dT)_{45}$ was added with constant stirring for a minute. Samples were excited at 250nm and emission spectra (310-360 nm) recorded. All reactions were performed at 25ºC.

5.2.5.2 Steady-state DNA binding

1.95 ml of Rad52-wt in reaction buffer was taken in a cuvette and titrated with increasing concentrations of $(dT)_{45}$. Samples was kept stirring throughout the reaction period. Samples were incubated for 60 sec after each addition to allow the Rad52-DNA complex to reach equilibrium. Samples were excited at 290nm and emission spectra (310-360 nm) monitored. Slit widths were maintained as in 5.2.4.1. The point of maximum amplitude as seen in the emission spectra was plotted as a function of $(dT)_{45}$ concentration and fit to a rectangular hyperbola to generate an apparant dissociation constant.

5.2.5.3 Site-size determination

The total number of nucleotides occupied by Rad52-wt in reaction buffer (30mM HEPES, pH 7.8, 5mM $MgCl_2$, 6% glycerol (v/v), 1 mM βME, 100mM KCl) was determined as previously described using poly(dT) ssDNA (Kumaran et. al., 2006) (see section 3.2.7 for detailed procedure). Briefly, increasing concentrations of poly(dT) were added to a 1.95 ml reaction with 100nM Rad52-wt (heptamer concentration, 700nM monomer concentration). The reaction was incubated for 60 sec after each addition to reach equilibrium. Changes in intrinsic tryptophan fluorescence were monitored by exciting the samples at 290nm and emission recorded at $\lambda_{emi\ (max)}$ (Kumaran et al., 2006)(Kumaran et al., 2006)(Kumaran et al., 2006)(Kumaran et al., 2006)(Kumaran et al., 2006)(Kumaran et al., 2006)(Kumaran et al., 2006)(Kumaran et al., 2006)(Kumaran et al., 2006)(Kumaran et al., 2006)(Kumaran et al., 2006)(Kumaran et al., 2006)(Kumaran et al., 2006)(Kumaran et al., 2006)(Kumaran et. al., 2006) Data were phenomenologically assessed to determine the influxtion points which denote the occluded site-size for ssDNA binding within Rad52. See section 3.2.7 for more details.

To determine, the effect of [NaCl] on Rad52's site-size the above mentioned experiment was repeated in reaction buffer containing 30mM HEPES, pH 7.8, 5mM $MgCl_2$, 6% glycerol (v/v), 1 mM βME and the concentration of NaCl varied in each experiment (25mM-1M).

5.2.6 Stopped flow analysis of Rad52-DNA interactions

Stopped-flow experiments to monitor Rad52-wt binding were performed using an Applied Photophysics SX20 instrument (Surrey, UK) in reaction buffer (50 mM Tris-Cl, pH 7.5, 100 mM KCl, 5 mM $MgCl_2$, 2mM β-mercaptoethanol and 6 % v/v glycerol) at 25 °C. All concentrations denoted are 'pre-mixing' which are reduced to half upon mixing the samples to provide final 'post- mixing' concentrations.

5.2.6.1 Changes in intrinsic tryptophan fluorescence

100nM Rad52-wt was rapidly mixed with increasing concentrations of $(dT)_{45}$ or $(dT)_{97}$. Samples were excited at 290nm and changes in intrinsic tryptophan fluorescence was monitored with a 350 nm cut-off filter for a total of 2.25 seconds. 5000 data points were collected in the first 250 milliseconds and 5000 data points collected over remaining 2 seconds. Resulting traces were analyzed using single-exponential + linear function (also denoted in the models as a composite single-step binding of Rad52 onto DNA) as shown below:

$$\Delta F = A\,(1 - e^{-k_1 t}) + k_2 t \qquad \text{(Eq. 2)}$$

Where, ΔF is change in Rad52 tryptophan fluorescence, A and k_1 are the amplitude and observed rate of the exponential phase, k_2 is the steady state rate and t is time.

5.2.6.2 Fluorescence measurements to determine polarity of Rad52-ssDNA interactions

To determine the polarity of Rad52-wt or Rad52-mutants (Rad52 variants) binding to ssDNA, 100nM of fluorescent deoxyoligonucleotide carrying a Cy3 fluorophore at either the 5′ end [5′ Cy3$(dT)_{40}$] or the 3′ end [3′ Cy3 $(dT)_{40}$] were rapidly mixed with increasing concentrations of Rad52 (0, 25, 50, 75, 100, 150, 200, 250 nM) in the stopped-flow instrument. Cy3 fluorophore was excited at 530nm and change in fluorescence monitored with a 555nm cut-off long pass filter. Binding was monitored for a total of 2.25 seconds with 5000 data points collected in the first 250 milliseconds and 5000 data points collected over 2 seconds. Raw traces were analyzed using a double exponential + linear state equation (also denoted as a composite two step model for Rad52 ssDNA binding):

$$[\Delta F = A_1(1 - e^{-k_1 t}) + A_2(1 - e^{-k_2 t}) + k_3 t] \qquad \text{(Eq. 3)}$$

Where, ΔF is change in Cy3 fluorescence, A_1 and k_1 are the amplitude and observed rate of the first exponential phase, A_2 and k_2 are the amplitude and observed rate of second exponential phase, k_3 is the steady state rate and *t* is time. Resulting k_{obs} values were plotted as a function of increasing concentration of Rad52 variants to determine their nature of binding.

As a control, 100nM 5′ 6-FAM $(dT)_{40}$ or 3′ 6-FAM $(dT)_{40}$ was rapidly mixed with increasing concentrations of Rad52-wt (0, 25, 50, 75, 100, 150, 200, 250 nM) in the stopped-flow instrument. 6-FAM fluorophore was excited at 490nm and change in fluorescence monitored with a 515nm cut-off long pass filter. Binding was monitored for a total of 2.25 seconds with 5000 data points collected in the first 250 milliseconds and

5000 data points collected over 2 seconds. Raw traces were analyzed using Eq. 3 and plotted as a function of increasing concentration of Rad52-wt.

5.2.6.3 FRET experiments to capture RPA-Rad52 assembly

FRET experiments were performed by rapidly mixing the preformed FRET complex consisting of 100nM RPA-DBD-A^{Cy3} (donor) and 100nM RPA-DBD-D^{Cy5} (acceptor) in one syringe with 100nM $(dT)_{45}$ in the second syringe. Samples were excited at 555nm and emission, i.e., increase in Cy5 fluorescence, was monitored with a 625nm long-pass cut off filter. To investigate positioning of Rad52 in RPA-DNA complex, a preformed RPA-DNA complex with 100nM (RPA-A^{cy3}, RPA-D^{Cy5} and 100nM $(dT)_{45}$) was rapidly mixed with 100nM Rad52-wt and change in Cy5 fluorescence monitored.

5.2.6.4 RPA-DBD dynamics on varying DNA-contexts

100nM RPA-DBD-A^{MB543} (RPA-A^{MB543}) and 100nM Rad52 variants, or, 100nM RPA-DBD-D^{MB543} (RPA-D^{MB543}) and 100nM Rad52 variants in one syringe were rapidly mixed with 100nM $(dT)_{25}$, $(dT)_{30}$, 5′$(dT)_{30}$ overhang, 3′ $(dT)_{30}$ overhang, or blocked end $(dT)_{30}$ substrates in a stopped-flow instrument. MB543 fluorescence was measured by exciting at 535nm and monitoring the emission with a 555nm cut-off long-pass filter. RPA-A^{MB543} or RPA-D^{MB543} engagement with distinct DNA structures in the presence of Rad52 variants was collected for a total of 60 seconds, where, 5000 data points were collected in the first 10 seconds and 5000 data points were collected over the remaining 50 seconds. All the raw traces for the reactions RPA-A^{MB543} were analyzed using Eq. 3 and for the reactions with RPA-D^{MB543} were analyzed using Eq. 2 and plotted.

5.3 Results

5.3.1 Occluded site-size of *Sc.* Rad52

Occluded site-size (or DNA footprint) represents the total number of nucleotides required to fully saturate the DNA binding site on a protein. Rad52 binds to ssDNA, dsDNA (A Shinohara et. al., 1998), and to ssDNA-dsDNA junctions. Rad52 functions as a heptamer and each monomer associates with ~ 4 nucleotides (nt) resulting in each Rad52 heptamer occupying ~ 28 nucleotides (Grimme et. al., 2010). To precisely determine the occluded site-size under our reaction conditions, we first tested if Rad52 produced a change in the intrinsic tryptophan fluorescence upon binding to ssDNA. The N-terminus of Rad52 is required for ssDNA binding and has two tryptophan residues. Excitation-emission spectra of Rad52 showed a maximum absorption (λ_{abs}) at ~285nm and emission (λ_{emi}) at ~ 325nm, which are characteristic spectroscopic properties for proteins with tryptophan residues (Fig. 5-2 a). Upon interaction with DNA, a quenching of the tryptophan signal is observed (Fig. 5-2 b). This finding contradicts a previous study that reported a lack of such intrinsic tryptophan fluorescence changes in Rad52 upon binding to ssDNA (Sugiyama & Kowalczykowski, 2002). However, in our hands, and under our experimental conditions, we observe a robust and quantifiable change in intrinsic tryptophan fluorescence. By quantitating the change in intrinsic tryptophan fluorescence as a function of increasing poly-deoxythymidine (poly-dT) ssDNA, we were able to determine the occluded site-size of *Sc.* Rad52. The decrease in tryptophan fluorescence was plotted as a function of number of nucleotides per Rad52 monomer to determine the occluded site-size as described in methods (Fig. 5-2 c). Under our reaction

conditions (30mM Hepes, pH 7.8, 100mM KCl, 2mM βme, 5mM $MgCl_2$, 6% glycerol (v/v)), there appears to be two transitions in the data reflecting two clear DNA bound states. The first DNA-bound state appears with a site size ~ 5.5±1.5 nt/ Rad52 monomer (Fig 5-2 c), and the second state appears at ~11 nt/Rad52. We interpret this finding to reflect DNA first wrapping around the Rad52 heptamer once (likely saturating the inner binding site, explained in detail in section 5.3.3 onwards) and then wrapping it again (likely saturating the outer binding site, explained in detail in section 5.3.3 onwards). Since Rad52 has prominent DNA annealing activity, our data agrees with a double-wrapping model for Rad52-ssDNA interactions.

Rad52 is widely assumed to be a heptamer, yet, there have been reports of higher order structures (Saotome, Saito, Onodera, Kurumizaka, & Kagawa, 2016; Saotome et. al., 2018). The oligomeric state of a protein can be influenced by ionic environment, until an equilibrium is established (Alford et. al., 2008). Although we did not investigate if Rad52 would shift structural states in response to changes in ionic conditions, we tested if site-size of Rad52 was affected by increasing [NaCl] concentrations. The rationale for this experiment arises from step-size measurements performed with SSB proteins, where changes in the monovalent or divalent ion concentrations give rise to unique structural transitions within protein-DNA complexes (Bujalowski et. al., 1988). We performed similar experiments with 100nM Rad52 and increasing concentrations of poly (dT) in the reaction (30mM Hepes, pH7.8, 5mM $MgCl_2$, 2mM βme, 6% glycerol (v/v)) supplemented with increasing concentrations of [NaCl] (25mM -500mM).We did not find change in the first occluded site-size (site-sze 1) within Rad52-DNA complex as a function of increasing [NaCl] (Fig. 5-2 d). Additional experiments need to be perfomed to understand

if the second occluded site-size (site-sze 1) within Rad52-DNA complex is affected as a function of increasing [NaCl].

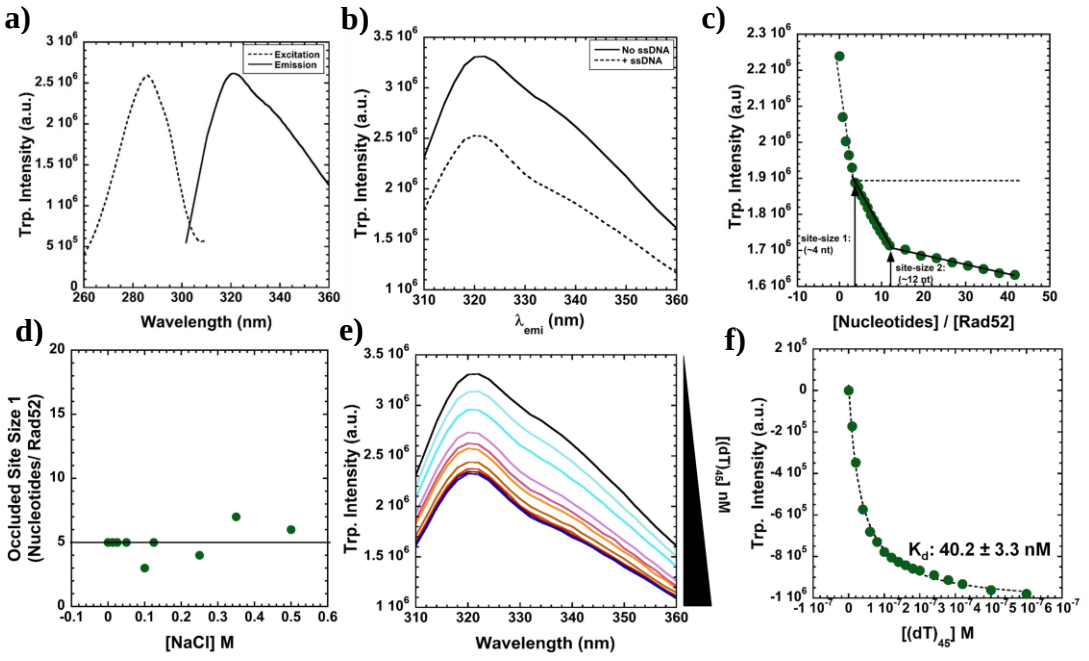

Figure 5-2: Characterization of Rad52 binding to ssDNA. a) Excitation-emission spectra of Rad52-wt. **b)** Emission spectra of 100nM Rad52-wt shows a decrease in intrinsic tryptophan fluorescence upon binding to DNA: 100nM $(dT)_{45}$. **c)** Representative plot of the site-size measurement of Rad52 shows a subsequent decrease in tryptophan fluorescence with increasing number of nucleotides. Two points of saturation are observed as shown by the dotted lines. The corresponding site-sizes are denoted. **d)** The first DNA bound site-size (site-size 1) does not change as a function of increasing concentrations of NaCl. **e)** Raw traces obtained from titrating 100nM Rad52- with increasing concentration of $(dT)_{45}$. Samples were excited at 290nm and emission spectra collected. **f)** Peak emission obtained for each concentration of $(dT)_{45}$ is normalized and plotted against individual $(dT)_{45}$ concentrations and yields a K_d of 40.2 ± 3.3 nM.

5.3.2 ssDNA binding properties of *Sc.* Rad52

We utilized the change in tryptophan fluorescence as a tool to determine the affinity of Rad52-ssDNA binding. Increasing concentrations of $(dT)_{45}$ oligonucleotide were added to 100nM Rad52, and the change in tryptophan fluorescence was measured. We obtained an apparent dissociation constant (K_d) of 40.2 ± 3.3 nM for *Sc.* Rad52 ssDNA binding (Fig 5-2 e, f), which agrees with the estimates of human Rad52-ssDNA interactions, with K_d values raning from sub-nM to 100 nM (Grimme et. al., 2010). Our study is the first detailed measurement for yeast Rad52 and is in the ballpark of the values measured for human Rad52.

This tight ssDNA binding is of interest, as it closely resembles to that of RPA. RPA has slightly higher affinity for binding to ssDNA (K_d of RPA: 29.2 ± 4 nM, Fig. 3-3 f). RPA and Rad52 function on the same ssDNA substrate during HR, and possibly compete for binding to the same DNA space. Therefore, given similar K_d values of RPA and Rad52 binding to ssDNA, one can speculate that both the proteins have equal opportunities to gain access to the available DNA space. To futher characterize Rad52-ssDNA binding in detail, we next sought to ascertain if kinetics of Rad52 binding to ssDNA was similar to RPA-wt. The rationale for this experiment is that if kinetics of RPA and Rad52 binding to ssDNA are similar, and they have slight difference in K_d values, it would suggest that the order of DNA occupancy could be driven by the local concentration of protein available. Whereas, differences in kinetics would suggest that an inherent biochemical property of the protein would drive DNA occupancy, i.e., the protein with higher ‘on-rate’ would occupy DNA first and the stability of protein on DNA would be determined by its off-rate/ on-rate. To this extent, we used stopped-flow

methodology to rapidly mix 100nM Rad52-wt with increasing concentrations of $(dT)_{45}$ and monitored changes in intrinsic tryptophan fluorescence (Fig. 5-3 a, d). Data obtained was quantitated and best described using a single exponential followed by linear phase equation. For 100nM Rad52 in the reaction, the $k_{obs,1}$ value i.e., the rate of initial engagement, showed an initial sigmodial behavior (see $k_{obs,1}$ value for 50nM and 75nM $(dT)_{45}$, Fig. 5-3 b), followed by linear increase until 200nM $(dT)_{45}$, after which it saturated (Fig. 5-3 b). Similar experiments with 100nM Rad52 and increasing concentrations of $(dT)_{97}$ resulted in saturation at 100nM $(dT)_{97}$ (Fig. 5-3 e). The initial sigmodial behavior suggest Rad52 binds cooperatively to ssDNA, and a single Rad52 heptamer is engaging with two molecules of $(dT)_{45}$ or with one molecule of $(dT)_{97}$.

Our site-size measurements show that a Rad52 heptamer occupies approximately 35 nucleotides (Fig 5-2 c, d) and the recently solved crystal structure of truncated Rad52-DNA complex shows that Rad52 is able to associate with DNA in two distinct ways: wrapping it around the circumference of the structure or sandwiching it in between two Rad52 molecules (Saotome et. al., 2018). Therefore, of the two $(dT)_{45}$, one could be wrapped around the circumference of Rad52 and the second could be sandwiched between two Rad52 heptamers (discussed in section 5.3.4). Whereas, in case of $(dT)_{97}$, a single $(dT)_{97}$ could be wrapped around Rad52 heptamer and provide with enough remaining DNA to be sandwiched between two heptamers. In both these DNA substrates, a cooperative binding behavior is seen at sub-stoichiometric concentrations of DNA (Fig. 5-3 b, e, until 75nM for $(dT)_{45}$ and 30nM for $(dT)_{97}$, respectively) suggesting possible communications between the inner and outer binding sites dictating overall Rad52-DNA engagement. Linear fit of the $k_{obs,1}$ plot until 200nM $(dT)_{45}$ and 100nM $(dT)_{97}$, yields the

bimolecular rate constant (k_{on}) value of 2.2 ± 1.0 x 10^8 M^{-1} s^{-1} which is slightly slower than RPA-wt (k_{on} 5.2 ± 0.3 x 10^8 $M^{-1}s^{-1}$, Fig 3-3 f). In our rate-constant calculations, we are assuming Rad52 to exist as a heptamer and all the protomers to simultaneously engage with the available DNA substrate. We recognize that this might not be the case under cellular conditions or in a multi-protein reaction. Rad52 heptamer dissociated from $(dT)_{45}$ with a rate of (k_{off}) 21.6 ± 7.8 s^{-1} (Fig. 5-3 b) which is slightly higher than the rate of dissociation of RPA from ssDNA (15.5 ± 0.8 s^{-1}, Fig 3-3 f). Interestingly, Rad52 dissociated from $(dT)_{97}$ with a k_{off} value of 9.5 ± 0.5 s^{-1}, while maintaining the same k_{on} as $(dT)_{45}$. This suggests that Rad52 forms a more stable complex on longer DNA.

Taken together our results suggests that although Rad52 heptamer has DNA binding affinity similar to RPA, it has slightly slower rate of binding (k_{on}) and a slightly higher rate of dissociation (for shorter DNA, i.e. $(dT)_{45}$) than RPA-wt. In our reaction conditions, RPA has an occluded site-size of 22 nucleotides, and 2 RPAs can stably engage on a $(dT)_{45}$ substrate. Therefore, under conditions where RPA is abundant, exposed ssDNA would be first occupied by RPA followed by Rad52 in the vicinity. However, in processes like alternative lengthening of telomere (ALT) with limiting RPA (Zhang et. al., 2019), Rad52 would bind with high affinity to long telomeric DNA repeats and perform annealing followed by subsequent recombination of telomeric DNA.

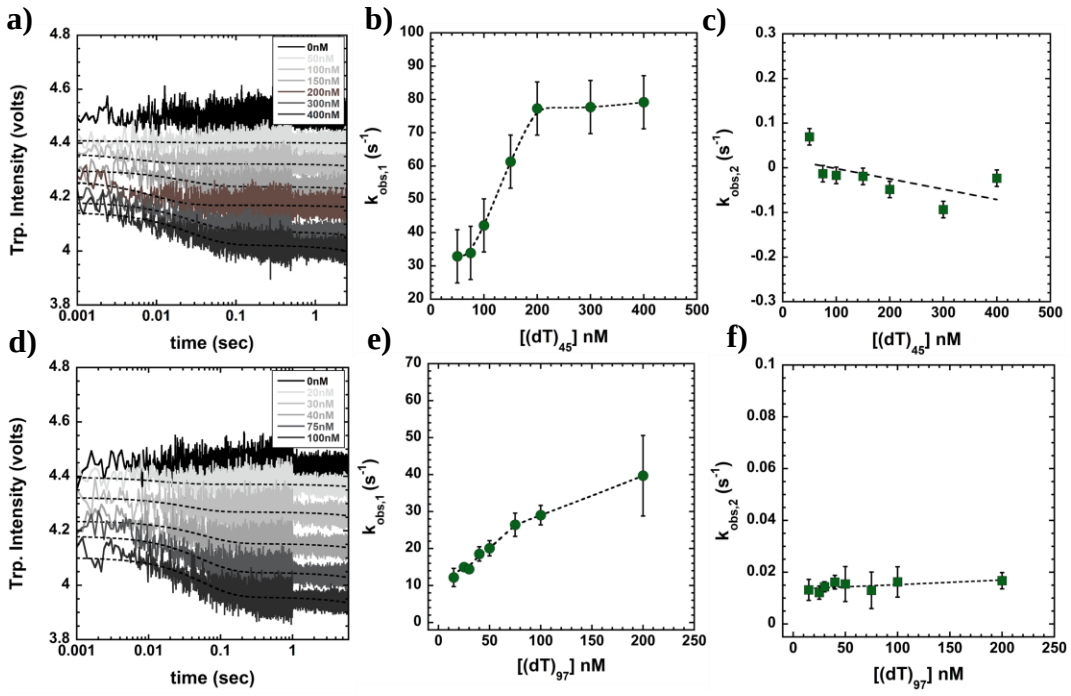

Figure 5-3: ssDNA binding kinetics of Rad52-wt. Representative traces from stopped-flow reaction showing increase in tryptophan quenching when 100nM Rad52-wt is mixed with increasing concentrations of **a)** $(dT)_{45}$ and **d)** $(dT)_{97}$, respectively. Fitting of the raw traces with equation as described in *methods* yields plot of initial rate of binding ($k_{obs,1}$) for **b)** $(dT)_{45}$ which shows initial cooperative binding followed by linear increase until 200nM after which it saturates and **e)** $(dT)_{97}$ which shows similar binding as $(dT)_{45}$ until 100nM and then saturates**.** Plot of $k_{obs,1}$ for 100nM Rad52-wt binding with **c)** $(dT)_{45}$ and **f)** $(dT)_{97}$ respectively.

5.3.3 Differential binding of *Sc.* Rad52 to ssDNA termini

Fundamentally, protein-DNA interactions are usually driven by availability of the reacting species, the rate at which the protein binds to DNA, and the affinity with which it maintains the binding. In most, if not all cases, the efficiency of this interaction can be further dictated by the directionality or orientation with which the protein associates with

DNA, also known as the polarity of binding. For example, RPA and Rad51, the two proteins that physically interact with Rad52 bind to DNA with a specific 5′ to 3′ polarity (Kolpashchikov et. al., 2001; Qiu et. al., 2013). RPA binds 5′-3′ with DBD-A situated close to the 5′ end and DBD-D situated close to the 3′ end. Rad51, in the presence of ATP, forms a nucleoprotein filament with preferential nucleation at the 5′ end followed by 5′-3′ growth of the filament (Antony et. al., 2009; Pokhrel et. al., 2019). The orientation of the protein binding to DNA can significantly impact the degree of DNA-protein interactions. Such polarity-specific positioning will also dictate the binding parameters when forming a higher order complexes on DNA. Since both Rad52 and RPA can bind with high affinity to ssDNA, we wanted to investigate if Rad52 had a preferential polarity of binding to ssDNA, and whether polarity of Rad52 binding to DNA affected RPA-Rad52-DNA binding dynamics.

We used Protein Induced Fluorescent Enhancement (PIFE) which employs monitoring protein binding by using end-labeled fluorescent oligos (Fischer & Lohman, 2004; Fischer et. al., 2010). When a protein binds to a fluorescently labeled oligonucleotide, local changes in the fluorophore's environment results in an overall change in the fluorescence intensity which can be quantified to determine the kinetic and thermodynamic parameters of a protein-DNA interaction (Morten et. al., 2015; Song et. al., 2016). Differences in kinetics of binding between the 5′-end lableled versus 3′-end labeled DNA can provide information about the polarity of binding.

We performed PIFE using stopped-flow analysis, where, 100nM 5′ Cy3 labeled $(dT)_{40}$ or 3′ Cy3 labeled $(dT)_{40}$ was rapidly mixed with increasing concentrations of *Sc.* Rad52 (Rad52-wt). The reaction was excited at 535nm and the emission monitored at

555nm, using a long-pass filter. A robust increase in Cy3 fluorescence was observed upon Rad52 binding to both 5′ Cy3 $(dT)_{40}$ and 3′ Cy3 $(dT)_{40}$ DNA (Fig 5-4 a, e), with an initial rate of engagement ($k_{obs,1}$) values of 138.0 ± 10.5 s^{-1} (Fig. 5-4 b) and 132.5 ± 17.6 s^{-1} (Fig 5-4 f), respectively. Similar rate of initial engagement for binding to both 5′ and 3′ Cy3 $(dT)_{40}$ DNA suggests that Rad52 does not differentiate between the DNA termini upon first encountering the DNA. In addition, the high $k_{obs,1}$ value probably reflects the sum of total rate of engagement of all seven subunits of Rad52 rather than a single subunit. Although binding of Rad52 to both 5′ Cy3 $(dT)_{40}$ and 3′ $(dT)_{40}$ DNA could be explained using a double exponential followed by a liner-phase model, there were subtle differences in the overall trend of binding between the 5′ and 3′ Cy3 end-labeled DNA. Rad52 displayed a cooperative binding behavior towards the 5′ end of the DNA as seen by the initial sigmoidal trend of the k_{obs1} and $k_{obs,2}$ plots (Fig. 5-4 b, c, see $k_{obs,1}$ values from 25nM until 100nM 5′ Cy3 $(dT)_{40}$). At sub-stoichiometric concentrations of Rad52, the initial increase in $k_{obs,1}$ decreased with increasing concentrations of Rad52 (compare the $k_{obs,1}$ values at 25nM , 50nM and 75nM Rad52-wt) until it reached a 1:1 molar ratio of DNA : protein, after which the $k_{obs,1}$ vaules exhibited a linear trend (Fig 5-4 b). However, binding towards the 3′ end did not exhibit a cooperative behavior and increased linearly with an increasing concentration of Rad52-wt (Fig. 5-4 f). As a control, to ensure the that cooperativity observed on a 5′Cy3$(dT)_{40}$ is not a fluorophore effect, we also performed similar PIFE experiments with 5′ or 3′ 6-FAM labeled $(dT)_{40}$. Rad52-wt bound cooperatively on a 5′ 6-FAM $(dT)_{40}$ and linearly on a 3′ 6-FAM $(dT)_{40}$ with ssDNA binding kinetics similar to 5′Cy3$(dT)_{40}$ and 3′ Cy3 $(dT)_{40}$, respectively (Fig. 5-24).

5.3.4 Mutations in the outer and inner binding site affect the cooperative binding behavior of *Sc.* Rad52

There are no crystal structures of apo or DNA-bound *Sc.* Rad52 that provide structural insights into *Sc.* Rad52-DNA engagement. Therefore, we utilized the extensively studied hRad52 as a guide to decipher the source of cooperativity observed in *Sc.* Rad52 binding to 5′ Cy3 labeled $(dT)_{40}$ DNA. The N-terminal ssDNA binding domains of *Sc.* Rad52 and hRad52 share remarkable sequence conservation and could engage with ssDNA via similar mechanisms. An apo structure of hRad52 fragment ($hRad52_{1\text{-}212}$) solved over a decade ago shows an undecamer with 11 protomers (Kagawa et. al., 2002; Singleton, Wentzell, Liu, West, & Wigley, 2002) (Fig 5-1 a, b). A positive groove along the circumference of undecamer, also called the 'inner binding site' was proposed to be well-adapted for accommodating negatively charged ssDNA (Fig 5-1 c, 5-5 a, b) (Kagawa et. al., 2002; Singleton et. al., 2002). Subsequent studies revealed a second binding site located outside this groove, also known as the 'outer binding site', which could engage to ssDNA and had implications in DNA annealing as well as D-loop formation (Fig 5-6 a, b). These findings suggest that there are at least two possible mechanisms by which Rad52 can engage to ssDNA, one involving the inner binding site and other involving the outer binding site.

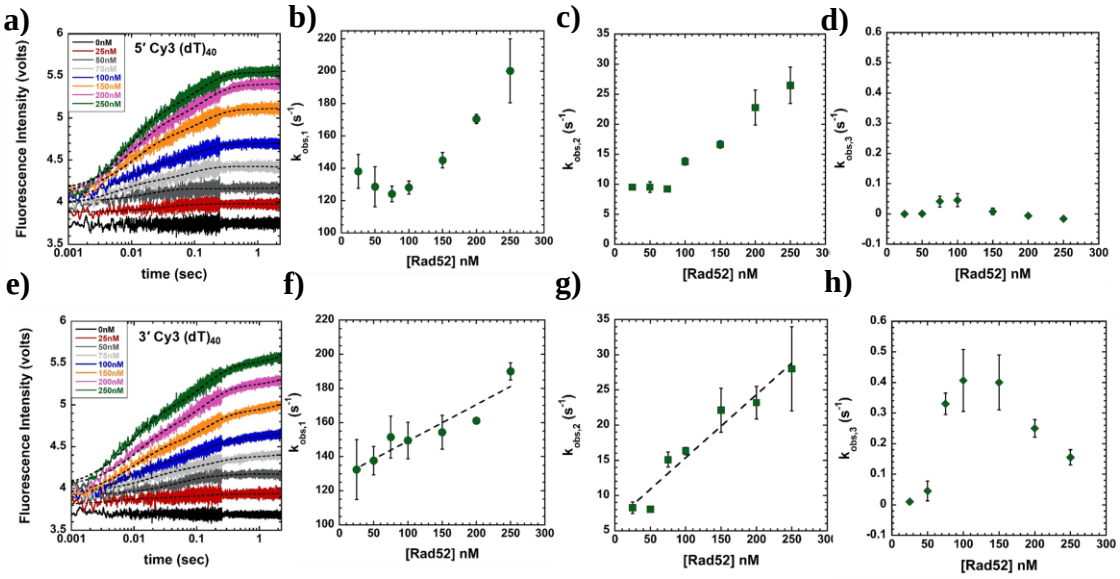

Figure 5-4: Cooperative binding between Rad52-wt inner and outer site. A robust increase in Cy3 fluorescence is observed when increasing concentration of Rad52-wt is reacted with 100nM **a)** 5′ Cy3 $(dT)_{40}$ or **e)** 3′ Cy3 $(dT)_{40}$ DNA. Fitting the raw traces with a double exponential followed by steady state model yields plot of **b)** initial engagement ($k_{obs,1}$) **c)** second phase/ step of binding ($k_{obs,2}$) and **d)** linear phase (kobs,3) for Rad52-wt binding on a 5′Cy3$(dT)_{40}$ DNA. Similar kinetic fitting of the raw traces obtained for Rad52-wt binding on a 3′ Cy3 $(dT)_{40}$ DNA yeilds plot of **f)** $k_{obs,1}$ **g)** $k_{obs,2}$ and **h)** $k_{obs,3}$.

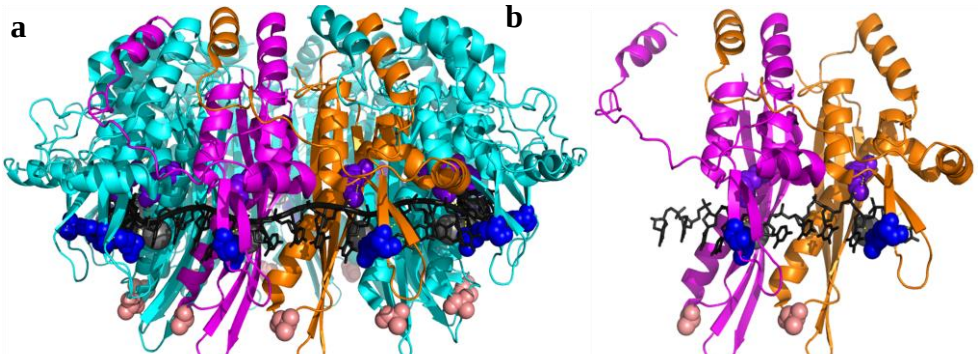

Figure 5-5: Crystal structure of hRad52$_{1-212}$ inner binding site-ssDNA complex. a) (Side-view) crystal structure of DNA of hRad52$_{1-212}$ with ssDNA (black sticks) wrapped around the undecamer (PDB: 5XRZ), nested in the groove, also known as inner binding site. Of the 11 subunits, two subunits are shown in magenta and orange color, respectively. R55 (navy blue sphere) and K152 (purple sphere), two important amino acids in the transition site and inner site, respectively, make critical electrostatic contacts (yellow dashed lines) with ssDNA. Each subunit coordinates a K^+ metal ion (gray sphere) that is located in between R55 and K152. Together R55, K152 and K^+ makes polar contacts with ssDNA to "lock" the ssDNA in inner binding site. K133 is mutated to alanine (light pink sphere) to obtain crystal structure of ssDNA bound to the inner binding site of hRad52$_{1-212}$. **b)** Same as in **a)** but showing only two subunits of the undecamer.

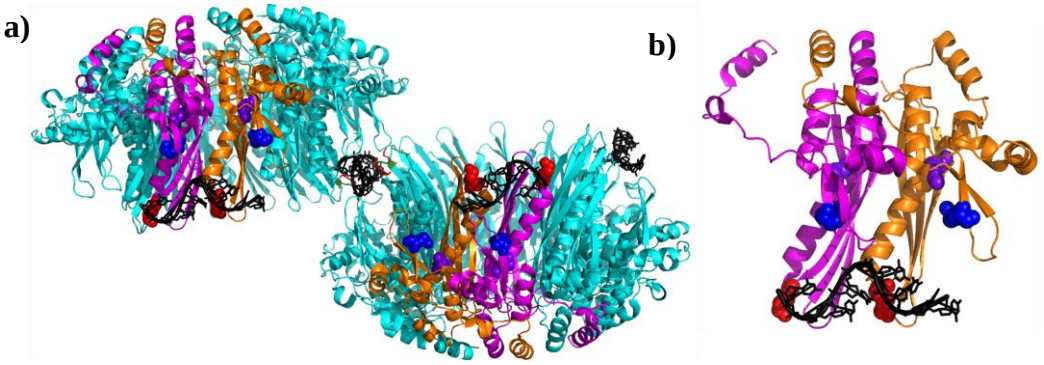

Figure 5-6: Crystal structure of hRad52$_{1-212}$-ssDNA complex with ssDNA bound to the outer binding side. a) (Side-view) hRad52$_{1-212}$ structures showing ssDNA (black sticks) bound to the edges of hRad52$_{1-212}$ undecamer or "sandwiched" between two undecamers (PDB: 5SX0). Of the 11 subunits, two subunits are shown in magenta and orange color, respectively. In each subunit, K133 (red sphere) is required for ssDNA binding to the outer side. R55 and K152, required for stable binding in the inner binding site are shown as navy blue spheres and purple spheres, respectively. Critical amino acids required for coordinating ssDNA between two undecamers are K133 (shown as red sticks) and K102 (shown as green sticks). Unlike in the crystal structure of inner binding site (PDB: 5XRZ), coordinating a metal ion is not required for binding to the outer binding site. **b)** Same as in **a)** but showing only two subunits of the undecamer.

After a decade of solving the apo structure of Rad52, ssDNA bound crystal structures of hRad52$_{1-212}$ were solved which shed key insights into the mechanism of hRad52-ssDNA engagement (Fig 5-5, 5-6). However, two lysine residues in the outer binding site were mutated to alanine (K102A/ K133A) in order to obtain a crystal structure of ssDNA occupying the inner binding site (Fig 5-5 a, b) (Saotome et. al., 2016, 2018). The hRad52$_{1-212}$ inner binding site-ssDNA complex shows an undecamer with ssDNA wrapped around nested in the positively charged groove (Fig 5-5 a, b), whereas, the outer binding site-ssDNA complex shows ssDNA trapped/sandwiched in between two hRad52$_{1-212}$ undecamers (Fig 5-6 a, b). We recognize that both the apo and DNA-bound structures of hRad52$_{1-212}$ lack the C-terminal domain which could highly impact the number of protomers present in the full length hRad52 or protomers that are actively engaging with ssDNA at a given point.

One key difference is the number of protomers in the oligomeric structure of *Sc*Rad52 and hRad52: 7 in *Sc*Rad52 while it is either 7, 10 or 11 in hRad52. Our interpretations and experimental designs for *Sc*Rad52 here are based its the heptameric nature. Our PIFE experiments with *Sc.* Rad52 showed two different binding behaviors, i.e., cooperative towards 5′ end and linear binding towards the 3′ end, suggesting existence of at least two different mechanisms for binding across the DNA substrate (Fig 5-4). In addition, the crystal structures of ssDNA-hRad52$_{1-212}$ displayed two distinct ways of engaging ssDNA (Saotome et. al., 2018). Therefore, we hypothesized that cooperative binding observed with *Sc.* Rad52 binding to 5′Cy3 $(dT)_{40}$ DNA could be due to coordination of ssDNA between the inner and outer binding sites. Moreover, linear

binding observed with 3′Cy3 $(dT)_{40}$ could represent the stable engagement of Rad52-ssDNA in the inner binding site carrying the positively charged groove.

To test this hypothesis, we generated *Sc.* Rad52 inner and/or outer binding site mutants, where Lys134 in the inner site and/or Arg 115 on the outer site were mutated to alanine (K134A and R115A), respectively. In addition, we also generated a transition-site mutant, where Arg 37 (R55 in hRad52) was mutated to alanine (R37A in *Sc*Rad52). In hRad52, Arg 55 has been shown to directly interact with ssDNA and is critical for proper ssDNA binding (Hengel et. al., 2016; Lloyd, McGrew, & Knight, 2005; Saotome et. al., 2018). Furthermore, R55 is located between the inner and outer binding sites (Kagawa et. al., 2002; Saotome et. al., 2018; Singleton et. al., 2002) and therefore, has the ability to function as a transition site for guiding the DNA binding from inner to outer site, or vice-versa (Fig 5-1 c, 5-5 b, 5-6 c). Finally, we generated a double binding site mutant, where both R37 and K134 are mutated to alanine (R37A K134A). We measured the ssDNA binding affinities of all these Rad52 mutants and observed varying degrees of net intrinsic tryptophan fluorescence (Fig. 5-7). Except for $Rad52^{R115A}$ which has mutation in the outer binding site, $Rad52^{R37A}$, $Rad52^{K134A}$ and $Rad52^{R37A\ K134A}$ (transition site- inner binding site- double binding mutant) had progressively lower affinity, with $Rad52^{R37A\ K134A}$ having the least affinity for binding to ssDNA (Table 5-1). Depending on the mutation (i.e inner, outer, transition or double), at any given time, individual protomers in Rad52 heptamer, or the entire Rad52 heptamer could be engaging differently on ssDNA, resulting in a multiplex of conformational assemblies, reflected as varying degrees of tryptophan quenching (Fig. 5-7, 5-12). Nonetheless, if 5′-3′ cooperativity is driven by ssDNA being guided from one binding site to another via the transition site, mutations in

either the inner, outer or transition site should result in loss of cooperativity observed at 5′ end of DNA. To this extent, we performed PIFE experiments with all three *Sc.* Rad52 mutants (inner binding site- $Rad52^{K134A}$, outer binding site- $Rad52^{R115A}$, and transition site- $Rad52^{R37A}$) and compared it with *Sc.* Rad52-wt.

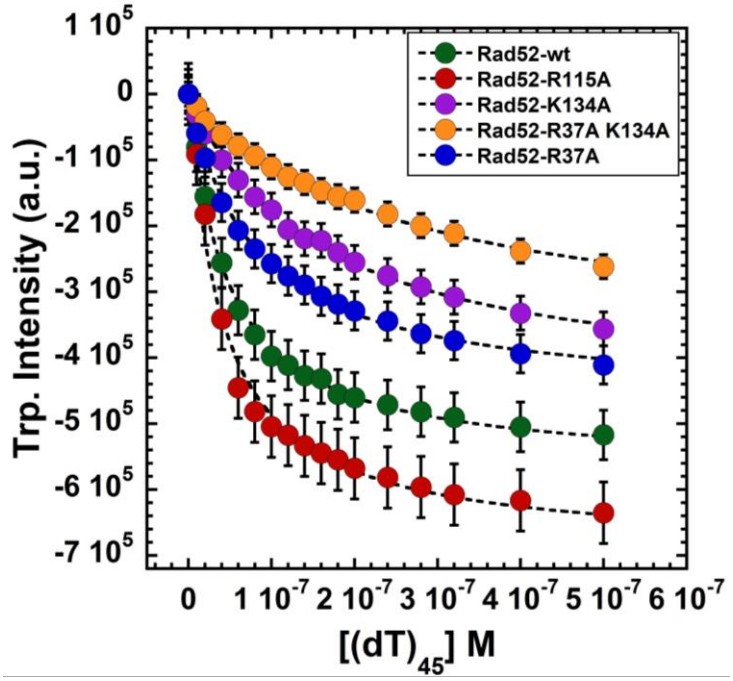

Figure 5-7: ssDNA binding affinity of Rad52 mutants. 100nM Rad52-wt or Rad52 mutants was titrated with increasing concentrations of $(dT)_{45}$. Samples were excited at 290nm and emission spectra (310-360 nm) collected. For each Rad52 variant, peak emission at ~330nm was plotted for individual $(dT)_{45}$ concentrations and data were fit using equation for binding isotherm to obtain the K_d values (Table 5-1). Data points are an average of at least three independent experiments.

Stopped flow experiments were performed by rapidly mixing increasing concentrations *Sc.* Rad52^{K134A}, Rad52^{R115A} or Rad52^{R37A} with 100nM 5′ Cy3 $(dT)_{40}$ or 3′ Cy3 $(dT)_{40}$ DNA. Cy3 was excited at 530nm and change in Cy3 fluorescence monitored using a 555nm long-pass emission filter. For all three *Sc.* Rad52 mutants, data obtained was quantitated using a double exponential followed by linear-state kinetic model. As expected, all three Sc. Rad52 mutants had a loss of cooperativity upon binding to 5′ Cy3 $(dT)_{40}$ DNA (Fig 5-7- 5-11). However, each binding site mutant showed subtle differences in binding to either 5′ or 3′ Cy3 $(dT)_{40}$ DNA, as described below.

5.3.4.1 Rad52 outer binding site mutant exhibits differential binding at DNA ends

PIFE experiments done with the outer site mutant (Rad52^{115A}) showed robust increase in Cy3 fluorescence with increasing concentrations of Rad52^{R115A} for both DNA substrates (Fig. 5-8 a, e). Loss of cooperative binding was observed in both 5′ Cy3 $(dT)_{40}$ and 3′ Cy3 $(dT)_{40}$ DNA (Fig. 5-8 b, f). However, there were subtle differences in events of binding between the two DNA substates. For 100nM 5′ Cy3 $(dT)_{40}$ DNA, a decrease in initial rate of binding ($k_{obs,1}$) was observed with increasing concentration of Rad52^{R115A}, until 100nM, following which the $k_{obs,1}$ values saturated (Fig. 5-8 b). In contrast, repeating similar binding reactions with 3′Cy3 $(dT)_{40}$ DNA produced a typical binding isotherm with increase in $k_{obs,1}$ until 100nM Rad52^{R115A} following which it saturated (Fig. 5-8 f). Furthermore, for binding to 5′ Cy3 $(dT)_{40}$ DNA, the rate of second phase of binding ($k_{obs,2}$) and linear phase ($k_{obs,3}$) remained constant with increasing concentrations of Rad52^{R115A}, whereas, $k_{obs,2}$ and $k_{obs,3}$ for binding to 3′Cy3 $(dT)_{40}$ resulted in a rectangular hyperbola (Fig 5-8 c-d, g-h). Taken together, these results suggest that

Rad52^{R115A} is not engaging DNA via similar mechanism as Rad52-wt. Opposite trends of $k_{obs,1}$ values for binding to 100nM 5′ Cy3 $(dT)_{40}$ versus 3′ $(dT)_{40}$ DNA until an equimolar concentration of Rad52^{R115A} is reached could resemble a repertoire of Rad52^{R115A}-ssDNA conformational assemblies, where engagement of DNA at one terminal allosterically affects the engagement of DNA at another end of DNA until substrate is limiting.

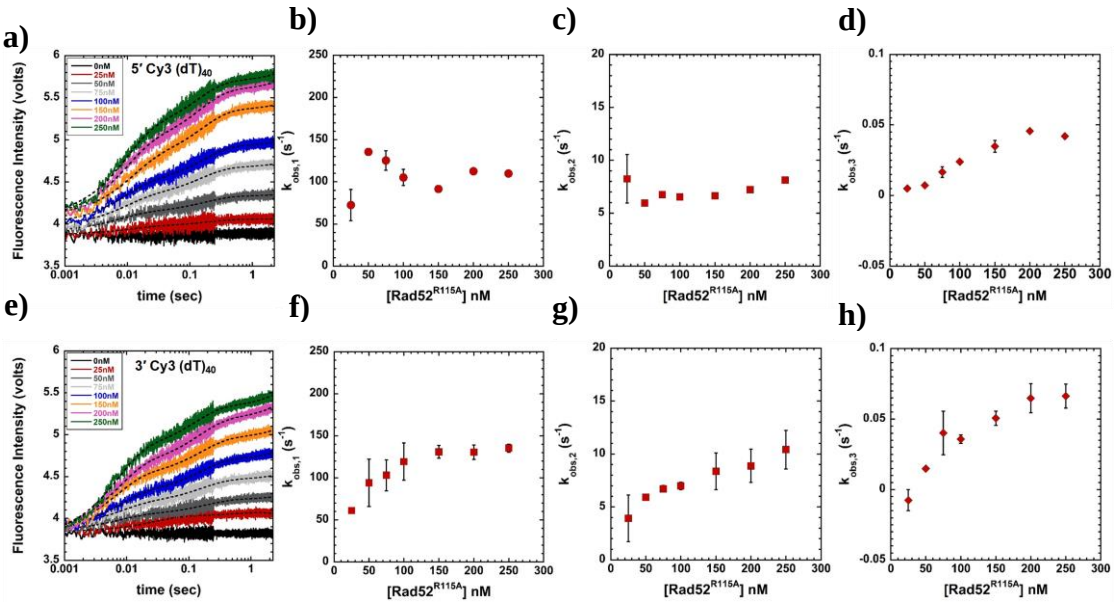

Figure 5-8: Rad52 outer binding site mutant (Rad52^{R115A}) binds differently to 5′ and 3′ end of DNA. Increasing concentrations of Rad52^{R115A} when rapidly reacted with 100nM **a)** 5′ $(dT)_{40}$ or **e**) 3′ $(dT)_{40}$, shows a robust increase in Cy3 fluorescence. Quantification of the obtained raw traces with appropriate kinetic models yields plot of initial engagement ($k_{obs,1}$) for **b)** 5′ $(dT)_{40}$ and **f)** 3′ $(dT)_{40}$, respectively. A plot of typical binding isotherm for all three distinct binding steps i.e. **f)** $k_{obs,1}$ **g)** $k_{obs,2}$ and **h)** $k_{obs,3}$, is obtained upon Rad52^{R115A} binding to 3′ Cy3 $(dT)_{40}$ which is not seen with 5′Cy3$(dT)_{40}$ DNA. Plot of **c)** $k_{obs,2}$ and **d)** $k_{obs,3}$ upon Rad52^{R115A} binding on a 5′ Cy3 $(dT)_{40}$ shows no significant change in the observed rates with increasing concentrations of Rad52^{R115A}.

5.3.4.2 Mutations in the inner binding site results in loss of polarity and cooperativity

Similar PIFE experiments performed with the inner site binding mutant ($Rad52^{K134A}$) produced robust increase in Cy3 fluorescence (Fig. 5-9 a, e) and upon quantification with a two- step binding model, revealed an extremely fast binding to both 5′ and 3′ Cy3 $(dT)_{40}$ DNA, with loss of cooperativity for both DNA substates (Fig. 5-9 b, f). $Rad52^{K134A}$ bound to both 5′ Cy3 and 3′ Cy3 $(dT)_{40}$ DNA with an initial rate of engagement ($k_{obs,1}$) of ~220 ± 35 s^{-1}, which remained constant irrespective of the increasing concentrations of $Rad52^{K134A}$ (Fig. 5-9 b, f). This $k_{obs,1}$ value is equivalent to maximal rate observed for Rad52-wt binding to 100nM 5′ or 3′ Cy3 labeled $(dT)_{40}$, under conditions with 2.5 fold molar excess of Rad52-wt (Compare, Fig. 5-9 b, f with Fig. 5-4 b, e, at 200nM Rad52-wt).The $k_{obs,2}$ values for binding to 5′ or 3′ Cy3 $(dT)_{40}$ showed a marginal increase proportional to the concentration of $Rad52^{K134A}$ (Fig. 5-9 c, g), with no change in $k_{obs,3}$ values (Fig. 5-9 d, h). We also performed similar PIFE experiments with double binding site mutant ($Rad52^{R37A\ K134A}$) which did not produce a significant change in Cy3 fluorescence denoting a severe defect in Rad52-DNA binding (Fig. 5-10 a, b). Taken together, mutations in the inner-binding sites disrupts the cooperativity that was observed in *Sc.* Rad52-wt. Since the inner binding site is comprised of the positively charged groove that is in a ‘ready’ state to accept and stabilize ssDNA, a single mutation in the inner binding site ($Rad52^{K134A}$) probably results in dynamic engagement of DNA between the outer site and transition site, which is fast and devoid of polarity. However, mutating the transition site along with critical amino acid residue in the inner site (eg: $Rad52^{R37AK134A}$) severely affects Rad52-ssDNA engagement.

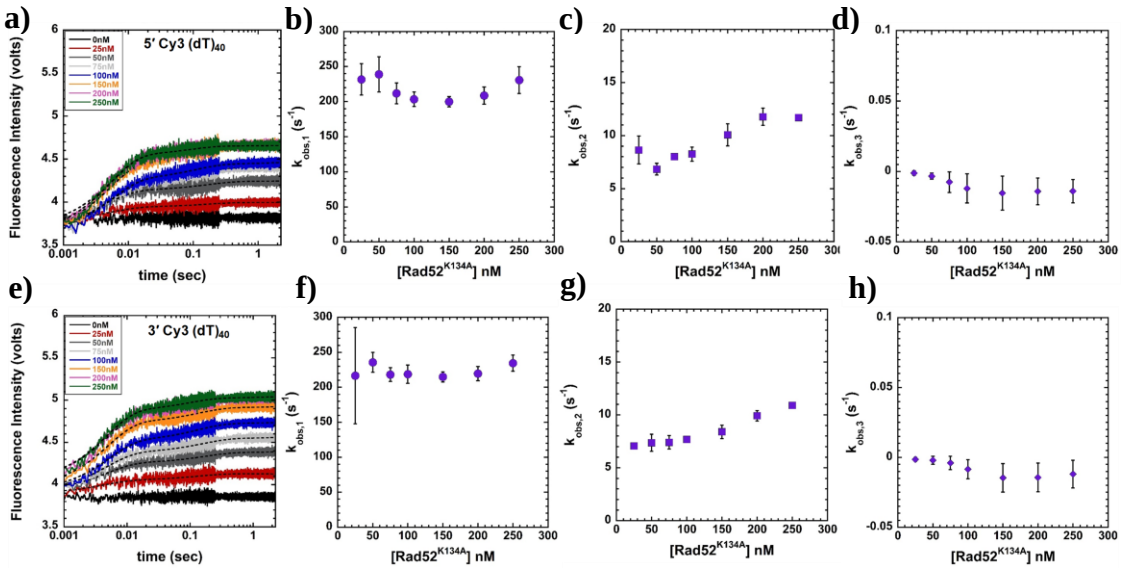

Figure 5-9: Rad52^{R134A} inner site binding mutant shows loss of cooperativity and polarity. Representative traces from the stopped-flow reactions show increase in Cy3 fluorescence when increasing concentration of Rad52^{R134A} mutant is mixed rapidly with 100nM **a)** 5′ Cy3 $(dT)_{40}$, **e)** 3′ Cy3 $(dT)_{40}$. All the samples were excited at 530 nm and emission monitored at 555nm. Fitting the raw traces with double exponential followed by a linear-phase model yields the plot of **b)**, **f)** $k_{obs,1}$ **c)**, **g)** $k_{obs,2}$ **d)**, **h)** $k_{obs,3}$ for binding to 5′ $(dT)_{40}$ and 3′ $(dT)_{40}$, respectively.

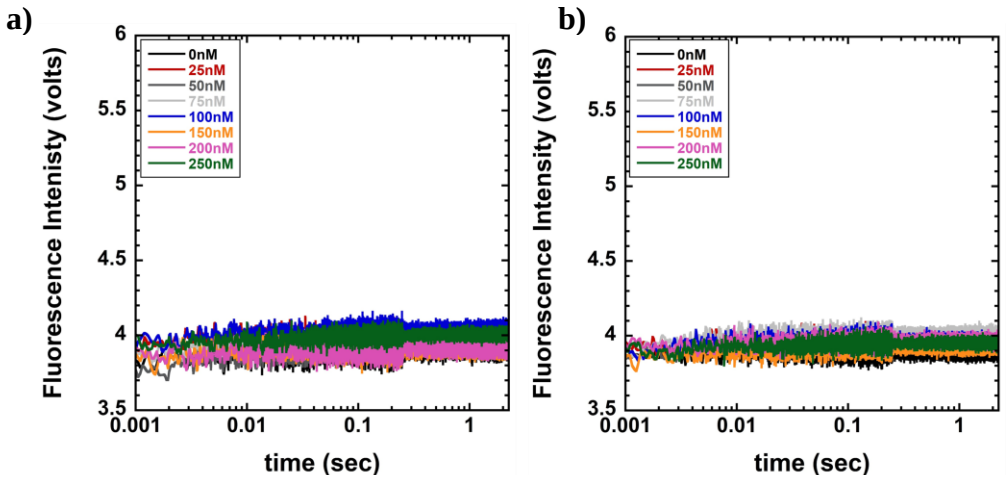

Figure 5-10: Rad52$^{R37A\ K134A}$ double mutant displays complete loss of binding to ssDNA in PIFE experiments. Representative traces from the stopped-flow reactions show no significant change in Cy3 fluorescence when increasing concentration of Rad52$^{R37A\ K134A}$ double mutant is rapidly mixed with 100nM **a)** 5′ Cy3 $(dT)_{40}$ and **b)** 3′ Cy3 $(dT)_{40}$ suggesting Rad52$^{R37A\ K134A}$ is unable to stably engage with ssDNA. All the reactions were excited at 530nm and emission monitored with 555nm cut-off long pass filter.

5.3.4.3 Transition site is required for cooperative binding in *Sc.* Rad52-wt

Rad52 inner and outer binding site mutants are able to engage with ssDNA in a way that is distinct from Rad52-wt, yet, a severe defect in ssDNA binding is observed when mutation in the inner binding site is coupled with mutation in the transition site ($Rad52^{R37A\ K134A}$) (Fig 5-8- 5-10). In hRad52, R55 (R37 in *Sc.* Rad52) forms electrostatic interactions with ssDNA backbone which primarily contributes to secure ssDNA in the inner binding site (Saotome et. al., 2018). This suggests that transition site plays a key role in ssDNA binding and could act as a lynchpin in coordinating ssDNA between the inner binding site and outer binding site. Therefore, we performed similar stopped flow experiments with $Rad52^{R37A}$ and 5′ Cy3 or 3′ Cy3 $(dT)_{40}$ DNA. A robust increase in Cy3 fluorescence was observed upon $Rad52^{R37A}$ binding to 100nM 5′ Cy3 $(dT)_{40}$ or 3′ Cy3 $(dT)_{40}$ DNA (Fig. 5-11 a, e). $Rad52^{R37A}$ showed a loss of cooperativity for binding to both fluorescent DNA, yet, subtle differences in binding between the 5′ Cy3 $(dT)_{40}$ and 3′ Cy3 $(dT)_{40}$ DNA were observed (Fig. 5-11 b). For reactions with 100nM 5′ Cy3 $(dT)_{40}$ or 3′ Cy3 $(dT)_{40}$ DNA and 25nM $Rad52^{R37A}$, the initial rate of binding ($k_{obs,1}$) was ~30 ± 2s^{-1} (Fig. 5-11 b, f). Increasing the concentration to 50nM $Rad52^{R37A}$ resulted in dramatic increase in $k_{obs,1}$ (~220 ± 40s^{-1}) for binding to 3′ Cy3 $(dT)_{40}$ DNA, yet, a steady increase in $k_{obs,1}$ which saturated at a maximum of ~ 180 ± 10 s^{-1} was observed for binding to 5′ Cy3 $(dT)_{40}$ (Fig. 5-11 b, f). Binding to either 5′ Cy3 $(dT)_{40}$ or 3′ Cy3 $(dT)_{40}$ showed a slight increase in $k_{obs,2}$ reaching with increasing concentration of $Rad52^{R37A}$ until 100nM, then saturated. No significant changes in $k_{obs,3}$ was observed. Therefore, R37 is required for maintaining cooperativity in Rad52-ssDNA binding.

The complex structure of Rad52 as a heptamer and its ability to exists as higher order structure has been a major roadblock in deciphering the precise mechanism underlying Rad52-ssDNA, for both yeast and human. Here, using PIFE and series of mutagenesis in full length *Sc.* Rad52, we showed that Rad52 undergoes cooperative assembly towards the 5′ end of DNA. Mutating key amino acid residues required in the inner binding site, outer binding site or transition sites result in loss of cooperativity and polarity but do not abolish Rad52 binding to ssDNA. Based on literature and our current findings, we propose a model detailing order of events in *Sc.* Rad52-ssDNA engagement. First, the outer binding site samples or engages the ssDNA which is then threaded into the inner binding site, via the transition site. Ionic interactions between R37 and ssDNA in the transition site stabilizes the ssDNA, favoring ssDNA binding to the inner binding site and preventing slipping of ssDNA back to the outer binding site. Finally, ssDNA is stably wrapped around the inner binding site which consists of a positively charged cleft well suited to accommodate the negatively charged ssDNA (Fig. 5-12).

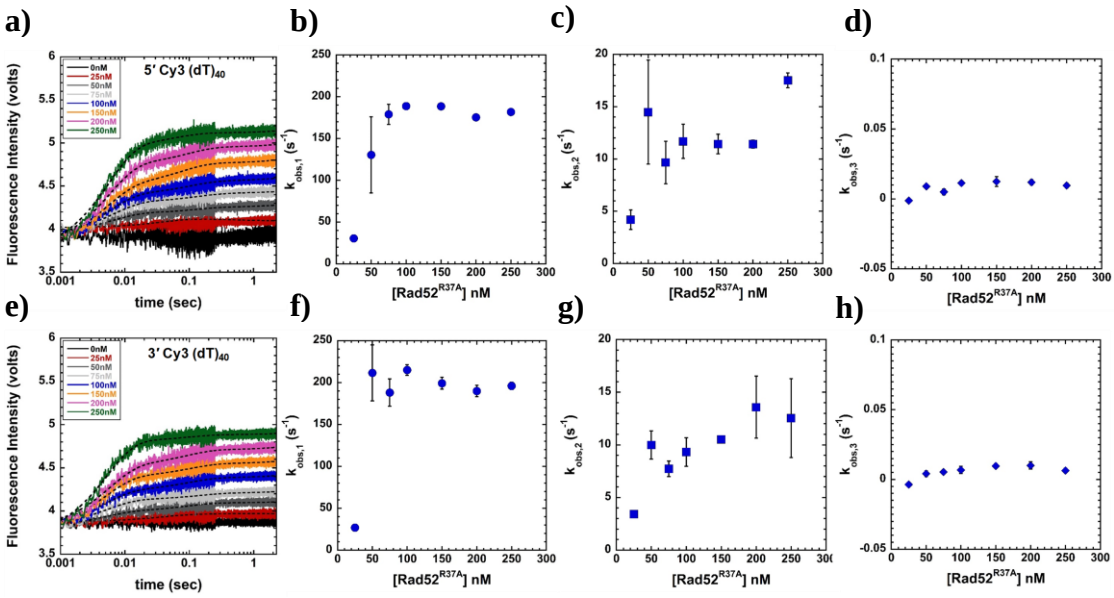

Figure 5-11: Rad52^{R37A} transition site mutant shows loss of cooperativity and exhibits differential binding in PIFE experiments. Representative traces from the stopped-flow reactions show robust increase in Cy3 fluorescence when increasing concentration of Rad52^{R37A} mutant is mixed rapidly with **a**) 5′ Cy3 $(dT)_{40}$, **e)** 3′ Cy3 $(dT)_{40}$. All the samples were excited at 530 nm and emission monitored at 555nm. Fitting the raw traces to a two-step binding model with a linear phase yields the plot of **b), f)** $k_{obs,1}$ **c), g)** $k_{obs,2}$ **d), h)** $k_{obs,3}$ for binding to 5′ $(dT)_{40}$ and 3′ $(dT)_{40}$, respectively.

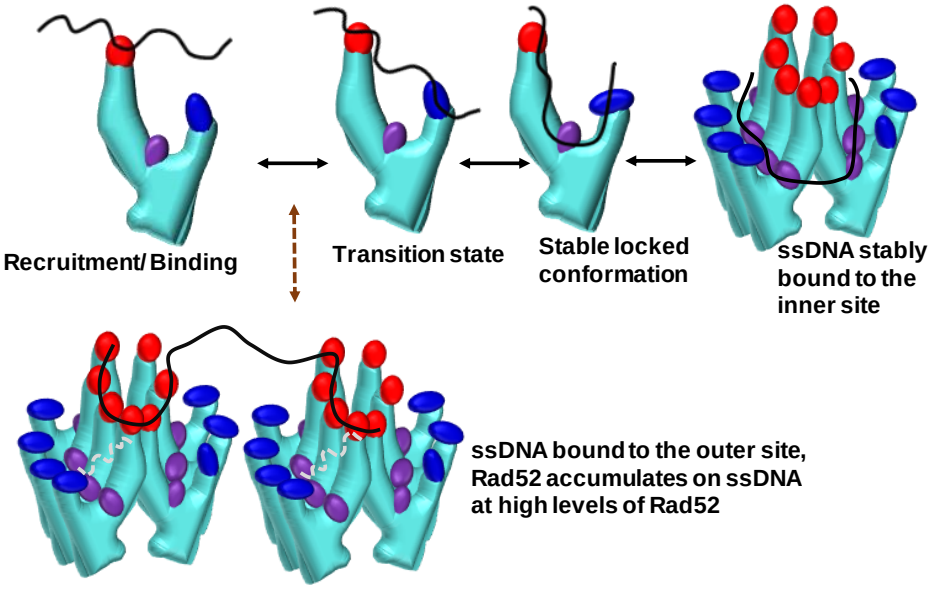

Figure 5-12: Model for *Sc.* Rad52-ssDNA engagement. The outer binding site of Rad52 (red circles) senses and binds to ssDNA (black lines). Two Rad52 complexes can engage to a single ssDNA and form higher order complexes, here, shown as two heptamers sharing a single ssDNA. ssDNA then passes through transition site (navy blue circles), which primes the DNA (dashed grey lines) for binding towards the inner binding site (purple circles) and could prevent ssDNA moving back to the outer site, locking ssDNA in place. The positively charged groove in the inner binding site along with R37 in the transition site stabilize ssDNA binding in the inner site to form a stable locked conformation. Dashed brown arrow shows switching of dimer of Rad52 heptamers with DNA engaged in the outer site to Rad52 heptamers with ssDNA bound to the inner site.

5.3.5 Rad52 does not invade the RPA nucleoprotein filament

Following in-depth investigation of *Sc.* Rad52 binding to ssDNA, we next wanted to understand how the DNA binding properties of Rad52 could promote, or in certain cases, result in displacement of RPA from ssDNA (Gibb, Ye, Kwon, et. al., 2014b; Sugiyama & Kowalczykowski, 2002a). In chapter 3, we showed that Rad52 selectively altered the DNA binding dynamics of DBD-D of RPA on a ssDNA, although it interacted with both DBD-A and DBD-D (Nilisha Pokhrel et. al., 2019). In addition, several studies have shown that Rad52 localizes with RPA on long stretches of ssDNA (Chu Jian Ma et. al., 2017b; Plate et. al., 2008). However, we lack a understanding of the positioning of Rad52 on DNA, especially when multiple RPA molecules are bound on DNA (the RPA nucleoprotein state).

Experimental bottlenecks have thwarted attempts to obtain a high resolution quantifiable readout of the Rad52-RPA interactions. For example, several studies investigating Rad52-RPA-DNA interactions had adopted the technique of tagging RPA, Rad52, and/or both with bulky GFP or RFP groups which could sterically impact their assembly on available DNA space. Both RPA and Rad52 have quantifiable tryptophan fluorescence. Therefore, using intrinsic tryptophan quenching as a readout to monitor RPA-Rad52 assembly on ssDNA would produce convoluted signal which is hard to dechipher, as the exact source of the signal cannot be assigned. Finally, PIFE experiments would not be suitable as both RPA and Rad52 produce a robust change in Cy3 fluorescence upon binding end-labeled fluorescent ssDNA. Therefore to overcome these roadblocks and investigate how Rad52 would interact on a ssDNA occupied by multiple RPA molecules, we performed bulk RPA-FRET experiments using Cy3-labeled DBD-A

(RPA-A^{cy3}), Cy5 labeled-DBD-D, and monitored FRET occurring on a $(dT)_{45}$ DNA substrate, in presence and absence of Rad52-wt (Fig 5-13 a, b). Stopped flow reactions performed by rapidly mixing 100nM each of RPA-A^{cy3}, RPA-D^{cy5} and $(dT)_{45}$, showed a robust increase in Cy5 fluorescence followed by a slow decrease which denotes the remodeling phase between the two DBDs (inter-RPA remodeling) (Fig. 5-13 b, orange trace). The highest amplitude of fluorescence observed in this reaction represent the high-FRET state. As a positive control, similar experiments with a preformed RPA-A^{cy3}-D^{cy5}-$(dT)_{45}$ complex when rapidly mixed with reaction buffer that did not contain Rad52, showed cy5 fluorescence at the high-FRET state (Fig. 5-13 b, grey trace). Finally, rapid mixing reaction with preformed RPA-A^{cy3}-D^{cy5}-$(dT)_{45}$ in presence of 100nM Rad52-wt showed no change in cy5 fluorescence i.e. the high FRET state (Fig. 5-13 b, olive green trace). In our experiments, FRET occurs between two RPA only when the Cy5 labeled DBD-D of the first RPA is adjacent to Cy3 labeled DBD-A of second RPA in a 5′-3′ direction (Fig. 5-13 a) (Yates et. al., 2018). Thus, no affect in the high-FRET state in presence of Rad52-wt suggests that Rad52 cannot position itself in between two RPA and would require access either from the 5′ end or 3′ end of the DNA. Based on our findings monitoring interaction between one RPA on DNA and Rad52, even for DNA occupied by multiple RPA, accessibility towards the 3′ end by selectively modulating DBD-D dynamics would be the most probable route for Rad52 to occupy DNA space.

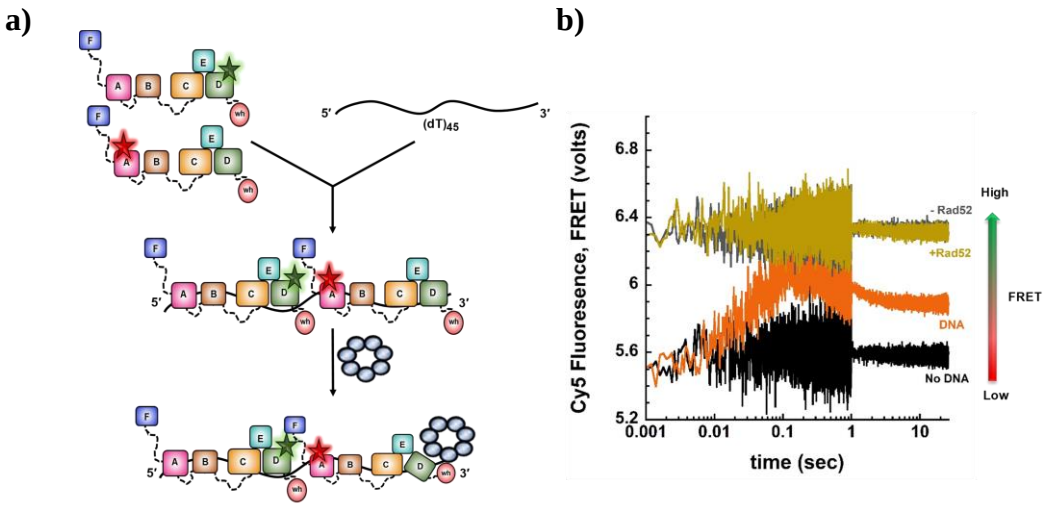

Figure 5-13: FRET experiments to monitor positioning of Rad52 between two RPA on a DNA. a) Model of stopped-flow mixing reaction. **b)** Representative traces show a robust increase in FRET followed by slight decrease when RPA-A^{cy3} and RPA-D^{cy5} in one syringe is rapidly mixed with $(dT)_{45}$ oligonucleotide in another syringe (orange trace). High-FRET state is maintained upon mixing of preformed RPA-A^{cy3}-D^{cy5}-$(dT)_{45}$ with equimolar Rad52-wt (olive green trace) or in absence of Rad52 (grey trace). No DNA (black trace) shows the base line FRET (low FRET) when RPA-A^{cy3} is mixed with RPA-D^{cy3}, and FRET monitored.

5.3.6 Rad52 selectively modifies the DNA binding dynamics of DBD-D on 5′ overhang DNA

In chapter 3, using single-molecule experiments, we showed that Rad52 selectively affected DNA binding events of RPA's DBD-D but not DBD-A on a $(dT)_{60}$ single-stranded DNA. This selective alteration in DBD dynamics was not visible when similar binding reactions were performed on a stopped flow instrument with $(dT)_{25}$ oligonucleotide (Fig. 5-14 a, b). Although stopped-flow reactions allow monitoring reaction in a millisecond timescale, the bulk signal output does not have the resolution to distinguish ongoing microscopic events, especially in situations where length of ssDNA directly affects the experimental results. Our current findings pertaining RPA-DBD dynamics in different DNA structures reveal requirement of a free 5′ end (5′ overhang) for remodeling of DBD-A , further suggesting RPA-DBDs could adopt different binding conformations when presented with ssDNA flanked by duplexes (chapter 4). While, Rad52 cannot position itself between two RPAs, it is able to bind to both ssDNA and dsDNA and could distinctly impact binding/dissociation/remodeling of both RPA-DBDs in DNA with a 5′ overhang, 3′ overhang, or blocked end DNA. These ssDNA with adjacent dsDNA are present in distinct cellular events like replication and recombination and require RPA and Rad52 to function on a common DNA template. Therefore, to determine if Rad52 distinctly affected RPA-DBD dynamics on ssDNA flanked by duplex structures, we performed sequential stopped-flow experiments to monitor binding of RPA-A^{MB543} or RPA-D^{MB543} to 5′ $(dT)_{30}$ overhang or, 3′ $(dT)_{30}$ overhang, or blocked end $(dT)_{30}$. RPA-A^{MB543} and RPA-D^{MB543} selectively report the DNA-binding dynamics of

DBD-A and DBD-D, respectively, in a multi-protein reaction (Pokhrel et. al., 2017; Pokhrel et. al., 2019).

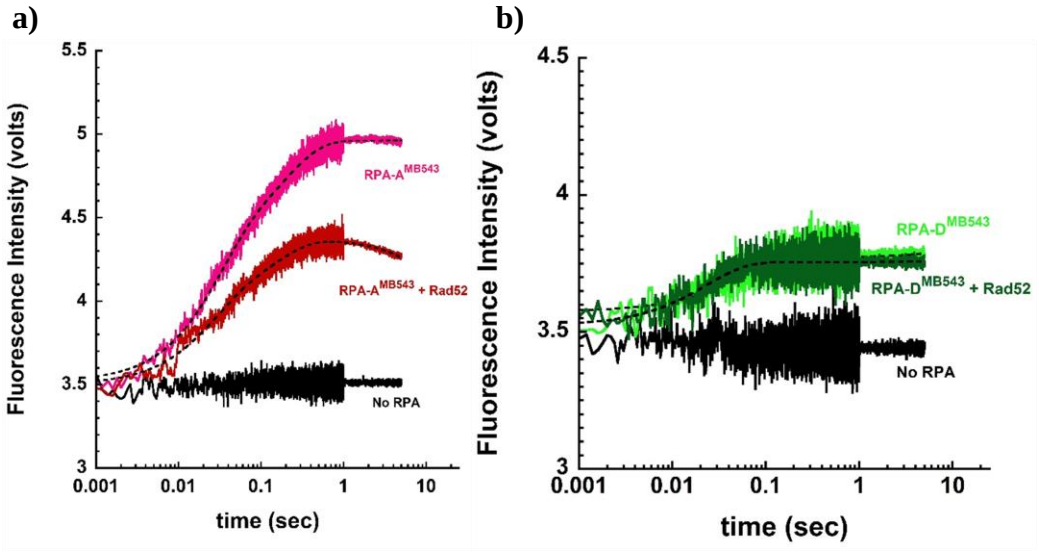

Figure 5-14: RPA-DBD binding to $(dT)_{25}$ in presence of Rad52-wt. Stopped-flow experiments show a robust increase in MB543 fluorescence upon **a)** RPA-A^{MB543} or **b)** RPA-D^{MB543} binding to $(dT)_{25}$. Performing the same binding experiment in presence of equimolar concentration of Rad52-wt shows quenching of MB543 fluorescence upon RPA-A^{MB543} binding (compare pink trace and red trace), but no difference in MB543 fluorescence is observed for RPA-D^{MB543} binding to $(dT)_{25}$ ssDNA (compare light green trace and dark green trace).

RPA-A^{MB543} produced a robust change in fluorescence upon binding with all three DNA substrates and bound with a rate of 24 ±2.3 s^{-1} to 5′ $(dT)_{30}$, 28.3 ± 2.1 s^{-1} to 3′ $(dT)_{30}$ and 22.4 ± 1.9 s^{-1} to blocked end $(dT)_{30}$ (Fig. 5-15 a-c) DNA. However, premixing RPA-A^{MB543} with Rad52-wt at 1:1 molar ratio and repeating the same binding reaction reduced the overall amplitude of MB543 fluorescence without changing the rates of DBD-A binding on all three DNA substrates (27.1 ± 15.0 s^{-1} for 5′ $(dT)_{30}$, 28.5 ± 9.5 s^{-1} for 3′ $(dT)_{30}$ and 20.7 ± 5.9 s^{-1} for blocked end $(dT)_{30}$ DNA, respectively) (Fig 5-15 a-c). Data obtained for all the experiments with RPA-A^{MB543} could be explained by a two-step binding equation. Similar experiments performed with RPA-D^{MB543} in presence of Rad52-wt, produced a robust increase in MB543 fluorescence upon binding to 3′ $(dT)_{30}$ and blocked end $(dT)_{30}$ DNA, with no significant changes in fluorescence intensity or initial rates of binding (Fig. 5-15 e, f) (Table 5-3). However, in presence of Rad52-wt, upon binding of RPA-D^{MB543} to a 5′ $(dT)_{30}$, the initial increase in MB543 fluorescence representing the initial engagement of DBD-D on 5′$(dT)_{30}$ was followed by a decrease in fluorescence. This suggests significant changes in the way DBD-D access/ binds to a 5′$(dT)_{30}$ in presence of Rad52-wt, since no significant changes in rates of binding were observed (Fig 5-15, d) (Table 5-3, 5-5). 5′ overhang is not a common substrate during pre-synapsis phase of HR but occurs frequently under conditions of replication stress (Ait Saada, Lambert, & Carr, 2018). Rad52 has been shown to facilitate restart of collapsed replication forks (Sotiriou et. al., 2016; Yeeles, Poli, Marians, & Pasero, 2013) and promote mitotic DNA synthesis following replication stress conditions (Bhowmick et. al., 2016). This function of Rad52 is independent of Rad51 recombinase but likely involves interaction with RPA, as RPA is recruited to these sites (Zou et. al., 2006b). Therefore,

Rad52 mediated change in DBD-D binding on a 5′ overhang could be a unique mechanism by which Rad52 interacts with the duplex junction and affects the DNA binding states as well as conformations of DBD-D.

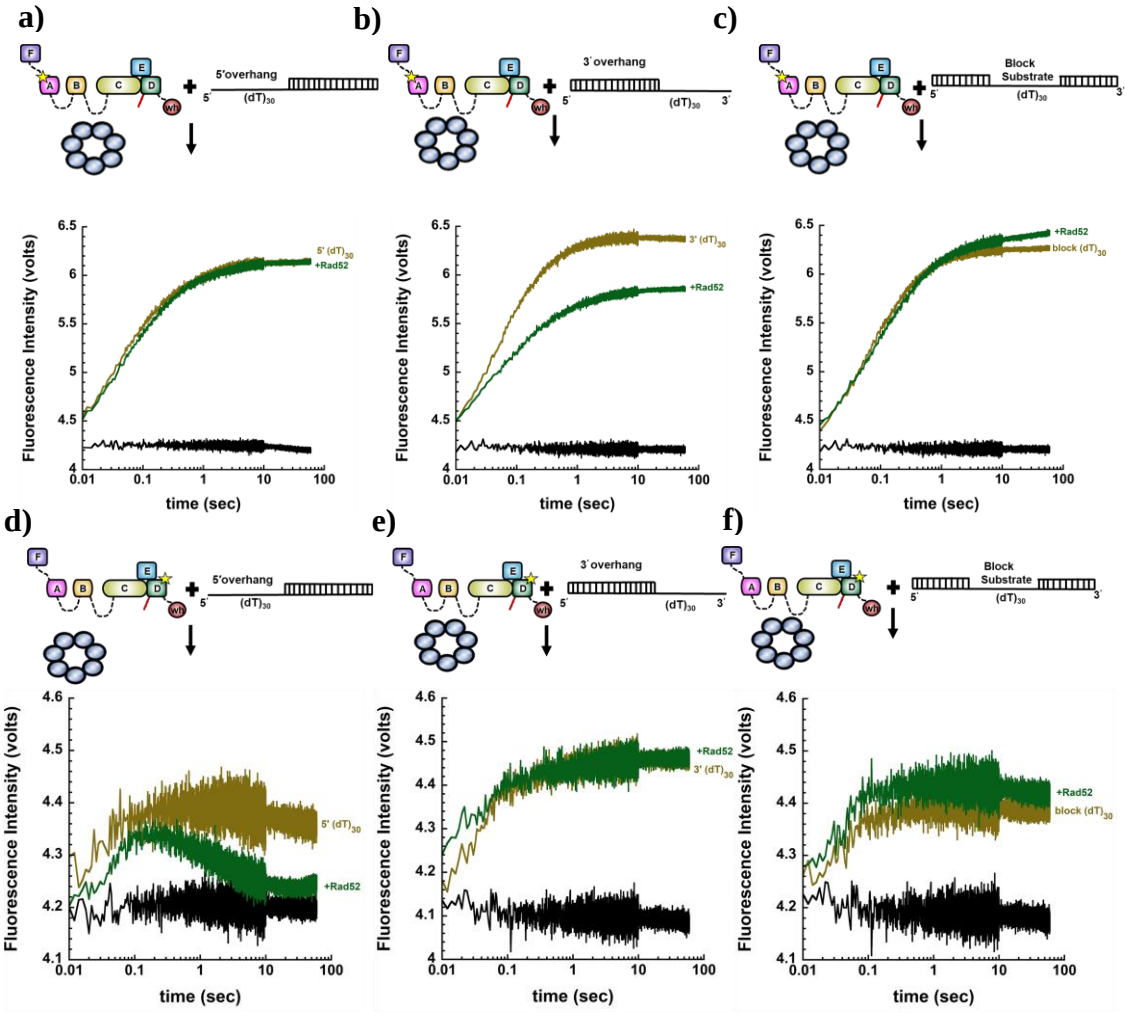

Figure 5-15: DNA structure specific remodeling of RPA-DBD-D by Rad52-wt. a), b), c) (Top) Schematic representation of the stopped-flow mixing reactions. RPA-A^{MB543} was incubated with Rad52-wt and rapidly mixed with 5′ $(dT)_{30}$ overhang, 3′ $(dT)_{30}$ overhang and blocked end $(dT)_{30}$ DNA, respectively. (Bottom) Stopped-flow raw traces show robust increase in MB543 fluorescence upon binding with DNA substrate alone (olive green trace) or in presence of Rad52-wt (forest green trace). Reactions are shown for binding with **a)** 5′ $(dT)_{30}$ overhang **b)** 3′ $(dT)_{30}$ overhang and **c)** blocked end $(dT)_{30}$ DNA. **d), e), f)** Similar binding reactions performed with RPA-D^{MB543} and 5′ $(dT)_{30}$ overhang, 3′ $(dT)_{30}$ overhang or blocked end $(dT)_{30}$ DNA, respectively. Rad52 selectively modulates binding of DBD-D on a 5′ $(dT)_{30}$ DNA which is seen as decrease in fluorescence signal (compare olive green trace in d) with forest green trace).

5.3.7 Effects of Rad52 inner site and outer site binding mutant on RPA-DBD-DNA engagement.

Rad52 prefers binding to single-stranded DNA and dramatically affects the mechanism of DBD-D binding on a 5′ overhang DNA. Our PIFE experiments monitoring polarity of Rad52 binding suggests cooperative binding between the inner and outer binding site, where, the outer binding site first engages on the 5′ end of DNA, following which DNA is threaded to the inner binding site. Therefore, we wanted to investigate if cooperativity between the inner and outer binding site could be one of the several factors contributing to selective remodeling of DBD-D particularly on a 5′ overhang DNA.

For the sake of clarity, from here onwards, Rad52 inner binding site mutant, outer binding site mutant, transition site mutant and double site mutant are collectively termed as 'Rad52 variants'.

To this extent, we preformed the following complexes:100nM RPA-A^{MB543} and Rad52-wt, 100nM RPA-A^{MB543} and Rad52 variants, 100nM RPA-D^{MB543} and Rad52-wt, or 100nM RPA-D^{MB543} and Rad52 variants at 1:1 molar ratio. Then, we performed sequential stopped flow reactions between the preformed complexes and 100nM $(dT)_{30}$, 5′ $(dT)_{30}$, 3′ $(dT)_{30}$ or blocked end $(dT)_{30}$ DNA, respectively (Fig. 5 -16- 5-21).

These reactions consist of unlabeled Rad52-wt or Rad52 variants precomplexed with fluorescently labeled RPA-A^{MB543} or RPA-D^{MB543}, and reacted against unlabeled DNA substrates. This experimental strategy enables direct and selective monitoring of DBD-A and DBD-D dynamics in all three DNA contexts, and effects of Rad52 in these scenarios. For all reactions, RPA-A^{MB543} or RPA-D^{MB543} was excited at 535nm and emission monitored with a 555nm long-pass filter. All the raw data obtained for RPA-

A^{MB543} could be fitted with a double-exponential + a linear state model and data obtained for RPA-D^{MB543} could be fitted using a single-exponential + a linear state model, irrespective of the kind of Rad52 variant or the type of DNA substrate used in the experiment. As a control, binding reactions performed between RPA-A^{MB543} and $(dT)_{30}$ showed similar change in MB543 fluorescence both in the presence and absence or Rad52-wt or Rad52 variants (Fig. 5-16 a). In addition, the rates of DBD-A binding to $(dT)_{30}$ i.e. $k_{obs,1}$ (initial engagement, first step of binding), $k_{obs,2}$ (second step of binding) and $k_{obs,3}$ (linear phase) remained unaffected in the presence of Rad52-wt or Rad52 variants (Fig. 5-16 c, 5-17 a, b) (Table 5-2, 5-4, 5-5). Similar experiments with RPA-D^{MB543} showed similar changes in MB543 fluorescence, both in the presence and absence of Rad52-variants (Fig. 5-16 b). A slight decrease in RPA-D^{MB543} fluorescence was observed when RPA-D^{MB543}: Rad52-wt complex was reacted with $(dT)_{30}$, with no significant changes in the rates of binding (Fig. 5-16 b, d). Furthermore, the rates of DBD-D binding to $(dT)_{30}$ i.e. $k_{obs,1}$ (initial engagement) and $k_{obs,2}$ (linear phase) (Fig. 5-16 d, 5-17 c) (Table 5-3, 5-6) remained unaffected in the presence of Rad52 variants.

Interestingly, MB543 fluorescence was slightly quenched upon RPA-A^{MB543} binding to $(dT)_{25}$ in presence of Rad52-wt (Fig. 5-14 a). Similar experiment with RPA-D^{MB543} showed no quenching of MB543 fluroescne upon binding to a $(dT)_{25}$ in presence of Rad52-wt (Fig. 5-14 b). In both these situations, presence of Rad52-wt did not change the rates of DBD-A or DBD-D binding to $(dT)_{25}$. Based on our site-size analysis, $(dT)_{30}$ oligonucleotide offers an additional 8 nucleotides for RPA diffusion which could also be utilized by Rad52 for initiating engagement on DNA. Therefore, it is possible that

modulation of DBD-D binding by Rad52 requires both interaction with RPA-DBD-D and engagement of some of Rad52 subunits, if not the entire heptamer, on DNA.

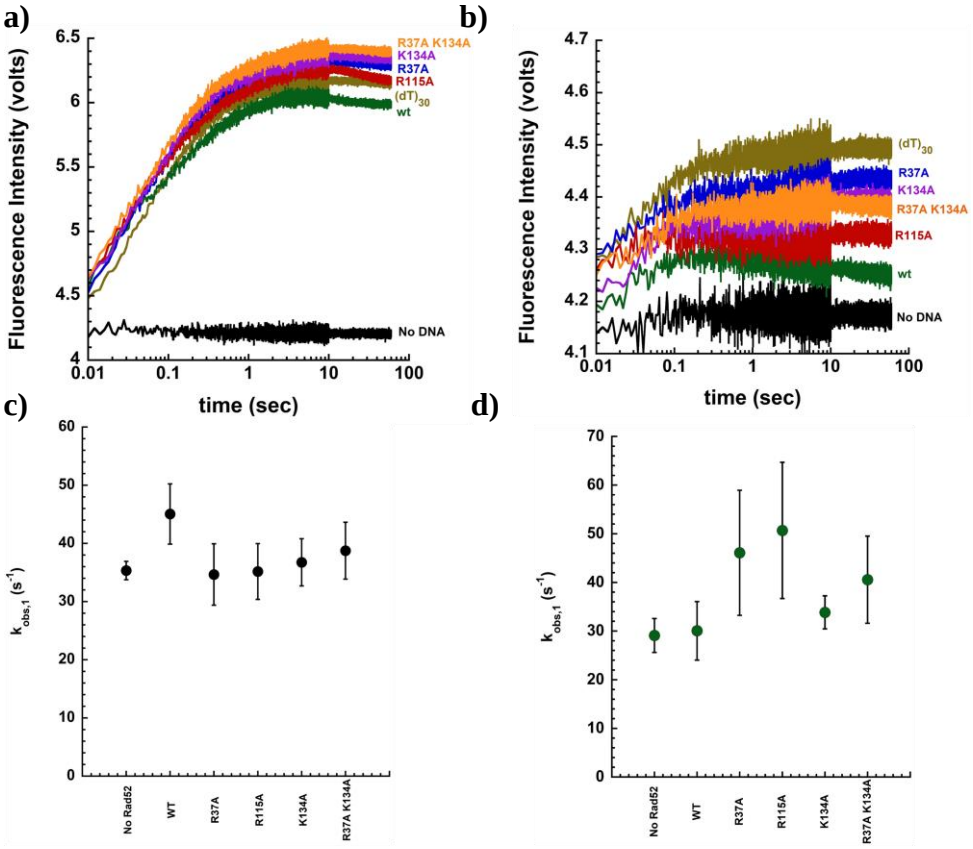

Figure 5-16: Effects of Rad52 on RPA-A^{MB543} and RPA-D^{MB543} binding to (dT)$_{30}$. a) RPA-A^{MB543} or **b)** RPA-D^{MB543} was preincubated with Rad52-wt or Rad52 variants and rapidly mixed with (dT)$_{30}$ oligonucleotide. In all the reactions, binding of DBD-A as seen in **a**), or DBD-D as seen in **b)** produces a robust change in MB543 fluorescence which can be quantified with appropriate kinetic equations (mentioned in *methods*) to obtain initial rate of engagement ($k_{obs,1}$) values plotted against individual Rad52 variants for **c)** DBD-A and **d)** DBD-D of RPA.

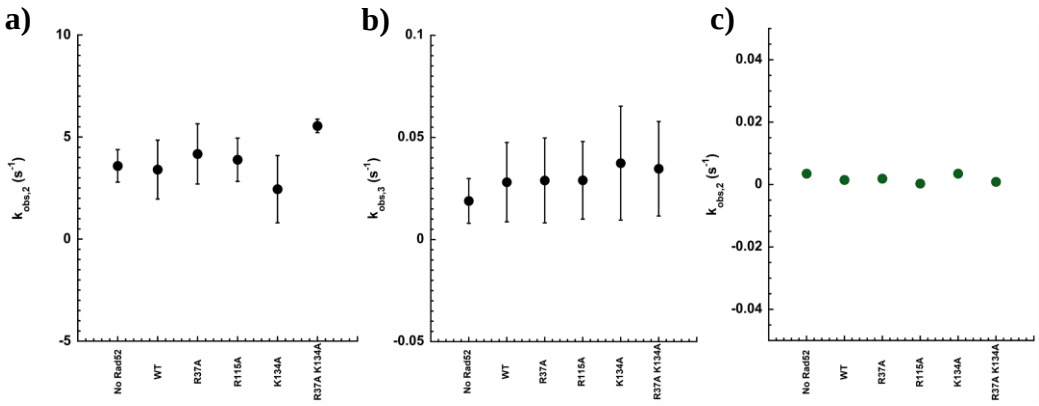

Figure 5-17: Quantification of rates of DBD-A and DBD-D binding to $(dT)_{30}$ in presence of Rad52-wt and Rad52 DNA binding mutants. a) Plot of the second exponential or second step of binding ($k_{obs,2}$), and **b)** linear phase ($k_{obs,3}$) for RPA-DBD-A binding to $(dT)_{30}$ when complexed with Rad52-wt or Rad52 variants. **c)** Similar plot of linear phase ($k_{obs,2}$) of RPA-D^{MB543} binding to $(dT)_{30}$ DNA.

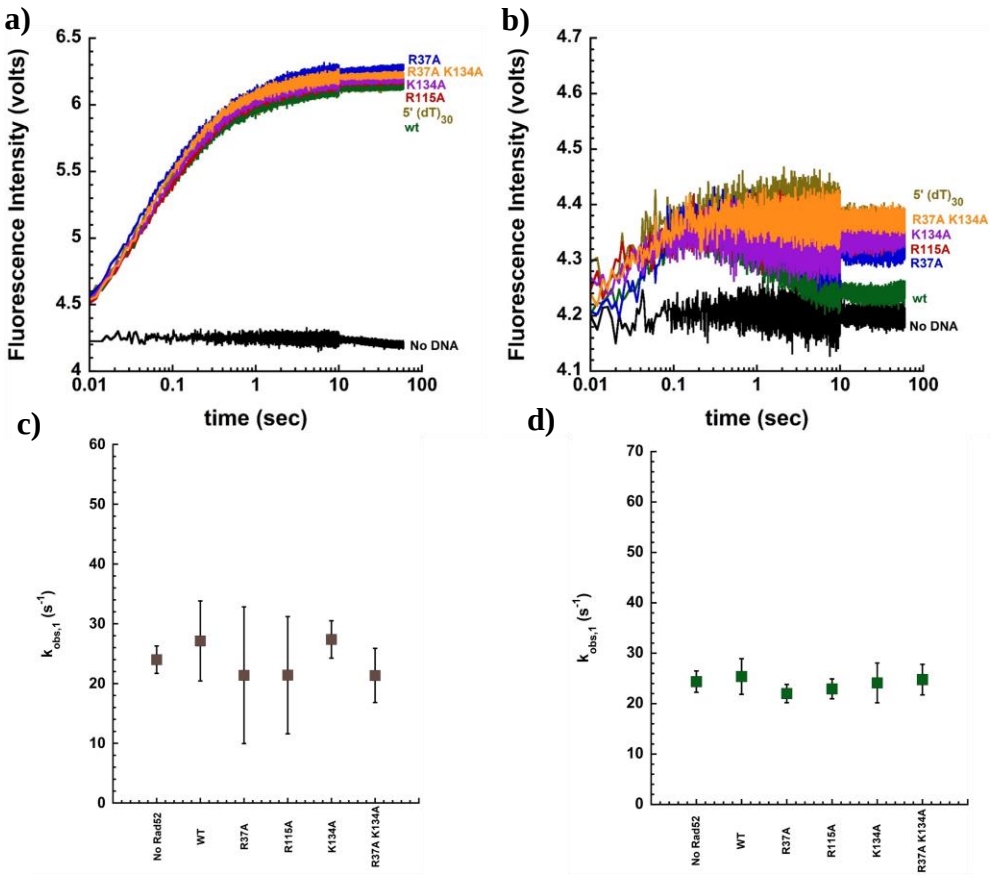

Figure 5-18: Cooperativity in Rad52 modulates RPA-DBD-D binding on a 5′ (dT)$_{30}$ overhang DNA. RPA-D^{MB543} was preincubated with Rad52-wt or Rad52 variants and rapidly mixed with 5′ (dT)$_{30}$ DNA. In all the reactions, **a)** binding of DBD-A, or **b)** DBD-D produces a robust change in MB543 fluorescence which can be quantified with appropriate kinetic equations (mentioned in *methods*) to obtain initial rate of engagement ($k_{obs,1}$) values plotted against individual Rad52 variants for **c)** DBD-A and **d)** DBD-D of RPA.

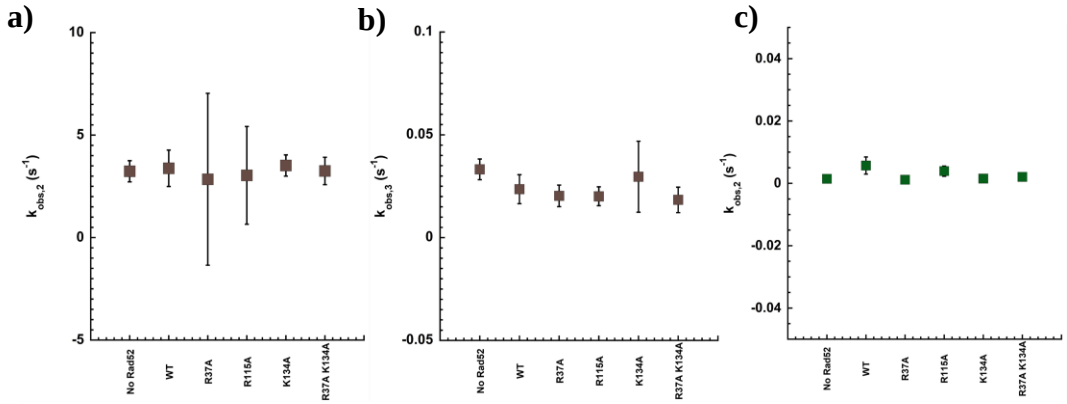

Figure 5-19: Quantification of rates of DBD-A and DBD-D binding to 5′ $(dT)_{30}$ in presence of Rad52-wt and DNA binding mutants. a) Plot of the second exponential or second step of binding ($k_{obs,2}$) and **b)** linear phase ($k_{obs,3}$) of RPA-DBD-A binding to 5′$(dT)_{30}$ DNA in presence of Rad52-wt or Rad52 variants. **c)** Similar plot of linear phase ($k_{obs,2}$) of RPA-DBD-D binding to 5′ $(dT)_{30}$ DNA in presence of Rad52 variants.

Next, we performed stopped flow experiments to monitor binding of RPA-A^{MB543} to 5′ $(dT)_{30}$ DNA in presence or Rad52-wt or Rad52 variants. Raw stopped flow traces show no differences in the intensity of MB543 fluorescence when RPA-A^{MB543} is precomplexed with Rad52-wt or Rad52 variants (Fig. 5-18 a) and mixed with 5′$(dT)_{30}$ DNA (Fig. 5-18 a). The rates of DBD-A binding to 5′ $(dT)_{30}$ DNA was similar both in presence and absence of Rad52-wt and Rad52 variants (Fig. 5-18 c; 5-19 a, b) (Table 5-2, 5-4, 5-5). However, on a 5′ $(dT)_{30}$ DNA, RPA-DBD-D:Rad52-wt complex showed a robust increase in MB543 fluorescence followed by a gradual decrease in fluorescence signal, with no affects on the k_{obs} values, suggesting affects in the DBD-D binding dynamics (Fig. 5-18 b, compare forest green trace with all other traces). Similar reactions monitoring RPA-DBD-D binding on a 5′ $(dT)_{30}$ DNA, when RPA-D^{MB543} was precomplexed with Rad52 variants showed no differences in MB543 fluorescence and similar k_{obs}values (Fig. 5-18 b, d, 5-19 c) (Table 5-3, 5-6). Taken together, these results suggests that cooperativity between the inner and outer binding site in Rad52 selectively affects RPA-DBD-D dynamics in a 5′ overhang DNA.

We also monitored engagement of both RPA-A^{MB543} and RPA-D^{MB543} on a 3′ $(dT)_{30}$ overhang and blocked end $(dT)_{30}$ DNA substrates, alone, or in complex with Rad52-wt and Rad52 variants. Stopped flow reactions performed with RPA-D^{MB543}: Rad52-wt or RPA-D^{MB543}:Rad52 variants versus 3′ $(dT)_{30}$ DNA showed a similar degree of increase in MB543 fluorescence with no significant differences in observed rates of binding (k_{obs}) values (Fig. 5-20 b, d, 5-21 c) (Table 5-3; 5-6). In the context of 3′ overhang DNA, DBD-A is situated close to the duplex junction which poses a structural hindrance to dynamic binding of DBD-A. A varying degree of RPA-A^{MB543} fluorescence

for each Rad52 variant was observed when rapidly mixed with 3′$(dT)_{30}$ DNA (Fig 5-20 a). However, quantification of the raw data, as described in *methods*, revealed no significant differences in the observed rates of binding (k_{obs}) of DBD-A (Fig 5-20 c, 5-21 a, b) (Table 5-2, 5-4, 5-5). Rad52 physically interacts with OB-F and DBD-A of RPA. Thus, differences in the degree of fluorescence but not in rates of binding on 3′ $(dT)_{30}$ DNA could arise due to differences in protein-protein interactions between Rad52-wt and Rad52 variants. Each Rad52 variant could differentially affect conformations of DBD-A on DNA without significantly impacting its rate of binding.

Finally, similar experiments performed with blocked end $(dT)_{30}$ showed no significant differences in MB543 fluorescence of RPA-A^{MB543} or RPA-D^{MB543} in presence of Rad52-wt or Rad52 variants (Fig 5-22 a, b). Quantification of the raw traces with appropriate kinetic models showed no differences in the rates of DBD-A or DBD-D binding (k_{obs}) to blocked end $(dT)_{30}$ DNA in presence Rad52-wt or Rad52 variants (Fig. 5-22 c, d; 5-23 a-c) (Table 5-2- 5-6). Taken together, our results show that Rad52-wt selectively affects DBD-D dynamics on a 5′ overhang DNA which is not a primary HR substrate, but is often found during DNA replication in the form of 5′ flap DNA (Burgers, 2011). Future implications involve selective and unique modifications of RPA-DBD dynamics by RPA interacting proteins adapted to ongoing cellular event.

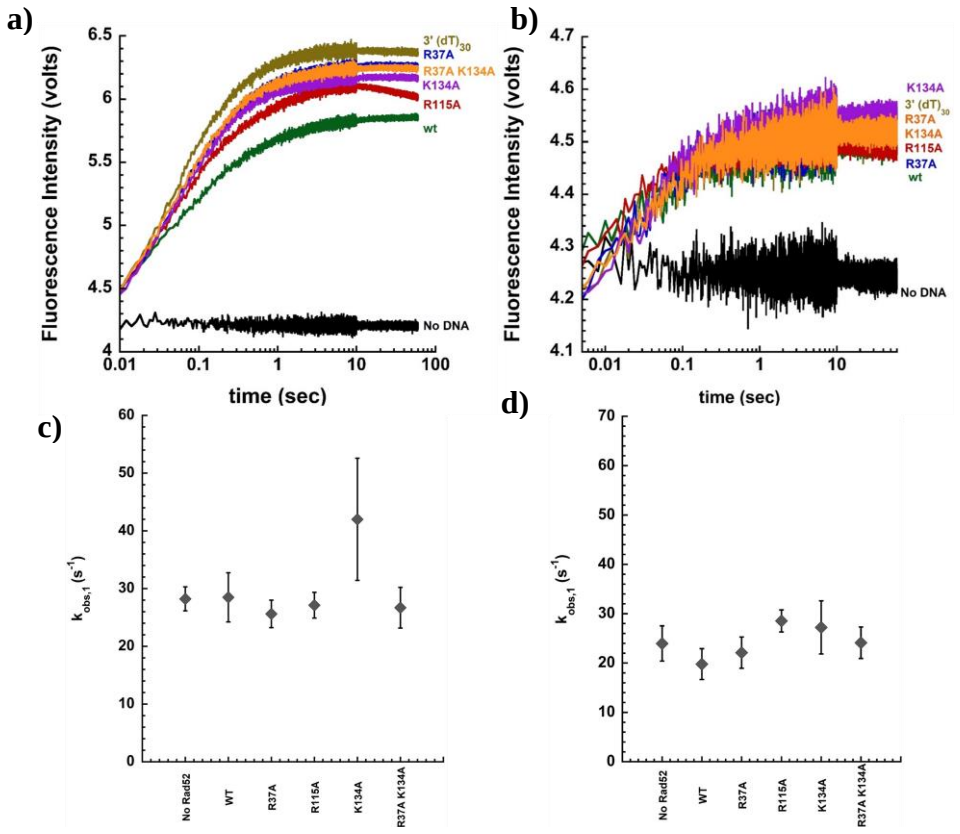

Figure 5-20: Rad52-wt and Rad52 variants do not affect binding of RPA-A^{MB543} and RPA-D^{MB543} to 3′ (dT)$_{30}$ DNA. 100nM **a)** RPA-A^{MB543} or **b)** RPA-D^{MB543} was preincubated with 100nM Rad52-wt or Rad52 variants and rapidly mixed with 100nM 3′ (dT)$_{30}$ DNA. In all the reactions, binding of **a)** DBD-A, or **b)** DBD-D produces a robust change in MB543 fluorescence which can be quantified with appropriate kinetic equations (mentioned in *methods*) to obtain initial rate of engagement ($k_{obs,1}$) values plotted against individual Rad52 variants for **c)** DBD-A and **d)** DBD-D of RPA.

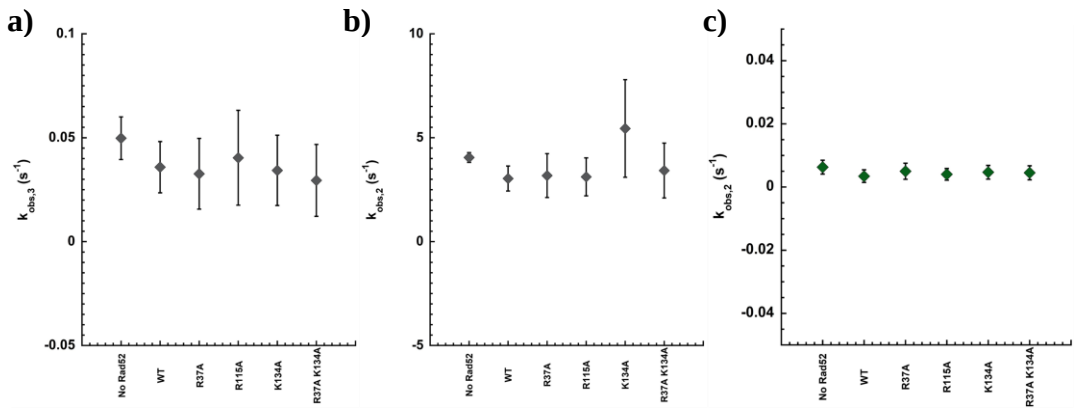

Figure 5-21: Quantification of rates of DBD-A and DBD-D binding to 3′ (dT)$_{30}$ DNA in presence of Rad52-wt and DNA binding mutants. a) Plot of the second exponential or second step of binding ($k_{obs,2}$), and **b)** linear phase ($k_{obs,3}$) for RPA-DBD-A binding to 3′(dT)$_{30}$ in presence of Rad52 variants. **c)** Similar plot of linear phase ($k_{obs,2}$) of RPA-DBD-D binding to 3′ (dT)$_{30}$ DNA in presence of Rad52 variants.

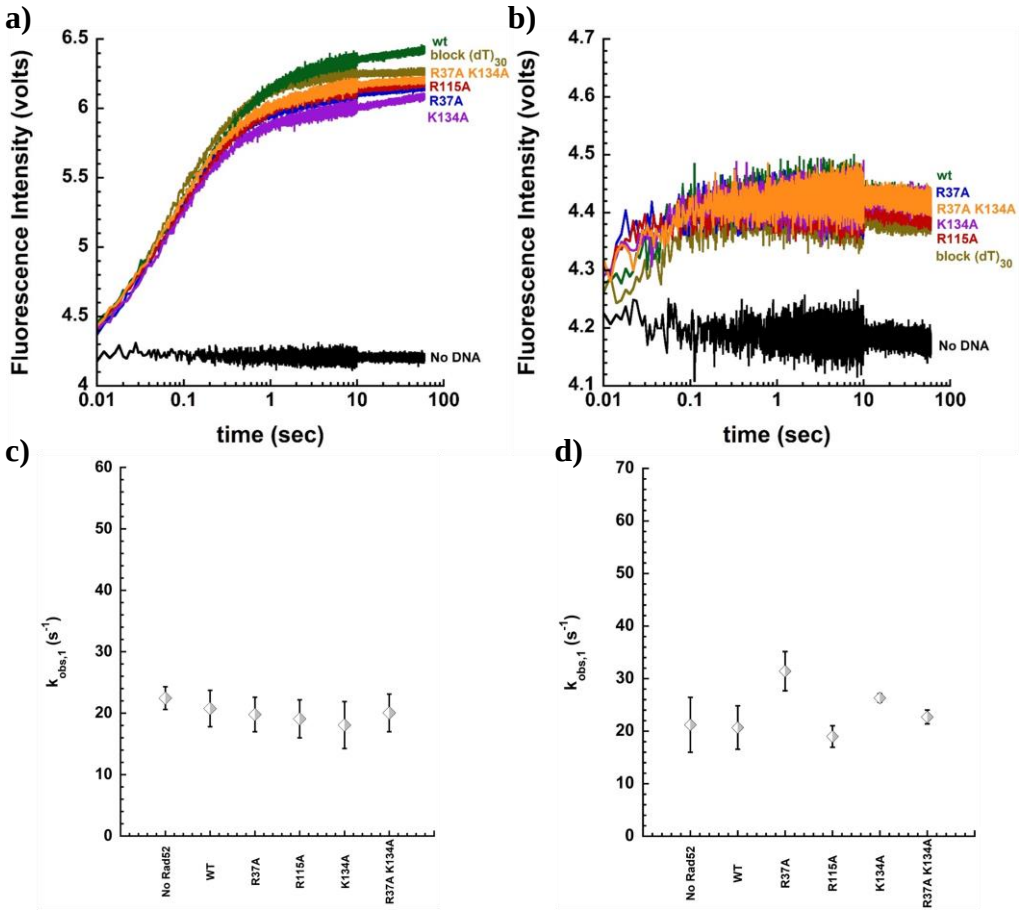

Figure 5-22: Binding of RPA-DBD-A and RPA-DBD-D on block $(dT)_{30}$ DNA in presence of Rad52-wt and Rad52 variants. Representative traces showing significant increase in MB543 fluorescence upon **a)** RPA-A^{MB543}, **b)** RPA-D^{MB543} binding to block end $(dT)_{30}$ DNA in presence of Rad52-wt or Rad52 variants. Quantification of data as described in the *methods* yields $k_{obs,1}$ plot for **c)** RPA-A^{MB543} and **d)** RPA-D^{MB543}, respectively.

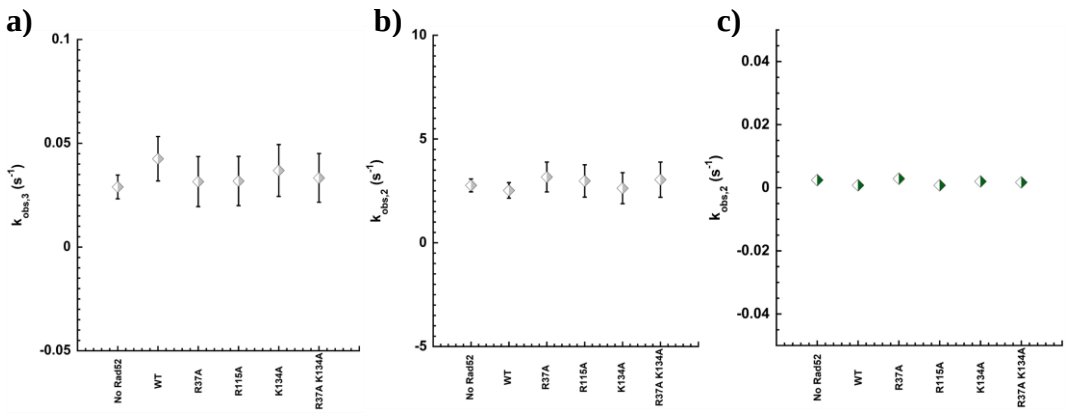

Figure 5-23: Quantification of rates of DBD-A and DBD-D binding to blocked end $(dT)_{30}$ in presence of Rad52-wt and Rad52 variants. a) Plot of the second exponential or second step of binding ($k_{obs,2}$), and **b)** linear phase ($k_{obs,3}$) for RPA-DBD-A binding to blocked end $(dT)_{30}$ in presence of Rad52 variants. **c)** Similar plot of linear phase ($k_{obs,2}$) of RPA-DBD-D binding to blocked end $(dT)_{30}$ DNA in presence of Rad52 variants.

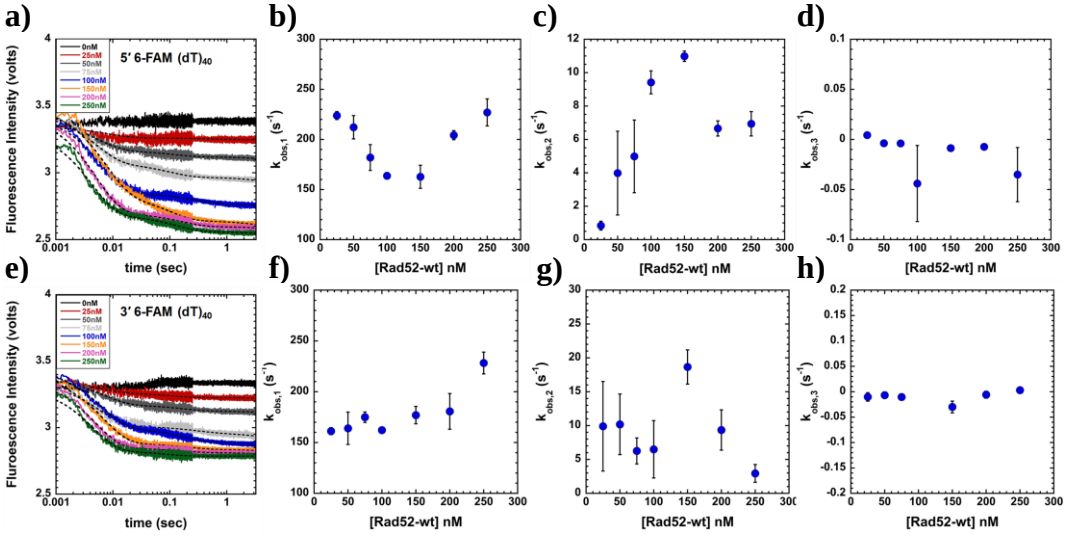

Figure 5-24: PIFE monitoring Rad52-wt binding on a 5′ 6-FAM (dT)$_{40}$ and 3′ 6-FAM (dT)$_{40}$ DNA. As a control, stopped-flow reactions monitoring binding between **a)** 100nM 5′ 6-FAM (dT)$_{40}$ with increasing concentrations of Rad52-wt show a proportional decrease in 6-FAM fluorescence. Fitting the raw traces with double-exponential + linear state model yields the plot of **b)** $k_{obs,1}$ **c)** $k_{obs,2}$ **and d**) $k_{obs,3}$ for Rad52-wt binding to 5′ 6-FAM (dT)$_{40}$**. e)** same as in a) but performed with 3′ 6-FAM (dT)$_{40}$. Fitting the raw traces with double-exponential + linear state model yields the plot of **f)** $k_{obs,1}$ **g)** $k_{obs,2}$ and **h)** $k_{obs,3}$ for Rad52-wt binding to 3′ 6-FAM (dT)$_{40}$.

Table 5-1: Binding affinity (K_d) of Rad52-wt, outer site binding mutant ($Rad52^{R115A}$), inner binding site mutant ($Rad52^{K134A}$), double mutant ($Rad52^{R37A\ K134A}$), transition site mutant ($Rad52^{R37A}$)

Rad52	**K_d (nM)**
Wt	40.2 ± 3.3
R115A	38.6 ± 1.0
K134A	165.8 ± 13.7
R37A K134A	226.7 ± 41.0
R37A	92.8 ± 11.2

Table 5-2: Initial rate of engagement ($k_{obs,1}$) values for RPA-A^{MB543} binding to various DNA substrates in presence of Rad52-wt and Rad52 variants.

DNA substrate	RPA-A^{MB543}					
	No Rad52	Rad52 variants				
		wt	R37A	R115A	K134A	R37AK134A
$(dT)_{30}$	35.5±0.8	45.1±1.4	34.6±1.5	35.2±1.1	36.7±1.7	38.7±0.3
5′ $(dT)_{30}$	24.0±2.3	27.1±6.7	21.3±11.4	21.4±9.8	27.4±3.1	21.3±4.5
3′ $(dT)_{30}$	28.2±2.1	28.5±4.3	25.6±2.4	27.1±2.2	42.0±10.6	26.7±3.5
Blocked end $(dT)_{30}$	22.5±1.9	20.8±3.0	19.8±2.8	19.1±3.1	18.1±3.8	20.1±3.1

Table 5-3: Initial rate of engagement ($k_{obs,1}$) values for RPA-D^{MB543} binding to various DNA substrates in presence of Rad52-wt and Rad52 variants

DNA substrate	RPA-D^{MB543}					
	No Rad52	Rad52 variants				
		wt	R37A	R115A	K134A	R37AK134A
$(dT)_{30}$	29.1±3.5	30.0±6.0	46.1±12.9	50.7±14.0	33.8±3.4	40.6±9.0
5′ $(dT)_{30}$	24.4±2.1	25.4±3.5	22.1±1.8	23.0±2.0	24.1±4.0	24.8±3.0
3′ $(dT)_{30}$	24.0±3.6	19.8±3.1	22.1±3.2	28.5±2.2	27.2±5.4	24.1±3.2
Blocked end $(dT)_{30}$	21.2±5.2	20.7±4.1	31.4±3.7	19.0±2.0	22.7±1.0	20.7±1.3

Table 5-4: Second exponential /second step of binding ($k_{obs,2}$) values for RPA-A^{MB543} binding to various DNA substrates in presence of Rad52-wt and Rad52 variants.

DNA substrate	RPA-A^{MB543}					
	No Rad52	Rad52 variants				
		wt	R37A	R115A	K134A	R37AK134A
$(dT)_{30}$	3.6±0.8	3.4±1.4	4.2±1.5	3.9±1.1	2.4±1.7	5.5±0.3
5′ $(dT)_{30}$	3.3±0.5	3.4±0.9	2.8±4.2	3.3±2.4	3.5±0.5	3.2±0.7
3′ $(dT)_{30}$	4.0±0.2	3.0±0.6	3.2±1.1	3.1±0.9	5.4±2.3	3.4±1.3
Blocked end $(dT)_{30}$	2.8±0.3	2.5±0.4	3.2±0.7	3.0±0.8	2.6±0.7	3.0±0.8

Table 5-5: Linear phase ($k_{obs,3}$) values for RPA-A^{MB543} binding to various DNA substrates in presence of Rad52-wt and Rad52 binding variants

Note: All the $k_{obs,3}$ values are in the order of 10^{-2}, i.e. 1.9±1.1 is equal to 0.019±0.01.

DNA substrate	**RPA-A^{MB543}**					
	No Rad52	**Rad52 variants**				
		wt	**R37A**	**R115A**	**K134A**	**R37AK134A**
$(dT)_{30}$	1.9±1.1	2.8±2.0	3.0±2.1	3.0±2.0	4.0±3.0	3.0±2.3
5′ $(dT)_{30}$	3.3±0.5	2.5±0.7	2.0±0.5	20.±0.5	3.0±1.7	2.8±0.7
3′ $(dT)_{30}$	5.0±1.0	3.6±1.2	3.3±1.7	4.0±2.9	3.4±1.7	2.9±1.7
Blocked end $(dT)_{30}$	2.9±0.5	4.3±1.0	3.1±1.2	3.2±1.2	3.7±1.2	3.3±1.2

Table 5-6: Linear phase ($k_{obs,2}$) values for RPA-D^{MB543} binding to various DNA substrates in presence of Rad52-wt and Rad52 variants.

DNA substrate	RPA-D^{MB543}					
	No Rad52	Rad52 variants				
		wt	R37A	R115A	K134A	R37AK134A
(dT)$_{30}$	3.5±1.4	1.5±0.5	1.9±0.9	0.3±0.1	3.5±1.1	0.9±0.4
5′ (dT)$_{30}$	1.4±0.4	5.7±2.8	1.2±0.4	3.9±1.6	1.5±0.5	2.1±0.6
3′ (dT)$_{30}$	6.3±2.2	3.4±2	5.0±2.5	4.0±1.8	4.7±2.2	4.5±2.2
Blocked end (dT)$_{30}$	2.4±1.0	0.8±0.4	2.8±1.1	0.8±0.2	2.0±0.5	1.7±0.9

Note: All the $k_{obs,2}$ values are in the order of 10^{-3}, i.e. 3.5±1.4 is equal to

0.0035±0.0014

5.4 Discussion

The order of protein recruitment, positioning and accessibility to DNA significantly regulates the process of DNA replication, recombination, repair, and transcription. In this chapter we investigated the DNA binding kinetics of yeast Rad52 and assed its influence on the engagement of RPA-DBDs in-context of different DNA structures. The myriad of processes required to maintain DNA structure and function often deal with processing single-stranded DNA intermediates which are usually protected by ssDNA binding proteins, which in-turn could pose to be steric hindrances for enzymes attempting to access the same DNA space. How individual proteins coordinate their turn to access the DNA in order to correctly process the DNA related functions is still an ongoing mystery awaiting answers. In this study we attempted to understand the interplay between two DNA interacting proteins, RPA and Rad52, which often act on the same DNA substrate in multiple DNA pathways. During the process of homologous recombination, Rad52 prevents facilitated exchange/ self-exchange of RPA from DNA, meanwhile it also recruits the ATP dependent Rad51 recombinase which in-turn displaces RPA from DNA (New et. al., 1998; Sugiyama & Kowalczykowski, 2002a). Studies have also shown that while Rad52 itself does not displace RPA from DNA, it enhances the ATP hydrolysis activity of Rad51 which leads to faster displacement of RPA (Sugiyama & Kowalczykowski, 2002a). Apart from its mediator function with Rad51, Rad52 has been shown to directly anneal homologous ssDNA strands or RPA-ssDNA complexes which encompasses homology (Brouwer et. al., 2017; Nimonkar et. al., 2009). Interaction between RPA-Rad52 yields unique outcomes based on the DNA-context and cellular pathways, yet, fundamentals underlying how similar

interaction results in unique functions was not well understood. To this extent, first we investigated the ssDNA binding properties of yeast Rad52 and found that Rad52 bound to ssDNA with relatively high affinity (Fig. 5-2 f) and this binding was not affected by increasing salt concentrations (Fig 5-2 c, d). Using tryptophan quenching as signal read-out we determined the pre-steady state binding kinetics of Rad52 on ssDNA and showed that Rad52 bound rapidly to ssDNA (Fig 5-3 a-f).

Rad52 forms a heptameric ring with a central pore, where the ssDNA is wrapped around the ring structure (Fig. 5-5 a) rather than being threaded through the pore which usually occurs in other hexameric ATPases (Saotome et. al., 2016, 2018; A Shinohara et. al., 1998). ssDNA bound crystal structure of truncated hRad52, that does not include the C-terminus of the protein shows an undecamer with two distinct ways of associating with single-stranded DNA. First includes a structure a with ssDNA wrapped around the undecamer when the outer binding site is mutated, and the second includes ssDNA sandwiched between two undecamer when the inner binding site is mutated (Fig. 5-5, 5-6 a, b, respectively). Based on additional biochemical analysis, a cooperative binding between the inner and outer-binding site was performed (Saotome et. al., 2018). Our PIFE analysis monitoring the binding of *Sc.* Rad52 with 5′Cy3 labeled or 3′ Cy3 labeled ssDNA shows a cooperative binding mechanism between the inner and outer binding sites which follows a 5′-3′ directionality (Fig. 5-4 a-c), as mutating key amino acid residues in either the inner or the outer binding site completely abolishes the observed cooperativity (Fig. 5-8- 5-10, b, f) . Furthermore, mutations in either inner or outer binding site rapidly increases the initial rate at which Rad52 binds to ssDNA independent of Rad52 concentration (Fig. 5-8- 5-10, b, f). Single molecule experiments monitoring

hRad52-ssDNA binding showed that hRad52 wrapped ssDNA around its structure when ssDNA was in excess. However, during the conditions of excess hRad52, multiple hRad52 bound to a single ssDNA (Grimme et. al., 2010). Taken together, these results suggest communication between the outer and inner binding sites play a critical role in defining the path and the rate at which DNA threads around a single Rad52, or DNA is occupied by multiple Rad52, or several DNA is occupied by a Rad52 (Fig. 5-12). Although Rad52 exists as a heptamer in solution, several studies monitoring Rad52-ssDNA binding have reported changes in the number of protomers present in the heptamer resulting in a 'horse-shoe shaped' structure (Deng et. al., 2009). There is a distinct possibility that Rad52 heptameric ring 'opens up' upon interaction with ssDNA and mutating amino acid residues important for ssDNA interaction alters the way ssDNA is engaged. These mutations could also induce a different conformational change in Rad52, which is seen as loss of cooperativity at the 5′ end along with increased rates of ssDNA binding at sub-stoichiometric Rad52 concentrations in our PIFE experiments. Since, the C-terminal end of Rad52 has been implicated in mediating DNA annealing and all our experiments have been performed with full-length yeast Rad52 (Kagawa et. al., 2014; Yan et. al., 2019), we used end labeled poly(dT)$_{40}$ to avoid any annealing situations. Thus, our PIFE observations are relevant to ssDNA binding and not Rad52 mediated DNA annealing.

RPA and Rad52 function together in several different DNA pathways. In chapter 3, we showed that despite its ability to interact with both DBD-A and DBD-D of RPA, Rad52 selectively altered the DNA binding state of DBD-D but not DBD-A on a ssDNA (Nilisha Pokhrel et. al., 2019). However, in native conditions RPA and Rad52 undergo

interactions along long stretches of ssDNA which are presented in the form of overhangs, or ssDNA with DNA duplexes present in both the ends. Furthermore, in a situation where ssDNA is occupied by multiple RPAs, whether Rad52 can access DNA between RPAs or if it requires access at the terminal ends of DNA is important towards understanding the functioning of these proteins. Therefore, to ascertain positioning of Rad52 when ssDNA is occupied by multiples RPAs, we performed RPA-FRET assays in presence of Rad52 and showed that Rad52 is unable to position itself in between two RPAs. Therefore, Rad52 would require access toward the 5′ or 3′ ends of DNA (Fig. 5-13 b). Our data is consistent with previous finding where access to either DNA termini was required for Rad52-ssDNA engagement even in the absence of RPA (Parsons, Baumann, Van Dyck, & West, 2000). Finally, we compared how binding of DBD-A and DBD-D to a 5′ overhang, 3′ overhang and blocked end DNA substrate is affected in presence of Rad52. Our study is unique in that we provide both RPA and Rad52 with an equal opportunity to bind to the DNA substrates rather than reacting Rad52 with a pre-formed RPA-DNA complex. We show that Rad52 selectively modulates the DNA binding dynamics of DBD-D on a 5′ overhang DNA (Fig. 5-15 d) without affecting the rate at which DBD-D engages on DNA (Table 5-3, 5-6). Furthermore, cooperativity between the inner and outer binding sites in Rad52 is required for this modulation of DBD-D dynamics (Fig. 5-18 b). Our studies provide critical insights into yeast Rad52-ssDNA behavior and unique modulation of DBD-D dynamics only on a 5′ DNA with future implications pertaining to RPA-Rad52 functioning in DNA related process other than homologous recombination mediated DNA repair.

CHAPTER 6: POST-TRANSLATIONAL MODIFICATION OF RPA MODULATES RPA-DBD DYNAMICS, ASSEMBLY AND FUNCTIONING

6.1 Introduction

Post translational modifications (PTM) is a common, yet, robust mechanism of tailoring protein functions and activities in a specific pathway. Replication Protein A (RPA), the most ubiquitous single-stranded DNA (ssDNA) binding protein in eukaryotes is extensively modified via phosphorylation, ubiquitination, SUMOylation (small ubiquitin- related modifier) etc. in a cell-cycle dependent manner or during stress conditions (Chung & Zhao, 2015; Dou, Huang, Singh, Carpenter, & Yeh, 2010; Dubois et. al., 2017; Hedglin, Aitha, Pedley, & Benkovic, 2019). In human RPA, the first 40 amino acids (aa) in the N-terminus of RPA32 consists of 9 serines (6 in *S. cerevisiae*) and 1 threonine (6 in *S. cerevisiae*) that undergo phosphorylation in accordance with cell-cycle checkpoint and during DNA damage. These serines and threonines are phosphorylated by members of PIKK (phosphatidylinositol-3-kinase-like kinases) family such as ATM (Ataxia telangiectasia mutated), ATR (Ataxia telangiectasia mutated and Rad3 related), DNA-PK, and cyclin-dependent kinase (Cdk) family such as Cdk-1/ Cyclin B and Cdk-2/ Cyclin-A; reviewed in (Anantha & Borowiec, 2009; Binz, Sheehan, & Wold, 2004b; Byrne & Oakley, 2019; Maréchal & Zou, 2015; Oakley & Patrick, 2010). Since these phosphorylation events are tightly coupled with cell-cycle regulation, deregulation of phosphorylation can have severe outcomes like oncogenesis.

In budding yeast, the Mec1-Ddc2 complex is homologous to the human ATR-ATRIP complex which initiates cell cycle checkpoint response upon DNA damage or during replication stalling (Bartrand et. al., 2004; Gangavarapu, Maria, Prakash, &

Prakash, 2011; Kondo, Wakayama, Naiki, Matsumoto, & Sugimoto, 2001; Pfander & Diffley, 2011; Tercero & Diffley, 2001). RPA is one of the several Mec1-Ddc2 targets that gets phosphorylated during DNA damage in order to trigger the DNA damage response (DDR). DDR then recruits appropriate repair factors at the sites of DNA damage to repair the damage and ensure cell viability.

Since Mec1 itself cannot interact with RPA, it uses the the coiled-coiled region in Ddc2 (ccDdc2) as a handle to interact with RPA and phosphorylate specific sites in RPA70 and RPA32 subunits (Biswas et. al., 2019; Brush et. al., 1996; Deshpande et. al., 2017; Majka & Burgers, 2007) (Fig. 6-1 a). The crystal structure of ccDdc2 in complex with the N-terminal protein interaction domain in RPA70 (ccDdc2-PID^{70N} complex) shows a homodimeric ccDdc2, where each ccDdc2 monomer interacts with one PID^{70N} (Deshpande et. al., 2017) (Fig. 6-1 a). In humans, similar coiled-coiled region in ATRIP (homolog of Ddc2) also mediates interaction between RPA and ATR (Ball & Cortez, 2005).

Apart from ccDdc2-PID^{70N} cystal structure showing a dimeric ccDdc2, where, each ccDdc2 is interacting with PID^{70N}, the stoichiometry of full length RPA-Mec1-Ddc2 complex with or without DNA has not been determined. Recent experiments monitoring Mec1 kinase activation in presence of RPA and Ddc2 showed an increase in kinase activity at sub-stoichiometric concentrations of RPA and on longer DNA. However, excess RPA attenuated the Mec1 kinase activity (Bartrand et. al., 2004; Biswas et. al., 2019) . This suggests an RPA concentration driven feedback mechanism of Mec1 kinase activity, where, phosphorylation of RPA by Mec1 kinase is dependent on the recruitment of Mec1 by Ddc2 and the effects of kinase activity are regulated by extent of RPA

phosphorylation, concentration of RPA and length of ssDNA available. A prime target of Mec1 phosphorylation in RPA is serine 178 (S178) which is located near lysine 170 (K170). S178 is phosphorylated by Mec1, while, S170 gets SUMOylated in response to DNA damage (Bartrand et. al., 2004; Bastos de Oliveira et. al., 2015; Brush et. al., 1996; Psakhye & Jentsch, 2012) . Mass proteomics studies have found an ATM-ATR mediated global regulation of SUMOylation levels in member proteins upon replication stress (Munk et. al., 2017). These findings suggest significant crosstalk between phosphorylation and SUMOylation in regulating the ATR-ATRIP (or Mec1-Ddc2) pathway, with RPA being at the center of this crosstalk.

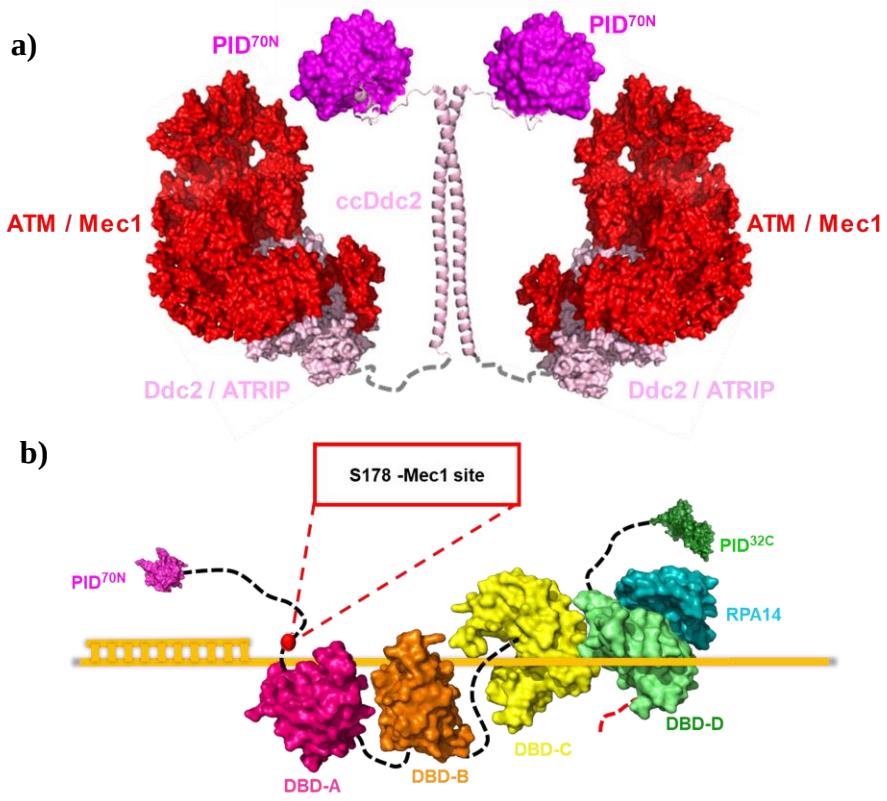

Figure 6-1: RPA-PID^{70N}-Mec1-Ddc2 interaction. a) Structure of PID^{70N}-ccDdc2-ATM-ATR (Sc. Mec1-Ddc2) complex. The crystal structure of PID^{70N}-ccDdcc2 complex (PDB: 5OMC) showing RPA-PID^{70N} (magenta) and coiled-coiled region of Ddc2 (pale pink cartoon helices). The ccDdc2 region could be connecting rest of the Ddc2-Mec1 complex via flexible linkers (dashed grey line). The human homolog of Mec1-Ddc2 complex is ATR-ATRIP which is shown as red and pale pink surface diagrams, respectively (PDB: 5X6O). **b)** Surface representation of RPA-DNA complex showing position of Serine 178 (red sphere) located in between PID^{70N} (pale pink) and DBD-A (hot pink). DBDs A (hot pink), B (orange), C (yellow) are connected by flexible linkers shown in dashed black lines. DBD-D (green) has an N-terminal phosphorylation domain (dashed red line) and is connected via flexible linker (black dashed line) to C-terminus protein interaction domain (PID^{32C}). A representative structure of ssDNA flanked by duplex DNA is shown in light orange.

In this chapter, we utilized mutagenesis, fluorescent enhancement using non-canonical amino acids (FencAA), and ensemble FRET to investigate how phosphorylation of S178 affected RPA-DBD dynamics and assembly. To investigate the effects of phsophorylation, we generated a phosphomimic RPA, where, serine at position 178 was mutated to aspartate (RPA-S178D) (Fig 6-1 b).

Our results show unique conformational changes in RPA-S178D-DNA engagement with assembly of multiple RPA-S178D on longer DNA exhibiting cooperative binding. The RPA-S178D nucleoprotein filament is comparatively resistant to displacement by Srs2 helicase but is sensitive to the activity of S1 endonuclease.

6.2 Materials and Methods

6.2.1 Plasmids for protein purification

6.2.1.1 4AZP incorporating plasmids

His- tag carrying RPA-A^{4AZP} and RPA-D^{4AZP} (chapter 3, section 3.2.3) were used as templates to generate the RPA-phosphomimic constructs: RPA-S178D- DBD-A^{4AZP} (RPA-S178D-A^{4AZP}) and RPA-S178D-DBD-D ^{4AZP}(RPA-S178D-D^{4AZP})

6.2.1.2 Non 4AZP incorporating plasmids

Sc. RPA70-RPA32-his-RPA14 was used as a template to generate *Sc.* RPA-S178D. For all the experiments, purified *Sc.* RPA70-RPA32-his-RPA14 was used as RPA-wt control.

6.2.2 Purification of 4AZP carrying RPA variants

The RPA-S178D-A^{4AZP} or RPA-S178D-D^{4AZP} were co-transformed with pDule2-pCNF plasmid in Rossetta-2 PlysS cells and were purified as described in section 3.2.4 of chapter 3.

6.2.3 Labeling proteins with fluorophores

RPA DBD-A or DBD-D variants carrying 4AZP were labeled with MB543, Cy3 or Cy5 as described. Approximately, 3 ml of (10 μM) RPA^{4AZP} was incubated on a rocker with 1.5-fold molar excess (15 μM) of either DBCO-MB543, DBCO-Cy3 or DBCO-Cy5 for 2 hours at 4 ^{o}C. Labeled RPA variants were separated from excess dye using a Biogel-P4 gel filtration column (65 ml bed volume) using storage buffer (30 mM HEPES, pH 7.8, 100 mM KCl, 0.1mM EDTA, pH 8.0 and 10% (v/v) glycerol). Fractions containing labeled RPA were pooled, concentrated using a 30 kDa cut-off spin concentrator and flash frozen using liquid nitrogen. Fluorescent RPA were stored at -80 ^{o}C. Labeling efficiency was calculated using absorption values measured at 280 nm and ε_{280}= 98500 $M^{-1}cm^{-1}$for RPA, at 543 nm with ε_{543}= 105,000 $M^{-1}cm^{-1}$ for DBCO-MB543, ε_{555}= 150,000 $M^{-1}cm^{-1}$ for DBCO-Cy3 and at 650 nm with ε_{650}= 250,000 $M^{-1}cm^{-1}$ for DBCO-Cy5 fluorophores. A correction factor was applied to the final concentration protein as described in the methods section of chapter 2.

6.2.4 Purification of non-4AZP carrying variants

Individual plasmids (*Sc.* RPA70-RPA32-his-RPA14 or *Sc.* RPA-S178D were transformed in Rossetta-2 PlysS cells, plated in LB agar$^{ampicillin\ R}$ plates and incubated overnight at 37^{o}C. At around 6 pm, individual 2.8l baffle flask (4 flasks in total), each containing autoclaved 1l LB medium supplemented with 100μg/ml ampicillin, was inoculated with a single transformed colony and incubated overnight at 37^{o}C, without agitation. Next morning, measurements for OD_{600} were collected, and the flasks were shaken at 250 rpm, at 37^{o}C. At OD_{600}: 0.5-0.8, cells were induced with 0.4mM IPTG and grown for an additional 3 hours at 37^{o}C, 250rpm. Cells were harvested, and purification was done following the same steps as for 4AZP carrying variants mentioned in section 3.2.4 of chapter 3, with the following modifications. All the buffers (cell resuspension buffer, H^{0}, H^{50}, H^{100}, H^{1000}, H^{1500}) were supplemented with 1mM tecep-HCl and RPA storage buffer was supplemented with 2mM tecep-HCl.

Sc. Srs2 was purified as described previously (Antony et. al., 2009a).

6.2.5 Fluorimeter measurements

Tryptophan quenching experiments were performed using a PTI QM40 instrument (Horiba Scientific, Edison, NJ). To determine the emission maxima, a 2ml reaction with 50nM RPA^{-wt} or RPA-S178D in reaction buffer (30 mM Hepes, pH 7.8, 100 mM KCl, 5 mM $MgCl_2$, 1 mM β-mercaptoethanol and 6 % v/v glycerol) was excited at 290 nm and emission spectra (310nm-350nm) recorded. Following determination of emission maximum, increasing concentration of $(dT)_{35}$ oligonucleotide was added to the

2ml reaction, excited at 290nm and emission recorded for 10 seconds at $\lambda_{emi\ (max)}$. Fluorescence measurements were normalized, plotted against [$(dT)_{35}$] and fit using single- step binding isotherm to determine the K_d values. All experiments were performed at 25 °C.

6.2.6 Stopped-flow analysis

All stopped-flow measurements were carried out with an Applied Photophysics SX20 instrument (Surrey, UK) at 25ºC. Reactions were performed in buffer (30 mM Hepes, pH 7.8, 100 mM KCl, 5 mM $MgCl_2$, 1 mM β-mercaptoethanol and 6 % v/v glycerol). It is important to note that the concentrations of reactants are reduced to half upon mixing in the stopped-flow instrument. Thus, all the concentrations mentioned below are post-mixing concentrations.

6.2.6.1 Tryptophan quenching experiments

To determine the rate of association of S178D, 100nM RPA variants (*Sc.* RPA70-RPA32-his-RPA14 or *Sc.* RPA-S178D-D^{4AZP}) in one syringe were rapidly mixed with increasing concentrations (25, 50, 75, 100, 150, 200nM) of $(dT)_{35}$ in another syringe. Optical parameters of λ_{exci}: 290nm and long pass cut-off emission filter with λ_{emi}: 350nm were used to monitor change in tryptophan fluorescence. In total 10000 data points were collected over a period of 2.25 seconds (5000 data points for first 250 milliseconds+ 5000 data points for rest 2 seconds). Raw traces obtained were fit in KaleidaGraph using the equation:

$$\Delta F = A_1 (1 - e^{-k_1 t}) + k_2 t \qquad \text{(Eq. 1)}$$

Where, ΔF is change in tryptophan fluorescence, A_1 and k_1 are the amplitude and observed rate of the exponential phase, k_2 is the steady state rate and t is time.

The values for $k_{obs,1}$ and $k_{obs,2}$ were plotted against the concentration of $(dT)_{35}$. A linear fit equation:

$$y = mx + c \qquad \text{(Eq.3)}$$

Where 'm', the slope represents the observed association constant (K_a) and 'c', the constant represents the rate of dissociation (k_{off}) was used to determine RPA-DBD-DNA binding characteristics. Observed dissociation constant (K_d) values were calculated using reciprocal of K_a i.e. $K_{d=} 1 \div K_a$.

6.2.6.2 ssDNA binding kinetics of RPA-S178D-DBDs

The rate of association of DBD-A and DBD were measured using RPA- S178D-A^{MB543} and RPA-S178D-D^{MB543}, respectively. 50nM RPA-S178D-A^{MB543} or RPA-S178D-D^{MB543} was rapidly mixed with increasing concentrations (10, 20, 50, 75, 100nM) of $(dT)_{35}$ oligonucleotide and increase in fluorescence signal monitored by exciting the sample at $\underline{\lambda}_{exci}$: 535nm and measuring emission using a long pass cut-off filter at λ_{emi}: 555nm. In total 10000 data points were collected over a period of 2.25 seconds (5000 data points for first 250 milliseconds+ 5000 data points for rest 2 seconds). Raw traces obtained for DBD-A binding were fit using equation:

$$\Delta F = A_1(1 - e^{-k_1 t}) + A_2(1 - e^{-k_2 t}) + k_3 t \qquad \text{(Eq. 2)}$$

Where, ΔF is change in fluorescence of A^{MB543}, A_1 and k_1 are the amplitude and observed rate of the first exponential phase, A_2 and k_2 are the amplitude and observed rate of the second exponential phase, k_3 is the steady state rate and t is time.

The raw data traces obtained for DBD-D binding were fit using Eq.1. The rates obtained for first exponential phase ($k_{obs,1}$), second exponential phase ($k_{obs,2}$) and steady state were plotted against $(dT)_{35}$ concentrations. Note: For DBD-D, $k_{obs,2}$ values represent steady state as there is no second exponential phase.

6.2.6.3 FRET analysis to monitor the binding of two RPA molecules

All samples were excited at 555nm and FRET was monitored with a 645nm cut-off emission filter. For FRET experiments with increasing lengths of oligonucleotides $(dT)_n$, where (n= 20, 35, 45, 60, 70, 79, 97, 140), 40nM RPA-A^{cy3}or RPA-S178D-A^{cy3} paired with 40nM RPA-D^{cy5} or RPA-S178D-D^{cy5} was rapidly mixed with 40nM (dT)n and FRET monitored. Resulting FRET was analyzed using Eq. 2 for all the oligonucleotides, except $(dT)_{140}$, which was analyzed using Eq.1 to obtain the observed rates.

6.2.6.4 Facilitated Exchange

Facilitated exchange experiments were performed with 150nM RPA-S178D-D^{MB543} bound to 50nM $(dT)_{60}$ or 100nM RPA-S178D-A^{MB543}/ RPA-S178D-D^{MB543} bound to 30nM $(dT)_{97}$ and challenged with increasing concentrations of RPA-wt. Samples were excited at λ_{exci}: 535nm and change in signal monitored with a λ_{emi}:555nm cut-off

emission filter. In total 10000 data points were collected over a period of 2.25 seconds (5000 data points for first 250 milliseconds+ 5000 data points for rest 2 seconds). Data obtained for RPA-S178D-D^{MB543} facilitated exchange was analyzed using Eq.1 and for RPA-S178D-A^{MB543} was analyzed using Eq.2. The k_{obs} values obtained were plotted against RPA-wt concentrations and fit using Eq.3.

6.2.7 Limited proteolysis

5μg of RPA-wt or RPA-S178D were treated with 50ng of trypsin or chymotrypsin (1:100 dilution) in 20μl reaction mixture containing 30mM Hepes, pH 7.8, 1mM EDTA, pH 8.0, 8mM Tecep-HCl; 60mM $MgCl_2$ with or without equal concentrations of $(dT)_{35}$ oligonucleotide. All the reactions were carried out at 30^{o}C. Unless specified, after 1 hour of incubation, the reactions were terminated by adding equal volume of 2X SDS-loading dye and boiling for 15 minutes. 35μl of the total sample (reaction mixture+ dye) was loaded on a 12% SDS-PAGE gel and the proteolyzed products separated by electrophoresis. The gel was stained with Coomassie brilliant blue followed by de-stain treatment to remove excess Coomassie blue stain. The resulting bands were compared with protein ladder as a reference.

6.2.8 Single-molecule TIRFM experiments

Single molecule TIRFM experiments to monitor DBD dynamics of RPA-S178D-DBD-A^{MB543} and RPA-S178D-DBD-D^{MB543} was performed as described in section 3.2.16 of chapter 3 and (Nilisha Pokhrel et. al., 2019). Single-molecule TIRFM experiments

were performed by Colleen Caldwell in the lab of Dr. Maria Spies, University of Iowa, IA.

6.3 Results

6.3.1 Mutations in the linker region connecting PID^{70N} and zinc finger alters the DNA bound conformation of RPA

Steady-state state tryptophan quenching experiments have been used to determine the affinity of protein-substrate interactions (Beattie & Merrill, 1999; Kozlov, Galletto, & Lohman, 2012; "Protein Fluorescence," 2006; Tworzydło, Polit, Mikołajczak, & Wasylewski, 2005). Each DBD of RPA consists of at least one tryptophan whose fluorescence is quenched upon engagement with DNA. Since the change in tryptophan fluorescence is intrinsic to RPA, it provides with a robust platform to monitor DBD-ssDNA engagement and determine binding affinity for RPA-DNA interactions (Kumaran et. al., 2006). In addition to providing kinetic information, tryptophan quenching can be used as an initial method of monitoring summation of global conformations that could be present during RPA-DBD-DNA engagement. Therefore, we performed steady-state tryptophan quenching experiments with fixed concentrations of RPA-S178D and titrated increasing concentrations of either $(dT)_{35}$ or $(dT)_{97}$ oligonucleotides. A robust increase in tryptophan quenching was observed with increasing concentrations of oligonucleotides of both lengths, until saturation. Surprisingly, net amplitude of tryptophan quenching upon DNA engagement for RPA-S178D was half of RPA-wt, although, binding stoichiometry of RPA: DNA was maintained at 1:1 (Fig 6-2 a, b). 50nM RPA-S178D or RPA-wt displayed 1:1 binding at 50nM $(dT)_{35}$ (Fig 6-2 a) and 100nM RPA-S178D or RPA-wt

binding was saturated at 18nM $(dT)_{97}$ (Fig 6-2 b). Under our experimental conditions, RPA requires 22-nt to stably engage all the DBDs, such that $(dT)_{35}$ would enable stable binding of one RPA and $(dT)_{97}$ would provide binding site for at least four RPA. Taken together, similar DNA binding stoichiometry of RPA-wt and RPA-S178D in both lengths of DNA suggests that bind to DNA with similar affinity. However, the 'half tryptophan quenching' in RPA-S178D DNA engagement would suggest that the conformations adopted by DBDs in mutational background is different than RPA-wt. Perhaps, the DBDs are more restricted in their conformational freedom which would inhibit exposure of tryptophan to polar environment as the DBDs engage with DNA resulting in less quenching of tryptophan signal. Another possibility is that only half of the total number of DBDs engage the ssDNA for RPA-S178D.

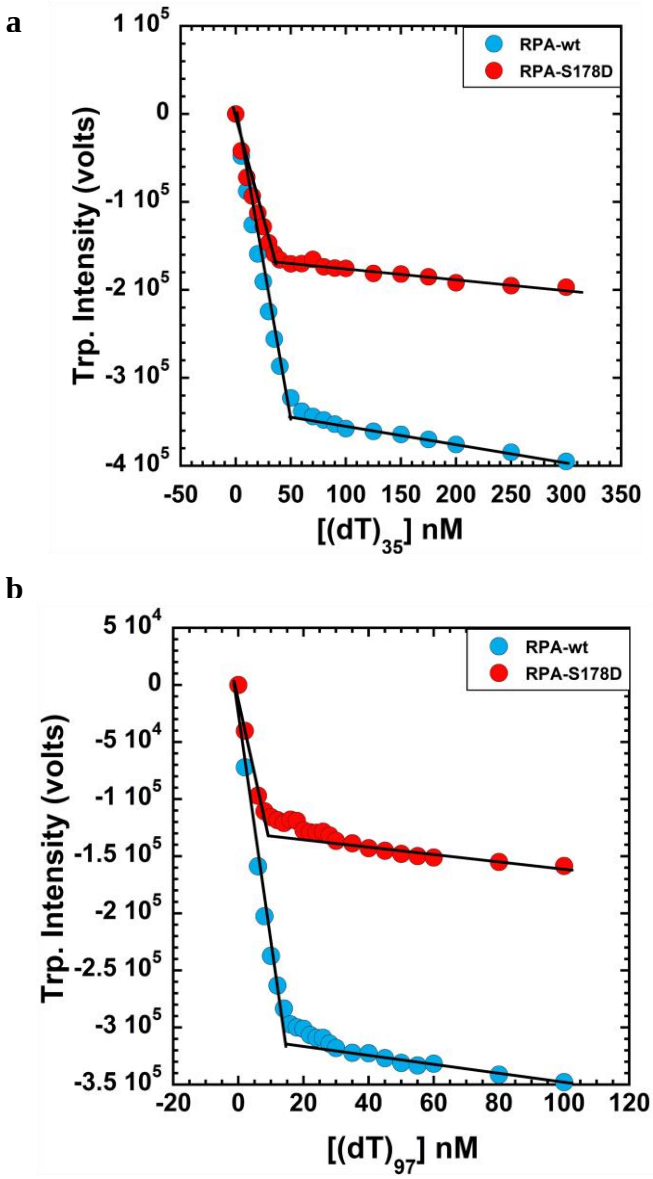

Figure 6-2: Steady-state tryptophan quenching experiments to determine binding affinity. Comparative tryptophan quenching experiments performed with **a)** 50nM RPA-wt or RPA-S178D in presence of $(dT)_{35}$ or **b)** 100nM RPA-wt or RPA-S178D in presence of $(dT)_{97}$ show both the variants have 1:1 binding to oligonucleotides, yet, the net amplitude of tryptophan quenching for RPA-S178D is half that of RPA-wt.

To better understand the 50% loss in fluorescence we performed stopped-flow measurements by rapidly mixing 100nM RPA-S178D with increasing concentrations of $(dT)_{35}$ and compared the observed rates (k_{obs}) with RPA-wt. Our results show that at 25nM $(dT)_{35}$ both RPA-S178D and RPA-wt bind to ssDNA with similar rate (k_{obs1}= 36.8 ± 20.5 s^{-1} for RPA-S178D and $k_{obs,1}$= 37 ± 2 for RPA-wt) (Fig. 6-3 a, c). Furthermore, both the variants had similar overall k_{on} and k_{off} for binding to ssDNA (RPA-S178D: k_{on}= 4.7± 0.2 $M^{-1}s^{-1}$, k_{off} = 23±7s^{-1}; RPA-wt: k_{on}= 5.2± 0.3 x $M^{-1}s^{-1}$, k_{off} = 23 ± 7s^{-1}) generating similar K_d values (K_d for RPA-wt: 17.3 ± 4 nM; K_d for RPA-S178D: 38.5 ± 12.8 nM) (Fig. 6-3 c). Yet, the 'half-tryptophan quenching' was observed for RPA-S178D even during pre-steady state experiments (Fig. 6-3 a, b).

Finally, we performed limited proteolysis of RPA-S178D in presence and absence of equimolar concentrations of $(dT)_{35}$ to validate the difference in conformational arrangement between RPA-wt and RPA-S178D. If both the variants have similar domain arrangement on DNA, the patterning and size of the bands upon SDS-PAGE analysis would be similar. As excepted, RPA-wt was more resistant to proteolytic cleavage by both trypsin and chymotrypsin in the presence of ssDNA (Fig. 6-4 a, c). Although, in absence of DNA, peptide fragments generated by chymotrypsin digestion of RPA-S178D were similar to RPA-wt (Fig. 6-4 c, d, -DNA lanes), they both showed different peptide fragments in presence of DNA (Fig. 6-4, c, d, +DNA lane). Furthermore, peptides fragments generated by trypsin treatment of RPA-wt and RPA-S178D were distinct from each other both in presence and absence of DNA (Fig 6-4 a, b). Taken together, these experiments confirm that RPA-S178D maintains the same rate and affinity for binding to DNA as RPA-wt and the 'half- tryptophan quenching' observed in RPA-S178D stems

from change in conformational arrangement of one or several DBDs within a single RPA or between multiple RPAs on DNA and is not due to change in ability of RPA-S178D to engage on ssDNA.

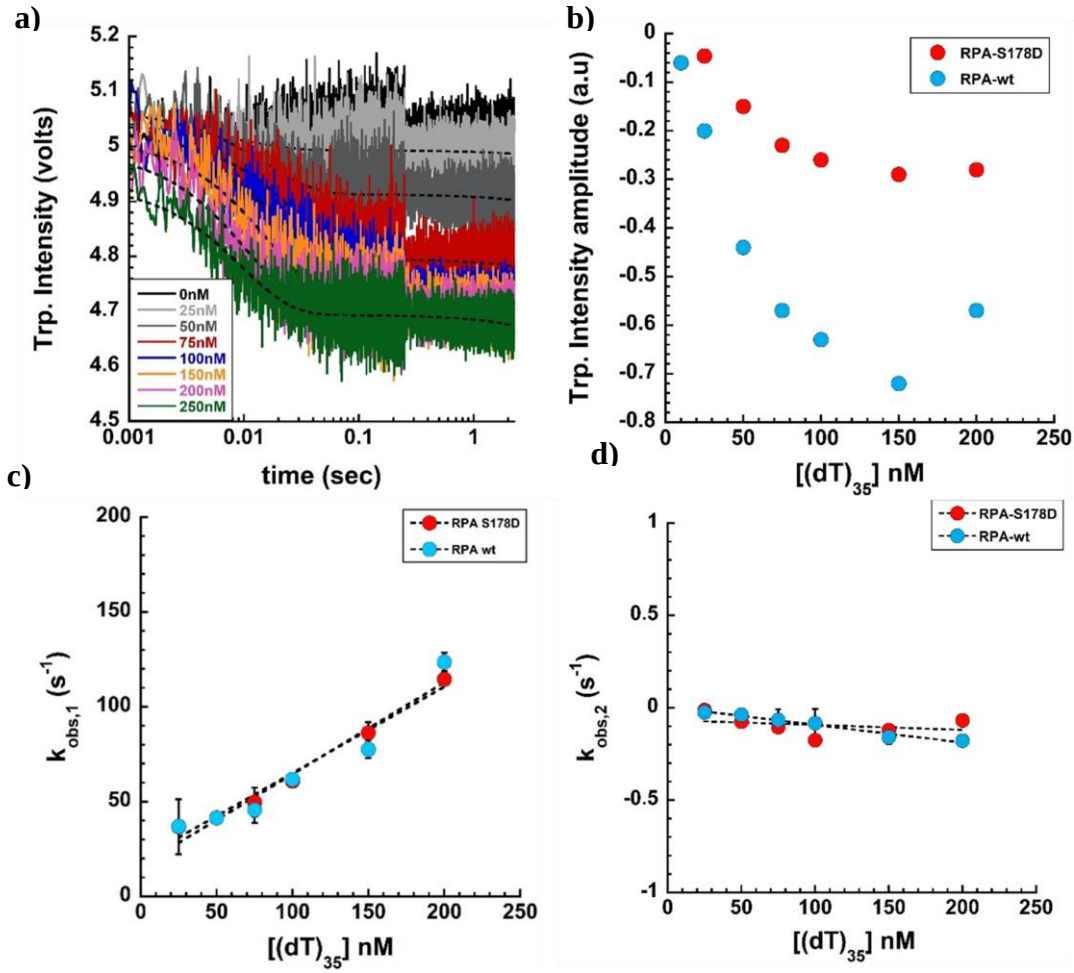

Figure 6-3: Pre-steady state binding kinetics of RPA-S178D. Stopped-flow instrument was used to rapidly mix increasing concentrations of $(dT)_{35}$ with 100nM RPA-S178D. **a)** Representative raw traces of the tryptophan quenching experiments. **b)** Plot of net amplitude of tryptophan quenching for RPA-wt and RPA-S178D plotted against $(dT)_{35}$ concentrations. Fitting of raw traces in **a)** as described in the *methods* result in **c)** plot of $k_{obs,1}$ **d)** $k_{obs,2}$ as a function of increasing concentrations of $(dT)_{35}$ where the $k_{obs,1}$ and k_{obs2} values are fit using a linear equation to obtain k_{on} and k_{off} parameters.

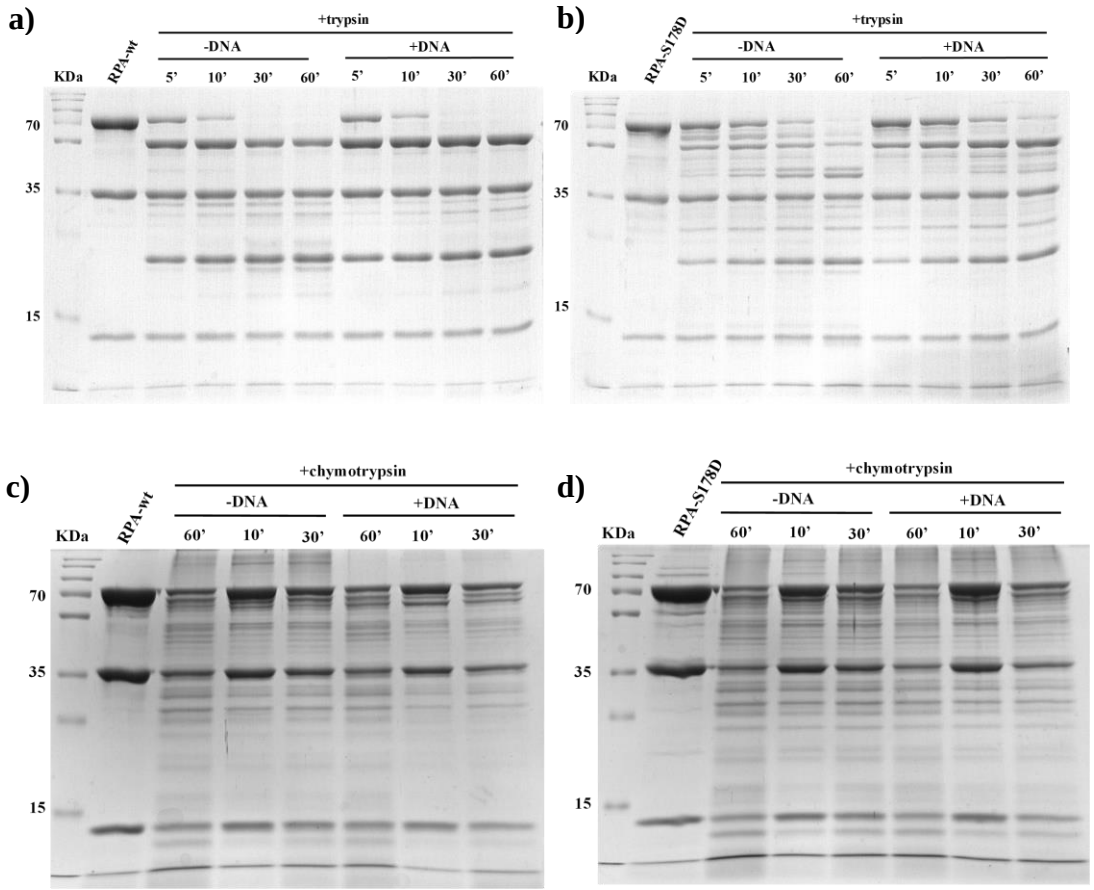

Figure 6-4: Time based limited- proteolysis analysis of RPA-wt and RPA-S178D. RPA-wt or RPA-S178D were digested with trypsin and chymotrypsin in presence or absence of DNA for specified time-periods and resulting peptides analyzed on 12% SDS-PAGE gel. Time-based tryptic digestion of **a)** RPA- wt **b)** RPA-S178D. Presence of more peptide bands for RPA-S178D both in presence and absence of DNA suggests that it is more sensitive to tryptic digestion than RPA-wt, probably due to difference site accessibility. Similar experiment with chymotrypsin digestion of **c)** RPA-wt **d)** RPA-S178D show slightly higher degree of degradation for RPA-S178D both in presence and absence of DNA.

6.3.2 RPA-S178D has altered DBD dynamics

The four DBDs in RPA bind in tandem to enable high affinity RPA-DNA association. Since RPA-S178D had 'half- tryptophan' quenching which suggested engagement of some but not all DBDs, next we wanted to investigate the binding dynamics of DBD-A and DBD-D in RPA-S178D. Our studies with RPA-wt DBD-A and DBD-D have shown that DBD-A binds rapidly to ssDNA but can be remodeled by its own trimerization core under sub-stoichiometric concentrations of ssDNA or shorter lengths of ssDNA (Pokhrel et. al., 2019). Using same strategy of incorporating ncAAs followed by click- chemistry based fluorescent labeling, we generated fluorescently labeled phosphomimic RPA-S178D-A^{MB543} and RPA-S178D-D^{MB543} with fluorophores incorporated at DBD-A and DBD-D respectively. Stopped-flow experiments performed with increasing concentrations of $(dT)_{35}$ and RPA-S178D-A^{MB543} showed a robust increase in fluorescence signal upon binding to ssDNA (Fig. 6-5 a). For RPA-S178D, DBD-A had DNA binding dynamics similar to RPA-wt with rapid initial engagement followed by remodeling phase. Data obtained for DBD-A engagement followed the two-step binding model, where the rates for first- step ($k_{obs,1}$, engagement phase) increased linearly with increase in $(dT)_{35}$ oligonucleotide concentrations (Fig. 6-5 b) and the rates for second-step ($k_{obs,2}$, rearrangement phase) showed a subsequent decrease under sub-stoichiometric concentrations of $(dT)_{35}$, followed by increase after 50nM $(dT)_{35}$ (Fig. 6-5 c). The k_{on} values obtained from linear fit of $k_{obs,1}$ was $1.4 \times 10^8\ M^{-1}s^{-1}$ for RPA-S178D-A^{MB543} which is similar to RPA-A^{MB543} with k_{on} of $1.1 \pm 0.6 \times 10^8\ M^{-1}s^{-1}$.

Interestingly, similar experiments performed with RPA-S178D-D^{MB543} showed differential binding dynamics for DBD-D (Fig 6-6 a, b). Consistent with RPA-D^{MB543},

RPA-S178D-DBD-D engagement to ssDNA could be best described with a one-step binding model, where, $k_{obs,1}$ increased linearly with increasing concentrations of $(dT)_{35}$ (Fig 6-6 b) with a k_{on} of 1.15 x 10^8 $M^{-1}s^{-1}$ .However, at higher concentrations of $(dT)_{35}$ RPA-S178D-DBD-D showed a decrease in fluorescence signal immediately after the initial increase, suggesting a remodeling step (Fig. 6-6 a, blue and red traces). This remodeling of DBD-D is not observed with RPA-wt-DBD-D and depicts a novel phosphorylation induced change in DBD-dynamics of RPA.

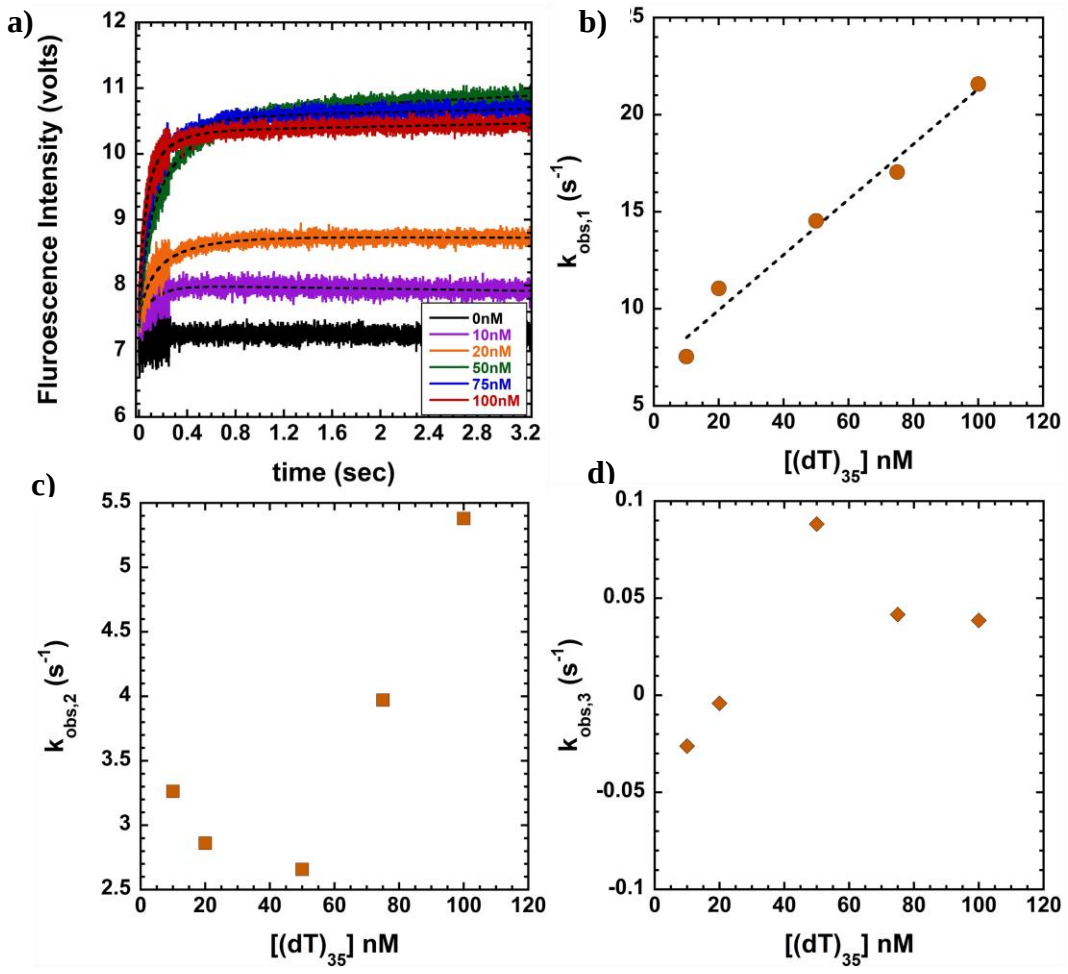

Figue 6-5: Monitoring DBD-A binding dynamics of RPA-S178D. Stopped-flow experiments were performed by rapidly mixing 50nM RPA-S178D-A^{MB543} with increasing concentrations of $(dT)_{35}$ with excitation at 535nm and robust change in MB543 fluorescence monitored using a 555nm long pass emission filter. **a)** Representative traces showing change in RPA-S178D-A^{MB543} with increasing concentrations of $(dT)_{35}$. Individual traces were fit with double exponential + linear phase equation to obtain **b)** plot of $k_{obs,1}$ (initial binding) **c)** $k_{obs,2}$ (rearrangement) **d)** $k_{obs,3}$ linear phase along increasing concentrations of $(dT)_{35}$ plotted along X-axis.

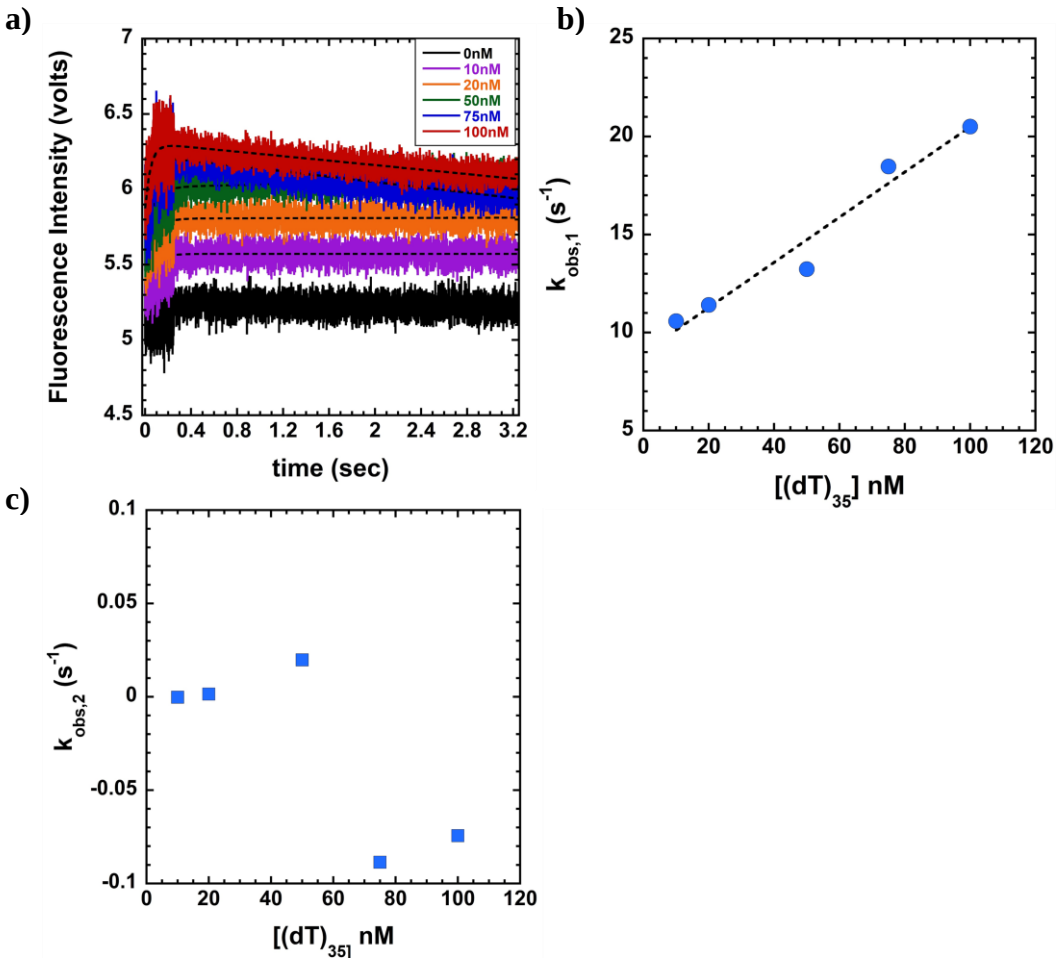

Figure 6-6: Monitoring DBD-D binding dynamics of RPA-S178D. Stopped-flow experiments were performed by rapidly mixing 50nM RPA-S178D-D^{MB543} with increasing concentrations of (dT)35. Samples were excited at 535nm and robust change in MB543 fluorescence was monitored using a 555nm long pass emission filter. **a)** Representative traces showing change in RPA-S178D-D^{MB543} with increasing concentrations of $(dT)_{35}$. Individual traces were fit with single exponential + linear phase equation to **b)** plot of $k_{obs,1}$ values and **c)** $k_{obs,2}$ plotted on Y-axis along increasing concentrations of $(dT)_{35}$ plotted along X-axis.

6.3.3 S178D selectively alters the DNA binding states of DBD-A

Our studies investigating the micro-dissociation states RPA revealed four distinct states of binding for DBD-A and DBD-D on DNA. These four states could be four distinct DBD driven conformations, as FAB, which has two DBDs showed two distinct states of binding on DNA (Pokhrel et. al., 2019). To probe if S178D had effects on the DNA binding states of RPA, we performed single- molecule TIRF analysis with RPA-S178D with fluorophore at DBD-A or DBD-D. Following fitting the traces from smTIRF- microscopy with appropriate FRET equations, data analysis showed loss of distinct states of binding for DBD-A whereas the DNA binding states of DBD-D remain unchanged (Fig. 6-7, 6-8). This is particularly interesting as the stopped-flow bulk fluorescence showed remodeling for DBD-D but not for DBD-A (Fig. 6-5 a, 6-6 a, compare red traces) which is in contradiction to smFRET results. It is possible that during S178D mutation, DBD-A is able to bind to DNA and maintain a slightly higher stable interaction than RPA-wt. As a result, DBD-A in RPA-S178D is unable to transition back and forth between the binding and unbinding state, or there is change in rotational freedom of DBD-A (microdomain dynamics) which is visible only at the single-molecule resolution. Using stopped flow to monitor the composite signal of all the binding events at a timescale of 3.25 seconds shows rate of DBD-A and DBD-D binding is unaffected, but there are changes in DBD-D binding to DNA in S178D mutation. However, smTIRF provides information once DBD-A and DBD-D are engaged on DNA and the data obtained is over a period of 60 seconds (steady- state). At this time period, the stopped-flow reactions would have already reached the steady-state. Further investigations have to be conducted to understand the mechanism underlying change in pre-steady state of

DBD-D dynamics in RPA-S178D yet changes in the steady state of DBD-A dynamics under conditions of excess ssDNA or binding sites.

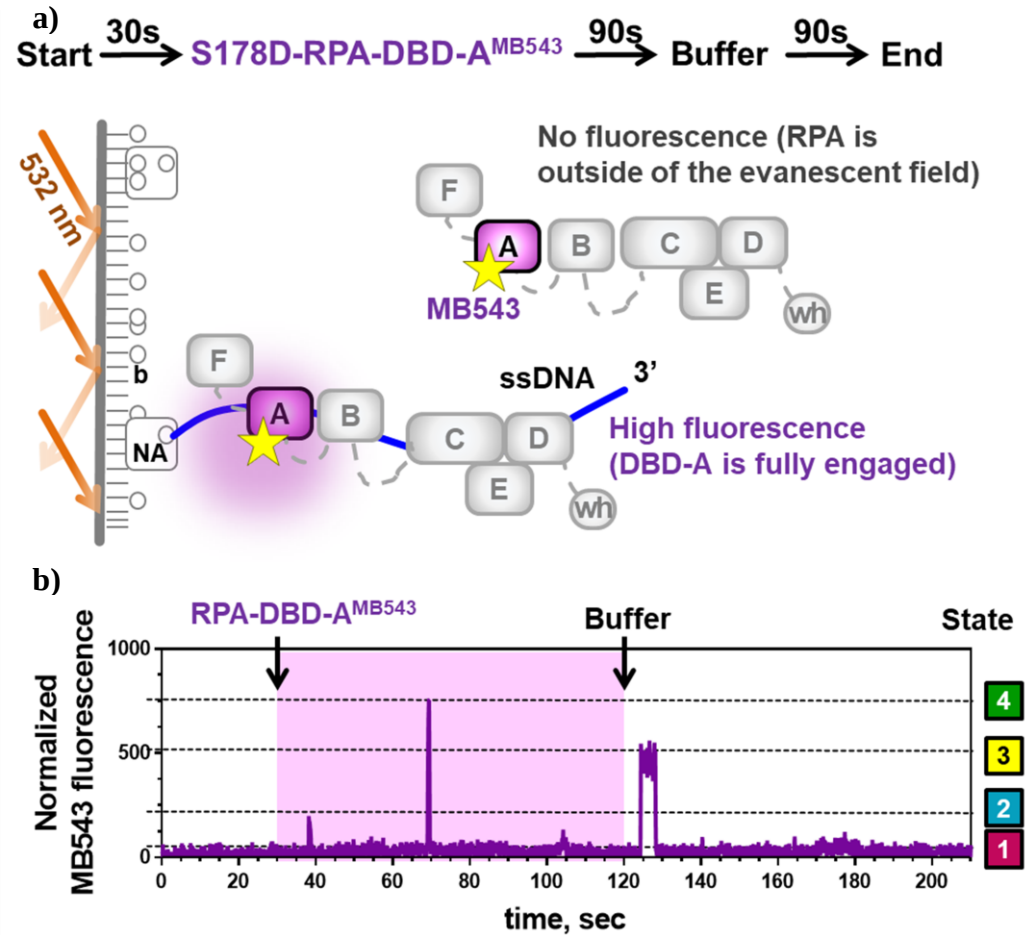

Data for figures 6-7 and 6-8 collected and analyzed by Colleen Caldwell and Maria Spies, University of Iowa, IA.

Figure 6-7: Single-molecule analysis to quantify the conformational dynamics of RPA-S178D-DBD-A. a) Experimental scheme for visualizing conformational dynamics of DBD-A. Binding of 100 pM RPA-S178D-A^{MB543} to ssDNA (blue line) tethered to the surface of the TIRFM flow cell (grey line) brings the MB543 fluorophore within the evanescent field and its excitation. NA – neutravidin, b – biotin. **b)** Representative fluorescence trajectory depicting conformational dynamics of individual RPA-S178D molecules labeled within DBD-A. Purple lines represent normalized fluorescence. Unlike RPA-wt-A^{MB543}, the four states for DBD-A engagement is not observable. The shaded area on graph represents the time where free RPA was present in the flow cell.

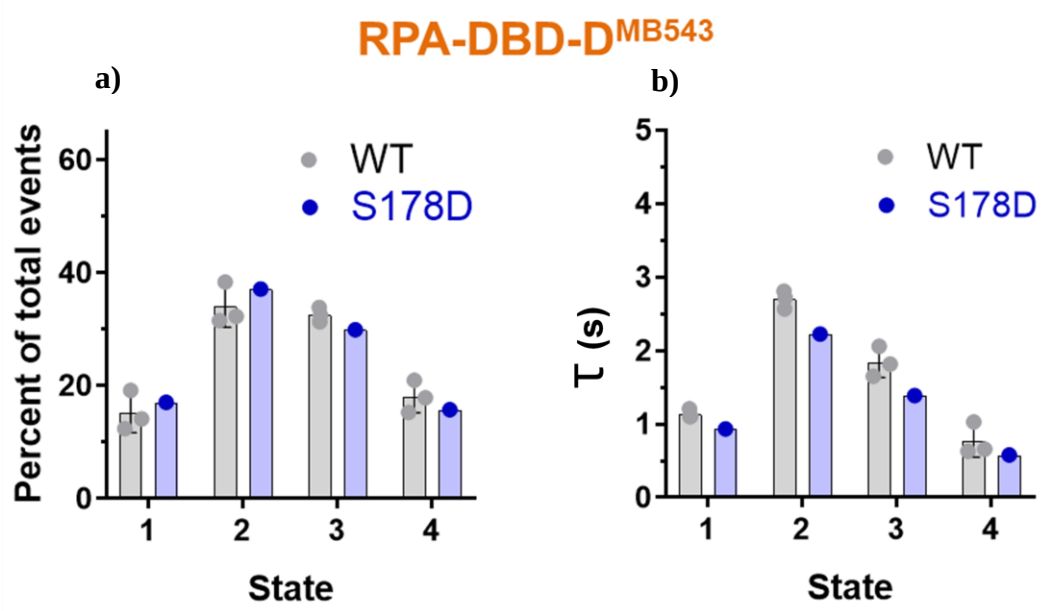

Figure 6-8: Quantification of ebFRET trajectories for RPA-S178D-D^{MB543} ssDNA binding. The trajectories from 120 -210 sec were taken for fitting. Comparison of the **a)** fractional visitation to each state available to RPA-DBD-D^{MB543} (grey) and RPA-S178D-D^{MB543}(blue). **b)** the stability of each state available to RPA-DBD-D^{MB543} (grey) and RPA-S178D-D^{MB543}(blue). The numbers on Y axis represent the four- states of binding of DBD-D.

6.3.4 S178D increases the cooperative assembly of RPA on ssDNA

Experiments performed with fluorescently labeled 100nM RPA-S178D with increasing concentrations of $(dT)_{35}$ enable monitoring binding of one RPA to an available DNA substrate and deduce the kinetics and dynamics of DBD-A and DBD-D binding. Under our experimental conditions, ssDNA of at least 20 ± 2nt is required to engage all the DBDs and experiments performed with a fixed concentration of fluorescent protein and increasing concentrations of $(dT)_{35}$ do not provide information concerning how multiple RPAs can assemble on ssDNA. To understand if S178D mutation affected the assembly of multiple RPA on DNA, we performed RPA-S178D-FRET with increasing lengths of ssDNA $(dT)_n$ (where n= 20 to 140 nucleotides) and compared it RPA-wt-FRET (Fig 6-9 a-d, 6-10 a-d). FRET experiments were performed with DBD-A^{cy3} as donor and DBD-D^{cy5} as acceptor. RPA binds with a polarity of 5′-3′ with DBD-A residing close to 5′ and DBD-D residing close to 3′ end of DNA. Stopped-flow experiments performed with RPA-A^{cy3} and RPA-D^{cy5} produces FRET only when DBD-A is adjacent to DBD-D. Bulk FRET analysis performed with fixed concentration (40nM) of wt or S178D A^{cy3} and D^{cy5} and 40nM ssDNA of increasing lengths showed observable FRET for $(dT)_n \geq$45-nt which is enough ssDNA space for two RPAs to stably bind (Fig. 6-9 a, 6-10 a). There was no observable FRET for $(dT)_{20}$ and $(dT)_{35}$ which allows stable engagement of only one RPA (Fig. 6-9 a, 6-10 a). Raw traces for increase in Cy5 fluorescence was fit using a two-step kinetic model where, the first step ($k_{obs,1}$) reflects a rate of association between RPA ssDNA and/or RPA heterotrimers and the second step ($k_{obs,2}$) reflects the arrangements/ movement of DBDs on ssDNA as both the RPAs attempt to undergo stable DNA interactions. The resulting $k_{obs,1}$ and $k_{obs,2}$ values for

S178D increased with increasing the length of ssDNA following a cooperative binding behavior as seen by the sigmoidal shape of the graph (Fig. 6-10 a, b), whereas, the $k_{obs,1}$ and $k_{obs,2}$ values for RPA-wt remained unchanged independent of the length of oligonucleotide (Fig. 6-9 a, b). This result suggests that formation of RPA-RPA complexes is promoted for RPAS178D. MST analysis to measure binding affinity between isolated DBD-A and RPA14 (OB-E) showed both the domains interacted with an affinity of ~100μM for RPA-wt which was increased to three-fold for S178D (~30μM) (Yates et. al., 2018). Similar binding experiments performed with full length protein and $(dT)_{100}$ showed S178D bound to $(dT)_{100}$ with one-fourth of the affinity of RPA-wt (~20nM for RPA-wt and ~80nM for RPA-S178D), yet, with increased cooperativity i.e Hill coefficient of ~1 for RPa-wt and ~2 for RPA-S178D (Yates et. al., 2018).

The FRET intensity signatures enable deeper understating regarding the positioning of the DBDs on ssDNA. Under excess condition of RPA-wt and shorter oligonucleotides like $(dT)_{45}$ there is not enough binding sites for all DBDs of two RPAs, leading to rapid increase in signal followed by a decrease to a lower FRET state, suggesting remodeling (Low FRET) (Fig. 6-9 a, light blue and light green trace; 6-11 light blue trace). However, similar experiments with RPA-S178D show a monophasic increase in FRET signal that is stable with loss of the remodeling phase, potentially due to enhanced interaction with RPA14 (Fig. 6-10 a, light blue trace). Increasing the length of ssDNA to $(dT)_{79}$ still displayed the engagement step with increase in FRET amplitude for both wt and S178D (Medium FRET) with slight remodeling step for RPA-wt only (Fig. 6-9 a and 6-10 a, orange trace, 6-11 yellow trace). Finally, additional experiments

with $(dT)_{140}$ showed a single-step binding with maximum FRET amplitude for RPA-wt but FRET amplitude still stayed at medium for S178D (Fig. 6-11, compare orange trace and navy-blue trace). Although there is enough binding space for all the DBDs to bind, diffuse and still maintain stable engagement, the medium FRET signal observed for S178D is potentially due to its inflexibility or inability to diffuse along ssDNA.

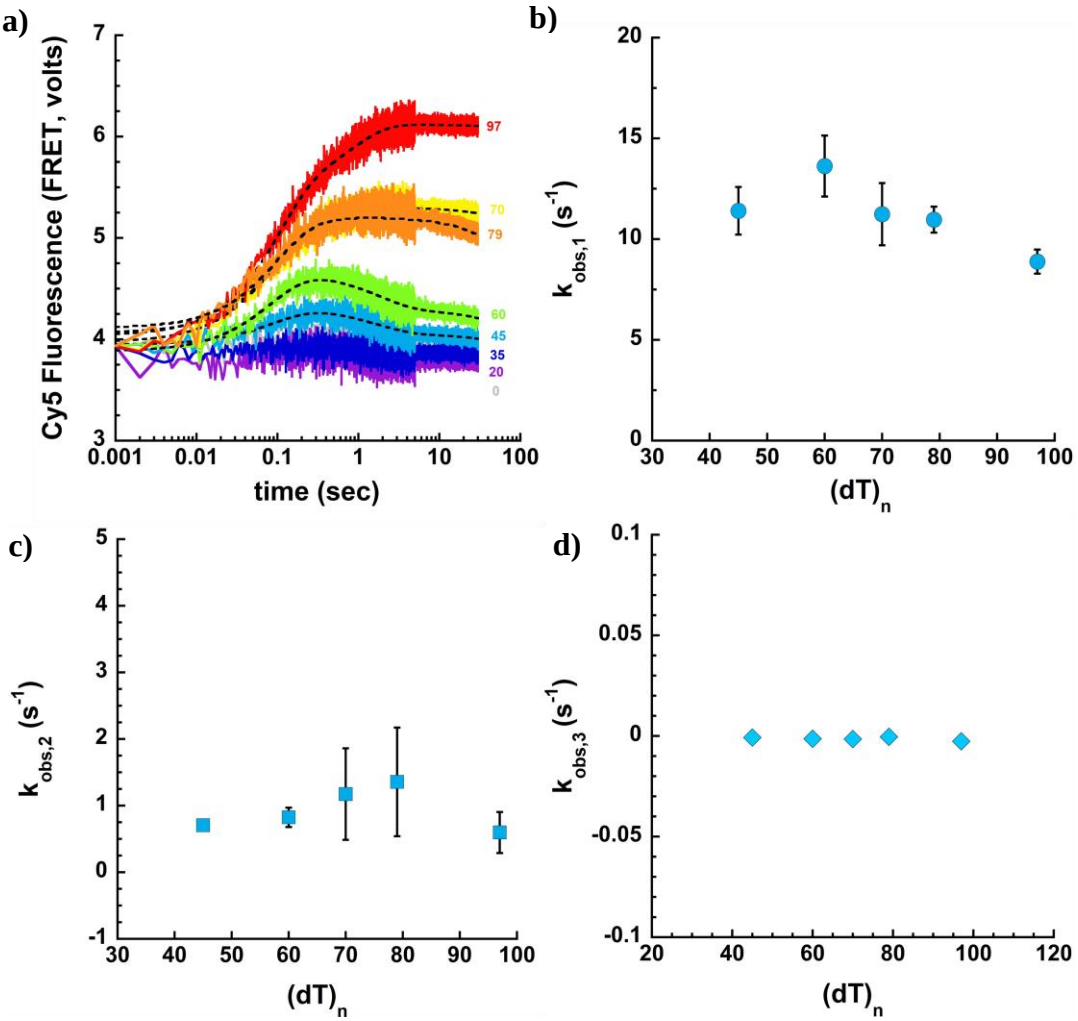

Figure 6-9: FRET experiment to monitor assembly of multiple RPA with increasing lengths of ssDNA. a) Representative traces of stopped-flow FRET experiments performed with RPA-wt-A^{cy3} and RPA-wt-$D^{cy5}$to monitor assembly of multiple RPA. The data was fit using a two- step model to obtain **b)** rate of association ($k_{obs,1}$) **c)** rearrangement step ($k_{obs,2}$) and **d)** steady state ($k_{obs,3}$) and are plotted along increasing lengths of ssDNA. $k_{obs,1}$, $k_{obs,2}$ and $k_{obs,3}$ values remain constant albeit the increase in the length of ssDNA. Data points are an average of three experiments and are shown with standard error.

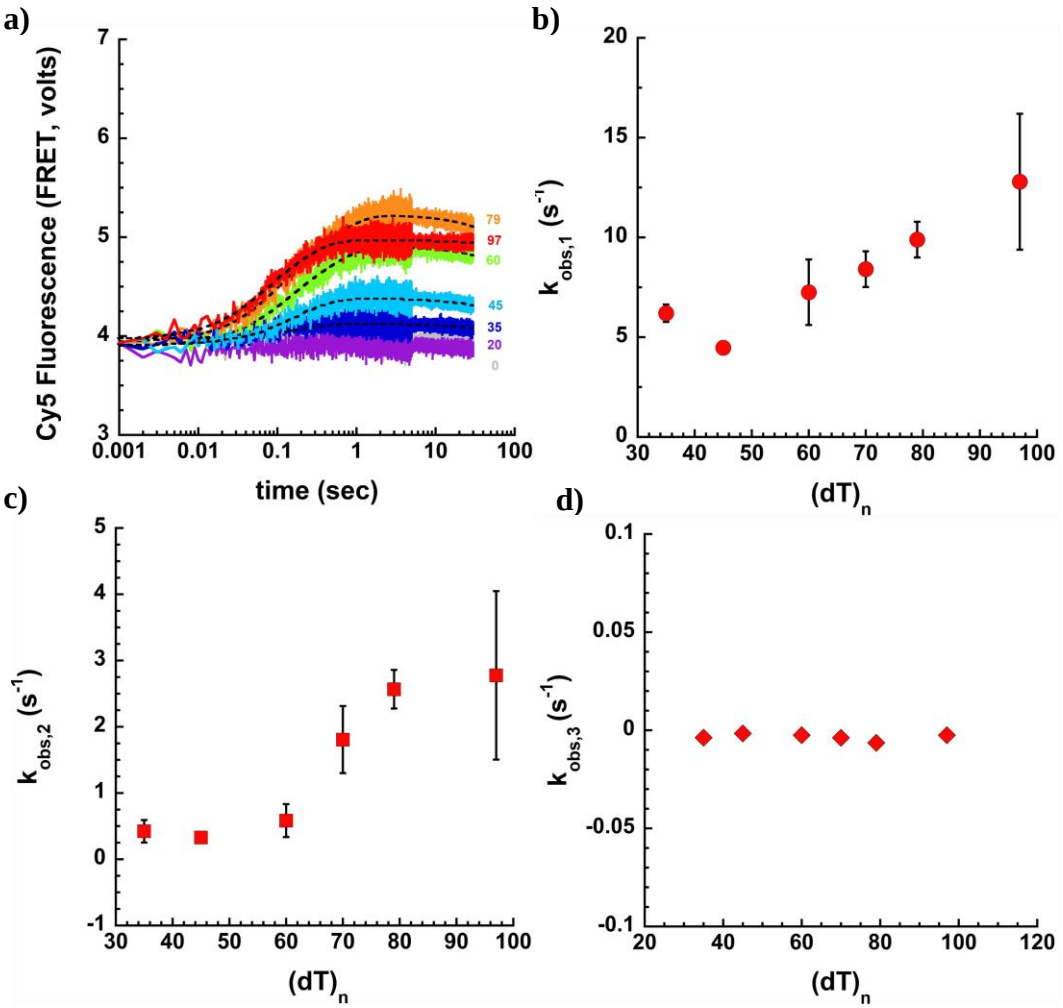

Figure 6-10: FRET experiment to monitor assembly of multiple RPA-S178D with increasing lengths of ssDNA. a) Representative traces of stopped-flow FRET experiments performed with RPA-S178D-A^{cy3} and RPA-S178D-D^{cy5} to monitor assembly of multiple RPA-S178D. The data was fit using a two- step model to obtain **b)** rate of association ($k_{obs,1}$) **c)** rearrangement step ($k_{obs,2}$) and **d)** steady state ($k_{obs,3}$) and are plotted along increasing lengths of ssDNA. $k_{obs,1}$, $k_{obs,2}$ show cooperative binding behavior along with increase in the length of ssDNA, whereas $k_{obs,3}$ remains unchanged.

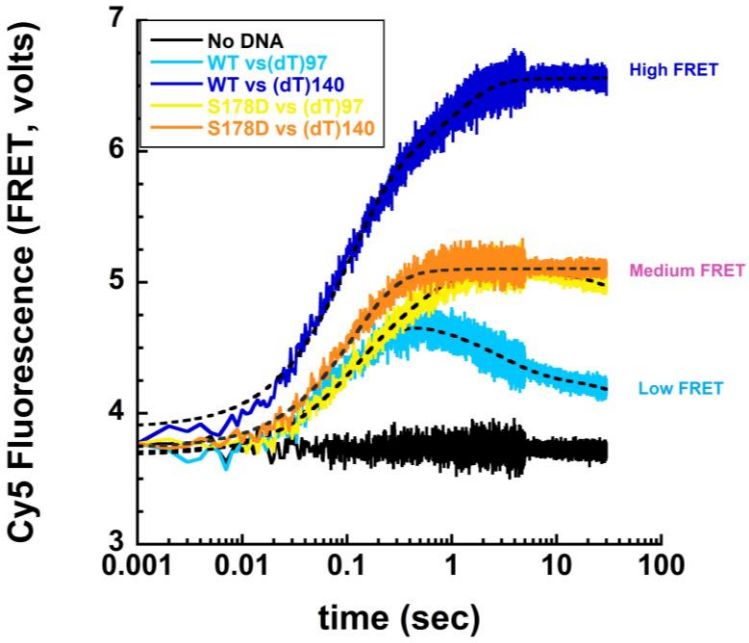

Figure 6-11: Assembly of multiple RPA-wt or RPAzm with increasing lengths of ssDNA. For RPA-wt or RPA-S178D, 40nM (A^{cy3}-D^{cy5}) complex was rapidly mixed with equimolar concentration of either $(dT)_{97}$ or $(dT)_{140}$ and the resulting increase in Cy5 fluorescence i.e FRET was monitored. FRET intensity was ascribed as Low FRET (blue) trace, medium FRET (orange and yellow trace) and high FRET (navy blue trace) based on the amplitude of Cy5 fluorescence observed.

6.3.5 RPA-S178D-DNA complex is resistant to clearing by Srs2 but sensitive to nuclease activity

The cryo-EM structure of two RPA-S178D revealed defined electron density for trimerization core of one RPA but a diffused density for trimerization core of the other RPA(Yates et. al., 2018). Subsequent MST analysis showed increase in interaction affinity between isolated DBD-A and RPA14, yet, weaker affinity for binding to $(dT)_{100}$. Finally, FRET analysis showed cooperative assembly of RPA-S178D, yet, loss of remodeling during assembly (Yates et. al., 2018). Taken together, these results suggest change in assembly of RPA during S178D. To understand how RPA-S178D assembly differed from RPA-wt, we treated RPA-S178D-ssDNA and RPA-wt -ssDNA complex with Srs2 helicase and S1 endonuclease (Yates et. al., 2018). Srs2 requires a 3′ open end to access the ssDNA and several studies including ours have shown that it can remove major players involved in homologous recombination pre-synaptic complex formation including RPA, Rad51 and Rad52.

47.5nM RPA-FRET-$(dT)_{97}$ complex was challenged with increasing concentrations of Srs2 (100- 400nM) in presence of 2.5mM ATP and decrease in FRET monitored. For both RPA-wt and RPA-S178D, decrease in FRET due to Srs2 clearing of RPA bound on ssDNA was explained with a single- step model. RPA-S178D-$(dT)_{97}$ complex was twice as resistant to clearing by Srs2 than RPA-wt (RPA-wt, $K_{removal}$: 2.01± 0.66 x10^6 $M^{-1}s^{-1}$ and RPA-S178D, $K_{removal}$: 0.9 ± 0.23 x10^6 $M^{-1}s^{-1}$) (Fig. 6-12 a, b). Cy5 labeled $(dT)_{100}$ was used to preform RPA-DNA complex for both wt and S178D. This complex was treated with increasing amounts of S1 nuclease and the resulting fragments analyzed using EMSA. Relative band intensities plotted to determine the effect of S1

nuclease treatment showed a mild increase in sensitivity to S1 nuclease for RPA-S178D-DNA complex compared to RPA-wt (Yates et. al., 2018). Compared to RPA-wt, resistance to removal by Srs2 helicase but increased sensitivity to S1 nuclease would suggest a model where multiple RPA-S178Ds assembly would expose segments of DNA within or between multiple RPAs which are easily accessible by nuclease. Meanwhile, the conformations adopted by RPA-S178D due to enhanced interaction between DBD-A and RPA14 and cooperative binding would result in slower removal of multiple RPA-S178D by Srs2.

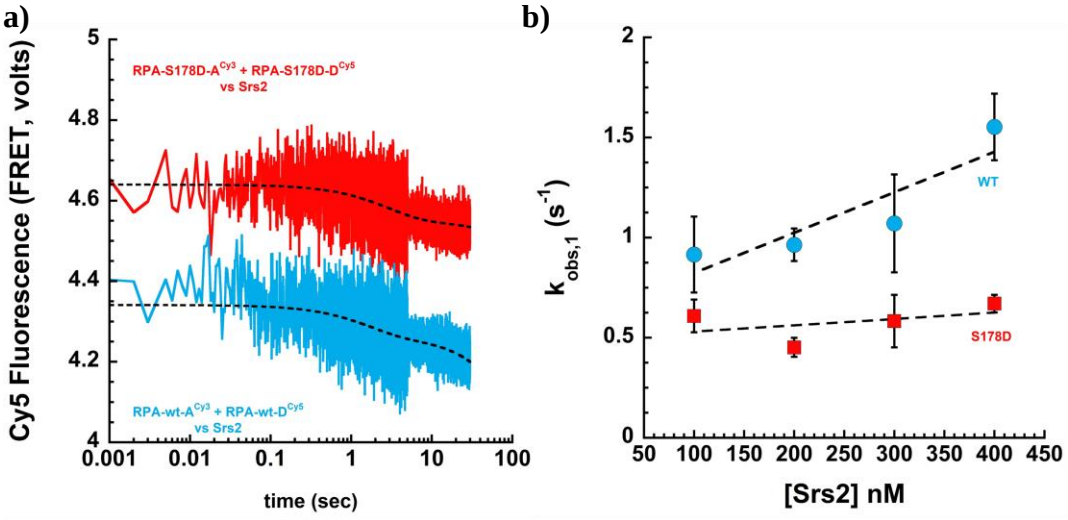

Figure 6-12: RPA-S178D-DNA complex is resistant to Srs2 helicase clearing. a) Representative traces showing decrease in FRET for RPA-wt-DNA (blue) or RPA-S178D-DNA (red) when rapidly mixed with Srs2. **b)** Quantitation of traces in **a)** using single exponential+ linear phase provides the rate of FRET decrease ($k_{obs,1}$) plotted along increasing concentrations of Srs2. The rate of loss of FRET i.e RPA displacement is directly proportional to concentration of Srs2, with RPA-S178D showing more resistance to clearing.

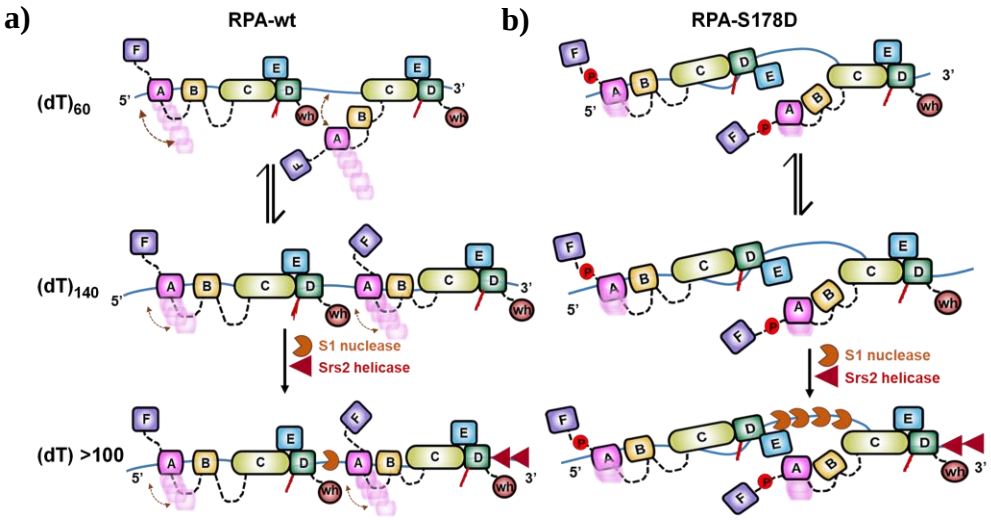

Figure 6-13: Proposed model of post-translational modifications affecting RPA-DBD arrangement and assembly. a) Schematics of RPA-wt assembly and DBD dynamics in three different lengths of ssDNA (shown as blue line). All the DBDs and PIDs follow the color scheme as shown in Fig. 6-1 b, except for OB-F (also known as PID^{70N}), which is shown in purple. In shorter DNA, such as $(dT)_{60}$ with enough space for two RPA molecules to assemble, rapid binding of two RPAs is followed by extensive remodeling of DBD-A, here shown as DBD-A of second RPA being pushed out of ssDNA. As a part of the flexible half of RPA, conformations that can be adopted by DBD-A in various lengths of DNA is shown as multiple pink rectangles extending from DBD-A and microdissociation states are indicated by brown arrows. In longer DNA, such as $(dT)_{140}$ or (dT) >100 with sub-stoichiometric concentration of RPA, trimerization core mediated remodeling of DBD-A is not observed. There is ample DNA space for rapid binding of RPA-DBDs, diffusion of RPA, and less impact of trimerization core mediated remodeling of DBD-A. (Bottom) Under this condition, an RPA nucleoprotein filament is comparatively resistant to both S1 nuclease and Srs2 helicase mediated displacement. **b)** Similar schematic representation showing the binding and remodeling of RPA-S178D-DBD dynamics. S178D mutation (shown as red circle) increases the affinity for interaction between DBD-A and RPA14 and changes conformations adopted by DBD-A This alters the arrangement of RPA domains as multiple RPA-S178D assemble on DNA resulting in exposure of more naked ssDNA between two RPA-S178D. Cooperativity between DBD-A and RPA14 makes RPA-S178D nucleoprotein filament resistant to Srs2 helicase activity but exposed DNA between RPA-S178D makes it sensitive to S1 nuclease.

6.4 Discussion

In general, nucleic acids interacting proteins undergo transient PTM which instills complexity in their functioning and behavior. Recently, several research publications investigating DNA damage response have elucidated towards a potential interrelationship between Mec1 kinase driven phosphorylation events and SUMOylation events, with RPA being at the junction of these two events (Cremona et. al., 2012; Psakhye & Jentsch, 2012; C.-S. Wu et. al., 2014). *In vivo*, how these distinct events simultaneously regulate RPA's ability to propagate phosphorylation and SUMOylation driven damage response is fascinating, but poorly understood. In this chapter we used *in vitro* biochemical and biophysical assays to understand how a single phosphorylation event could potentially regulate RPA-DNA engagement, and how this might translate to customizing RPA's functions towards distinct DNA pathways.

Using RPA-S178D, we show a loss of the intra-DBD remodeling (i.e. trimerization core mediated remodeling of DBD-A) when one RPA-S178D binds to DNA. Furthermore, we show a change in the assembly of multiple RPA-S178D molecules on DNA. In addition, steady state tryptophan quenching experiments with RPA-S178D showed 'half-tryptophan quenching', while, maintaining the DNA binding stoichiometry suggesting a different conformation being adopted than RPA-wt (Fig. 6-2, 6-3). The conformational difference was qualitatively validated by comparative protease digest in both presence and absence of DNA (Fig. 6-4). Since tryptophan quenching provides a global measure of engagement of all DBD on DNA, the half quenching would imply either not all DBDs are engaging the ssDNA, or, if they are, they do not have the

same conformational freedom. Yet, the stoichiometry points that one RPA-S178D is still binding to one $(dT)_{35}$ and the rates of binding to DNA remain unchanged.

These subtle differences in conformational translate into specific outcomes in complex processes such as HR that requires collective and orderly functioning of a range of DNA modifying factors. In this chapter, we show several lines of evidence where a specific PTM in RPA has the potential to yeild distinct outcome in the context of HR. First, using bulk fluorescence experiments we show an alteration in DBD-A and DBD-D dynamics in RPA-S178D compared to RPA-wt (Fig. 6-5, 6-6). Furthermore, in-depth single molecule analysis revealed S178D mutation to completely alter the microscopic binding states of DBD-A (Fig. 6-7). DBD-A could barely engage with DNA but the microscoping binding states of DBD-D remained unaffected (Fig. 6-7, 6-8). This is perhaps the first documentation where a phosphomimic mutation in a non-DNA binding region has the capability to alter conformation of the DNA binding domain in RPA. Although not yet documented, it is possible that PID^{70N} occasionally interacts with DBD-A and the linker connecting these two regions regulates this interaction. Therefore, modification in the linker region could translate to affect behavior of both PID^{70N} and DBD-A, as well as regions of RPA that DBD-A comes into contact with. In a recent publication portraying cryo-EM structure of RPA-DNA complex, Yates et. al., showed that ssDNA occupied by two RPA-S178D had an overall poor electron density for the second RPA-S178D, while, the trimerization core of the first RPA-S178D was better resolved, further suggesting that S178D mutation altered conformation of RPA assembled on DNA (Yates et. al., 2018). Our ensemble FRET experiments monitoring binding of multiple RPAs provide with molecular details underlying this observation.

Although, RPA-wt assembly is a non-cooperative binding event, RPA-S178D assembles in a cooperative manner on longer ssDNAs (Fig. 6-9, 6-10, 6-11). Furthermore, this assembly does not involve DBD-A remodeling by its trimerization core and possibly perturbs RPA diffusion, as RPA-S178D-FRET complexes are unable to achieve the high-FRET state even when ssDNA is not limiting (Fig. 6-11). Finally, RPA-S178D-DNA complex is more resistant to Srs2 mediated clearing (Fig. 6-12, 6-13) but sensitive to S1 nuclease treatment (Yates et. al., 2018).

The process of HR relies on protection of 3′ exposed ssDNA by RPA, timely and regulated displacement of RPA by Rad51 and associated factors, and control of Rad51 nucleoprotein filament by Srs2 helicase. In addition, Srs2 helicase can also displace RPA and therefore has the ability to tip the level of HR in either direction. RPA-S178D-DNA complex which mimics the Mec1 kinase mediated single-site phosphorylation during DNA damage shows a minimal displacement of RPA-S178D by Srs2 helicase and possibly Rad51 recombinase but can be easily targeted by endonucleases. This could be a defense mechanism to prevent passage of damaged DNA or to ensure proper repair before DNA propagation, disfavoring HR. Our study provides mechanistic insights into how phosphorylation events could make slight modifications in RPA-DBD dynamics to yeild distinct global output (Fig. 6-25), and can be extended to processes which involves similar modification of RPA.

Chapter 7: CONCLUSIONS

In a multi-domain protein like RPA, the fundamental mechanism underlying conformational regulation of each domain is affected by plethora of factors. These include cellular localization, cell- cycle stage, interacting proteins, type of DNA substrates, post-translational modifications, and overall conformational freedom available to individual units in the heterotrimeric complex (reviewed in (Maréchal & Zou, 2015; A. Prakash & Borgstahl, 2012; Zou et. al., 2006a)). Two functional modules that include DBDs (A, B, C and D) and PIDs (PID^{70N} and PID^{32C}) connected by flexible linkers (Fig. 7-1 a), are charged with the prime responsibilities of protecting single-stranded DNA (ssDNA), recruiting appropriate DNA binding factors and coordinating the process of handing over ssDNA to an incoming protein. In the absence of ssDNA, linkers connecting individual units in these two functional modules provide RPA with high degree of conformational flexibility. However, upon binding to ssDNA, the random conformations of RPA are comparatively restricted, albeit there still exists multitude of conformations that can be adopted by RPA on DNA (Arunkumar, Stauffer, Bochkareva, Bochkarev, & Chazin, 2003c; Brosey et. al., 2015a). Given the complex architecture of RPA, several studies aimed at understanding the contribution of each DBD towards overall binding and displacement of RPA, including simultaneous protein recruitment and DNA hand over have developed their models based on the use of truncated DBDs. Of the most common being DBDs A and B assigned as the ‘high affinity’ domains that bind stably to ssDNA and the trimerization core (DBDs C, D and RPA14) being the ‘low affinity’ domain that bind weakly to ssDNA. These models while informative are incomplete, as they often lack all four DBDs whose coordinated action renders RPA with

nanomolar DNA binding affinity. Furthermore, they do not account for linkers mediated conformational regulation of RPA-DBDs and its functional implications.

The central aim of this dissertation research was to probe individual RPA-DBDs in the context of full-length RPA, with an intent of obtaining real-time assessment of the global conformational regulation and deciphering how individual conformations adopted by RPA could potentially translate into specific functions.

To this extent, this chapter summarizes the key findings which include but are not limited to: a) development of RPA as a fluorescent probe to track RPA-DBDs in a multiprotein reaction, such as during homologous recombination; b) establishment of a novel concept for RPA as containing a highly-dynamic half (DBDs A and B) and a stable-half (trimerization core); c) differential dynamics and states for each domain on ssDNA; d) regulation of RPA-DBDs dynamics and conformations by external factors, such as, post translational modifications, RPA interacting proteins (RIPs), and DNA structures.

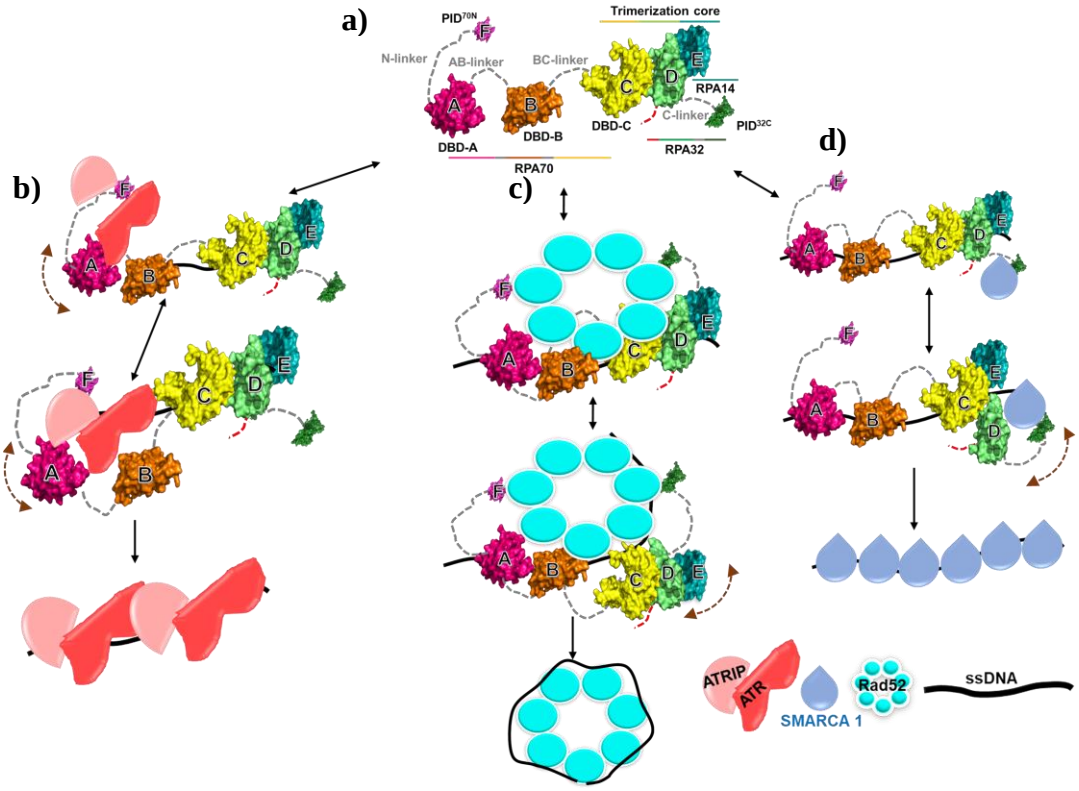

Figure 7-1: Model for DBD specific remodeling by RIPs. a) Diagrammatic representation of RPA DBDs, PIDs and linkers connecting the functional modules. DBDs A, B and PID^{70N} form the flexible half of RPA, and the trimerization core with DBDs C, D and RPA14 forms the stable half of RPA. Possible modes of DBD modulation by RIPs that specifically interact with **b)** PID^{70N} and DBD-A, **c)** share composite interaction site with multiple DBDs and PIDs, or d) interact specifically interact with PID^{32C}, leading to displacement of RPA from ssDNA.

7.1 Probing dynamic nature of RPA-DNA binding into quantifiable events

The advent of site-specifically incorporating non-canonical amino acids (ncAAs) in protein engineering circumvents the limitations of maleimide chemistry that often requires mutating all the cysteine residues, except one (or most surface exposed Cys residues), required to form the thioether (C-S-C) linkage. In addition, it provides freedom of incorporation site-selection, as any amino acid residue located in any region of the protein can be substituted with an ncAA. As a first step towards achieving the central aim, I incorporated 4-Azidophenyalanine (4AZP) in individual DBDs and tethered fluorescent probes using click-chemistry. We termed this methodology FEncAA (Fluorescence Enhancement using non-canonical amino acids) as the positions we selected produced a change in fluorescence upon interactions with ssDNA for a specific DBD. Although 4AZP could be site-specifically incorporated in all four DBDs and labeled with fluorophores, only RPA with fluorophores incorporated at DBDs-A and -D retained DNA binding properties similar to RPA-wt (Chapter 2 and 3). Our results with RPA-DBD-A^f and RPA-DBD-D^f revealed that DBD-A bound first to ssDNA with binding events being highly prone to modulation, followed by DBD-D binding which was stable in nature. Furthermore, this modulation of DBD-A observed under restrictive conditions, i.e. shorter ssDNA, or lower concentration ssDNA, was caused by its own trimerization core. A phenomenon that we termed as “intra-DBD remodeling” (chapter 3). Our finding stands in stark contrast to long held principles of the Sequential Binding Model that describes RPA-DNA binding. According to this model, DBDs A and B bind to ssDNA first and are the high-affinity binding domains, whereas, trimerization core follows DBDs A, B binding and is the ‘low affinity’, easy-to-modulate, part of RPA. Our

finding establishes DBD-A (possibly with DBD-B) binding first with a slightly faster k_{on} rates; ~50 s^{-1}), but is the flexible half of RPA as it dissociates; whereas DBD-D (and possibly the trimerization core) binds with a slower k_{on} rates ~40 s^{-1}) but is the stable half of RPA as it does not dissociate. In fact, we now have further unpublished data showing proteins such as Rtt105 preferentially working to modulate even more stable conformations of the trimerization core on ssDNA during formation of the RPA-ssDNA nucleoprotein filament.

Site-specific incorporation of 4AZP (ncAA) followed by thethering a fluorophore (performing click-chemistry) can impact the functioning of a protein. Therefore, finding a suitable position which allows for ncAA incorporation, subsequent chemistry while still retaining 100% of the protein activity is not a trivial task. In our endeavor of generating site-specifically labeled RPA-DBDs, I tried incorporating 4AZP followed by click-chemistry to attach the fluorophore at several positions in DBD-A (W212, F215, L280 and T211), DBD-B (positions S334, A336, F385 and G387), DBD-C (positions E462 and Y586) and DBD-D (F143 and W101). Only positins T211 in DBD-A and W101 in DBD-D retained 100% of the protein activity after 4AZP incorporation and fluorescent labeling. All the RPA-DBD-B^f and RPA-DBD-C^f variants retained only ~40% of ssDNA binding ability compared to RPA-wt. Therefore, using RPA-DBD-A^f and RPA-DBD-D^f, I was able to capture the dynamics of DBD-A and DBD-D.

Since I was unable to generate a 100% RPA-DBD-B^f and RPA-DBD-C^f variant, I would like to acknowledge that our assignment of DBDs A, B as ‘flexible half’ and DBDs C, D, RPA14 as the ‘stable half’ still draws on the assumption based on the crytal structure of the protein showing extensive interactions within the trimerization core along

with the extensive disordered linkers that connect DBDs A and B with the trimerization core. The model also builds on earlier work made with isolated DBDs that show DBDs A and B to behave as a unit and DBDs C, D and RPA14 to behave as a separate unit (Arunkumar et. al., 2003c; Elena Bochkareva et. al., 2002b).

A possible explanation for our inability to generate RPA-DBD-B^{f} and RPA-DBD-C^{f} with ssDNA binding properties similar to RPA-wt could be attributed to the sites at which ncAAs were incorporated and then labeled with fluorophore. To elaborate, our strategy for choosing 4AZP incorporation site with aim of monitoring dynamics of individual DBDs required fulfilment of three specific criteria: a) the site of incorporation be located away from the secondary structures such as α-helix and β-sheets in order to maintain the structure of OB folds. This would often result in substitution of amino acid residues located in the loops of OB folds with 4AZP; b) following incorporation of 4AZP and fluorescent labeling, the fluorescently labeled DBD required to be ssDNA responsive, i.e., produce specific and quantifiable change in fluorescence intensity that could be used to deduce kinetic parameters. This would narrow the site-selection, as residues in the vicinity of ssDNA but not too close to impose a significant steric hindrance were chosen; and finally c) the fluorescently-labeled RPA maintains ssDNA binding properties similar to RPA-wt.

Using the crystal structure of *U. maydis* RPA as a guide and comparing the amino acids residues with *Sc*. RPA, in case of DBD-B, positions S334 and A336 lie in the conserverd motif ‘SRAG’ (in *Sc.* RPA) and ‘SKAS’ in (*U. maydis* RPA) which also makes the loop structure. In this loop, S334 forms polar contacts with G337 and R335 forms ionic interactions with the phosphate backbone of the ssDNA. In addition,

positions F385 and G387 is located in the conserved motif ‘DFGGRAL’ (*Sc.* RPA) of the BC-linker which has been shown to play a significant role in communication between DBD-B and DBD-C, and in the stability of the overall tertiary structure of RPA on DNA. While F385 could potentially from base stack interactions with DNA, G387 forms polar contacts with D384 and R388 in the motif ‘DFGGRAL’. Similarly, in case of DBD-C, E462 lies in the conserved motif ‘EKGDFF’and can make transient ionic contacts with the solvent during ssDNA binding and Y586 which is located in the conserved motif ‘DTYND’ forms base-stacking interaction with the nitrogen base of the ssDNA. Therefore, perturbing either S334, A336, F385 or G387 in DBD-B, or, E462, Y586 in DBD-C via incorporation of 4AZP and fluorescent labeling could significantly impact the extent of the specific interactions made by the amino acids in this loop. Furthermore, incorporation of flurophore, which is fairly bulky compared to single amino acid, could pose a significant steric hindrance, disrupting overall loop structure and affecting majority of interactions that this loop participates in. Therefore, inability to fulfill these three criteria to obtain RPA-DBD-B^{f} and RPA-DBD-C^{f}, albeit having experimented with several positions suggests that DBDs B and C are comparatively sterically restricted and not amenable to structural perturbation. Therefore, inability to fulfill these three criteria to obtain RPA-DBD-B^{f} and RPA-DBD-C^{f}, albeit having experimented with several positions suggests that DBDs B and C are comparatively sterically restricted and not amenable to structural perturbation. The crystal structure of *U.maydis* RPA depicts individual loops in DBDs B and C that could be considered as candidate sites for incorporating ncAA to be intimately positioned with respect to ssDNA (Fig. 7-2). Therefore, along with AB-linker and BC-linker that have been shown to adopt defined

structures upon binding to ssDNA, the loops present in DBDs B and C could be equally responsible for coordinating the overall RPA-DNA binding, and also dictate the path of ssDNA in the RPA complex.

The two DBDs that I was able to fluorescently label are connected to two PIDs (PID^{70N} is connected to DBD-A via the long N- linker, and PID^{32C} is connected to DBD-D via C- linker) (Fig. 7-1 a). Therefore, it is possible that loops in DBDs A and D are more amenable to structural perturbation, as binding of these two DBDs are often directly affected by RPA interacting proteins. In the future, additional sites within DBD-B and DBD-C, including non-tested sites in the loops or position in the surface of the DBD which would still provide DNA dependent change in fluorescence could be tested in order to develop RPA-wt like RPA-DBD-B^f and RPA-DBD-C^f. An alternative to this would be introducing ncAA in the BC linker positioned close to DBD-B and at the C-terminus of RPA70 followed by labeling with fluorophore to generate RPA-DBD-B^f and RPA-DBD-C^f, respectively.

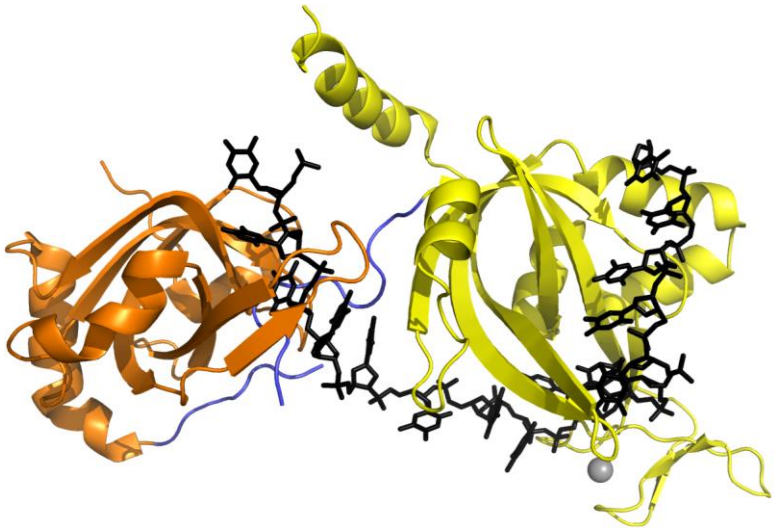

Figure 7-2: Crystal structure of *U.maydis* RPA (PDB: 4GNX) bound to ssDNA (black sticks) showing DBD-B (orange) and DBD-C (yellow). BC-linker connecting the two DBDs is shown in purple blue. Part of the BC-linker forms an α-helix structure as the two DBDs arrange themselves on ssDNA. DBD-C has a zinc-finger motif that binds a Zn^{2+} metal ion (grey sphere) and is required for stable ssDNA binding. All the candidate loop structures for incorporating ncAA reside close to ssDNA or in the BC-linker that undergo major conformational transitions. Thus, architecture of DBDs B and C on ssDNA makes it particularly challenging for incorporating ncAA without perturbing their functions.

In summary, this distinction in dynamics (binding, dissociation, and remodeling) of DBD-A and DBD-D resulting in 'flexible-half' and 'stable-half' could be one of the several ways by which RPA controls and coordinates ssDNA protection with protein recruitment and DNA handover in distinct DNA metabolic processes. For example, the DNA damage response protein SMARCALl, which also remodels stalled replications forks, interacts with PID^{32C} which is a part of RPA32 i.e., stable half of RPA, whereas proteins involved in checkpoint responses such as ATR, ATRIP, p53 etc. interact with PID^{70N} present in the flexible half of RPA, and several proteins crucial for HR share

composite interaction site involving both the halves (Fig. 7-1 a-d) (Elena Bochkareva et. al., 2005; Feldkamp, Mason, Eichman, & Chazin, 2014; Hays, Firmenich, Massey, Banerjee, & Berg, 1998b; D. Jackson et. al., 2002; Mer et. al., 2000; Stauffer & Chazin, 2004b; Xu et. al., 2008). Therefore, the type and extent of interaction could selectively affect conformations attained by individual DBDs or the two distinct halves (Fig. 7-1 a-d), ultimately regulating RPA displacement and handing over of ssDNA.

7.2 RPA has defined microdissocaiton states on DNA

Two interesting characteristics which are in contrast to each other but are often used together to describe RPA-DNA engagement are ‘high-affinity’ and ‘highly dynamic’ ssDNA binding protein. Several studies have monitored transitions in RPA-DNA binding in response to changes in ionic environment, external applied force or in presence of higher concentrations of RPA in the surrounding (Gibb, Ye, Gergoudis, et. al., 2014; Kemmerich et. al., 2016; Kumaran et. al., 2006). These transitions can be categorized into two groups: microdissociation and facilitated exchange.

Microdissociation (also called microdissociation states) can be attributed to local thermal motions (differences in energy levels during conformational sampling to attain the lowest free energy state) of individual DBDs, PIDs or linkers connecting these individual units (R. Chen et. al., 2016a; Kemmerich et. al., 2016). Microdissociation of RPA bound on ssDNA exists independent of free RPA or RIPs in the surrounding. However, the latter can influence microdissociation. For example, diffusion of RPA on DNA is a direct result of microdissociation.

Facilitated exchange is the process in which RPA bound on DNA is exchanged with excess RPA in the surrounding. In case of facilitated exchange, RPA in the surrounding allosterically displaces RPA bound on DNA, possibly by affecting/ changing the microdissociation (Gibb, Ye, Gergoudis, et. al., 2014). I would like to distinguish facilitated exchange from facilitated dissociation, where, the later involves displacement of RPA by RIPs. Microdissociation, facilitated exchange and facilitated dissociation of RPA have been extensively demonstrated using single-molecule FRET, atomic force microscopy, NMR, and conventional biophysical techniques. However, the spatial and temporal resolution of occurrence of these events, number of transitions present within and the functional implications of individual transitions had not been explored.

Using RPA-DBD-A^f and RPA-DBD-D^f, combined with single molecule fluorescence microscopy, we demonstrated that RPA has four distinct microdissociation states on DNA (Chapter 3). The factors that promote microdissociation are experimentally intractable at the moment. Therotically, the most straight-forward explanation is that each microdissociation state arises from the thermal motions, i.e., sampling of conformational states by individual DBDs in order to attain the lowest free energy levels of binding on ssDNA. Therefore, the conformations adopted by four DBDs would account for the four microdissociation states. This is supported by our finding that truncated RPA with PID^{70N}-DBDs A, B (FAB) had two microdissociation states. However, this explanation does not account for the action of linkers connecting individual domains that provide RPA with high degree of mobility, are potentially critical in coordinating RIP recruitment, and ssDNA handover. RPA has four linkers in total: N-linker, AB linker, BC linker and C-linker (Fig. 7-1 a). Therefore, an alternative

explanation could be that individual microdissocaiton states are driven by the concerted motions of one or more linkers. Therefore, a full-length RPA has four microdissocaiton states and FAB consisting of N-linker and AB-linker has two microdissociation states. It is also possible that the local conformations adopted by both linkers and DBDs drive the microdissociation states of RPA. This explanation is supported by our findings with RPA-S178D-A^f and RPA-S178D-D^f which has a single-site mutation incorporated at N-linker and shows loss of microdissociation state of DBD-A with no effects in states of DBD-D (Chapter 6).

Each of these possibilities can be additionally experimentally verified. If microdissociation states are solely based on motion of DBDs on DNA then a truncated RPA with DBDs C, D and RPA14 (CD14) would constitute two microdissociation states. In addition, introducing mutations in each DBD to perturb DNA binding of that DBD would proportionally decrease the number of microdissocaiton states. In case of CD14 that has only C-linker, if these states are linker driven, only one microdissociation state would be present. Furthermore, changing the length of the linker should affect the residence time and occurrence of this state. Finally, if microdissocaiton state are a result of both DBD-DNA binding and linker motions then, in either full-length or truncated RPA, perturbing ssDNA binding in either DBDs, changing the length of linker, or combination of both should result in change in number of states, frequency of occurrence and residence time of each state. We do caution that such mutations could also perturb important allosteric motions within the protein and might not be a straightforward interpretation of a loss or gain in microdynamic states.

7.3 Conformational regulation of RPA-DNA binding

Modern experimental tools have expanded what ‘structure’ could actually mean, as structures can now be defined as unique conformations in spatial and temporal dimension, each with a potential of fulfilling specific function. Modular structure and dynamicity (microdissociation/ facilitated exchange/ facilitated dissociation) in RPA has often been attributed for its ability to adopt multiple conformations, although only a finite number of conformations can be attained owing to propensity of rotational freedom of each molecule coupled with steric clashes. The dynamicity in RPA could be one of the driving forces which allow RPA to perform multiple functions on DNA but are also the underlying cause for displacement of RPA from ssDNA. To this extent, we investigated how RPA’s conformations are affected upon interactions with RIPs, interaction with different types of DNA substrates and during situations of post-translational modifications.

7.3.1 Regulation of RPA conformations by RIPs

A common recurring theme in models that depict RPA function posits RPA being displaced from ssDNA by a RPA-interacting protein and the buried ssDNA being handed over to the incoming DNA-binding protein. But newer findings looking at multi-protein reactions using single-molecule DNA curtain experiments show higher order complexes on ssDNA that build on RPA and not remove it from DNA (Gibb, Ye, Kwon, et. al., 2014b). These findings agree with our findings, as the stable-half of RPA can remain on the DNA, and the less-stable, dynamic-half, can be displaced while allowing the vacated

DNA to be occupied by the RPA-interacting protein. At a minimum, this co-complex or remodeled RPA and the RIP is a long-lived transition state during the DNA hand-off process. To directly test how an incoming RIP might influence the dynamics of the two RPA halves, we looked at RPA dynamics with two distinct RPA-interacting proteins: Rad52 and Rad51, and one motor protein, Srs2, that does not interact with RPA, but can remove it from DNA by coupling ATP hydrolysis to physical translocation on the DNA. All four proteins work together in the pre-synaptic step in homologous recombination.

Of the three, the interplay between Rad52 and RPA has been fraught with most juxtaposing models. This is further compounded by presence of BRCA2 in humans which fulfills the role of Rad52, and Rad52 is generally considered as the ancillary protein in the HR pathway. Therefore, depending on the species being investigated, there could be slight variants in the proposed models. Both yeast and human Rad52 share a composite interaction site with RPA. Rad52 binds to both PID^{32C} and DBD-A (Hays et. al., 1998a; Mer et. al., 2000; Park et. al., 1996). In yeast, Rad52 has been shown to inhibit the facilitated exchange of RPA but enhance the displacement of RPA from ssDNA in the presence of Rad51 recombinase (Gibb, Ye, Kwon, et. al., 2014b; Sugiyama & Kowalczykowski, 2002b). It has been proposed that Rad52 stabilizes the microdissociation states of RPA (Gibb, Ye, Kwon, et. al., 2014b; Chu Jian Ma et. al., 2017b). In presence of Rad52, this stabilization of microdissocation states combined with the stimulatory effect of increasing the rate of ATP hydrolyis by Rad51 could be speeding up the Rad51-nucleoprotein filament formation (Fig 7-3 a-c) (Sugiyama & Kowalczykowski, 2002b). Therefore, to dissect the mechanisms involved, we used single molecule TIRF analysis to monitor microdissociation states of DBD-A and DBD-D of

DNA bound RPA in presence of Rad52. Our results showed that Rad52 selectively altered the number of states, including the frequency and residence time for DBD-D but not DBD-A. Since facilitated exchange is dependent on two distinct parameters, microdissocaiton states and local concentrations of free RPA, decreasing the number of states and stabilizing DBD-D binding would explain how Rad52 inhibits facilitated exchange of RPA, but this stabilization could help other proteins attempting to displace RPA, as they now have one less conformational barrier to overcome; and also have access to ssDNA now vacated by DBD-D. We demonstrated that this property of selective DBD modulation by Rad52 was dependent on Rad52 binding to ssDNA. Therefore, it seems like Rad52 'takes over' the fourth state of DBD-D ssDNA binding by engaging itself on DNA. Since we did not perturb RPA-Rad52 interaction in these experiments, future experiments can target selectively mutating Rad52-DBD-D or Rad52-DBD-A interaction sites followed by monitoring effects on microdissociation states. Such a study would decipher if this domain specific modulation is due to Rad52 binding to ssDNA or a combination of Rad52-ssDNA binding with Rad52-DBD interaction.

Rad51 interacts directly with DBD-A, regions spanning DBD-B (amino acid residues 169-326 in human RPA) and the middle subunit RPA32 (Golub, Gupta, Haaf, Wold, & Radding, 1998; Stauffer & Chazin, 2004b). In addition, a physical interaction between Rad51 and RPA is required for displacement of RPA by Rad51 (facilitated dissociation) (Stauffer & Chazin, 2004b). Competition between ssDNA and the N-terminus of Rad51 for binding to same site in DBD-A could be responsible for displacement of DBD-A by Rad51(Stauffer & Chazin, 2004b). To test this model, I here

show preliminary data collected by challenging RPA-DBD-A^{f} or RPA-DBD-D^{f} complex with Rad51, and show that Rad51 can displace both DBD-A and DBD-D from DNA, with faster displacement of DBD-A than DBD-D (Fig. 7-4 a-b, 7-5 a-c). In figure 7-5, the Rad51 mediated displacement of RPA as a function of increasing lengths of DNA has a $k_{obs,1}$ value of ~20 s^{-1} until $(dT)_{60}$ followed by decrease in the $k_{obs,1}$ to ~ 4s^{-1} for $(dT)_{97}$. The $k_{obs,2}$ values remain relatively constant with increasing lengths of ssDNA. Therefore, $k_{obs,1}$ value might be reflecting the rate of initial interaction between Rad51 and DBD-A and $k_{obs,2}$ might be reflecting the rate of displacement of DBD-A. It is also likely that we are observing a two-step mechanism for Rad51 binding, where, the first step involves nucleation of one- three Rad51 molecules on the RPA-coated ssDNA, and, the second step involves growth of the Rad51 nucleoprotein. Our RPA-FRET experiments monitoring the assembly of two RPA molecules with increasing lengths of ssDNA have shown substantial remodeling of DBD-A until $(dT)_{79}$ which is not observed for $(dT)_{97}$ (Chapter 6, Fig. 6-9 a). Since Rad51 directly interacts with both PID^{70N} and DBD-A, both of which are also the flexible part of RPA and are being remodeled by trimerization core in a ssDNA length dependent manner, the rate of interaction ($k_{obs,1}$) between DBD-A (including possibly PID^{70N}) and Rad51 is fast until $(dT)_{60}$ (and possibly until $(dT)_{79}$) following which it decreases. Preferential binding of Rad51 from 5′ to 3′ (Antony et. al., 2009) coincides with faster displacement of DBD-A. This would ease Rad51 nucleation which is shown to be the rate-limiting step in Rad51 nucleofilament formation (Miné et. al., 2007; Sugiyama & Kowalczykowski, 2002b). However, displacement of DBD-D by Rad51 likely involves two routes: a) preferential binding of Rad51 in a 5′->3′ direction requiring displacement of DBDs A-C preceding DBD-D, and b) accessing ssDNA at the

3′ end of DNA which is the unfavorable direction for Rad51 nucleation and filament formation. Thus, all these factors could contribute to faster displacement of DBD-A than DBD-D by Rad51. In presence of Rad52 which selectively modulates the microdissociation states of DBD-D, the combined effects of Rad51 and Rad52 on DBD-A and DBD-D results in faster displacement of RPA, possibly because it stimulates DBD-D displacement from DNA (Fig. 7-3, 7-4, 7-5). Another likely scenario is that Rad52-RPA form a complex at the 3′ end of the ssDNA overhang (as found during HR) and remain on the ssDNA to serve as a capping mechanism to foster the second-strand capture. Future studies investigating the dynamics of all three proteins will be required to further tease apart the details of this mechanism.

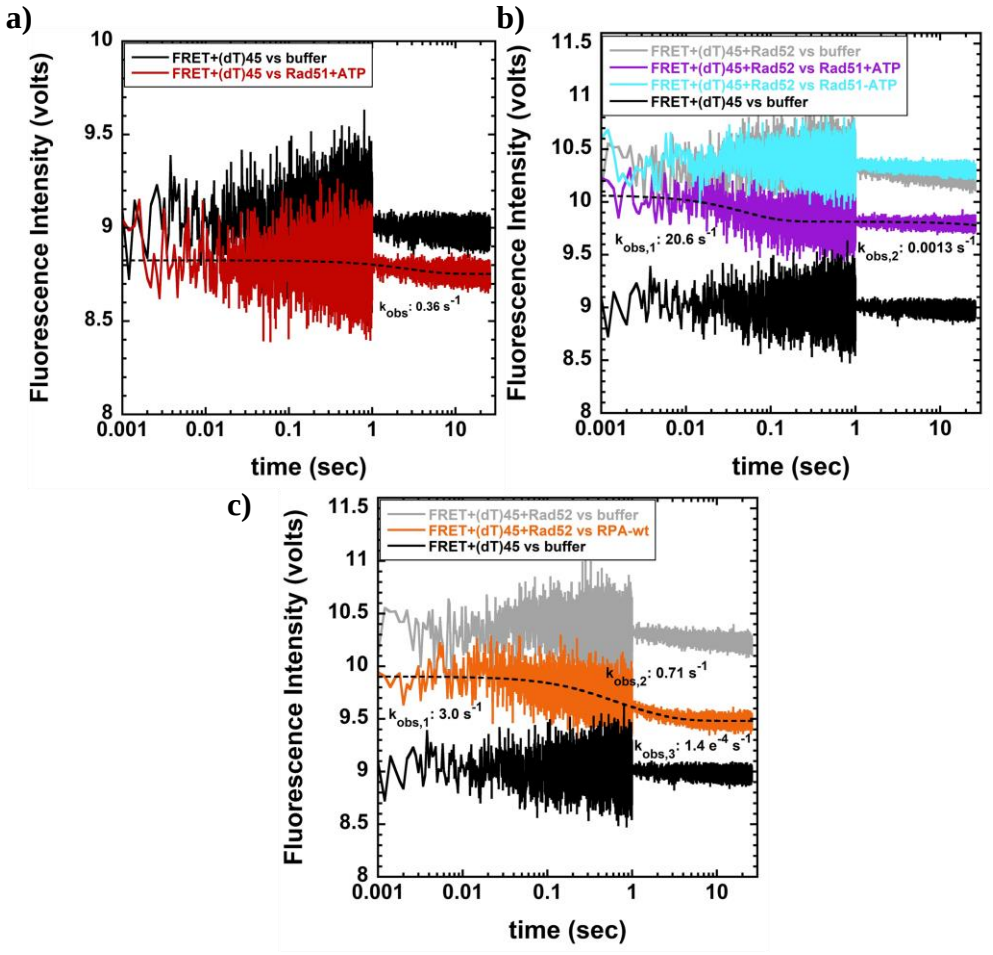

Figure 7-3: Rad52 enhances Rad51 mediated displacement of RPA from ssDNA. a) 100nM RPA-DBD-A^{cy3}, RPA-DBD-D^{cy5} and $(dT)_{45}$ (FRET+$(dT)_{45}$) complex was challenged with 150nM Rad51 in presence of 2.5mM ATP in RPA reaction buffer (30mM Hepes, pH 7.8, 100mM KCl, 1mM βME, 5mM MgCl2, 6% glycerol) at 25ºC. Cy3 was excited at 555nm and decrease in Cy5 fluorescence was monitored with a 645nm emission filter. Raw data was fit with single exponential. **b)** Same as in a) but FRET+$(dT)_{45}$ complex in presence of 100nM Rad52-wt is challenged with 150nM Rad51. Fitting the raw data with double exponential kinetic model shows increase in rate of displacement of RPA from DNA **c)** Same as in b) but challenging FRET+$(dT)_{45}$ complex in presence of 100nM Rad52-wt with 200nM RPA-wt. Fitting the raw traces with double exponential followed by a linear phase model shows facilitated exchange is slower than displacement by Rad51-wt in presence of Rad52.

Srs2 helicase is an anti-recombination mediator enzyme that physically interacts with Rad51 and disrupts Rad51 nucleoprotein filaments (Antony et. al., 2009b; Krejci et. al., 2003; Qiu et. al., 2013). Using RPA-DBD-D^f, I showed that following Srs2 mediated displacement of DNA-bound Rad51, RPA present in the surrounding can rebind to the open ssDNA spaces. Interestingly, Srs2 also displaces RPA and Rad52 from DNA but does not physically interact with both these proteins (Seong et. al., 2009). RPA also significantly impedes the DNA unwinding activity of Srs2 (Fig. 6-23 b, e compare red trace with grey trace; c, f). In all these scenarios, Srs2 translocates in a 3′->5′ direction on ssDNA (Antony et. al., 2009b) and the template here is a long RPA-coated ssDNA filament. During DNA unwinding, a dsDNA with the ssDNA overhang will be the substrate. When multiple RPA molecules are bound, Srs2 needs to gain access to the DNA. It either has to somehow disengage the trimerization core at the 3′, or, be able to access the DNA when DBD-A & D dynamically disengage from the DNA. Follow up work can entail detailed measurements of the DBD dissociation kinetics during DNA unwinding and translocation by Srs2 on RPA-coated nucleoprotein substrates.

7.3.2 Effects of DNA context on RPA-DBD dynamics

As discussed in section 5.4.2 changes in DNA topology (that includes nucleotide orientation) can affect protein-DNA interactions. To directly investigate how changing the topology of DNA encountered by RPA could affect its DBD dynamics (i.e. binding, dissociation and remodeling), I reacted RPA-DBD-A^f or RPA-DBD-D^f with either 5′ overhang, 3′ overhang or ssDNA flanked by duplex (blocked-end) DNA, with varying lengths of overhangs or intervening ssDNA. I show that intra-DBD remodeling (i.e the

trimerization core mediated remodeling of DBD-A upon monitoring binding of one RPA to one ssDNA) requires an open 5′ end at the DNA,whereas DBD-D dynamics changes in all three DNA contexts (Chapter 4). Interestingly Rad52 mediated remodeling of DBD-D was more pronounced on a 5′ overhang than the remaining two DNA substrates, and this remodeling was driven by cooperativity between the inner and outer DNA binding sites in Rad52 (Chapter 5). In these experiments, I could only monitor dynamics of either DBD-A or DBD-D, but not both simulteneously. Such a measurement is important because RPA should not be envisioned as a linear assembly of DBDs, and interactions between the DBDs should also be quantitated. Such interactions could be inter-RPA (involving interactions between DBDs of multiple RPAs on DNA) or intra-RPA (involving ineractions between DBDs of one RPA on DNA). Experimentally, such experiments would require two site-specific fluorophores (FRET pair) engineered into a single RPA molecule, e.g., Cy3 at DBD-A and Cy5 at DBD-D , followed by capturing FRET changes on ssDNA, DNA with overhangs, and blocked end DNA. This will provide understanding of how dynamics of DBD-A is affected with respect to DBD-D in each of these DNA contexts. Introduction of RIPs such as Rad52 or Rad51 should then provide in-depth detail into how RIPs affect the intra-DBD dynamics.

We are now working on a second ncAA incorporation using Tet 3.0 as the unnatural amino acid. Fluorophores to Tet 3.0 can be tethered using TCO conjugation. The idea here is that 4AZP and Tet 3.0 can be simultaneously engineered at different positions within a single RPA trimer. Since the click-chemistry conjucation are different, we can attach Cy3-DBCO to 4AZP and Cy5-TCO to Tet3.0 (Antony and Mehl; unpublished work). In case, implementing the dual- incorporation of ncAA affects the

DNA binding properties of RPA, an alternative approach could be placing either a FRET donor (or acceptor) in the ssDNA-dsDNA junctions or the open termini of the DNA substrate and then performing FRET with acceptor (or donor) labeled RPA-DBD-A and RPA-DBD-D (Fig. 7-6). This method, while logistically easier, would only provide information with respect to distance of FRET pairs (i.e RPA-DBD and DNA) and would limit monitoring to just one DBD at a time.

In terms of global regulation of DNA metabolic processes with ssDNA intermediates, each of these subtle modifications in DBD-dynamics could be unique scenarios enabling an incoming protein to either interact with RPA, occupy ssDNA space or both. For example, on 3′ overhang or blocked end substrates where DBD-A is 'stuck', conformations of N-linker and PID^{70N} would be different than if DBD-A were flexible and easily remodeled. Therefore, it would assist in recruitment of RIPs that would require DBD-A (and possibly other RPA-DBDs) to remain bound on ssDNA. In addition, it could affect RIPs requiring synergistic interaction with both PID^{70N} and DBD-A. RIPs such as Rad52 and Rad51 that have ability to bind to dsDNA and ssDNA-dsDNA junctions, would be able to modulate DBD dynamics of both the flexible half and stable half. It would not be too far-fetched to postulate that unique conformations adopted by each DBD, in a particular DNA context, regulates the level and types of RIPs being

recruited to the DNA substrates, ultimately guiding the choice of DNA repair pathway and regulating continuation of DNA metabolic processes.

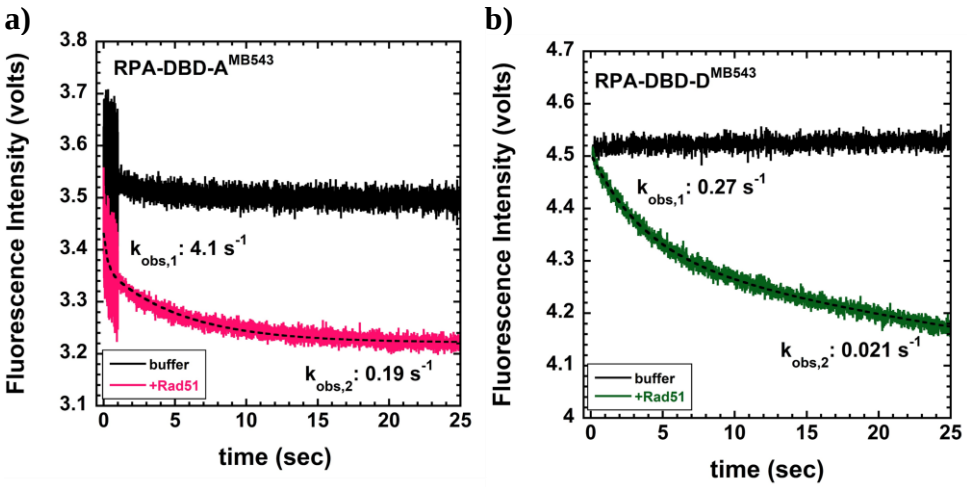

Figure 7-4: Rad51 displaces DBD-A faster than DBD-D. a) 100nM RPA-DBD-A^{MB543} was pre-incubated with 23nM $(dT)_{97}$ or **b)** 100nM RPA-DBD-D^{MB543} was pre-incubated with 30nM $(dT)_{97}$, to form a RPA-DNA complex and challenged with a) 750nM b) 1μM Rad51 in in RPA reaction buffer (30mM Hepes, pH 7.8, 100mM KCl, 1mM βME, 5mM $MgCl_2$ and 6% glycerol (v/v)) supplemented with 2.5mM ATP, at 25°C. Samples were excited at 535nm and decrease in MB543 fluorescence monitored with 555nm long pass emission filter. Fitting data for both a) and b) with double exponential (without linear phase) shows, displacement of DBD-A is faster than DBD-D.

7.3.3 Microscopic and macroscopic regulation of RPA's conformation by post-translational modifications

RPA is post-translationally modified by addition of various groups, such as, phosphate (Pi), small ubiquitin like modifier (SUMO), ubiquitin (ub), acetyl (Ac) etc. (Maréchal & Zou, 2015). How each of these modifications affect DNA binding properties of RPA-DBDs, or the assembly of multiple RPA molecules, is poorly understood. Here, using DBD specific fluorescently labeled RPAs and single molecule, bulk fluorescence as well as ensemble FRET, I showed that a single phosphomimic site can affect both

microdissociation and arrangement of multiple RPAs on DNA. RPA-S178D is unable to move/ diffuse on ssDNA which is a direct consequence of its changed microdissociation dynamics (Chapter 6). Altered conformation but not DNA binding ability is further supported as I showed RPA-S178D had DNA binding affinity and kinetics similar to RPA-wt but showed half quenching of intrinsic tryptophan fluorescence (chapter 6). Using smTIRF, no quantifiable microscopic binding states of DBD-A could be captured, whereas, DBD-D retained all four states. Since, serine to aspartate substitution is located in the N-linker, this selective effect in the states of one DBDs vs other would favor a model where each microscopic binding state is affected by the short-range communication of conformations adopted by the DBD and the linkers connecting DBDs and PIDs. To further test this, similar phosphomimic mutations in the C-linker could be introduced and DBD-D dynamics monitored. A possible phosphomimic candidate to experimentally test is S189 located in C-linker close to K199 SUMOylation site that gets phosphorylated and SUMOylated, respectively, in response to genotoxic stress (Albuquerque et. al., 2008; Psakhye & Jentsch, 2012).

Subsets of serines/ threonines are phosphorylated by specific kinases in cell-cycle dependent manner and to elicit a DNA damage response. It would be interesting to modify (phosphomimic) kinase respective groups of serine/ threonine (for eg: S4, S8, S12 that get phosphorylated by ATM; S23, S29 that gets phosphorylated by CDK etc) and investigate how this might affect RPA-DBD dynamics and assembly. Alternatively, generating fluorescent phosphorylated RPA by dual incorporation of ncAAs that involves incorporation of phosphoserine (an ncAA) and 4AZP would provide precise results regarding how phosphorylation events affect RPA-DBD-DNA binding and assembly of

multiple RPAs. Dual incorporation of ncAA can also be used to incorporate two chemical handles, one for fluorescent labeling, and the other for ligation of functional group (such as Ub or SUMO). This would enable the unravelling of the exact underlying mechanisms by which PTMs affect RPA-DBD dynamics on DNA or in presence of RIPs. Adopting ncAAs based methods to answer mechanistic questions is extremely appealing. However, compared to the production of wild-type protein, the yield of full-length purified protein decreases dramatically even with a single ncAA incorporation. The 4AZP carrying RPA-DBD-A and RPA-DBD-D have the ncAA incorporated at the loop of respective DBDs, ensuring that the positioning of 4AZP does not affect the overall tertiary structure of RPA. Hence, upon dual incorporation of ncAAs, extensive biochemical assessments have to be carried out to ensure that modifications at two different sites do not perturb the local secondary structure and overall tertiary structure of RPA.

7.4 Post-translational modifications dictate differential DBD dynamics

DBD dynamics and stabilization of specific conformational states of RPA can be achieved through post-translational modifications. RPA is extensively phosphorylated; however, the precise functional roles for specific phosphorylations with respect to how DNA binding is modulated, have not been established. Our work has now shed light on how phosphorylation at S178 can affect RPA-DNA binding properties and RPA assembly on DNA *in vitro*. In vivo S178 is phosphorylated by Mec1 kinase in response to DNA damage (Bartrand et. al., 2004; Brush & Kelly, 2000).

In chapter 6, I show that RPA harboring a phosphomimetic S178D substitution has selective changes in microdissociation states, lack of diffusion, and enhanced

cooperative assembly on ssDNA making it resistant to displacement by Srs2. Furthermore nucleoprotein filaments made by RPA-S178D make the ssDNA more susceptible to degradation by S1 nuclease (Yates et. al., 2018). I have also shown that for RPA-wt, Rad51 can displace DBD-A faster than DBD-D from DNA. Taken together, extrapolation of these observations would mean that phosphorylation of S178 by Mec1 kinase in response to DNA damage would make it harder to displace phosphorylated RPA by both Rad51 and Srs2. Rad51 filaments will be formed to a lesser extent and this would tip the scale of HR occurring in cells. Meanwhile, nucleases in the surrounding can degrade the accessible DNA and recruit additional factors to repair the damage before progressing to S-phase. Indeed, for this model to be valid for RPA-S178D, the rate of displacement of both DBD-A and DBD-D by Rad51 should be comparatively slower than for RPA-wt. As a control, physical interaction between Rad51 and phosphomimic RPA-S178D need to be performed to ensure that phosphorylation does not affect RPA-Rad51 interaction, which has been shown to be critical for RPA displacement.

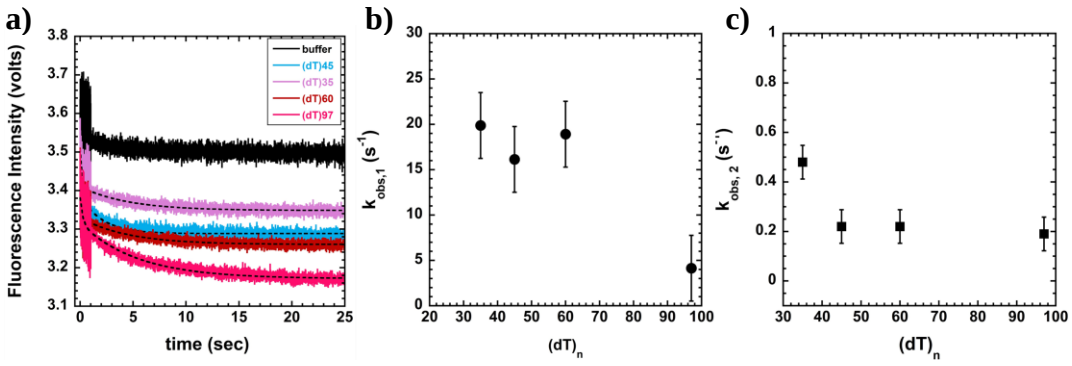

Figure 7-5: ssDNA length dependent displacement of DBD-A by Rad51. a) Raw traces obtained from the stopped-flow experiments when 100nM RPA-DBD-A^{MB543} was preincubated with 62.5nM $(dT)_{35}$, 50nM $(dT)_{45}$, 37nM $(dT)_{60}$ or 23nM $(dT)_{97}$ to form RPA-DBD-A^{MB543}-DNA complexes. Individual RPA-DNA complex was challenged with 750nM Rad51 in RPA reaction buffer supplemented with 2.5mM ATP. Reactions were performed under similar conditions as described in figure 7-4 and data obtained was fit using a double exponential kinetic model to yield plot of **b)** $k_{obs,1}$ and **c)** $k_{obs,2}$.

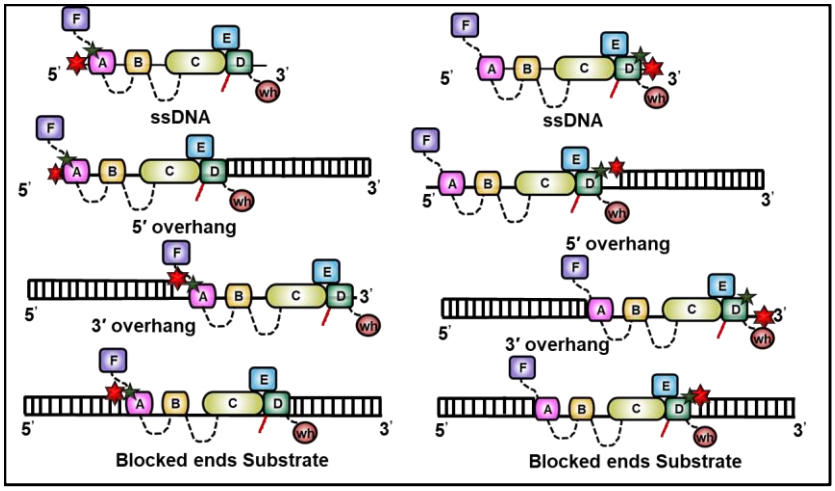

High FRET

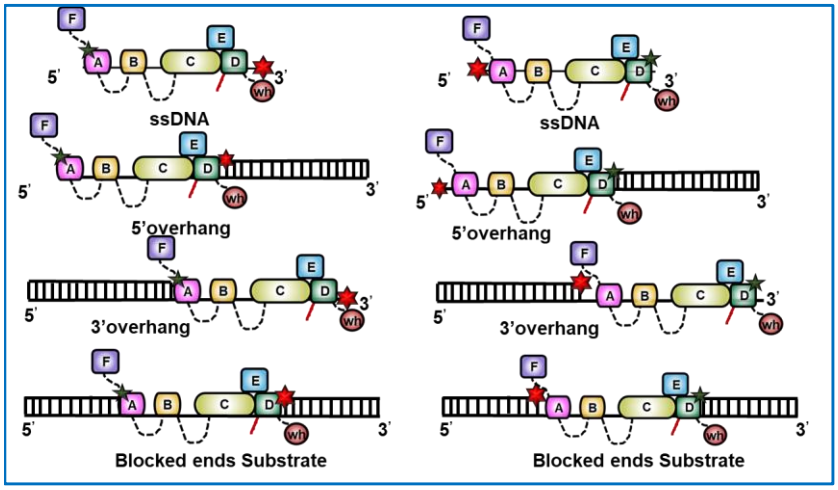

Low FRET

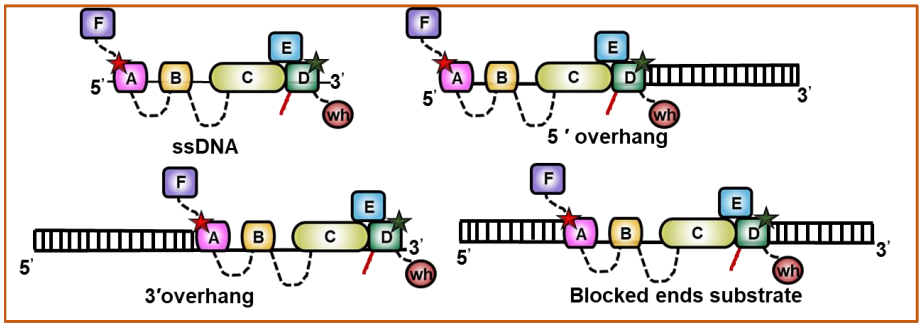

Dual labeled RPA

Cy3; Cy5

Figure 7-6: Schematics of FRET pairs that can be employed to understand RPA-DBD dynamics in various DNA-contexts. FRET can be performed with either fluorescently labeled DNA and Single- fluorescent labeled RPA-DBD (top and middle), or with dual fluorescently labeled RPA (bottom). Each combination should ideally provide unique FRET signatures to understand DBD dynamics.

7.5 Proposed model of RPA's conformation driving specific functions

This dissertation research highlights the mechanistic intricacies of how a multidomain protein, such as RPA, can achieve functional versatility by the virtue of conformational arrangements and rearrangements. Several process such as cell-cycle regulation, DNA replication, recombination, repair, telomere maintenance, transcription etc., are extensively regulated and are critical for cell survivability. RPA functions in several of these critical pathways, often acting as a hub protein to control and coordinate the flux of these pathways. How a single protein regulates/ is regulated to control these pathways is still far from being understood. Yet, it is conceivable that there has to be a mechanism in place that allows to fine-tune RPA-DNA binding that would be favorable for continuing a particular pathway over others.

Our study reveals that RPA-DNA binding is very dynamic in nature and can be modulated in distinct ways by several factors: concentration of ssDNA, length of ssDNA, structure of ssDNA encountered, modifications of several key amino acids and in presence of RIPs. Each of these factors can selectively affect the nature of RPA-DNA binding which could ultimately drive specific processes. For example, in a scenario where there are long ssDNAs but not enough RPA to completely saturate the long ssDNA, binding of RPA to DNA would still leave excess ssDNA space. This particular structure could be a potential recognition signal for recruitment of a particular RIP that

requires both RPA-DNA filament and additional free nucleotides to initially gain access to ssDNA. This RIP could now modulate RPA-DNA binding, to either stabilize or displace RPA from DNA. In scenarios where ssDNA is flanked by duplex DNA, conformational freedom of DBDs close to the duplex region can be affected, as RPA does not bind to dsDNA. Similarly, conformations of DBDs in the vicinity of an RNA-DNA hybrid would potentially be different than on only ssDNA (with no RNA-DNA hybrid), as RPA has a weaker binding affinity to RNA. Under these conditions, a protein that can bind to both dsDNA and ssDNA, or, ssDNA and RNA, respectively, would potentially affect conformations of DNA bound RPA in distinct ways. Each of these effects could then dictate the nature and extent of RPA-DNA binding and progression of specific pathways.

During cell-cycle regulation or DDR, phosphorylation of one or several serine/ threonine could further affect the conformations of individual RPA-DBDs, or, overall RPA assembly on DNA (as seen in chapter 6 with RPA-S178D). Subsequent changes in conformations could be recognized by a particular RIP or several RIPs. These RIPs are then recruited to the RPA nucleoprotein filament to further continue an ongoing process. In addition, modification of key amino acid residues that are actively participating in either protein-protein interactions, subunit-subunit interactions, DBD-DBD interactions or DBD-DNA interactions can further streamline how RPA functions in a particular pathway. An example of this is shown in appendix II, where, mutating the conserved NKK motif in DBD-C affected overall conformation of RPA on DNA. It should be noted that mutating NKK to DRR, or, NKK to NKA, did not affect the DBD-A or DBD-D dynamics. Therefore, the change in conformation probably arises due to effects in DBD-

B and DBD-C interaction, or, change in the way DNA passes from DBD-B to DBD-C. RPA with mutations in the NKK motif are readily displaced by Srs2 helicase, when compared to RPA-wt. *In vivo*, RPA with mutations in the NKK motif rescues the Δ *Srs2* phenotype (Dhingra et. al., unpublished). Therefore, modulating the interactions between NKK motif and DNA could directly affect HR, as it would result in RPA being easily outcompeted by other proteins (such as Rad51) attempting to gain access to the DNA.

The dynamicity of RPA is further highlighted by the fact that RPA- DBDs undergo several association-dissociation events on ssDNA, independent of the external factors. Each of these association-dissociation events could serve as a potential opportunity for a RIP to change the pre-existing nature of RPA-DNA binding. This could either stabilize RPA, completely displace RPA from DNA, or enable a second RIP to gain access to DNA. The latter is seen in case of Rad52, where, it selectively abolishes the fourth binding state of DBD-D. In presence of Rad52, loss of this fourth state combined with stimulation of Rad51's ATPase activity, could be a synergistic effect in enhancing RPA displacement by Rad51, potentially because Rad51 has to now overcome 3 binding states of RPA, instead of 4.

In summary, our research highlights the various aspects of RPA's conformations playing a key role in driving RPA's specific functions in various DNA metabolic pathways. The methodology used throughout this dissertation research and the insights gained highlighting a multi-domain protein can be implemented to understanding of similar proteins that participate in DNA related processes like replication, transcription, recombination, and repair.

BIBLIOGRAPHY

Ait Saada, A., Lambert, S. A. E., & Carr, A. M. (2018). Preserving replication fork integrity and competence via the homologous recombination pathway. *DNA Repair*, *71*, 135–147. https://doi.org/10.1016/J.DNAREP.2018.08.017

Albuquerque, C. P., Smolka, M. B., Payne, S. H., Bafna, V., Eng, J., & Zhou, H. (2008). A multidimensional chromatography technology for in-depth phosphoproteome analysis. *Molecular and Cellular Proteomics*, *7*(7), 1389–1396. https://doi.org/10.1074/mcp.M700468-MCP200

Alford, J. R., Kwok, S. C., Roberts, J. N., Wuttke, D. S., Kendrick, B. S., Carpenter, J. F., & Randolph, T. W. (2008). High concentration formulations of recombinant human interleukin-1 receptor antagonist: I. Physical characterization. *Journal of Pharmaceutical Sciences*, *97*(8), 3035–3050. https://doi.org/10.1002/jps.21199

Anantha, R. W., & Borowiec, J. A. (2009). Mitotic crisis: the unmasking of a novel role for RPA. *Cell Cycle (Georgetown, Tex.)*, *8*(3), 357–361. https://doi.org/10.4161/cc.8.3.7496

Anderson, B. J., Larkin, C., Guja, K., & Schildbach, J. F. (2008). Chapter 12 Using Fluorophore-Labeled Oligonucleotides to Measure Affinities of Protein–DNA Interactions. *Methods in Enzymology*, *450*, 253–272. https://doi.org/10.1016/S0076-6879(08)03412-5

Antony, E., Tomko, E. J., Xiao, Q., Krejci, L., Lohman, T. M., & Ellenberger, T. (2009a). Article Srs2 Disassembles Rad51 Filaments by a Protein-Protein Interaction Triggering ATP Turnover and Dissociation of Rad51 from DNA. *Molecular Cell*, *35*, 105–115. https://doi.org/10.1016/j.molcel.2009.05.026

Antony, E., Tomko, E. J., Xiao, Q., Krejci, L., Lohman, T. M., & Ellenberger, T. (2009b). Srs2 Disassembles Rad51 Filaments by a Protein-Protein Interaction Triggering ATP Turnover and Dissociation of Rad51 from DNA. *Molecular Cell*, *35*(1), 105. https://doi.org/10.1016/J.MOLCEL.2009.05.026

Arunkumar, A. I., Stauffer, M. E., Bochkareva, E., Bochkarev, A., & Chazin, W. J. (2003a). Independent and coordinated functions of replication protein A tandem high affinity single-stranded DNA binding domains. *The Journal of Biological Chemistry*, *278*(42), 41077–41082. https://doi.org/10.1074/jbc.M305871200

Arunkumar, A. I., Stauffer, M. E., Bochkareva, E., Bochkarev, A., & Chazin, W. J. (2003b). Independent and Coordinated Functions of Replication Protein A Tandem High Affinity Single-stranded DNA Binding Domains. *Journal of Biological*

Chemistry, *278*(42), 41077–41082. https://doi.org/10.1074/jbc.M305871200

Arunkumar, A. I., Stauffer, M. E., Bochkareva, E., Bochkarev, A., & Chazin, W. J. (2003c). Independent and Coordinated Functions of Replication Protein A Tandem High Affinity Single-stranded DNA Binding Domains. *Journal of Biological Chemistry* , *278*(42), 41077–41082. https://doi.org/10.1074/jbc.M305871200

Awate, S., & Brosh, R. M. (2017, June 8). Interactive roles of DNA helicases and translocases with the single-stranded DNA binding protein RPA in nucleic acid metabolism. *International Journal of Molecular Sciences*. MDPI AG. https://doi.org/10.3390/ijms18061233

Ball, H. L., & Cortez, D. (2005). ATRIP oligomerization is required for ATR-dependent checkpoint signaling. *The Journal of Biological Chemistry*, *280*(36), 31390–31396. https://doi.org/10.1074/jbc.M504961200

Bartrand, A. J., Iyasu, D., & Brush, G. S. (2004). DNA stimulates Mec1-mediated phosphorylation of replication protein A. *The Journal of Biological Chemistry*, *279*(25), 26762–26767. https://doi.org/10.1074/jbc.M312353200

Bastos de Oliveira, F. M., Kim, D., Cussiol, J. R., Das, J., Jeong, M. C., Doerfler, L., … Smolka, M. B. (2015). Phosphoproteomics Reveals Distinct Modes of Mec1/ATR Signaling during DNA Replication. *Molecular Cell*, *57*(6), 1124–1132. https://doi.org/10.1016/J.MOLCEL.2015.01.043

Beattie, B. K., & Merrill, A. R. (1999). A fluorescence investigation of the active site of Pseudomonas aeruginosa exotoxin A. *The Journal of Biological Chemistry*, *274*(22), 15646–15654. https://doi.org/10.1074/jbc.274.22.15646

Benson, F. E., Baumann, P., & West, S. C. (1998). Synergistic actions of Rad51 and Rad52 in recombination and DNA repair. *Nature*, *391*(6665), 401–404. https://doi.org/10.1038/34937

Bhat, K. P., Bétous, R., & Cortez, D. (2015). High-affinity DNA-binding domains of replication protein A (RPA) direct SMARCAL1-dependent replication fork remodeling. *The Journal of Biological Chemistry*, *290*(7), 4110–4117. https://doi.org/10.1074/jbc.M114.627083

Bhowmick, R., Minocherhomji, S., & Hickson, I. D. (2016). RAD52 Facilitates Mitotic DNA Synthesis Following Replication Stress. *Molecular Cell*, *64*(6), 1117–1126. https://doi.org/10.1016/j.molcel.2016.10.037

Binz, S. K., Sheehan, A. M., & Wold, M. S. (2004a). Replication Protein A

phosphorylation and the cellular response to DNA damage. *DNA Repair*, *3*(8–9), 1015–1024. https://doi.org/10.1016/J.DNAREP.2004.03.028

Binz, S. K., Sheehan, A. M., & Wold, M. S. (2004b). Replication Protein A phosphorylation and the cellular response to DNA damage. *DNA Repair*, *3*(8–9), 1015–1024. https://doi.org/10.1016/j.dnarep.2004.03.028

Binz, S. K., & Wold, M. S. (2008). Regulatory functions of the N-terminal domain of the 70-kDa subunit of replication protein A (RPA). *The Journal of Biological Chemistry*, *283*(31), 21559–21570. https://doi.org/10.1074/jbc.M802450200

Biswas, H., Goto, G., Wang, W., Sung, P., & Sugimoto, K. (2019). Ddc2ATRIP promotes Mec1ATR activation at RPA-ssDNA tracts. *PLOS Genetics*, *15*(8), e1008294. https://doi.org/10.1371/journal.pgen.1008294

Bjornson, K. P., Amaratunga, M., Moore, K. J. M., & Lohman, T. M. (1994). Single-turnover kinetics of helicase-catalyzed DNA unwinding monitored continuously by fluorescence energy transfer. *Biochemistry*, *33*(47), 14306–14316. https://doi.org/10.1021/bi00251a044

Blizzard, R. J., Backus, D. R., Brown, W., Bazewicz, C. G., Li, Y., & Mehl, R. A. (2015). Ideal Bioorthogonal Reactions Using A Site-Specifically Encoded Tetrazine Amino Acid. *Journal of the American Chemical Society*, *137*(32), 10044–10047. https://doi.org/10.1021/jacs.5b03275

Bochkarev, A., Bochkareva, E., Frappier, L., & Edwards, A. M. (1999). The crystal structure of the complex of replication protein A subunits RPA32 and RPA14 reveals a mechanism for single-stranded DNA binding. *The EMBO Journal*, *18*(16), 4498–4504. https://doi.org/10.1093/emboj/18.16.4498

Bochkareva, E, Belegu, V., Korolev, S., & Bochkarev, A. (2001). Structure of the major single-stranded DNA-binding domain of replication protein A suggests a dynamic mechanism for DNA binding. *The EMBO Journal*, *20*(3), 612–618. https://doi.org/10.1093/emboj/20.3.612

Bochkareva, Elena, Frappier, L., Edwards, A. M., & Bochkarev, A. (1998). The RPA32 Subunit of Human Replication Protein A Contains a Single-stranded DNA-binding Domain. *Journal of Biological Chemistry*, *273*(7), 3932–3936. https://doi.org/10.1074/jbc.273.7.3932

Bochkareva, Elena, Kaustov, L., Ayed, A., Yi, G.-S., Lu, Y., Pineda-Lucena, A., … Bochkarev, A. (2005). Single-stranded DNA mimicry in the p53 transactivation domain interaction with replication protein A. *Proceedings of the National Academy of Sciences of the United States of America*, *102*(43), 15412–15417.

https://doi.org/10.1073/pnas.0504614102

Bochkareva, Elena, Korolev, S., Lees-Miller, S. P., & Bochkarev, A. (2002a). Structure of the RPA trimerization core and its role in the multistep DNA-binding mechanism of RPA. *The EMBO Journal*, *21*(7), 1855–1863. https://doi.org/10.1093/emboj/21.7.1855

Bochkareva, Elena, Korolev, S., Lees-Miller, S. P., & Bochkarev, A. (2002b). Structure of the RPA trimerization core and its role in the multistep DNA-binding mechanism of RPA. *The EMBO Journal*, *21*(7), 1855–1863. https://doi.org/10.1093/emboj/21.7.1855

Boehm, E. M., Subramanyam, S., Ghoneim, M., Washington, M. T., & Spies, M. (2016). Quantifying the Assembly of Multicomponent Molecular Machines by Single-Molecule Total Internal Reflection Fluorescence Microscopy. *Methods in Enzymology*, *581*, 105–145. https://doi.org/10.1016/bs.mie.2016.08.019

Brill, S. J., & Bastin-Shanower, S. (1998). Identification and characterization of the fourth single-stranded-DNA binding domain of replication protein A. *Molecular and Cellular Biology*, *18*(12), 7225–7234. https://doi.org/10.1128/mcb.18.12.7225

Brosey, C. A., Chagot, M.-E., Ehrhardt, M., Pretto, D. I., Weiner, B. E., & Chazin, W. J. (2009). NMR analysis of the architecture and functional remodeling of a modular multidomain protein, RPA. *Journal of the American Chemical Society*, *131*(18), 6346–6347. https://doi.org/10.1021/ja9013634

Brosey, C. A., Soss, S. E., Brooks, S., Yan, C., Ivanov, I., Dorai, K., & Chazin, W. J. (2015). Functional dynamics in replication protein A DNA binding and protein recruitment domains. *Structure (London, England : 1993)*, *23*(6), 1028–1038. https://doi.org/10.1016/j.str.2015.04.008

Brosey, C. A., Yan, C., Tsutakawa, S. E., Heller, W. T., Rambo, R. P., Tainer, J. A., … Chazin, W. J. (2013). A new structural framework for integrating replication protein A into DNA processing machinery. *Nucleic Acids Research*, *41*(4), 2313–2327. https://doi.org/10.1093/nar/gks1332

Brouwer, I., Zhang, H., Candelli, A., Normanno, D., Peterman, E. J. G., Wuite, G. J. L., & Modesti, M. (2017). Human RAD52 Captures and Holds DNA Strands, Increases DNA Flexibility, and Prevents Melting of Duplex DNA: Implications for DNA Recombination. *Cell Reports*, *18*(12), 2845–2853. https://doi.org/10.1016/j.celrep.2017.02.068

Brush, G. S., & Kelly, T. J. (2000). Phosphorylation of the replication protein A large subunit in the Saccharomyces cerevisiae checkpoint response. *Nucleic Acids*

Research, *28*(19), 3725–3732. https://doi.org/10.1093/nar/28.19.3725

Brush, G. S., Morrow, D. M., Hieter, P., & Kelly, T. J. (1996). The ATM homologue MEC1 is required for phosphorylation of replication protein A in yeast. *Proceedings of the National Academy of Sciences of the United States of America*, *93*(26), 15075–15080. https://doi.org/10.1073/pnas.93.26.15075

Bujalowski, W., Overman, L. B., & Lohman, T. M. (1988). Binding mode transitions of Escherichia coli single strand binding protein-single-stranded DNA complexes. Cation, anion, pH, and binding density effects. *Journal of Biological Chemistry* , *263*(10), 4629–4640. Retrieved from http://www.jbc.org/content/263/10/4629.abstract

Burgers, P. M. (2011). It's all about flaps: Dna2 and checkpoint activation. *Cell Cycle (Georgetown, Tex.)*, *10*(15), 2417–2418. https://doi.org/10.4161/cc.10.15.16201

Byrne, B. M., & Oakley, G. G. (2019). Replication protein A, the laxative that keeps DNA regular: The importance of RPA phosphorylation in maintaining genome stability. *Seminars in Cell & Developmental Biology*, *86*, 112–120. https://doi.org/10.1016/J.SEMCDB.2018.04.005

Candelli, A., Holthausen, J. T., Depken, M., Brouwer, I., Franker, M. A. M., Marchetti, M., … Peterman, E. J. G. (2014). Visualization and quantification of nascent RAD51 filament formation at single-monomer resolution. *Proceedings of the National Academy of Sciences of the United States of America*, *111*(42), 15090–15095. https://doi.org/10.1073/pnas.1307824111

Ceccaldi, R., Rondinelli, B., & D'Andrea, A. D. (2016). Repair Pathway Choices and Consequences at the Double-Strand Break. *Trends in Cell Biology*, *26*(1), 52–64. https://doi.org/10.1016/j.tcb.2015.07.009

Chan, H., Wang, Y., & Feigon, J. (2017). Progress in Human and Tetrahymena Telomerase Structure Determination. *Annual Review of Biophysics*, *46*, 199–225. https://doi.org/10.1146/annurev-biophys-062215-011140

Chatterjee, A., Guo, J., Lee, H. S., & Schultz, P. G. (2013). A genetically encoded fluorescent probe in mammalian cells. *Journal of the American Chemical Society*, *135*(34), 12540–12543. https://doi.org/10.1021/ja4059553

Chen, J., Le, S., Basu, A., Chazin, W. J., & Yan, J. (2015). Mechanochemical regulations of RPA's binding to ssDNA. *Scientific Reports*, *5*, 9296. https://doi.org/10.1038/srep09296

Chen, R., Subramanyam, S., Elcock, A. H., Spies, M., & Wold, M. S. (2016a). Dynamic binding of replication protein a is required for DNA repair. *Nucleic Acids Research*, *44*(12), 5758–5772. https://doi.org/10.1093/nar/gkw339

Chen, R., Subramanyam, S., Elcock, A. H., Spies, M., & Wold, M. S. (2016b). Dynamic binding of replication protein a is required for DNA repair. *Nucleic Acids Research*, *44*(12), 5758–5772. https://doi.org/10.1093/nar/gkw339

Chen, R., & Wold, M. S. (2014a). Replication protein A: single-stranded DNA's first responder: dynamic DNA-interactions allow replication protein A to direct single-strand DNA intermediates into different pathways for synthesis or repair. *BioEssays : News and Reviews in Molecular, Cellular and Developmental Biology*, *36*(12), 1156–1161. https://doi.org/10.1002/bies.201400107

Chen, R., & Wold, M. S. (2014b). Replication protein A: Single-stranded DNA's first responder. *BioEssays*, *36*(12), 1156–1161. https://doi.org/10.1002/bies.201400107

Chung, I., & Zhao, X. (2015). DNA break-induced sumoylation is enabled by collaboration between a SUMO ligase and the ssDNA-binding complex RPA. *Genes & Development*, *29*(15), 1593–1598. https://doi.org/10.1101/gad.265058.115

Cobb, J. A., Schleker, T., Rojas, V., Bjergbaek, L., Tercero, J. A., & Gasser, S. M. (2005). Replisome instability, fork collapse, and gross chromosomal rearrangements arise synergistically from Mec1 kinase and RecQ helicase mutations. *Genes & Development*, *19*(24), 3055–3069. https://doi.org/10.1101/gad.361805

Collins, B. E., Ye, L. F., Duzdevich, D., & Greene, E. C. (2014). DNA curtains. In *Methods in cell biology* (Vol. 123, pp. 217–234). https://doi.org/10.1016/B978-0-12-420138-5.00012-4

Cooper, G. M. (2000). DNA Repair. Retrieved from https://www.ncbi.nlm.nih.gov/books/NBK9900/

Cremona, C. A., Sarangi, P., Yang, Y., Hang, L. E., Rahman, S., & Zhao, X. (2012). Extensive DNA Damage-Induced Sumoylation Contributes to Replication and Repair and Acts in Addition to the Mec1 Checkpoint. *Molecular Cell*, *45*(3), 422–432. https://doi.org/10.1016/J.MOLCEL.2011.11.028

Daley, J. M., Gaines, W. A., Kwon, Y., & Sung, P. (2014). Regulation of DNA pairing in homologous recombination. *Cold Spring Harbor Perspectives in Biology*, *6*(11), a017954. https://doi.org/10.1101/cshperspect.a017954

Daley, J. M., Kwon, Y., Niu, H., & Sung, P. (2013). Investigations of homologous

recombination pathways and their regulation. *The Yale Journal of Biology and Medicine*, *86*(4), 453–461. Retrieved from http://www.ncbi.nlm.nih.gov/pubmed/24348209

Danyal, K., Shaw, S., Page, T. R., Duval, S., Horitani, M., Marts, A. R., … Antony, E. (2016). Negative cooperativity in the nitrogenase Fe protein electron delivery cycle. *Proceedings of the National Academy of Sciences of the United States of America*, *113*(40), E5783–E5791. https://doi.org/10.1073/pnas.1613089113

Davenport, E. P., Harris, D. F., Origanti, S., & Antony, E. (2016). Rad51 Nucleoprotein Filament Disassembly Captured Using Fluorescent Plasmodium falciparum SSB as a Reporter for Single-Stranded DNA. *PloS One*, *11*(7), e0159242. https://doi.org/10.1371/journal.pone.0159242

de Laat, W. L., Appeldoorn, E., Sugasawa, K., Weterings, E., Jaspers, N. G. J., & Hoeijmakers, J. H. J. (1998). DNA-binding polarity of human replication protein A positions nucleases in nucleotide excision repair. *Genes & Development*, *12*(16), 2598–2609. https://doi.org/10.1101/gad.12.16.2598

Deng, X., Prakash, A., Dhar, K., Baia, G. S., Kolar, C., Oakley, G. G., & Borgstahl, G. E. O. (2009). Human Replication Protein A−Rad52−Single-Stranded DNA Complex: Stoichiometry and Evidence for Strand Transfer Regulation by Phosphorylation. *Biochemistry*, *48*(28), 6633–6643. https://doi.org/10.1021/bi900564k

Deshpande, I., Seeber, A., Shimada, K., Keusch, J. J., Gut, H., & Gasser, S. M. (2017). Structural Basis of Mec1-Ddc2-RPA Assembly and Activation on Single-Stranded DNA at Sites of Damage. *Molecular Cell*, *68*(2), 431-445.e5. https://doi.org/10.1016/J.MOLCEL.2017.09.019

Dickson, A. M., Krasikova, Y., Pestryakov, P., Lavrik, O., & Wold, M. S. (2009). Essential functions of the 32 kDa subunit of yeast replication protein A. *Nucleic Acids Research*, *37*(7), 2313–2326. https://doi.org/10.1093/nar/gkp090

Dou, H., Huang, C., Singh, M., Carpenter, P. B., & Yeh, E. T. H. (2010). Regulation of DNA repair through deSUMOylation and SUMOylation of replication protein A complex. *Molecular Cell*, *39*(3), 333–345. https://doi.org/10.1016/j.molcel.2010.07.021

Dubois, J.-C., Yates, M., Gaudreau-Lapierre, A., Clément, G., Cappadocia, L., Gaudreau, L., … Maréchal, A. (2017). A phosphorylation-and-ubiquitylation circuitry driving ATR activation and homologous recombination. *Nucleic Acids Research*, *45*(15), 8859–8872. https://doi.org/10.1093/nar/gkx571

Eckerich, C., Fackelmayer, F. O., & Knippers, R. (2001). Zinc affects the conformation

of nucleoprotein filaments formed by replication protein A (RPA) and long natural DNA molecules. *Biochimica et Biophysica Acta - Molecular Cell Research*, *1538*(1), 67–75. https://doi.org/10.1016/S0167-4889(00)00138-5

Fan, J., & Pavletich, N. P. (2012a). Structure and conformational change of a replication protein A heterotrimer bound to ssDNA. *Genes & Development*, *26*(20), 2337–2347. https://doi.org/10.1101/gad.194787.112

Fan, J., & Pavletich, N. P. (2012b). Structure and conformational change of a replication protein A heterotrimer bound to ssDNA. *Genes & Development*, *26*(20), 2337–2347. https://doi.org/10.1101/gad.194787.112

Fanning, E., Klimovich, V., & Nager, A. R. (2006). A dynamic model for replication protein A (RPA) function in DNA processing pathways. *Nucleic Acids Research*, *34*(15), 4126–4137. https://doi.org/10.1093/nar/gkl550

Feldkamp, M. D., Mason, A. C., Eichman, B. F., & Chazin, W. J. (2014). Structural analysis of replication protein a recruitment of the DNA damage response protein SMARCAL1. *Biochemistry*, *53*(18), 3052–3061. https://doi.org/10.1021/bi500252w

Feng, Z., Scott, S. P., Bussen, W., Sharma, G. G., Guo, G., Pandita, T. K., & Powell, S. N. (2011). Rad52 inactivation is synthetically lethal with BRCA2 deficiency. *Proceedings of the National Academy of Sciences of the United States of America*, *108*(2), 686–691. https://doi.org/10.1073/pnas.1010959107

Ferrari, M. E., Bujalowski, W., & Lohman, T. M. (1994). Co-operative Binding of Escherichia coli SSB Tetramers to Single-stranded DNA in the (SSB)35 Binding Mode. *Journal of Molecular Biology*, *236*(1), 106–123. https://doi.org/10.1006/jmbi.1994.1122

Fischer, C. J., & Lohman, T. M. (2004). ATP-dependent Translocation of Proteins along Single-stranded DNA: Models and Methods of Analysis of Pre-steady State Kinetics. *Journal of Molecular Biology*, *344*(5), 1265–1286. https://doi.org/10.1016/j.jmb.2004.10.004

Fischer, C. J., Tomko, E. J., Wu, C. G., & Lohman, T. M. (2012). Fluorescence Methods to Study DNA Translocation and Unwinding Kinetics by Nucleic Acid Motors. In *Methods in molecular biology (Clifton, N.J.)* (Vol. 875, pp. 85–104). https://doi.org/10.1007/978-1-61779-806-1_5

Fischer, C. J., Wooten, L., Tomko, E. J., & Lohman, T. M. (2010). Kinetics of motor protein translocation on single-stranded DNA. *Methods in Molecular Biology (Clifton, N.J.)*, *587*, 45–56. https://doi.org/10.1007/978-1-60327-355-8_4

Fox, C. F., & Kennedy, E. P. (1965). Specific labeling and partial purification of the M protein, a component of the beta-galactoside transport system of Escherichia coli. *Proceedings of the National Academy of Sciences*, *54*(3), 891–899. https://doi.org/10.1073/pnas.54.3.891

Game, J. C., & Mortimer, R. K. (1974). A genetic study of X-ray sensitive mutants in yeast. *Mutation Research/Fundamental and Molecular Mechanisms of Mutagenesis*, *24*(3), 281–292. https://doi.org/10.1016/0027-5107(74)90176-6

Gangavarapu, V., Maria, S. R. S., Prakash, S., & Prakash, L. (2011). Requirement of Replication Checkpoint Protein Kinases Mec1/Rad53 for Postreplication Repair in Yeast. *MBio*, *2*(3), e00079-11. https://doi.org/10.1128/MBIO.00079-11

Gasior, S. L., Wong, A. K., Kora, Y., Shinohara, A., & Bishop, D. K. (1998). Rad52 associates with RPA and functions with rad55 and rad57 to assemble meiotic recombination complexes. *Genes & Development*, *12*(14), 2208–2221. https://doi.org/10.1101/gad.12.14.2208

Ghoneim, M., & Spies, M. (2014). Direct correlation of DNA binding and single protein domain motion via dual illumination fluorescence microscopy. *Nano Letters*, *14*(10), 5920–5931. https://doi.org/10.1021/nl502890g

Gibb, B., Ye, L. F., Gergoudis, S. C., Kwon, Y., Niu, H., Sung, P., & Greene, E. C. (2014). Concentration-Dependent Exchange of Replication Protein A on Single-Stranded DNA Revealed by Single-Molecule Imaging. *PLoS ONE*, *9*(2), e87922. https://doi.org/10.1371/journal.pone.0087922

Gibb, B., Ye, L. F., Kwon, Y., Niu, H., Sung, P., & Greene, E. C. (2014a). Protein dynamics during presynaptic-complex assembly on individual single-stranded DNA molecules. *Nature Structural & Molecular Biology*, *21*(10), 893–900. https://doi.org/10.1038/nsmb.2886

Gibb, B., Ye, L. F., Kwon, Y., Niu, H., Sung, P., & Greene, E. C. (2014b). Protein dynamics during presynaptic-complex assembly on individual single-stranded DNA molecules. *Nature Structural & Molecular Biology*, *21*(10), 893–900. https://doi.org/10.1038/nsmb.2886

Glover, L., Marques, C. A., Suska, O., & Horn, D. (2019). Persistent DNA Damage Foci and DNA Replication with a Broken Chromosome in the African Trypanosome. *MBio*, *10*(4), e01252-19. https://doi.org/10.1128/mBio.01252-19

Gnügge, R., & Symington, L. S. (2017). Keeping it real: MRX-Sae2 clipping of natural substrates. *Genes & Development*, *31*(23–24), 2311–2312. https://doi.org/10.1101/gad.310771.117

Golub, E. I., Gupta, R. C., Haaf, T., Wold, M. S., & Radding, C. M. (1998). Interaction of human Rad51 recombination protein with single-stranded DNA binding protein, RPA. *Nucleic Acids Research*, *26*(23), 5388–5393. https://doi.org/10.1093/nar/26.23.5388

Gorman, J., Wang, F., Redding, S., Plys, A. J., Fazio, T., Wind, S., … Greene, E. C. (2012). Single-molecule imaging reveals target-search mechanisms during DNA mismatch repair. *Proceedings of the National Academy of Sciences*, *109*(45), E3074–E3083. https://doi.org/10.1073/pnas.1211364109

Grimme, J. M., Honda, M., Wright, R., Okuno, Y., Rothenberg, E., Mazin, A. V, … Spies, M. (2010). Human Rad52 binds and wraps single-stranded DNA and mediates annealing via two hRad52-ssDNA complexes. *Nucleic Acids Research*, *38*(9), 2917–2930. https://doi.org/10.1093/nar/gkp1249

Hammill, J. T., Miyake-Stoner, S., Hazen, J. L., Jackson, J. C., & Mehl, R. A. (2007). Preparation of site-specifically labeled fluorinated proteins for 19F-NMR structural characterization. *Nature Protocols*, *2*, 2601. Retrieved from https://doi.org/10.1038/nprot.2007.379

Hamon, L., Pastré, D., Dupaigne, P., Le Breton, C., Le Cam, E., & Piétrement, O. (2007). High-resolution AFM imaging of single-stranded DNA-binding (SSB) protein - DNA complexes. *Nucleic Acids Research*, *35*(8). https://doi.org/10.1093/nar/gkm147

Hanamshet, K., Mazina, O. M., & Mazin, A. V. (2016). Reappearance from Obscurity: Mammalian Rad52 in Homologous Recombination. *Genes*, *7*(9), 63. https://doi.org/10.3390/genes7090063

Haring, S. J., Mason, A. C., Binz, S. K., & Wold, M. S. (2008). Cellular functions of human RPA1. Multiple roles of domains in replication, repair, and checkpoints. *The Journal of Biological Chemistry*, *283*(27), 19095–19111. https://doi.org/10.1074/jbc.M800881200

Hass, C. S., Lam, K., & Wold, M. S. (2012). Repair-specific functions of replication protein A. *The Journal of Biological Chemistry*, *287*(6), 3908–3918. https://doi.org/10.1074/jbc.M111.287441

Hays, S. L., Firmenich, A. A., Massey, P., Banerjee, R., & Berg, P. (1998a). Studies of the interaction between Rad52 protein and the yeast single-stranded DNA binding protein RPA. *Molecular and Cellular Biology*, *18*(7), 4400–4406. https://doi.org/10.1128/mcb.18.7.4400

Hays, S. L., Firmenich, A. A., Massey, P., Banerjee, R., & Berg, P. (1998b). Studies of

the interaction between Rad52 protein and the yeast single-stranded DNA binding protein RPA. *Molecular and Cellular Biology*, *18*(7), 4400–4406. https://doi.org/10.1128/mcb.18.7.4400

Hedglin, M., Aitha, M., Pedley, A., & Benkovic, S. J. (2019). Replication protein A dynamically regulates monoubiquitination of proliferating cell nuclear antigen. *The Journal of Biological Chemistry*, *294*(13), 5157–5168. https://doi.org/10.1074/jbc.RA118.005297

Hengel, S. R., Malacaria, E., Folly da Silva Constantino, L., Bain, F. E., Diaz, A., Koch, B. G., … Spies, M. (2016). Small-molecule inhibitors identify the RAD52-ssDNA interaction as critical for recovery from replication stress and for survival of BRCA2 deficient cells. *ELife*, *5*. https://doi.org/10.7554/eLife.14740

Hillisch, A., Lorenz, M., & Diekmann, S. (2001). Recent advances in FRET: distance determination in protein-DNA complexes. *Current Opinion in Structural Biology*, *11*(2), 201–207. Retrieved from http://www.ncbi.nlm.nih.gov/pubmed/11297928

Hwang, H., & Myong, S. (2014). Protein induced fluorescence enhancement (PIFE) for probing protein–nucleic acid interactions. *Chemical Society Reviews*, *43*(4), 1221. https://doi.org/10.1039/C3CS60201J

Iftode, C., & Borowiec, J. A. (2000). 5‘ → 3‘ Molecular Polarity of Human Replication Protein A (hRPA) Binding to Pseudo-Origin DNA Substrates †. *Biochemistry*, *39*(39), 11970–11981. https://doi.org/10.1021/bi0005761

Ikegami, T., Kuraoka, I., Saijo, M., Kodo, N., Kyogoku, Y., Morikawa, K., … Shirakawa, M. (1998). Solution structure of the DNA- and RPA-binding domain of the human repair factor XPA. *Nature Structural & Molecular Biology*, *5*(8), 701–706. https://doi.org/10.1038/1400

Iwona M. Wyka, ‡, Kajari Dhar, ‡, Sara K. Binz, and, & Wold*, M. S. (2003). Replication Protein A Interactions with DNA: Differential Binding of the Core Domains and Analysis of the DNA Interaction Surface†. https://doi.org/10.1021/BI034930H

Jackson, D., Dhar, K., Wahl, J. K., Wold, M. S., & Borgstahl, G. E. O. (2002). Analysis of the human replication protein A:Rad52 complex: evidence for crosstalk between RPA32, RPA70, Rad52 and DNA. *Journal of Molecular Biology*, *321*(1), 133–148. https://doi.org/10.1016/s0022-2836(02)00541-7

Jeggo, P. A., & Lobrich, M. (2015). How cancer cells hijack DNA double-strand break repair pathways to gain genomic instability. *Biochemical Journal*, *471*(1), 1–11. https://doi.org/10.1042/BJ20150582

Jeggo, Penny A., Pearl, L. H., & Carr, A. M. (2016). DNA repair, genome stability and cancer: a historical perspective. *Nature Reviews Cancer*, *16*(1), 35–42. https://doi.org/10.1038/nrc.2015.4

Kagawa, W., Arai, N., Ichikawa, Y., Saito, K., Sugiyama, S., Saotome, M., … Kurumizaka, H. (2014). Functional analyses of the C-terminal half of the Saccharomyces cerevisiae Rad52 protein. *Nucleic Acids Research*, *42*(2), 941–951. https://doi.org/10.1093/nar/gkt986

Kagawa, W., Kurumizaka, H., Ishitani, R., Fukai, S., Nureki, O., Shibata, T., & Yokoyama, S. (2002). Crystal Structure of the Homologous-Pairing Domain from the Human Rad52 Recombinase in the Undecameric Form. *Molecular Cell*, *10*(2), 359–371. https://doi.org/10.1016/S1097-2765(02)00587-7

Kaniecki, K., De Tullio, L., Gibb, B., Kwon, Y., Sung, P., & Greene, E. C. (2017). Dissociation of Rad51 Presynaptic Complexes and Heteroduplex DNA Joints by Tandem Assemblies of Srs2. *Cell Reports*, *21*(11), 3166–3177. https://doi.org/10.1016/j.celrep.2017.11.047

Kemmerich, F. E., Daldrop, P., Pinto, C., Levikova, M., Cejka, P., & Seidel, R. (2016). Force regulated dynamics of RPA on a DNA fork. *Nucleic Acids Research*, *44*(12), 5837–5848. https://doi.org/10.1093/nar/gkw187

Kim, C, Snyder, R. O., & Wold, M. S. (1992). Binding properties of replication protein A from human and yeast cells. *Molecular and Cellular Biology*, *12*(7), 3050–3059. https://doi.org/10.1128/mcb.12.7.3050

Kim, Changsoo, Paulus, B. F., & Wold, M. S. (1994). Interactions of human replication protein A with oligonucleotides. *Biochemistry*, *33*(47), 14197–14206. https://doi.org/10.1021/bi00251a031

Kolpashchikov, D. M., Khodyreva, S. N., Khlimankov, D. Y., Wold, M. S., Favre, A., & Lavrik, O. I. (2001). Polarity of human replication protein A binding to DNA. *Nucleic Acids Research*, *29*(2), 373–379. https://doi.org/10.1093/nar/29.2.373

Kondo, T., Wakayama, T., Naiki, T., Matsumoto, K., & Sugimoto, K. (2001). Recruitment of Mec1 and Ddc1 Checkpoint Proteins to Double-Strand Breaks Through Distinct Mechanisms. *Science*, *294*(5543), 867–870. https://doi.org/10.1126/science.1063827

Kowalczykowski, S C. (2000). Initiation of genetic recombination and recombination-dependent replication. *Trends in Biochemical Sciences*, *25*(4), 156–165. Retrieved from http://www.ncbi.nlm.nih.gov/pubmed/10754547

Kowalczykowski, S C, Dixon, D. A., Eggleston, A. K., Lauder, S. D., & Rehrauer, W. M. (1994). Biochemistry of homologous recombination in Escherichia coli. *Microbiological Reviews*, *58*(3), 401–465. Retrieved from http://www.ncbi.nlm.nih.gov/pubmed/7968921

Kowalczykowski, Stephen C., New, J. H., Sugiyama, T., & Zaitseva, E. (1998). Rad52 protein stimulates DNA strand exchange by Rad51 and replicationprotein A. *Nature*, *391*(6665), 407–410. https://doi.org/10.1038/34950

Kozlov, A. G., Cox, M. M., & Lohman, T. M. (2010). Regulation of single-stranded DNA binding by the C termini of Escherichia coli single-stranded DNA-binding (SSB) protein. *The Journal of Biological Chemistry*, *285*(22), 17246–17252. https://doi.org/10.1074/jbc.M110.118273

Kozlov, A. G., Galletto, R., & Lohman, T. M. (2012). SSB-DNA binding monitored by fluorescence intensity and anisotropy. *Methods in Molecular Biology (Clifton, N.J.)*, *922*, 55–83. https://doi.org/10.1007/978-1-62703-032-8_4

Krasikova, Y. S., Rechkunova, N. I., Maltseva, E. A., & Lavrik, O. I. (2018). RPA and XPA interaction with DNA structures mimicking intermediates of the late stages in nucleotide excision repair. *PloS One*, *13*(1), e0190782. https://doi.org/10.1371/journal.pone.0190782

Krejci, L., Van Komen, S., Li, Y., Villemain, J., Reddy, M. S., Klein, H., … Sung, P. (2003). DNA helicase Srs2 disrupts the Rad51 presynaptic filament. *Nature*, *423*(6937), 305–309. https://doi.org/10.1038/nature01577

Krogh, B. O., & Symington, L. S. (2004). Recombination Proteins in Yeast. *Annual Review of Genetics*, *38*(1), 233–271. https://doi.org/10.1146/annurev.genet.38.072902.091500

Kumaran, S., Kozlov, A. G., & Lohman, T. M. (2006). *Saccharomyces cerevisiae* Replication Protein A Binds to Single-Stranded DNA in Multiple Salt-Dependent Modes †. *Biochemistry*, *45*(39), 11958–11973. https://doi.org/10.1021/bi060994r

Laat, Wouter L. de, Appeldoorn, E., Sugasawa, K., Weterings, E., Jaspers, N. G. J., & Hoeijmakers, J. H. J. (1998). DNA-binding polarity of human replication protein A positions nucleases in nucleotide excision repair. *Genes & Development*, *12*(16), 2598. Retrieved from https://www.ncbi.nlm.nih.gov/pmc/articles/PMC317078/

Lao, Y., Lee, C. G., & Wold, M. S. (1999). Replication Protein A Interactions with DNA. 2. Characterization of Double-Stranded DNA-Binding/Helix-Destabilization Activities and the Role of the Zinc-Finger Domain in DNA Interactions †. *Biochemistry*, *38*(13), 3974–3984. https://doi.org/10.1021/bi982371m

Lavrik, O. I., Kolpashchikov, D. M., Weisshart, K., Nasheuer, H. P., Khodyreva, S. N., & Favre, A. (1999). RPA subunit arrangement near the 3'-end of the primer is modulated by the length of the template strand and cooperative protein interactions. *Nucleic Acids Research*, *27*(21), 4235–4240. https://doi.org/10.1093/nar/27.21.4235

Lee, H. S., Guo, J., Lemke, E. A., Dimla, R. D., & Schultz, P. G. (2009). Genetic incorporation of a small, environmentally sensitive, fluorescent probe into proteins in Saccharomyces cerevisiae. *Journal of the American Chemical Society*, *131*(36), 12921–12923. https://doi.org/10.1021/ja904896s

Lee, K. S., Marciel, A. B., Kozlov, A. G., Schroeder, C. M., Lohman, T. M., & Ha, T. (2014). Ultrafast redistribution of E. coli SSB along long single-stranded DNA via intersegment transfer. *Journal of Molecular Biology*, *426*(13), 2413–2421. https://doi.org/10.1016/j.jmb.2014.04.023

Leisle, L., Valiyaveetil, F., Mehl, R. A., & Ahern, C. A. (2015). Incorporation of Non-Canonical Amino Acids. *Advances in Experimental Medicine and Biology*, *869*, 119–151. https://doi.org/10.1007/978-1-4939-2845-3_7

Li, S., Xu, Z., Xu, J., Zuo, L., Yu, C., Zheng, P., … Li, Q. (2018). Rtt105 functions as a chaperone for replication protein A to preserve genome stability. *The EMBO Journal*, *37*(17). https://doi.org/10.15252/embj.201899154

Li, Y., Hoskins, J. N., Sreerama, S. G., & Grayson, S. M. (2010). MALDI−TOF Mass Spectral Characterization of Polymers Containing an Azide Group: Evidence of Metastable Ions. *Macromolecules*, *43*(14), 6225–6228. https://doi.org/10.1021/ma100599n

Liao, H., Ji, F., Helleday, T., & Ying, S. (2018). Mechanisms for stalled replication fork stabilization: new targets for synthetic lethality strategies in cancer treatments. *EMBO Reports*, *19*(9). https://doi.org/10.15252/embr.201846263

Lisby, M., Barlow, J. H., Burgess, R. C., & Rothstein, R. (2004). Choreography of the DNA Damage Response. *Cell*, *118*(6), 699–713. https://doi.org/10.1016/j.cell.2004.08.015

Liu, C. C., & Schultz, P. G. (2010). Adding New Chemistries to the Genetic Code. *Annual Review of Biochemistry*, *79*(1), 413–444. https://doi.org/10.1146/annurev.biochem.052308.105824

Liu, S., Xu, Z., Leng, H., Zheng, P., Yang, J., Chen, K., … Li, Q. (2017). RPA binds histone H3-H4 and functions in DNA replication-coupled nucleosome assembly. *Science (New York, N.Y.)*, *355*(6323), 415–420. https://doi.org/10.1126/science.aah4712

Liu, W., Brock, A., Chen, S., Chen, S., & Schultz, P. G. (2007). Genetic incorporation of unnatural amino acids into proteins in mammalian cells. *Nature Methods*, *4*(3), 239–244. https://doi.org/10.1038/nmeth1016

Lloyd, J. A., McGrew, D. A., & Knight, K. L. (2005). Identification of Residues Important for DNA Binding in the Full-length Human Rad52 Protein. *Journal of Molecular Biology*, *345*(2), 239–249. https://doi.org/10.1016/J.JMB.2004.10.065

Lohman, T. M., Green, J. M., & Beyer, R. S. (1986). Large-scale overproduction and rapid purification of the Escherichia coli ssb gene product. Expression of the ssb gene under .lambda. PL control. *Biochemistry*, *25*(1), 21–25. https://doi.org/10.1021/bi00349a004

Lucius, A. L., Vindigni, A., Gregorian, R., Ali, J. A., Taylor, A. F., Smith, G. R., & Lohman, T. M. (2002). DNA Unwinding Step-size of E.coli RecBCD Helicase Determined from Single Turnover Chemical Quenched-flow Kinetic Studies. *Journal of Molecular Biology*, *324*(3), 409–428. https://doi.org/10.1016/S0022-2836(02)01067-7

Lytle, A. K., Origanti, S. S., Qiu, Y., VonGermeten, J., Myong, S., & Antony, E. (2014). Context-Dependent Remodeling of Rad51–DNA Complexes by Srs2 Is Mediated by a Specific Protein–Protein Interaction. *Journal of Molecular Biology*, *426*(9), 1883–1897. https://doi.org/10.1016/j.jmb.2014.02.014

Ma, C.J., Steinfeld, J. B., & Greene, E. C. (2017). Single-Stranded DNA Curtains for Studying Homologous Recombination. In *Methods in enzymology* (Vol. 582, pp. 193–219). https://doi.org/10.1016/bs.mie.2016.08.005

Ma, Chu Jian, Gibb, B., Kwon, Y., Sung, P., & Greene, E. C. (2017a). Protein dynamics of human RPA and RAD51 on ssDNA during assembly and disassembly of the RAD51 filament. *Nucleic Acids Research*, *45*(2), 749–761. https://doi.org/10.1093/nar/gkw1125

Ma, Chu Jian, Gibb, B., Kwon, Y., Sung, P., & Greene, E. C. (2017b). Protein dynamics of human RPA and RAD51 on ssDNA during assembly and disassembly of the RAD51 filament. *Nucleic Acids Research*, *45*(2), 749–761. https://doi.org/10.1093/nar/gkw1125

Macris, M. A., & Sung, P. (2005). Multifaceted role of the Saccharomyces cerevisiae Srs2 helicase in homologous recombination regulation. *Biochemical Society Transactions*, *33*(6), 1447. https://doi.org/10.1042/BST20051447

Majka, J., & Burgers, P. M. (2007). Clamping the Mec1/ATR Checkpoint Kinase into Action. *Cell Cycle*, *6*(10), 1157–1160. https://doi.org/10.4161/cc.6.10.4221

Maréchal, A., & Zou, L. (2015). RPA-coated single-stranded DNA as a platform for post-translational modifications in the DNA damage response. *Cell Research*, *25*(1), 9–23. https://doi.org/10.1038/cr.2014.147

Matsuda, T., Saijo, M., Kuraoka, I., Kobayashi, T., Nakatsu, Y., Nagai, A., … Tanaka, K. (1995). DNA repair protein XPA binds replication protein A (RPA). *The Journal of Biological Chemistry*, *270*(8), 4152–4157. https://doi.org/10.1074/JBC.270.8.4152

Mazón, G., Mimitou, E. P., & Symington, L. S. (2010). SnapShot: Homologous Recombination in DNA Double-Strand Break Repair. *Cell*, *142*(4), 648.e1-648.e2. https://doi.org/10.1016/j.cell.2010.08.006

Mer, G., Bochkarev, A., Gupta, R., Bochkareva, E., Frappier, L., Ingles, C. J., … Chazin, W. J. (2000). Structural Basis for the Recognition of DNA Repair Proteins UNG2, XPA, and RAD52 by Replication Factor RPA. *Cell*, *103*(3), 449–456. https://doi.org/10.1016/S0092-8674(00)00136-7

Mimitou, E. P., & Symington, L. S. (2009). Nucleases and helicases take center stage in homologous recombination. *Trends in Biochemical Sciences*, *34*(5), 264–272. https://doi.org/10.1016/j.tibs.2009.01.010

Miné, J., Disseau, L., Takahashi, M., Cappello, G., Dutreix, M., & Viovy, J. L. (2007). Real-time measurements of the nucleation, growth and dissociation of single Rad51-DNA nucleoprotein filaments. *Nucleic Acids Research*, *35*(21), 7171–7187. https://doi.org/10.1093/nar/gkm752

Miyake-Stoner, S. J., Miller, A. M., Hammill, J. T., Peeler, J. C., Hess, K. R., Mehl, R. A., & Brewer, S. H. (2009). Probing Protein Folding Using Site-Specifically Encoded Unnatural Amino Acids as FRET Donors with Tryptophan. *Biochemistry*, *48*(25), 5953–5962. https://doi.org/10.1021/bi900426d

Miyazaki, T., Bressan, D. A., Shinohara, M., Haber, J. E., & Shinohara, A. (2004). In vivo assembly and disassembly of Rad51 and Rad52 complexes during double-strand break repair. *The EMBO Journal*, *23*(4), 939–949. https://doi.org/10.1038/sj.emboj.7600091

Morten, M. J., Peregrina, J. R., Figueira-Gonzalez, M., Ackermann, K., Bode, B. E., White, M. F., & Penedo, J. C. (2015). Binding dynamics of a monomeric SSB protein to DNA: a single-molecule multi-process approach. *Nucleic Acids Research*, *43*(22), 10907–10924. https://doi.org/10.1093/nar/gkv1225

Mularoni, L., Zhou, Y., Bowen, T., Gangadharan, S., Wheelan, S. J., & Boeke, J. D. (2012). Retrotransposon Ty1 integration targets specifically positioned asymmetric nucleosomal DNA segments in tRNA hotspots. *Genome Research*, *22*(4), 693–703.

https://doi.org/10.1101/gr.129460.111

Munk, S., Sigurðsson, J. O., Xiao, Z., Batth, T. S., Franciosa, G., von Stechow, L., … Olsen, J. V. (2017). Proteomics Reveals Global Regulation of Protein SUMOylation by ATM and ATR Kinases during Replication Stress. *Cell Reports*, *21*(2), 546–558. https://doi.org/10.1016/J.CELREP.2017.09.059

Nehring, S., Budisa, N., & Wiltschi, B. (2012). Performance Analysis of Orthogonal Pairs Designed for an Expanded Eukaryotic Genetic Code. *PLoS ONE*, *7*(4), e31992. https://doi.org/10.1371/journal.pone.0031992

New, J. H., Sugiyama, T., Zaitseva, E., & Kowalczykowski, S. C. (1998). Rad52 protein stimulates DNA strand exchange by Rad51 and replication protein A. *Nature*, *391*(6665), 407–410. https://doi.org/10.1038/34950

Nguyen, B., Sokoloski, J., Galletto, R., Elson, E. L., Wold, M. S., & Lohman, T. M. (2014a). Diffusion of human replication protein A along single-stranded DNA. *Journal of Molecular Biology*, *426*(19), 3246–3261. https://doi.org/10.1016/j.jmb.2014.07.014

Nguyen, B., Sokoloski, J., Galletto, R., Elson, E. L., Wold, M. S., & Lohman, T. M. (2014b). Diffusion of Human Replication Protein A along Single-Stranded DNA. *Journal of Molecular Biology*, *426*(19), 3246–3261. https://doi.org/10.1016/j.jmb.2014.07.014

Nguyen, H. D., Yadav, T., Giri, S., Saez, B., Graubert, T. A., & Zou, L. (2017). Functions of Replication Protein A as a Sensor of R Loops and a Regulator of RNaseH1. *Molecular Cell*, *65*(5), 832-847.e4. https://doi.org/10.1016/j.molcel.2017.01.029

Niedziela-Majka, A., Chesnik, M. A., Tomko, E. J., & Lohman, T. M. (2007). *Bacillus stearothermophilus* PcrA Monomer Is a Single-stranded DNA Translocase but Not a Processive Helicase *in Vitro*. *Journal of Biological Chemistry*, *282*(37), 27076–27085. https://doi.org/10.1074/jbc.M704399200

Nimonkar, A. V., Genschel, J., Kinoshita, E., Polaczek, P., Campbell, J. L., Wyman, C., … Kowalczykowski, S. C. (2011). BLM-DNA2-RPA-MRN and EXO1-BLM-RPA-MRN constitute two DNA end resection machineries for human DNA break repair. *Genes and Development*, *25*(4), 350–362. https://doi.org/10.1101/gad.2003811

Nimonkar, A. V, Sica, R. A., & Kowalczykowski, S. C. (2009). Rad52 promotes second-end DNA capture in double-stranded break repair to form complement-stabilized joint molecules. *Proceedings of the National Academy of Sciences of the United States of America*, *106*(9), 3077–3082. https://doi.org/10.1073/pnas.0813247106

Nord, F. F. (2009). *Advances in Enzymology and Related Areas of Molecular Biology, 27.* John Wiley & Sons. Retrieved from https://books.google.com/books?hl=en&lr=&id=btV9xK0UADAC&oi=fnd&pg=PA239&dq=Siebert,+G.+and+Humphrey,+G.B.+(1965)+Enzymology+of+the+nucleus.+Advances+in+enzymology+and+related+areas+of+molecular+biology,+27,+239-288.&ots=CnNVO2_dob&sig=4GeiSYcSOuOqighuPL8Hbvbsfdg#v=onepage&q&f=false

Oakley, G. G., & Patrick, S. M. (2010). Replication protein A: directing traffic at the intersection of replication and repair. *Frontiers in Bioscience (Landmark Edition)*, *15*, 883–900. Retrieved from http://www.ncbi.nlm.nih.gov/pubmed/20515732

Park, J.-S., Wang, M., Park, S.-J., & Lee, S.-H. (1999). Zinc Finger of Replication Protein A, a Non-DNA Binding Element, Regulates Its DNA Binding Activity through Redox. *Journal of Biological Chemistry*, *274*(41), 29075–29080. https://doi.org/10.1074/jbc.274.41.29075

Park, M. S., Ludwig, D. L., Stigger, E., & Lee, S.-H. (1996). Physical Interaction between Human RAD52 and RPA Is Required for Homologous Recombination in Mammalian Cells. *Journal of Biological Chemistry*, *271*(31), 18996–19000. https://doi.org/10.1074/jbc.271.31.18996

Parsons, C. A., Baumann, P., Van Dyck, E., & West, S. C. (2000). Precise binding of single-stranded DNA termini by human RAD52 protein. *The EMBO Journal*, *19*(15), 4175–4181. https://doi.org/10.1093/emboj/19.15.4175

Patrick, S. M., & Turchi, J. J. (2001). Stopped-flow Kinetic Analysis of Replication Protein A-binding DNA. *Journal of Biological Chemistry*, *276*(25), 22630–22637. https://doi.org/10.1074/jbc.M010314200

Peeler, J. C., & Mehl, R. A. (2012). Site-Specific Incorporation of Unnatural Amino Acids as Probes for Protein Conformational Changes. In *Methods in molecular biology (Clifton, N.J.)* (Vol. 794, pp. 125–134). https://doi.org/10.1007/978-1-61779-331-8_8

Pestryakov, P. E., Khlimankov, D. Y., Bochkareva, E., Bochkarev, A., & Lavrik, O. I. (2004). Human replication protein A (RPA) binds a primer-template junction in the absence of its major ssDNA-binding domains. *Nucleic Acids Research*, *32*(6), 1894–1903. https://doi.org/10.1093/nar/gkh346

Pfander, B., & Diffley, J. F. X. (2011). Dpb11 coordinates Mec1 kinase activation with cell cycle-regulated Rad9 recruitment. *The EMBO Journal*, *30*(24), 4897–4907. https://doi.org/10.1038/emboj.2011.345

Plate, I., Hallwyl, S. C. L., Shi, I., Krejci, L., Müller, C., Albertsen, L., … Mortensen, U. H. (2008). Interaction with RPA is necessary for Rad52 repair center formation and for its mediator activity. *The Journal of Biological Chemistry*, *283*(43), 29077–29085. https://doi.org/10.1074/jbc.M804881200

Pokhrel, N., Origanti, S., Davenport, E. P., Gandhi, D., Kaniecki, K., Mehl, R. A., … Antony, E. (2017). Monitoring Replication Protein A (RPA) dynamics in homologous recombination through site-specific incorporation of non-canonical amino acids. *Nucleic Acids Research*, *45*(16). https://doi.org/10.1093/nar/gkx598

Pokhrel, Nilisha, Caldwell, C. C., Corless, E. I., Tillison, E. A., Tibbs, J., Jocic, N., … Antony, E. (2019). Dynamics and selective remodeling of the DNA-binding domains of RPA. *Nature Structural & Molecular Biology*, *26*(2), 129–136. https://doi.org/10.1038/s41594-018-0181-y

Prakash, A., & Borgstahl, G. E. O. (2012). The structure and function of replication protein A in DNA replication. *Sub-Cellular Biochemistry*, *62*, 171–196. https://doi.org/10.1007/978-94-007-4572-8_10

Pretto, D. I., Tsutakawa, S., Brosey, C. A., Castillo, A., Chagot, M.-E., Smith, J. A., … Chazin, W. J. (2010). Structural Dynamics and Single-Stranded DNA Binding Activity of the Three N-Terminal Domains of the Large Subunit of Replication Protein A from Small Angle X-ray Scattering. *Biochemistry*, *49*(13), 2880–2889. https://doi.org/10.1021/bi9019934

Protein Fluorescence. (2006). In *Principles of Fluorescence Spectroscopy* (pp. 529–575). Boston, MA: Springer US. https://doi.org/10.1007/978-0-387-46312-4_16

Psakhye, I., & Jentsch, S. (2012). Protein Group Modification and Synergy in the SUMO Pathway as Exemplified in DNA Repair. *Cell*, *151*(4), 807–820. https://doi.org/10.1016/J.CELL.2012.10.021

Qi, Z., Redding, S., Lee, J. Y., Gibb, B., Kwon, Y., Niu, H., … Greene, E. C. (2015). DNA sequence alignment by microhomology sampling during homologous recombination. *Cell*, *160*(5), 856–869. https://doi.org/10.1016/j.cell.2015.01.029

Qiu, Y., Antony, E., Doganay, S., Koh, H. R., Lohman, T. M., & Myong, S. (2013). Srs2 prevents Rad51 filament formation by repetitive motion on DNA. *Nature Communications*, *4*, 2281. https://doi.org/10.1038/ncomms3281

Ragunathan, K., Joo, C., & Ha, T. (2011). Real time observation of strand exchange reaction with high spatiotemporal resolution. *Structure (London, England : 1993)*, *19*(8), 1064. https://doi.org/10.1016/J.STR.2011.06.009

Ranatunga, W., Jackson, D., Lloyd, J. A., Forget, A. L., Knight, K. L., & Borgstahl, G. E. (2001). Human RAD52 exhibits two modes of self-association. *The Journal of Biological Chemistry*, *276*(19), 15876–15880. https://doi.org/10.1074/jbc.M011747200

Raney, K. D., Byrd, A. K., & Aarattuthodiyil, S. (2013). Structure and mechanisms of SF1 DNA helicases. *Advances in Experimental Medicine and Biology*, *767*, 17–46. https://doi.org/10.1007/978-1-4614-5037-5_2

Rasnik, I., Myong, S., Cheng, W., Lohman, T. M., & Ha, T. (2004). DNA-binding Orientation and Domain Conformation of the E.coli Rep Helicase Monomer Bound to a Partial Duplex Junction: Single-molecule Studies of Fluorescently Labeled Enzymes. *Journal of Molecular Biology*, *336*(2), 395–408. https://doi.org/10.1016/j.jmb.2003.12.031

Redding, S., & Greene, E. C. (2013). How do proteins locate specific targets in DNA? *Chemical Physics Letters*, *570*, 1–11. https://doi.org/10.1016/j.cplett.2013.03.035

Rosenkranz, K., Birschmann, I., Grunau, S., Girzalsky, W., Kunau, W.-H., & Erdmann, R. (2006). Functional association of the AAA complex and the peroxisomal importomer. *The FEBS Journal*, *273*(16), 3804–3815. https://doi.org/10.1111/j.1742-4658.2006.05388.x

Roy, R., Kozlov, A. G., Lohman, T. M., & Ha, T. (2009). SSB protein diffusion on single-stranded DNA stimulates RecA filament formation. *Nature*, *461*(7267), 1092–1097. https://doi.org/10.1038/nature08442

Salas, T. R., Petruseva, I., Lavrik, O., Bourdoncle, A., Mergny, J.-L., Favre, A., & Saintomé, C. (2006). Human replication protein A unfolds telomeric G-quadruplexes. *Nucleic Acids Research*, *34*(17), 4857–4865. https://doi.org/10.1093/nar/gkl564

Saotome, M., Saito, K., Onodera, K., Kurumizaka, H., & Kagawa, W. (2016). Structure of the human DNA-repair protein RAD52 containing surface mutations. *Acta Crystallographica Section F Structural Biology Communications*, *72*(8), 598–603. https://doi.org/10.1107/S2053230X1601027X

Saotome, M., Saito, K., Yasuda, T., Ohtomo, H., Sugiyama, S., Nishimura, Y., … Kagawa, W. (2018). Structural Basis of Homology-Directed DNA Repair Mediated by RAD52. *IScience*, *3*, 50–62. https://doi.org/10.1016/J.ISCI.2018.04.005

Scholes, D. T., Banerjee, M., Bowen, B., & Curcio, M. J. (2001). Multiple regulators of Ty1 transposition in Saccharomyces cerevisiae have conserved roles in genome maintenance. *Genetics*, *159*(4), 1449–1465. Retrieved from

http://www.ncbi.nlm.nih.gov/pubmed/11779788

Seong, C., Colavito, S., Kwon, Y., Sung, P., & Krejci, L. (2009). Regulation of Rad51 recombinase presynaptic filament assembly via interactions with the Rad52 mediator and the Srs2 anti-recombinase. *The Journal of Biological Chemistry*, *284*(36), 24363–24371. https://doi.org/10.1074/jbc.M109.032953

Shao, N., Singh, N. S., Slade, S. E., Jones, A. M. E., & Balasubramanian, M. K. (2015). Site Specific Genetic Incorporation of Azidophenylalanine in Schizosaccharomyces pombe. *Scientific Reports*, *5*(1), 17196. https://doi.org/10.1038/srep17196

Shinohara, A, Shinohara, M., Ohta, T., Matsuda, S., & Ogawa, T. (1998). Rad52 forms ring structures and co-operates with RPA in single-strand DNA annealing. *Genes to Cells : Devoted to Molecular & Cellular Mechanisms*, *3*(3), 145–156. Retrieved from http://www.ncbi.nlm.nih.gov/pubmed/9619627

Shinohara, Akira, & Ogawa, T. (1998). Stimulation by Rad52 of yeast Rad51- mediated recombination. *Nature*, *391*(6665), 404–407. https://doi.org/10.1038/34943

Sibenaller, Z. A., Sorensen, B. R., & Wold, M. S. (1998). The 32- and 14-kilodalton subunits of replication protein A are responsible for species-specific interactions with single-stranded DNA. *Biochemistry*, *37*(36), 12496–12506. https://doi.org/10.1021/bi981110+

Singleton, M. R., Wentzell, L. M., Liu, Y., West, S. C., & Wigley, D. B. (2002). Structure of the single-strand annealing domain of human RAD52 protein. *Proceedings of the National Academy of Sciences*, *99*(21), 13492–13497. https://doi.org/10.1073/pnas.212449899

Song, D., Graham, T. G. W., & Loparo, J. J. (2016). A general approach to visualize protein binding and DNA conformation without protein labelling. *Nature Communications*, *7*(1), 10976. https://doi.org/10.1038/ncomms10976

Sotiriou, S. K., Kamileri, I., Lugli, N., Evangelou, K., Da-Ré, C., Huber, F., … Halazonetis, T. D. (2016). Mammalian RAD52 Functions in Break-Induced Replication Repair of Collapsed DNA Replication Forks. *Molecular Cell*, *64*(6), 1127–1134. https://doi.org/10.1016/j.molcel.2016.10.038

Stauffer, M. E., & Chazin, W. J. (2004a). Physical interaction between replication protein A and Rad51 promotes exchange on single-stranded DNA. *The Journal of Biological Chemistry*, *279*(24), 25638–25645. https://doi.org/10.1074/jbc.M400029200

Stauffer, M. E., & Chazin, W. J. (2004b). Physical Interaction between Replication Protein A and Rad51 Promotes Exchange on Single-stranded DNA. *Journal of Biological Chemistry*, *279*(24), 25638–25645. https://doi.org/10.1074/jbc.M400029200

Stein, A., Kalifa, L., & Sia, E. A. (2015). Members of the RAD52 Epistasis Group Contribute to Mitochondrial Homologous Recombination and Double-Strand Break Repair in Saccharomyces cerevisiae. *PLOS Genetics*, *11*(11), e1005664. https://doi.org/10.1371/journal.pgen.1005664

Subramanyam, S., Ismail, M., Bhattacharya, I., & Spies, M. (2016). Tyrosine phosphorylation stimulates activity of human RAD51 recombinase through altered nucleoprotein filament dynamics. *Proceedings of the National Academy of Sciences of the United States of America*, *113*(41), E6045–E6054. https://doi.org/10.1073/pnas.1604807113

Subramanyam, S., Kinz-Thompson, C. D., Gonzalez, R. L., Spies, M., & Spies, M. (2018). Observation and Analysis of RAD51 Nucleation Dynamics at Single-Monomer Resolution. *Methods in Enzymology*, *600*, 201–232. https://doi.org/10.1016/bs.mie.2017.12.008

Sugitani, N., & Chazin, W. J. (2015). Characteristics and concepts of dynamic hub proteins in DNA processing machinery from studies of RPA. *Progress in Biophysics and Molecular Biology*, *117*(2–3), 206–211. https://doi.org/10.1016/j.pbiomolbio.2014.12.001

Sugiyama, T., & Kowalczykowski, S. C. (2002a). Rad52 protein associates with replication protein A (RPA)-single-stranded DNA to accelerate Rad51-mediated displacement of RPA and presynaptic complex formation. *The Journal of Biological Chemistry*, *277*(35), 31663–31672. https://doi.org/10.1074/jbc.M203494200

Sugiyama, T., & Kowalczykowski, S. C. (2002b). Rad52 protein associates with replication protein A (RPA)-single-stranded DNA to accelerate Rad51-mediated displacement of RPA and presynaptic complex formation. *The Journal of Biological Chemistry*, *277*(35), 31663–31672. https://doi.org/10.1074/jbc.M203494200

Summerer, D., Chen, S., Wu, N., Deiters, A., Chin, J. W., & Schultz, P. G. (2006). A genetically encoded fluorescent amino acid. *Proceedings of the National Academy of Sciences of the United States of America*, *103*(26), 9785–9789. https://doi.org/10.1073/pnas.0603965103

Sung, P. (1997). Function of yeast Rad52 protein as a mediator between replication protein A and the Rad51 recombinase. *The Journal of Biological Chemistry*, *272*(45), 28194–28197. https://doi.org/10.1074/jbc.272.45.28194

Symington, L. S., Rothstein, R., & Lisby, M. (2014). Mechanisms and Regulation of Mitotic Recombination in Saccharomyces cerevisiae. *Genetics*, *198*(3), 795–835. https://doi.org/10.1534/genetics.114.166140

Tercero, J. A., & Diffley, J. F. X. (2001). Regulation of DNA replication fork progression through damaged DNA by the Mec1/Rad53 checkpoint. *Nature*, *412*(6846), 553–557. https://doi.org/10.1038/35087607

Tomko, E. J., Fischer, C. J., & Lohman, T. M. (2010). Ensemble methods for monitoring enzyme translocation along single stranded nucleic acids. *Methods (San Diego, Calif.)*, *51*(3), 269–276. https://doi.org/10.1016/j.ymeth.2010.03.010

Tomko, E. J., Fischer, C. J., & Lohman, T. M. (2012). Single stranded DNA translocation of E. coli UvrD monomer is tightly coupled to ATP hydrolysis. *Journal of Molecular Biology*, *418*(1–2), 32. https://doi.org/10.1016/J.JMB.2012.02.013

Tworzydło, M., Polit, A., Mikołajczak, J., & Wasylewski, Z. (2005). Fluorescence quenching and kinetic studies of conformational changes induced by DNA and cAMP binding to cAMP receptor protein from Escherichia coli. *FEBS Journal*, *272*(5), 1103–1116. https://doi.org/10.1111/j.1742-4658.2005.04540.x

Valuchova, S., Fulnecek, J., Petrov, A. P., Tripsianes, K., & Riha, K. (2016). A rapid method for detecting protein-nucleic acid interactions by protein induced fluorescence enhancement. *Scientific Reports*, *6*(1), 39653. https://doi.org/10.1038/srep39653

van de Meent, J.-W., Bronson, J. E., Wiggins, C. H., Gonzalez, R. L., & Jr. (2014). Empirical Bayes methods enable advanced population-level analyses of single-molecule FRET experiments. *Biophysical Journal*, *106*(6), 1327–1337. https://doi.org/10.1016/j.bpj.2013.12.055

Van Komen, S., Reddy, M. S., Krejci, L., Klein, H., & Sung, P. (2003). ATPase and DNA Helicase Activities of the *Saccharomyces cerevisiae* Anti-recombinase Srs2. *Journal of Biological Chemistry*, *278*(45), 44331–44337. https://doi.org/10.1074/jbc.M307256200

Verma, P., Dilley, R. L., Zhang, T., Gyparaki, M. T., Li, Y., & Greenberg, R. A. (2019). RAD52 and SLX4 act nonepistatically to ensure telomere stability during alternative telomere lengthening. *Genes & Development*, *33*(3–4), 221–235. https://doi.org/10.1101/gad.319723.118

Verma, P., & Greenberg, R. A. (2016). Noncanonical views of homology-directed DNA repair. *Genes & Development*, *30*(10), 1138–1154. https://doi.org/10.1101/gad.280545.116

Walther, A. P., Gomes, X. V., Lao, Y., Lee, C. G., & Wold, M. S. (1999). Replication Protein A Interactions with DNA. 1. Functions of the DNA-Binding and Zinc-Finger Domains of the 70-kDa Subunit †. *Biochemistry*, *38*(13), 3963–3973. https://doi.org/10.1021/bi982370u

Wittschieben, B. Ø., Iwai, S., & Wood, R. D. (2005). DDB1-DDB2 (Xeroderma Pigmentosum Group E) Protein Complex Recognizes a Cyclobutane Pyrimidine Dimer, Mismatches, Apurinic/Apyrimidinic Sites, and Compound Lesions in DNA. *Journal of Biological Chemistry*, *280*(48), 39982–39989. https://doi.org/10.1074/jbc.M507854200

Wold, M. S. (1997). REPLICATION PROTEIN A:A Heterotrimeric, Single-Stranded DNA-Binding Protein Required for Eukaryotic DNA Metabolism. *Annual Review of Biochemistry*, *66*(1), 61–92. https://doi.org/10.1146/annurev.biochem.66.1.61

Wu, C.-S., Ouyang, J., Mori, E., Nguyen, H. D., Maréchal, A., Hallet, A., … Zou, L. (2014). SUMOylation of ATRIP potentiates DNA damage signaling by boosting multiple protein interactions in the ATR pathway. *Genes & Development*, *28*(13), 1472–1484. https://doi.org/10.1101/gad.238535.114

Wu, C. G., Bradford, C., & Lohman, T. M. (2010). E. coli RecBC Helicase has Two Translocase Activities Controlled by a Single ATPase Motor. *Nature Structural & Molecular Biology*, *17*(10), 1210. https://doi.org/10.1038/NSMB.1901

Xie, F., Wu, C. G., Weiland, E., & Lohman, T. M. (2013). Asymmetric regulation of bipolar single-stranded DNA translocation by the two motors within Escherichia coli RecBCD helicase. *The Journal of Biological Chemistry*, *288*(2), 1055–1064. https://doi.org/10.1074/jbc.M112.423384

Xu, X., Vaithiyalingam, S., Glick, G. G., Mordes, D. A., Chazin, W. J., & Cortez, D. (2008). The basic cleft of RPA70N binds multiple checkpoint proteins, including RAD9, to regulate ATR signaling. *Molecular and Cellular Biology*, *28*(24), 7345–7353. https://doi.org/10.1128/MCB.01079-08

Yan, Z., Xue, C., Kumar, S., Crickard, J. B., Yu, Y., Wang, W., … Ira, G. (2019). Rad52 Restrains Resection at DNA Double-Strand Break Ends in Yeast. *Molecular Cell*, *0*(0). https://doi.org/10.1016/j.molcel.2019.08.017

Yates, L. A., Aramayo, R. J., Pokhrel, N., Caldwell, C. C., Kaplan, J. A., Perera, R. L., … Zhang, X. (2018). A structural and dynamic model for the assembly of Replication Protein A on single-stranded DNA. *Nature Communications*, *9*(1), 5447. https://doi.org/10.1038/s41467-018-07883-7

Yeeles, J. T. P., Poli, J., Marians, K. J., & Pasero, P. (2013). Rescuing stalled or damaged

replication forks. *Cold Spring Harbor Perspectives in Biology*, *5*(5), a012815. https://doi.org/10.1101/cshperspect.a012815

You, J. S., Wang, M., & Lee, S. H. (2000). Functional characterization of zinc-finger motif in redox regulation of RPA-ssDNA interaction. *Biochemistry*, *39*(42), 12953–12958. https://doi.org/10.1021/bi001206f

Young, T. S., & Schultz, P. G. (2010). Beyond the canonical 20 amino acids: expanding the genetic lexicon. *The Journal of Biological Chemistry*, *285*(15), 11039–11044. https://doi.org/10.1074/jbc.R109.091306

Yuzhakov, A., Kelman, Z., Hurwitz, J., & O'Donnell, M. (1999). Multiple competition reactions for RPA order the assembly of the DNA polymerase delta holoenzyme. *The EMBO Journal*, *18*(21), 6189–6199. https://doi.org/10.1093/emboj/18.21.6189

Zhang, J.-M., Yadav, T., Ouyang, J., Lan, L., & Zou, L. (2019). Alternative Lengthening of Telomeres through Two Distinct Break-Induced Replication Pathways. *Cell Reports*, *26*(4), 955-968.e3. https://doi.org/10.1016/j.celrep.2018.12.102

Zhou, R., Kozlov, A. G., Roy, R., Zhang, J., Korolev, S., Lohman, T. M., & Ha, T. (2011). SSB Functions as a Sliding Platform that Migrates on DNA via Reptation. *Cell*, *146*(2), 222–232. https://doi.org/10.1016/J.CELL.2011.06.036

Zou, Y., Liu, Y., Wu, X., & Shell, S. M. (2006a). Functions of human replication protein A (RPA): from DNA replication to DNA damage and stress responses. *Journal of Cellular Physiology*, *208*(2), 267–273. https://doi.org/10.1002/jcp.20622

Zou, Y., Liu, Y., Wu, X., & Shell, S. M. (2006b). Functions of human replication protein A (RPA): From DNA replication to DNA damage and stress responses. *Journal of Cellular Physiology*, *208*(2), 267–273. https://doi.org/10.1002/jcp.20622

APPENDIX I: ROLE OF THE CONSERVED NKK MOTIF IN REGULATING RPA-DNA BINDING AND ITS IMPLICATIONS IN HOMOLOGOUS RECOMBINATION

8.1 Introduction

The DNA binding proteins often contain zinc finger motif as a key component that regulates their DNA binding activity. The eukaryotic ssDNA binding protein RPA consists an evolutionary conserved 4-cysteine type zinc finger motif (X(3) CX(2-4) CX(12-15) CX(2) C, where X represents any amino acid other than C) located in DBD-C (Brill & Bastin-Shanower, 1998) required for performing redox reactions that regulate RPA-ssDNA binding (J.-S. Park, Wang, Park, & Lee, 1999; You, Wang, & Lee, 2000). The zn-finger motif directly interacts with ssDNA and contributes towards the helix destablilation role of RPA (Lao et al., 1999). Coordination of Zn^{2+} by four cystenies stabilizes the L12 loop structure froming a three-β-strand structure. Direct interactions between amino acids in the three-β-strand structure and ssDNA forms a stable Zn domain (Fan & Pavletich, 2012b). In the crystal structure of *U.maydis* RPA, N496, K497, K498 (NKK motif) in the Zn domain make specific interactions with the phosphodiester backbone of ssDNA that could contribute towards DBD-C-ssDNA binding. N496, K497 amide backbone forms hydrogen bonding with the phosphate group of ssDNA, and the side chains of K497, K498 make ionic interactions with the phosphodiester backbone of ssDNA (Fan & Pavletich, 2012).

The NKK motif is conserved from yeast to humans. It has been postulated that the specific interactions made by NKK motif could facilitate initial binding of DBD-C to DNA and transitioning of ssDNA from a loosely-bound state to a tightly-bound state as it

passes through DBD-C (Fan & Pavletich, 2012). Indeed, addition of micromolar concentrations of zinc in RPA-ssDNA binding experiments resulted in a highly stiff, more compact ssDNA (J. Chen et al., 2015). Surprisingly, i*n vivo*, mutation of NKK motif rescued Srs2 null phenotype upon dsDNA damage (Dhiungra et. al., unpublished). Srs2 helicase is an anti-HR meditor that antagonizes Rad51 nucleoprotein filament formation and plays a key-role balancing the levels of HR in yeast cells. Following dsDNA damage, suvival of yeast cells in absence of Srs2 when NKK motif is mutated suggests a gain-of-function, possibly due to effects in the RPA-ssDNA filament that allows RPA to be easily displaced by other proteins trying to access the ssDNA space.

Therefore, in this chapter, I investigated how mutations in the NKK motif affected RPA-DNA binding characteristics that could contribute towards survivability of yeast in absence of Srs2. Our results show RPA with mutations in the NKK motif do not result in change in DBD-A or DBD-D DNA binding dynamics or RPA assembly, but have distinct conformational arrangement on DNA making them more susceptible to Srs2 clearing. RPA-NKK mutants, also known as RPAzm had DNA binding properties similar to wild-type RPA, albeit changes in conformations adopted on DNA.

8.2 Materials and Methods

8.2.1 Plasmids for protein purification

8.2.1.1 RPAzm-4AZP incorporating plasmids

His- tag carrying RPA-A^{4AZP} and RPA-D^{4AZP} (chapter 3, section 3.2.3) were used as templates to generate RPA-NKK mutant (RPAzm) constructs: RPA-K494A-A^{4AZP},

RPA-K494A-D^{4AZP}, RPA-K493A K494A-A^{4AZP} (RPA-KK-AA-A^{4AZP}), RPA-K493A K494A-D^{4AZP} (RPA-KK-AA-D^{4AZP}), RPA-N492D K493R K494R-A^{4AZP} (RPA-NKK-DRR-A^{4AZP}), RPA-N492D K493R K494R-D^{4AZP} (RPA-NKK-DRR-D^{4AZP}). All the constructs were generated with NEB Q5 site- directed mutagenesis kit, using the plasmids as described in Table 8-1.

Table 8-1: List of primers used to generate RPAzm

Mutation	Forward primer (5′-3′)	Reverse primer (5′-3′)	Annealing temperature (^{o}C)
RPA-K494A	TTGTAATAAGGCAGTTCTGGAACAGC	TTCTCATTAGAACAGGCAG	59
RPA-KK-AA	GAATTGTAATGCTGCTGTTCTGGAACAGCCTG	TCATTAGAACAGGCAGGATATG	58
RPA-NKK-DRR	TCGAGTTCTGGAACAGCCTGATG	CGATCACAATTCTCATTAGAACAGGC	61

8.2.1.2 Non 4AZP incorporating RPAzm plasmids

Sc. RPA70-RPA32-his-RPA14 (*Sc.* RPA-wt) was used as a template to generate *Sc.* RPA-NKK-DRR; *Sc.* RPA-KK-AA and *Sc.* RPA-K494A using Q5 site- directed mutagenesis and primers described in table 8-1. For all the experiments, purified *Sc.* RPA-wt was used as control.

8.2.2 Purification of 4AZP carrying RPAzm variants

The RPAzm^{4AZP} variants (RPA-K494A-A^{4AZP}, RPA-K494A-D^{4AZP}, RPA-KK-AA-A^{4AZP}, RPA-KK-AA-D^{4AZP}, RPA-NKK-DRR-A^{4AZP}, RPA-NKK-DRR-D^{4AZP}) were co-transformed with pDule2-pCNF plasmid in Rossetta-2 PlysS cells and were purified as described in section 3.2.4 of chapter 3.

8.2.3 Labeling RPAzm^{4AZP} with fluorophores

RPAzm^{4AZP} variants were labeled with MB543, Cy3 or Cy5 as described. Approximately, 3 ml of (10 μM) RPAzm^{4AZP} was incubated on a rocker with 1.5-fold molar excess (15 μM) of either DBCO-MB543, DBCO-Cy3 or DBCO-Cy5 for 2 hours at 4 ^{o}C. Labeled RPAzm variants were separated from excess dye using a Biogel- P4 gel filtration column (65 ml bed volume) using storage buffer (30 mM HEPES, pH 7.8, 100 mM KCl, 0.1mM EDTA, pH 8.0 and 10% (v/v) glycerol). Fractions containing labeled RPAzm were pooled, concentrated using a 30 kDa cut-off spin concentrator and flash frozen using liquid nitrogen. Fluorescent RPAzm were stored at -80 ^{o}C. Labeling efficiency was calculated using absorption values measured at 280 nm and ε_{280}= 98500 $M^{-1}cm^{-1}$for RPAzm, at 543

nm with ε_{543}= 105,000 $M^{-1}cm^{-1}$ for DBCO-MB543, ε_{555}= 150,000 $M^{-1}cm^{-1}$ for DBCO-Cy3 and at 650 nm with ε_{650}= 250,000 $M^{-1}cm^{-1}$ for DBCO-Cy5 fluorophores. A correction factor was applied to the final concentration protein. See appendix II (section 9.1-9.4) for detailed procedure on calculation of correction factor.

8.2.4 Purification of non-4AZP carrying RPAzm

Individual plasmids (*Sc.* RPA-wt; *Sc.* RPA- NKK-DRR; *Sc.* RPA- KK-AA and *Sc.* RPA-K494A) were transformed in Rossetta-2 PlysS cells, plated in LB $agar^{ampicillin\ R}$ plates and incubated overnight at 37°C. At around 6 pm, individual 2.8l baffle flask (4 flasks in total), each containing autoclaved 1l LB medium supplemented with 100µg/ml ampicillin, was inoculated with a single transformed colony and incubated overnight at 37°C, without agitation. Next morning, measurements for OD_{600} were collected, and the flasks were shaken at 250 rpm, at 37°C. At OD_{600}: 0.5-0.8, cells were induced with 0.4mM IPTG and grown for an additional 3 hours at 37°C, 250rpm. Cells were harvested, and purification was done following the same steps as for 4AZP carrying variants mentioned in section 3.2.4 of chapter 3, with the following modifications. All the buffers (cell resuspension buffer, H^0, H^{50}, H^{100}, H^{1000}, H^{1500}) were supplemented with 1mM tecep-HCl and RPA storage buffer was supplemented with 2mM tecep-HCl.

Sc. Srs2 was purified as described previously (Antony et. al., 2009a).

8.2.5 Fluorescence measurements of RPAzm

Tryptophan quenching experiments was performed using a PTI QM40 instrument (Horiba Scientific, Edison, NJ). To determine the emission maxima, a 2ml reaction with 50nM RPA-wt or RPAzm in reaction buffer (30 mM Hepes, pH 7.8, 100 mM KCl, 5 mM $MgCl_2$, 1 mM β-mercaptoethanol and 6 % v/v glycerol) was excited at 290 nm and emission spectra (310nm-350nm) recorded. Following determination of emission maximum, increasing concentrations of $(dT)_{35}$ oligonucleotide was added to the 2ml reaction, excited at 290nm and emission recorded for 10 seconds at $\lambda_{emi\ (max)}$. Fluorescence measurements were normalized, plotted against $[(dT)_{35}]$ and fit using single- step binding isotherm to determine the K_d values. All experiments were performed at 25 °C.

8.2.6 Stopped-flow analysis of RPAzm DNA binding

All stopped-flow measurements were carried out with an Applied Photophysics SX20 instrument (Surrey, UK) at 25ºC. Reactions were performed in buffer (30 mM Hepes, pH 7.8, 100 mM KCl, 5 mM $MgCl_2$, 1 mM β-mercaptoethanol and 6 % v/v glycerol). It is important to note that the concentrations of reactants are reduced to half upon mixing in the stopped-flow instrument. Thus, all the concentrations mentioned below are post-mixing concentrations.

8.2.6.1 Tryptophan quenching experiments

To determine the rate of association of RPAzm, 100nM RPA-wt or RPAzm (*Sc.* RPA- NKK-DRR, *Sc.* RPA- KK-AA or *Sc.* RPA-K494A) in one syringe were rapidly mixed with increasing concentrations (25, 50, 75, 100, 150, 200nM) of $(dT)_{35}$ in another syringe. Optical parameters of λ_{exci}: 290nm and long pass cut-off emission filter with λ_{emi}: 350nm were used to monitor change in tryptophan fluorescence. In total 10000 data points were collected over a period of 2.25 seconds (5000 data points for first 250 milliseconds+ 5000 data points for rest 2 seconds). Raw traces obtained were fit in KaleidaGraph using the equation:

$$\Delta F = A_1 (1 - e^{-k_1 t}) + k_2 t \qquad \text{(Eq. 1)}$$

Where, ΔF is change in tryptophan fluorescence, A_1 and k_1 are the amplitude and observed rate of the exponential phase, k_2 is the steady state rate and t is time.

The values for $k_{obs,1}$ and $k_{obs,2}$ were plotted against the concentration of $(dT)_{35}$. A linear fit equation:

$$y = mx + c \qquad \text{(Eq.3)}$$

Where ‘m’, the slope represents the observed association constant (K_a) and ‘c’, the constant represents the rate of dissociation (k_{off}) was used to determine RPA-DBD-DNA binding characteristics. Observed dissociation constant (K_d) values were calculated using +reciprocal of K_a i.e. $K_{d=} 1 \div K_a$.

8.2.6.2 ssDNA binding kinetics of RPAzm

The rate of association of DBD-A for RPAzm was measured using *Sc.* RPA-NKK-DRR-A^{MB543}, *Sc.* RPA- KK-AA-A^{MB543} and *Sc.* RPA-K494A-A^{MB543}. The rate of association of DBD-D was measured using *Sc.* RPA- NKK-DRR-D^{MB543} and *Sc.* RPA-K494A-D^{MB543}.

For RPAzm, 100nM of fluorescently labeled protein (either DBD-A or DBD-D labeled) was rapidly mixed with increasing concentrations (25, 50, 75, 100, 150, 200nM) of $(dT)_{35}$ oligonucleotide. For RPAS178D. 50nM of fluorescently labeled protein (either DBD-A or DBD-D labeled) was rapidly mixed with increasing concentrations (10, 20, 50, 75, 100nM) of $(dT)_{35}$ oligonucleotide. Increase in fluorescence signal was monitored by exciting the sample at $\underline{\lambda}_{exci}$: 535nm and measuring emission using a long pass cut-off filter at λ_{emi}: 555nm. In total 10000 data points were collected over a period of 2.25 seconds (5000 data points for first 250 milliseconds+ 5000 data points for rest 2 seconds). Raw traces obtained for DBD-A binding were fit using equation:

$$\Delta F = A_1(1 - e^{-k_1 t}) + A_2(1 - e^{-k_2 t}) + k_3 t \qquad \text{(Eq. 2)}$$

Where, ΔF is change in fluorescence of A^{MB543}, A_1 and k_1 are the amplitude and observed rate of the first exponential phase, A_2 and k_2 are the amplitude and observed rate of the second exponential phase, k_3 is the steady state rate and t is time.

The raw data traces obtained for DBD-D binding were fit using Eq.1. The rates obtained for first exponential phase ($k_{obs,1}$), second exponential phase ($k_{obs,2}$) and steady state were plotted against $(dT)_{35}$ concentrations. Note: For DBD-D, $k_{obs,2}$ values represent steady state as there is no second exponential phase. Similar experiments were performed

with 50nM RPA-S178D-A^{MB543} and 50nM RPA-S178D-D^{MB543} with increasing concentrations (10, 20, 50, 75, 100nM) of $(dT)_{35}$. Data were analyzed and plotted as mentioned above.

8.2.6.3 FRET analysis to monitor the binding of two RPAzm

All samples were excited at 555nm and FRET was monitored with a 645nm cut-off emission filter. For FRET experiments with increasing lengths of oligonucleotides $(dT)_n$, where (n= 20, 35, 45, 60, 70, 79, 97, 140), 40nM RPA-A^{cy3}or RPAzm-A^{cy3} paired with 40nM RPA-D^{cy5} or RPAzm-D^{cy5} was rapidly mixed with 40nM $(dT)_n$ and FRET monitored. Resulting FRET was analyzed using Eq. 2 for all the oligonucleotides, except $(dT)_{140}$, which was analyzed using Eq.1 to obtain the observed rates.

8.2.6.4 Srs2 clearing experiments

The following oligos were annealed as described in methods section of chapter 5 to prepare DNA substrates for Srs2 clearing experiments are:

i) 5′Cy5 20bp-ds_3′ $(dT)_{25}$ overhang, also known as DNA subs-1: 5′-/5Cy5/ ACC GCT GCC GTC GCT CCG GGT TTT TTT TTT TTT TTT TTT TTT TTT -3′ and 5′-CCC GGA GCG ACG GCA GCG GT/ 3BHQ_2/-3′

ii) 5′Cy5 20bp-ds_3′ $(dT)_{50}$ overhang, also known as DNA subs-2: 5′-/5Cy5/ ACC GCT GCC GTC GCT CCG GGT TTT TTT TTT TTT TTT TTT TTT TTT TTT TTT TTT TTT TTT TTT TTT TTT T-3′ and 5′-CCC GGA GCG ACG GCA GCG GT/ 3BHQ_2/-3′

50nM RPA-wt or RPAzm was prebound with 50nM 5′Cy5 20bp-ds_3′ $(dT)_{25}$ overhang and mixed rapidly with 100nM Srs2 in reaction buffer supplemented with 2.5mM ATP. Samples were excited at l_{exci}: 625nm and Cy5 fluorescence monitored with a l_{emi}: 635nm cut- off long pass filter. Similarly, 100nM RPA-wt or RPAzm was prebound with 50nM 5′Cy5 20bp-ds_3′ $(dT)_{50}$ overhang and mixed rapidly with 100nM Srs2 in presence of 2.5mM ATP. In total 10000 data points were collected over a period of 2minuts (5000 data points for first 30 seconds+ 5000 data points for rest 90 seconds). All the raw traces obtained were analyzed using Eq.1 and the k_{obs} values obtained were plotted against RPA-wt or RPAzm variants for comparative analysis.

8.2.7 Limited proteolysis

5μg of RPA-wt or RPAzm were treated with 50ng of trypsin or chymotrypsin (1:100 dilution) in 20μl reaction mixture containing 30mM Hepes, pH 7.8, 1mM EDTA, pH 8.0, 8mM Tecep-HCl; 60mM $MgCl_2$ with or without equal concentrations of $(dT)_{35}$ oligonucleotide. All the reactions were carried out at 30^{o}C. Unless specified, after 1 hour of incubation, the reactions were terminated by adding equal volume of 2X SDS-loading dye and boiling for 15 minutes. 35μl of the total sample (reaction mixture+ dye) was loaded on a 12% SDS-PAGE gel and the proteolyzed products separated by electrophoresis. The gel was stained with Coomassie brilliant blue followed by de-stain treatment to remove excess Coomassie blue stain. The resulting bands were compared with protein ladder as a reference.

8.3 Results

8.3.1 Mutations in zinc finger alters the DNA bound conformation of RPA

We investigated the DNA binding properties of RPAzm, as residues in the NKK motif directly interact with ssDNA and are in close proximity to Zn^{2+} ion (Fig. 8-1). To this extent, we measured changes in intrinsic tryptophan fluorescence when RPAzm bound to ssDNA. Titrating increasing concentration of $(dT)_{35}$ with 50nM RPAzm showed

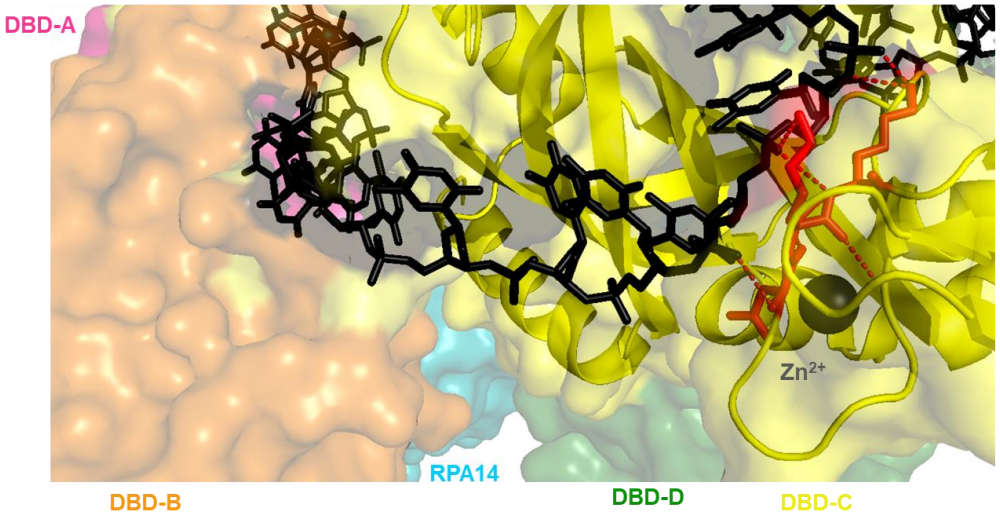

Figure 8-1: Structure of *U. maydis* RPA showing NKK motif. The three amino acid residues in the NKK motif (red sticks) make direct contact with ssDNA backbone (red dashes). ssDNA is shown as black sticks. Cystines in the L12 loop in DBD-C coordinate Zn^{2+} ion (black sphere) resulting in a defined structure.

varying degrees of change in intrinsic tryptophan fluorescence. Compared to RPA-wt, RPA-KK-AA mutation showed the least change in tryptophan fluorescence followed by RPA-K494A and RPA-NKK-DRR (Fig.8-2). Quantification of the binding isotherm

revealed RPA-KK-AA required approximately 5-fold more DNA to saturate 50nM protein, whereas, RPA-K494A and RPA-NKK-DRR maintained 1:1 (protein: DNA) binding stoichiometry (Fig. 8-2, Table 8-2). This observation combined with differences in the degree of tryptophan quenching suggest that specific mutations in the NKK motif alters the way RPA-DBDs are associating to DNA, an perhaps the overall all conformations adopted by RPAzm on DNA.

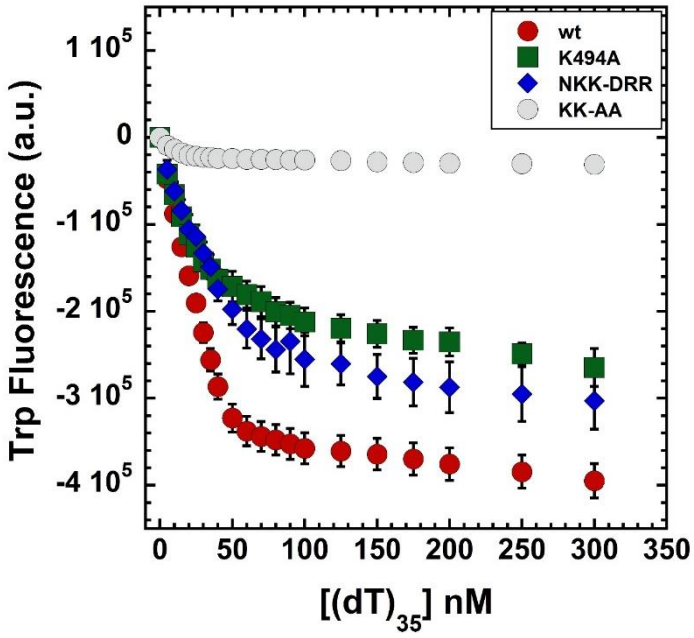

Figure 8-2: Fluorimeter experiments to monitor steady-state tryptophan quenching of RPA-wt and RPAzm. 50nM RPA-wt or RPAzm mutants were titrated with increasing concentrations of $(dT)_{35}$ and change in tryptophan fluorescence was monitored. Data were fit as described in methods to obtain dissociation constant (K_d) values. RPAzm mutant have DNA binding affinity similar to RPA-wt but display a reduction in net amplitude of tryptophan quenching than RPAwt.

Table 8-2: Binding affinity for RPA-wt and RPAzm determined from the steady-state tryptophan quenching fluorimeter experiments.

RPA variants	Saturation point
RPA-wt	46.5 ± 5.5
RPA-K494A	40.8 ± 1.7
RPA-NKK-DRR	58.6 ± 1.6
RPA-KK-AA	117.3 ± 13.7

The data points for individual RPA variant in Fig. 8-2 was fit using single-site binding isotherm to determine the saturation point.

Next, we wanted to investigate if RPAzm bound with similar kinetics as RPA-wt to ssDNA. 100nM RPAzm mutants were rapidly mixed with increasing concentrations of $(dT)_{35}$ and change in tryptophan fluorescence monitored at 350nm with a long-pass emission filter. Resulting traces (Fig 8-3 a-d) were analyzed using Eq.1 *(methods)* and rate of initial engagement ($k_{obs,1}$) and steady state ($k_{obs,2}$) plotted as a function of $(dT)_{35}$ (Fig. 8-4 a, b). All three mutant variants in RPAzm had k_{on} and k_{off} values similar to RPA-wt resulting in similar K_d (Table 8-3). Taken together, similar k_{on} and k_{off} values suggests that mutations in the NKK motif do not affect the overall kinetics of binding or binding affinity (K_d), but it affects the equilibrium state, i.e arrangement of RPAzm-DBDs on DNA, as seen by differences in net tryptophan quenching (Fig. 8-2, Table 8-2).

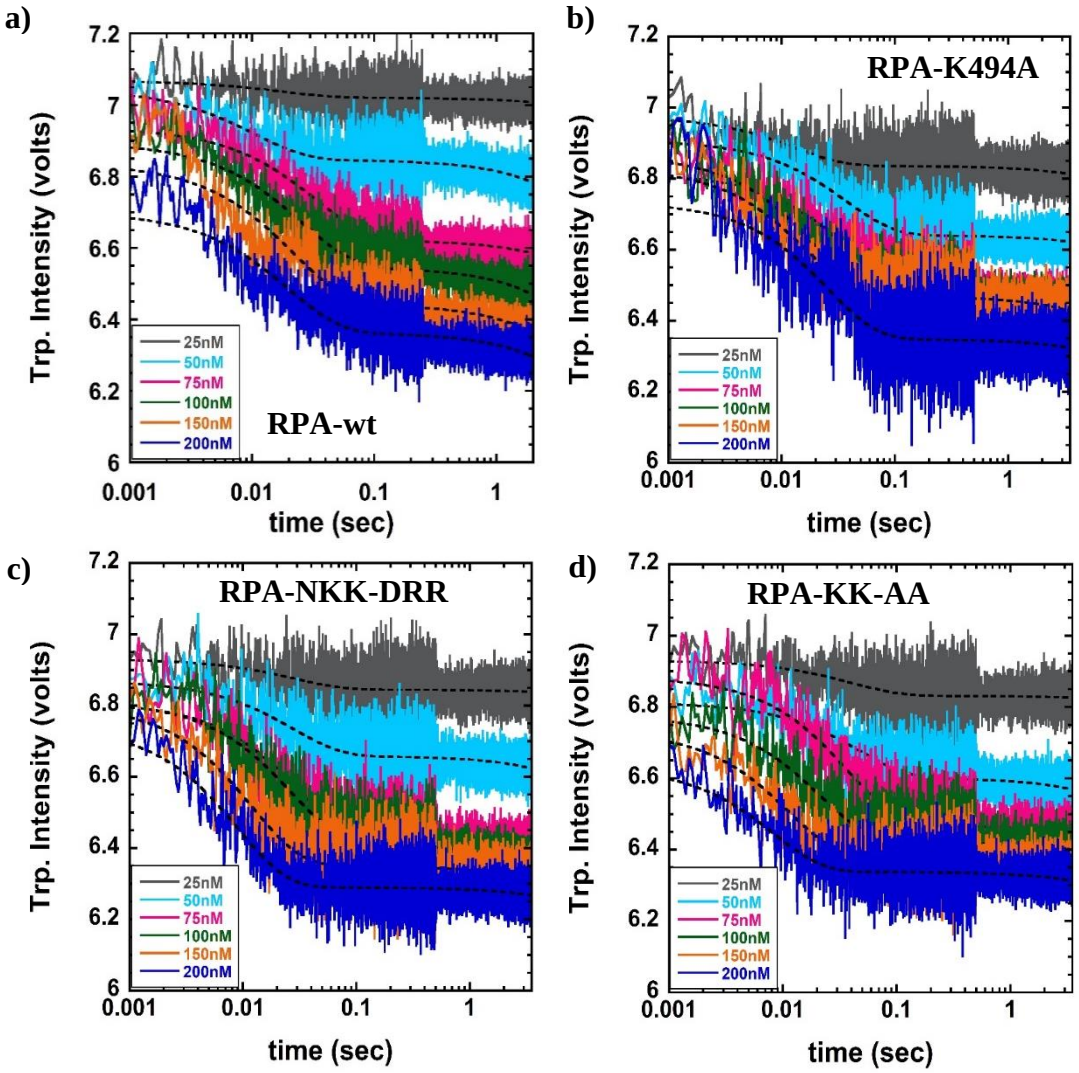

Figure 8-3: Pre-steady state binding kinetics of RPA-wt and RPAzm. Stopped-flow instrument was used to rapidly mix 100nM RPA-wt and RPAzm with increasing concentrations of $(dT)_{35}$. Representative raw traces of the tryptophan quenching experiment for **a)** RPA-wt **b)** RPA-K494A **c)** RPA-NKK-DRR **d)** RPA-KK-AA

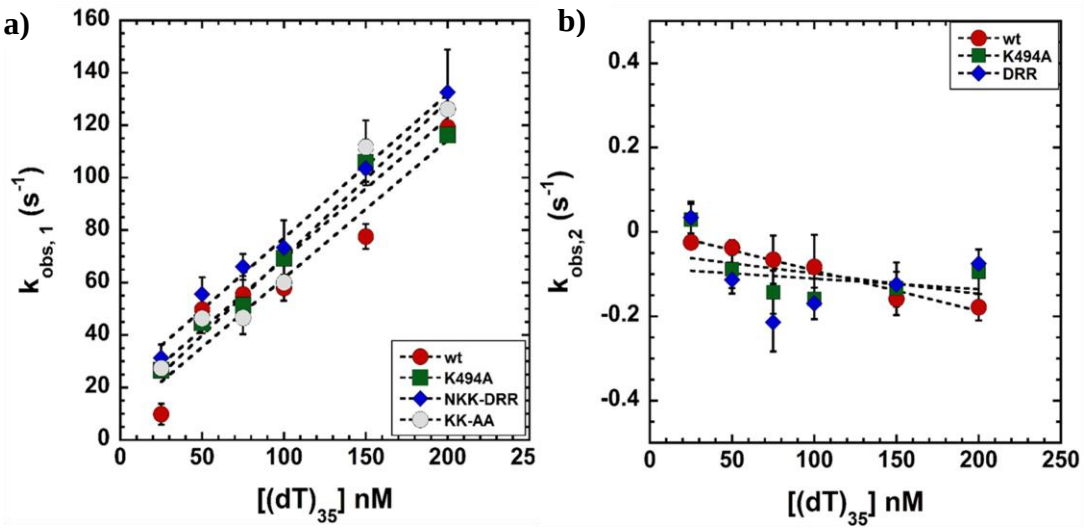

Figure 8-4: Plot of observed rates (k_{obs}) of binding for RPAwt and RPAzm stopped-flow experiments. Quantitative analysis of raw traces in figure 8-3 yield **a)** plot of $k_{obs,1}$ and **b)** plot of $k_{obs,2}$ with $(dT)_{35}$ concentration plotted along the X-axis. Linear fit of the plots gives binding parameters shown in table 8-3.

Table 8-3: Kinetics of RPA-wt and RPAzm binding to ssDNA determined from the tryptophan quenching experiments.

	k_{on} ($M^{-1}s^{-1}$)	k_{off} (s^{-1})	K_d (nM)
RPA-wt	**5.2 ± 0.3**	**9 ± 0.8**	**17.3 ± 4**
RPA-K494A	**5.35 ± 0.4**	**15.3 ± 5.8**	**28.6 ± 11**
RPA-NKK-DRR	**5.48 ± 1**	**12.6 ± 3.7**	**23.0 ± 5.2**
RPA-KK-AA	**6.0 ± 0.27**	**13.4 ± 3.7**	**22.0 ± 5.2**

Finally, to confirm if differences in the degree of tryptophan quenching at steady-state measurements but similarity in rates of initial binding could indicate differential arrangement of RPAzm domains after DNA binding is completed, we carried out limited proteolysis experiments in presence and absence of DNA and compared it with RPA-wt (Fig. 8-5, 8-6). Chymotrypsin digestion of RPA-wt in absence of DNA showed distinct peptide fragments which are further degraded in RPAzm (Fig. 8-5, numbers 1-7). Similar digestion in presence of DNA showed a large peptide fragment of ~60KDa for RPA-wt, which is further degraded in RPAzm (Fig. 8-5, band labeled ‘a’). Furthermore, several peptide bands observed for RPA-wt were absent in RPAzm (Fig. 8-5, bands labeled a-f). We also performed similar limited proteolysis of RPA-wt and RPAzm with trypsin and observed distinct peptide fragments present in RPA-wt that were absent in RPAzm independent of DNA (Fig. 8-6, bands labeled as 1’, 2’ for no DNA and a’-d’ for +DNA)

Asparagine and the two lysine residues present in the loop of DBD-C that holds the Zn^{2+} metal ion makes electrostatic interactions with the phosphate backbone of ssDNA. Mutating any lysine residue in this motif perturbs interaction with ssDNA as observed with the single or double lysine mutants (K494A or KK-AA). The double lysine mutant has the most severe perturbation in ssDNA binding ability, possibly due to increased loop flexibility and loss in positive charge to interact with the negatively charged ssDNA backbone. NKK-DRR mutation introduces a negative charge (N-D), meanwhile maintains the positive charge required to interact with the DNA (KK-RR). Although the negative charge carried by aspartate has the potential to repel the DNA and length of the positive sidechain of amino acid is increased, the net charge of this motif is still positive in nature. Thus, this mutation produces the least effect in tryptophan quenching compared to other RPAzm variants. Perhaps, minimal differences in the observed rates of engagement (k_{on}) and dissociation (k_{off}) stems from the fact that RPA-DNA binding is coordinated by engagement of all four DBDs. Since RPAzm has particular mutations in a defined loop structure, this may particularly affect the path of DNA as it passes through DBD-C and change the way DBD-C is engaging with DNA. It could also affect how DNA passes from DBD-C to DBD-D. The effects of all these possibilities in is highlighted by the limited proteolysis experiments that shows altered conformation for RPAzm on DNA (Fig. 8-5, 8-6). Taken together, our results suggest that RPAzm has DNA binding properties similar to RPA-wt but differences in the way DBDs (in particular DBD-C) may arrange themselves on DNA.

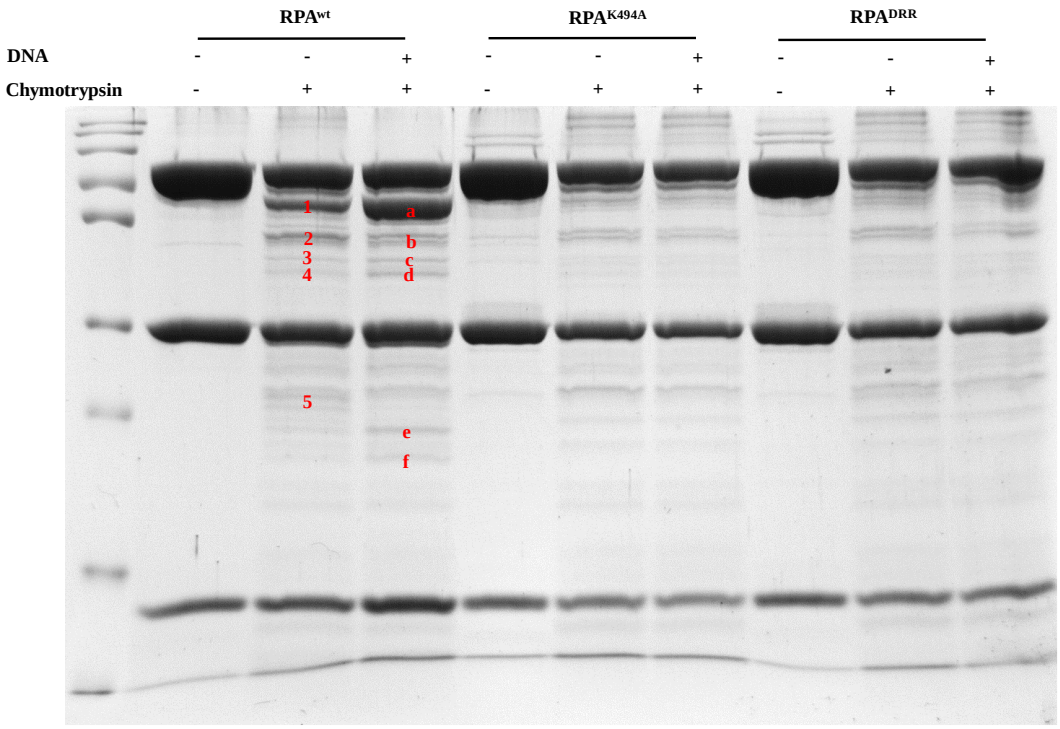

Figure 8-5: Limited proteolytic digestion of RPA-wt and RPAzm with chymotrypsin. Qualitative assessment for understanding conformation of RPA-wt and RPAzm, alone and in presence of ssDNA, shows regions that are protected from protease digest in RPA-wt but not in RPAzm. For each RPA variant (RPA-wt or RPAzm), the first lane represents RPA in absence of chymotrypsin and ssDNA, the second lane represents chymotrypsin treated RPA in absence of ssDNA and the third lane represents chymotrypsin treated RPA in presence of ssDNA. The numbered bands (1-5) show the protected fragments that are present only in RPA-wt in absence of ssDNA. Bands with alphabets (a-f) show fragments that are protected distinctly in RPA-wt in presence of ssDNA.

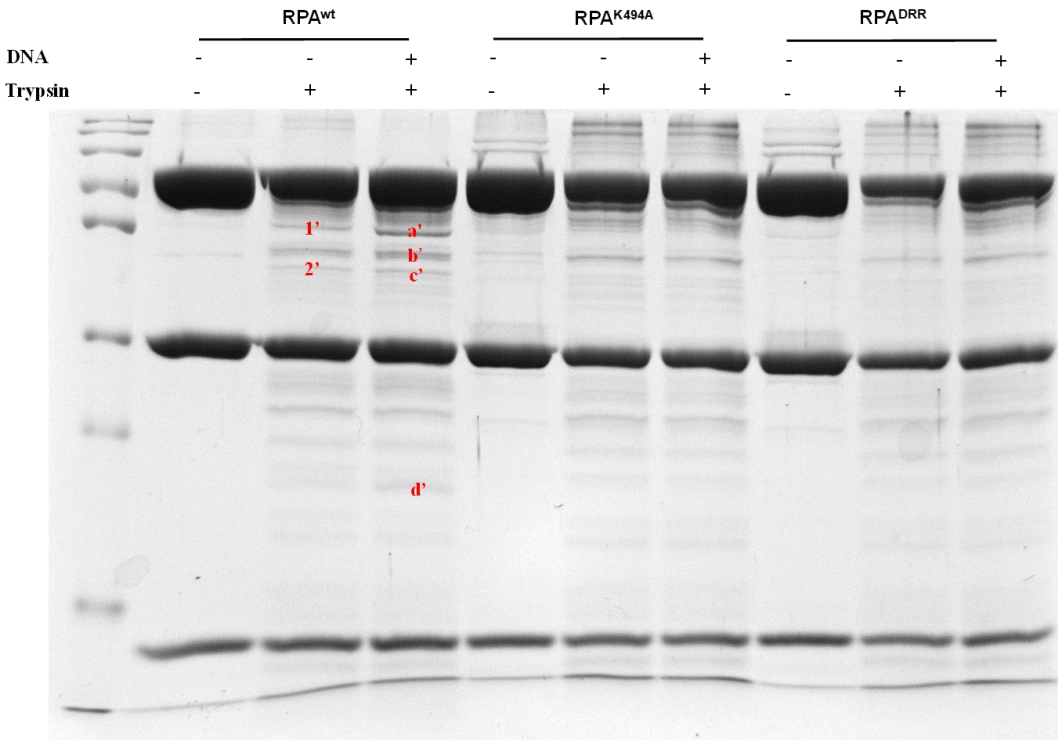

Figure 8-6: Limited proteolytic digestion of RPA-wt and RPAzm with trypsin. Qualitative assessment for understanding conformation of RPA and lysine mutants alone and in presence of ssDNA shows regions are protected from tryptic digestion in RPA-wt but not in RPAzm. For each RPA variant, left lane represents undigested RPA variant without ssDNA, the middle lane represents trypsin treated RPA in absence of ssDNA and the right lane represents trypsin treated RPA in presence of ssDNA. The numbered bands (1',2') show the protected fragments that are present only in RPA-wt in absence of ssDNA. Bands with alphabets (a'-d') show fragments that are protected distinctly in RPA-wt in presence of ssDNA.

8.3.2 RPAzm has DBD-A and DBD-D binding dynamics similar to RPA-wt

Tryptophan quenching and limited- proteolysis experiments suggested RPAzm-DBDs potentially adopted different conformation on DNA. To understand if this was due to change in characteristics of DBD-A and DBD-D engagement, we developed RPAzm-A^{MB543} (RPA-K494A-A^{MB543}, RPA-NKK-DRR-A^{MB543}, RPA-KK-AA-A^{MB543}) and RPAzm-D^{MB543} (RPA-K494A-D^{MB543} and RPA-NKK-DRR-D^{MB543}) and investigated its DNA binding properties in real-time. Both RPAzm-A^{MB543} and RPAzm-D^{MB543} produced a robust increase in MB543 fluorescence upon binding to ssDNA (Fig. 8-7 a-d, 8-9 a-c). Similar to RPA-A^{MB543} and RPA-D^{MB543}, data obtained for RPAzm-A^{MB543} was best described by double exponential with a linear phase and the data obtained for RPAzm-D^{MB543} was best described by single exponential with linear phase. The first exponential represents the initial engagement of DBD-A and DBD-D and the second exponential represents the trimerization core mediated remodeling phase observed for DBD-A.

RPAzm-A^{MB543} had reduced initial rate of engagement than RPA-wt but overall bound to the ssDNA with similar affinity ($k_{obs,1}$ at 25nM $(dT)_{35}$ for RPA-A^{MB543} : 47.7± 14.8; K494A-A^{MB543}: 29.7 ± 2.03; NKK-DRR-A^{MB543}: 25.8 ± 2.0; KK-AA-A^{MB543}: 22.8 ± 1.05) (Fig. 8-8 a, d). Consistent with RPA-A^{MB543} binding to $(dT)_{35}$, RPAzm-A^{MB543} showed an initial increase in signal upon engagement of DBD-A with ssDNA (250 milliseconds) followed by a decrease in the fluorescence signa. This decrease in signal has been attributed to trimerization core mediated remodeling of DBD-A (see chapter 3). For RPAzm, there were subtle differences in the observed rates of the trimerization core mediated remodeling phase of DBD-A (Fig. 6-12 a-d, 6-13 b, d). For 100nM RPAzm-A^{MB543}, instead of decrease in the rate of remodeling until 75nM $(dT)_{35}$ (i.e. sub-

stoichiometric concentration ssDNA: protein) as seen for RPA-A^{MB543}, RPAzm showed a steady increase in the rate of remodeling with increasing concentrations of $(dT)_{35}$ (Fig 8-8 b). Since RPAzm mutations are located in DBD-C which is a component of the trimerization core, a possible explanation for increase in the rate of remodeling could be reduction in the binding affinity of the trimerization core. This could then lead to partial loss of trimerization core mediated intra-DBD remodeling of DBD-A, perhaps by changing the dynamics of linker connecting DBDs B, C which is then propagated to changes in the dynamics of linker connecting DBDs A, B.

To understand if RPAzm affected the binding of trimerization core, we probed the DNA binding dynamics of DBD-D for RPAzm. Stopped flow experiments performed with RPAzm-D^{MB543} and increasing concentrations of $(dT)_{35}$ showed a robust increase in fluorescence signal upon binding to ssDNA with subtle differences in the $k_{obs,1}$ values for individual RPAzm (Fig. 8-9 a-c, 8-10 a). For 100nM RPA-K494A-D^{MB543}, the rate at which DBD-D binds to $(dT)_{35}$ increases linearly until 100nM $(dT)_{35}$, following which it saturates, whereas, RPA-NKK-DRR-D^{MB543} binds comparatively faster until 100nM $(dT)_{35}$ following which it binds to $(dT)_{35}$ similar to RPA-wt (Fig 8-10 a). Since this project was done in collaboration with Dr. Xiaolan Zhang (MSKCC), we did not perform RPA-KK-AA- DBD-D engagement with $(dT)_{35}$ as this mutation caused poor viability of *S. cerevisiae*. Taken together these results suggest mutation in the NKK motif causes subtle change in the intrinsic DBD dynamics with modest effects in DNA binding ability.

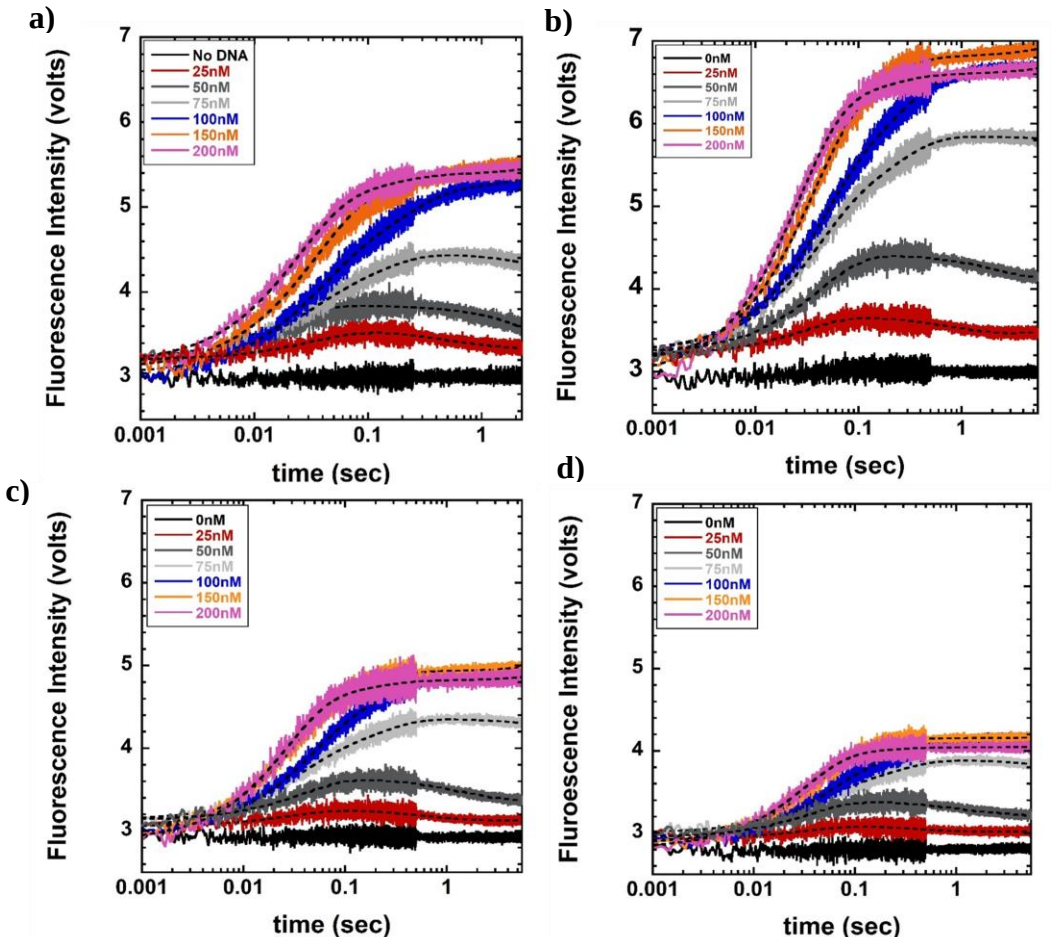

Figure 8-7: Monitoring DBD-A binding dynamics of RPA-wt and RPAzm mutants. Stopped-flow experiments were conducted by rapidly mixing 100nM **a)** RPA-A^{MB543} **b)** RPA-K494A-A^{MB543} and **c)** RPA-NKK-DRR-A^{MB543} **d)** RPA-KK-AA-A^{MB543} with increasing concentrations of $(dT)_{35}$. Samples were excited at 535nm and robust change in MB543 fluorescence was monitored using a 555nm long pass emission filter. At sub-stoichiometric concentrations of $(dT)_{35}$ (red and gray traces) initial increase in MB543 fluorescence followed by slight decrease can be observed for all RPA variants. This is suggestive of remodeling of DBD-A by the trimerization core of RPA.

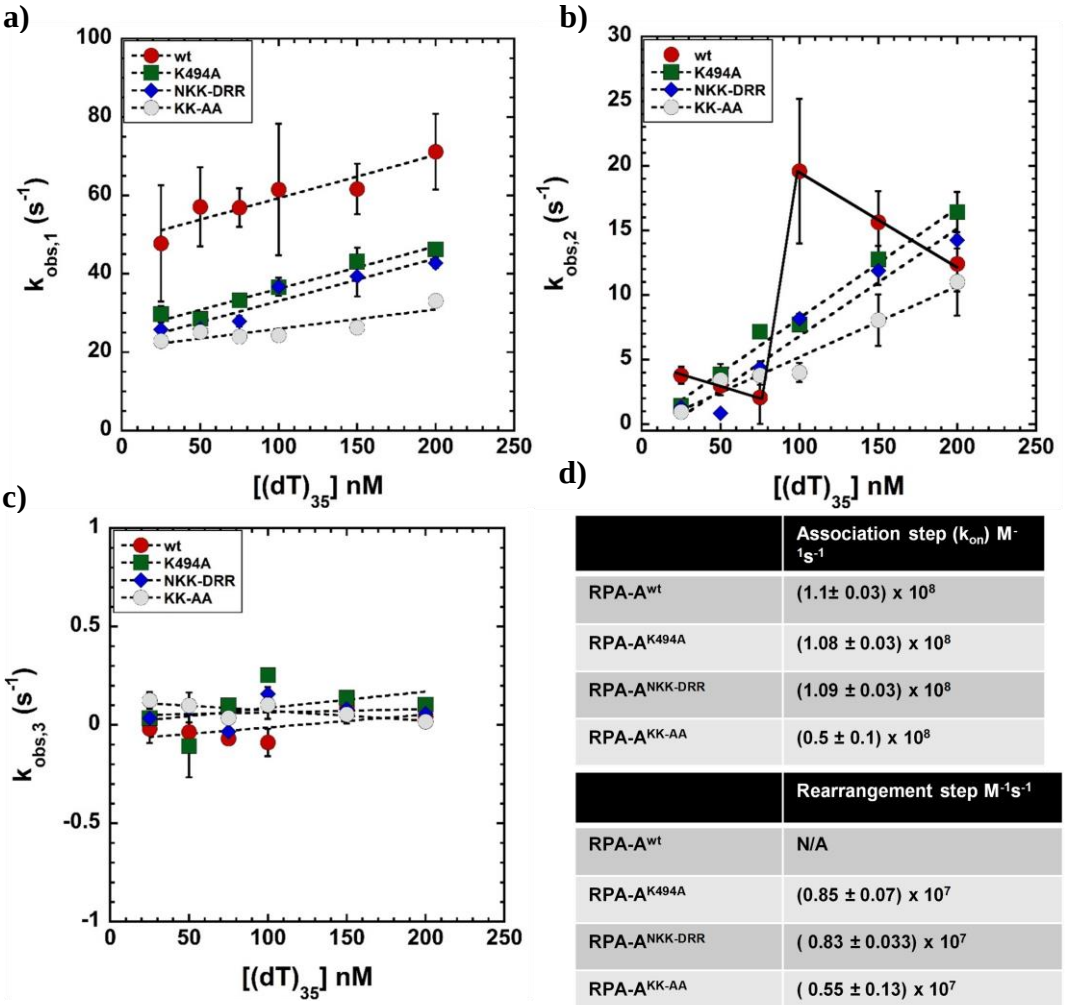

	Association step (k_{on}) $M^{-1}s^{-1}$
RPA-A^{wt}	(1.1± 0.03) x 10^8
RPA-A^{K494A}	(1.08 ± 0.03) x 10^8
RPA-A$^{NKK-DRR}$	(1.09 ± 0.03) x 10^8
RPA-A^{KK-AA}	(0.5 ± 0.1) x 10^8

	Rearrangement step $M^{-1}s^{-1}$
RPA-A^{wt}	N/A
RPA-A^{K494A}	(0.85 ± 0.07) x 10^7
RPA-A$^{NKK-DRR}$	(0.83 ± 0.033) x 10^7
RPA-A^{KK-AA}	(0.55 ± 0.13) x 10^7

Figure 8-8: Quantitative analysis of DBD-A binding dynamics of RPA-wt and RPAzm. Quantitation of the raw traces obtained in Fig. 8-7 using a two-step binding + liner fit model provides observed rates for **a)** initial binding phase ($k_{obs,1}$) **b)** remodeling/ rearrangement phase ($k_{obs,2}$) **c)** linear phase ($k_{obs,3}$). Fitting the plot of **a)** $k_{obs,1}$ **b)** $k_{obs,2}$ **c)** $k_{obs,3}$ to linear equation (except for $k_{obs,2}$ of RPA-A^{MB543}) yields the **d)** apparent association and rearrangements rates for individual steps in DBD-A engagement on ssDNA. It should be noted that solid black line for $k_{obs,2}$ values of RPA-A^{MB543} is not a true fit but representation of a trend depicting trimerization core mediated remodeling of DBD-A.

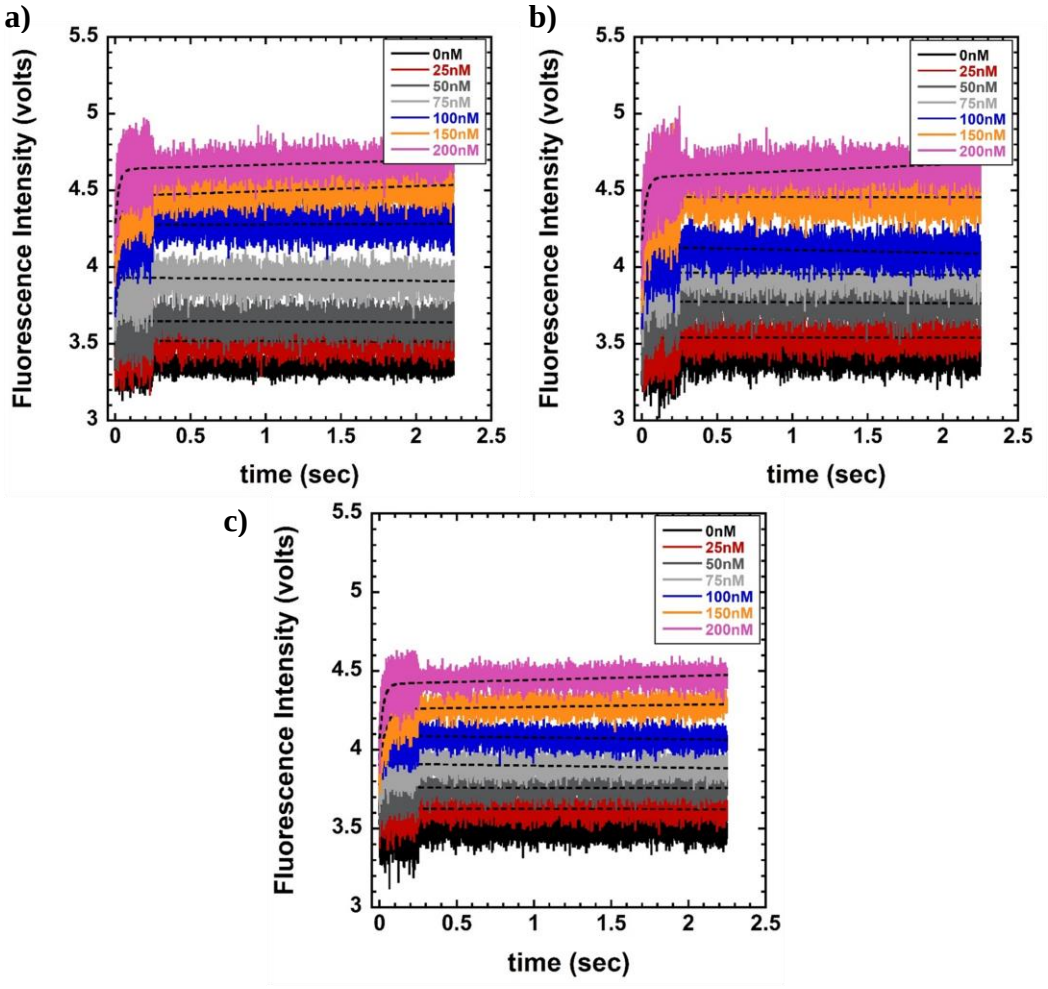

Figure 8-9: Monitoring DBD-D binding dynamics of RPA^{wt} and RPA^{zm} mutants. Stopped-flow experiments were conducted by rapidly mixing 100nM a) RPA-D^{MB543} **b)** RPA-K494A-A^{MB543} and **c)** RPA-NKK-DRR-D^{MB543} with increasing concentrations of $(dT)_{35}$. Samples were excited at 535nm and robust change in MB543 fluorescence was monitored using a 555nm long pass emission filter. No remodeling phase is obtained for all the variants of RPA-D^{MB543} after binding to $(dT)_{35}$.

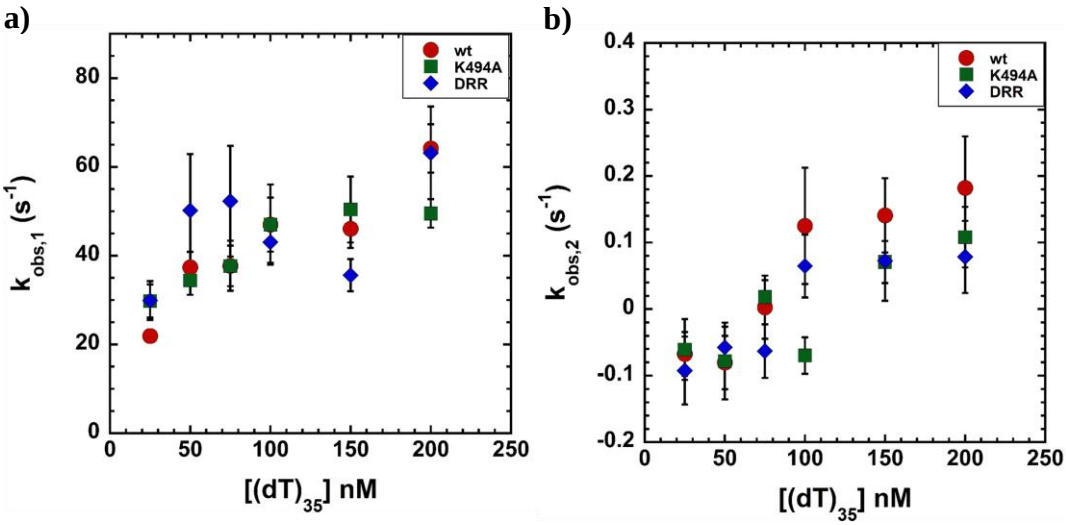

Figure 8-10: Quantitative analysis of DBD-D binding dynamics of RPA-wt and RPAzm. Quantitation of the raw traces obtained in Fig. 8-9 using a one-step binding + liner fit model provides observed rates for **a)** initial binding phase ($k_{obs,1}$) and **b)** linear phase ($k_{obs,2}$) plotted along increasing concentrations of $(dT)_{35}$.

8.3.3 Assembly of RPAzm is similar to RPA-wt on ssDNA

Following subtle differences in overall conformations adopted and in DNA binding dynamics of DBD-A and DBD-D for RPAzm, we wanted to investigate if multiple RPAzm assembled similar to RPA-wt on ssDNA. Therefore, we generated RPAzm FRET pairs with RPAzm-A^{cy3} and RPAzm-D^{cy3} and monitored occurrence of FRET with increasing lengths of oligonucleotides ($(dT)_n$, where n= 20 to 140 nucleotides). Previous FRET experiments performed with Cy3 labeled ssDNA and cy5 labeled RPA-A or RPA-D have shown maximum FRET between 5′ Cy3 ssDNA and RPA-A^{Cy5} and 3′cy3 ssDNA and RPA-D^{Cy5} bolstering the fact that RPA binds to DNA with 5′-3′ polarity (Pokhrel et. al., 2019). Therefore, for FRET to occur, DBD-A^{cy3} from one RPA has to be in tandem with DBD-D^{cy5} form another RPA. Bulk FRET experiments performed with 40nM RPAzm-A^{cy3}, 40nM RPAzm-D^{cy5} and 40nM increasing lengths of

oligonucleotides show that RPAzm assembly on ssDNA can be explained by two- step kinetic process for all ssDNA (Fig. 8-11 a-c). The first step ($k_{obs,1}$) represents the engagement of two DBDs along with ssDNA and the second step ($k_{obs,2}$) represents the rearrangement DBDs between the RPAs on ssDNA. RPAzm had assembly kinetics similar to RPA-wt (Fig. 8-12 a, b). Similar to RPA-wt, quantifiable FRET intensity for RPAzm was observed with ssDNA greater than 45 nucleotides and the increase is FRET intensity was directly proportional to the length of ssDNA (Fig. 8-11 a-c). Robust rearrangement step can be observed for $(dT)_{60}$, $(dT)_{70}$ and $(dT)_{79}$ that have ample space for assembly of at least 2 RPAs, but, have additional DNA space to allow transient interaction/ binding of few DBDs from third RPA (Fig. 8-11 a-c). Thus, the rearrangement step could be reflecting arrangement of DNA bound DBDs attempting to attain stability, diffusion of at least two DNA bound RPAs or transient binding of an incoming DBD-A which exists in association/ dissociation equilibrium.

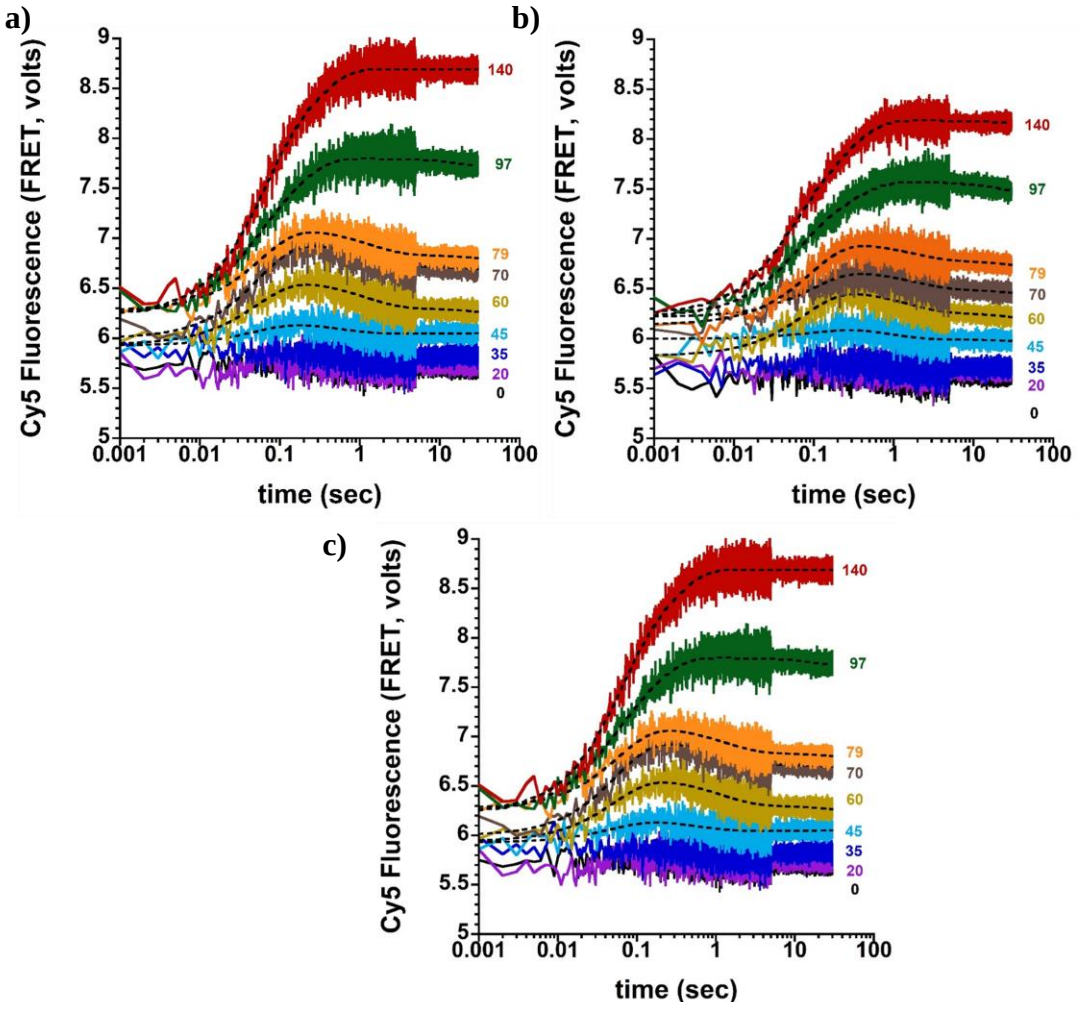

Figure 8-11: Monitoring assembly of multiple RPAzm with increasing lengths of ssDNA. Representative traces of stopped-flow experiments where, RPA-wt or RPAzm, labeled with cy3 at DBD-A and Cy5 at DBD-D were mixed rapidly with increasing lengths of ssDNA for **a)** RPA-A^{cy3} and RPA-D^{cy5} **b)** RPA-K494A-A^{cy3} and RPA-K494A-D^{cy5} **c)** RPA-NKK-DRR-A^{cy3} and RPA-NKK-DRR-$D^{cy5.}$ All the experiments were performed for n=3.

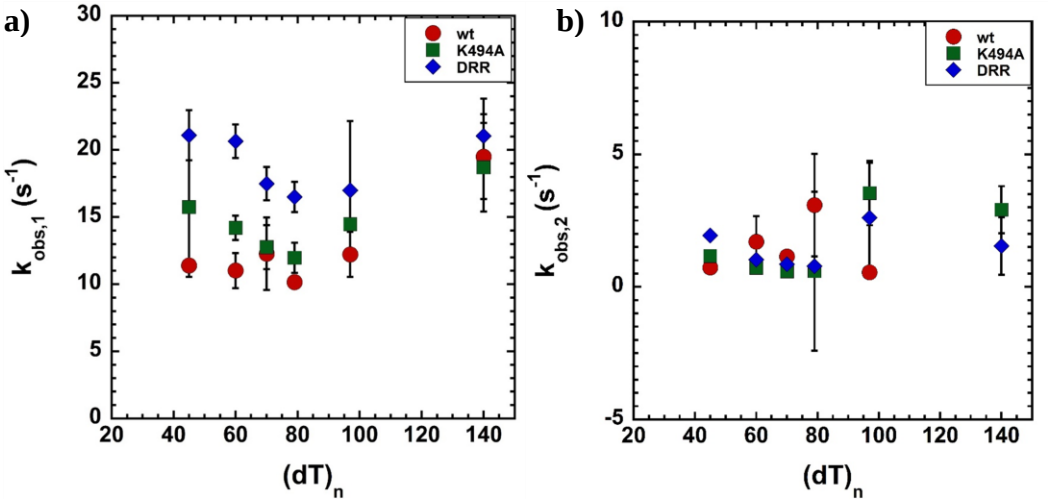

Figure 8-12: Quantification of the bulk FRET experiments in Fig. 8-11. All the data obtained in Fig. 8-11 were analyzed using a two-step binding+ linear state model and plotted along the increasing lengths of ssDNA. **a)** Plot showing the rate of engagement phase ($k_{obs,1}$) for RPA-wt and RPAzm. **b)** Plot showing rates for rearrangement phase for RPA-wt and RPAzm. The rates for both the phases for RPAzm are within error of RPAwt. All the experiments were performed for n=3.

8.3.4 RPAzm are sensitive to clearing by Srs2 helicase

A delicate balance between the activity of pro-HR mediators (facilitating HR) and anti HR- mediators (inhibiting HR) drive the regulated process of HR. *In vivo*, upon mitomycin or camptothecin induced DNA damage, RPAzm rescued survivability of *S. cerevisiae* in a Srs2 null background (Dhingran *et. al.,* to be published). Furthermore, this rescue of cell viability was dependent on interaction between Srs2 and Rad51 as, Srs2 Δ 875–902 which is deficient for interaction with Rad51 did not rescure cell survivability upon DNA damage for both RPA-wt and RPAzm (Dhingran *et. al.,* to be published). In context of RPA, our ensemble stopped flow experiments showed only subtle distinction in DBD dynamics with no significant differences in assembly of RPAzm compared to RPA-wt. During HR, the main function of Srs2 is to disrupt Rad51-nucleoprotein filaments in an attempt to prevent excess/ unregulated HR from occurring. Therefore, we wanted to investigate effects of Srs2 helicase activity on a RPAzm-ssDNA complex to understand how this complex could be contributing in rescuing cell survivability during loss of Srs2. For this, we used a 20-bp duplex DNA consisting either a 3′ $(dT)_{25}$ (DNA subs-1) or a 3′ $(dT)_{50}$ overhang (DNA subs-2) with Cy5 fluorophore attached at 5′ of the long strand and Black Hole Quencher 2 (BHQ2) quencher attached at 5′ of the short strand (Fig. 8-13 a, d). When annealed, BHQ2 quenches Cy5 fluorescence as they are in close proximity to each other, followed by $(dT)_{25}$ overhang in DNA subs-1 that has enough space for only one RPA to bind and $(dT)_{50}$ overhang in DNA subs-2 that has enough DNA binding space for two RPAs. We preformed RPA**:**DNA subs-1 or RPA**:**DNA-subs-2 complex with either RPA-wt or RPAzm and challenged it with 100nM Srs2 helicase in presence of ATP. Each reaction cycle would sequentially involve ATP

dependent loading of Srs2 towards the 3′ end for both DNA subs-1 and DNA subs-2, translocation along the DNA, removal of any RPA bound on the DNA and unwinding of the duplex DNA. Upon unwinding the duplex DNA, Cy5 attached to long strand would move away from BHQ2 resulting in increase in Cy5 fluorescence. As expected, our results showed much slower Srs2 mediated unwinding of duplex DNA in presence of RPA-wt (Fig. 8-13 b, e, red trace) compared to in absence of any protein i.e DNA subs only (Fig. 8-13 b, e, grey trace). In absence of any protein bound to the DNA substrates, unwinding of DNA duplex was approximately 3-fold faster for DNA subs-2 (Fig. 8-13 f) (k_{obs} 0.13 ± 0.02 s^{-1}) than DNA subs-1 (Fig. 8-13 c) (k_{obs} 0.045 ± 0.017 s^{-1}). Displacement of RPAzm from ssDNA was faster compared to RPA-wt, with RPA-NKK-DRR showing the least and RPA-K494A displaying intermediate resistance to clearing by Srs2 for both DNA substrates (Fig. 8-13 c, f).

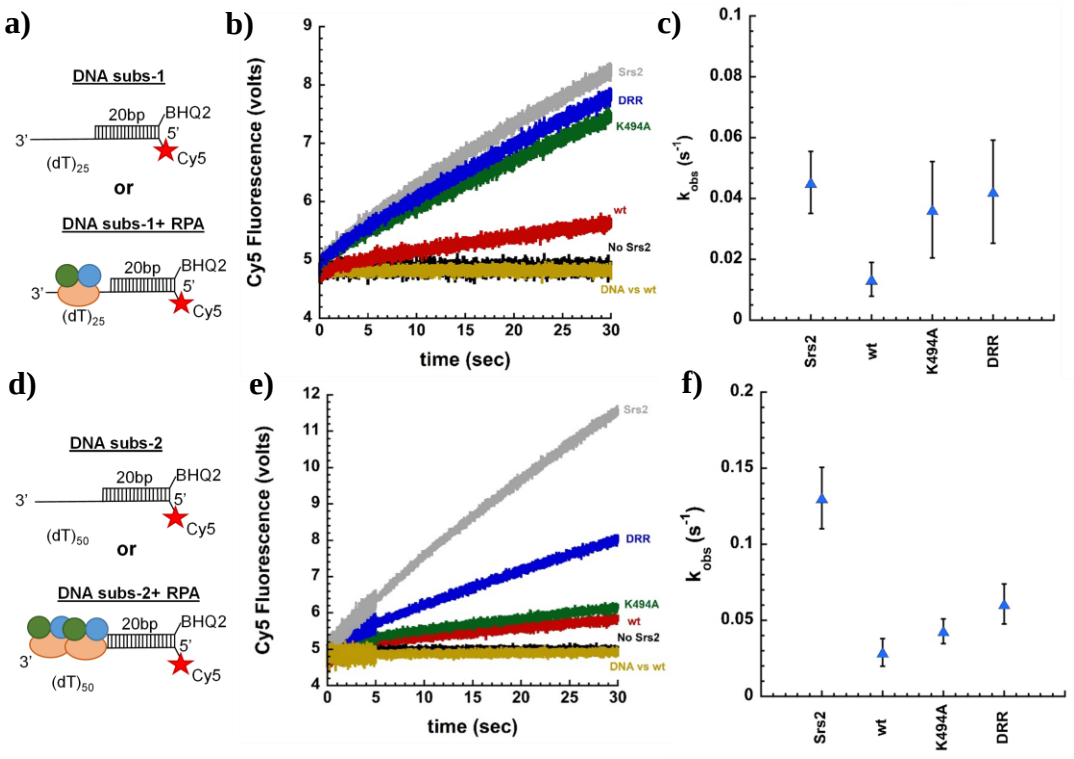

Figure 8-13: Unwinding of duplex DNA by Srs2. Stopped flow experiments were performed to monitor Srs2 mediated unwinding of 50nM DNA sub-1 with 3'$(dT)_{25}$ or 50nM DNA-subs2 with 3'$(dT)_{50}$ overhang either in presence or absence of RPAwt and RPAzm. **a), d)** Schematic representation of RPA bound or unbound DNA-subs1 and DNA subs-2, respectively. **b)** Stopped flow traces obtained when 50nM DNA-subs-1 was incubated with 50nM RPA-wt or RPAzm and rapidly with 100nM Srs2 in presence of ATP. Samples were excited at 625nm and increase in Cy5 fluorescence monitored at 645nm. As a control, Srs2 unwinding of DNA susb-1 was performed either in presence (grey trace) or absence of ATP (olive green trace). Data obtained for DNA subs-1 unwinding experiments were fit with single-exponential+ linear phase, where the linear phase represents the rate of unwinding (k_{obs}). **c)** Plot of k_{obs} of 50nM DNA susb-1 either alone or prebound to 50nM RPA-wt or 50nM RPAzm when challenged with 100nM Srs2. **e)** Similar experiments as mentioned in **b)** performed with 50nM DNA subs-2, 100nM RPA-wt or 100nM RPAzm and challenged with 100nM Srs2 in presence of ATP. The reaction condition results in displacement of two RPAs bound to DNA subs-2 in presence of Srs2. **f)** Plot of k_{obs} (rate of unwinding) of 50nM DNA susb-2 alone or pre-bound to 100nM RPA-wt or 100nM RPAzm in presence of Srs2.

8.4 Discussion

A key feature of RPAzm is that all the mutations are located in DBD-C which also makes maximum contact with ssDNA (Fan & Pavletich, 2012b). The 32-deoxythymidine oligonucleotide bound crystal structure of *U. maydis* RPA (4GNX) shows ssDNA following a S-shaped path in DBD-C where, the "S" encompasses 10^{th} deoxythymidine to 20^{th} deoxyhymidine (Thy10-Thy20). Amino acids in the NKK motif form the bottom of the "S" and make direct contact with Thy10-Thy13 that stabilizes the smaller DNA binding groove (L12 loop) (Fan & Pavletich, 2012a). In addition, cysteine preceeding NKK motif is one of the four cysteines coordinating the Zn^{2+} metal ion. Therefore, NKK motif is important in stabilizing the binding of DBD-C to DNA.

In this chapter, we showed that mutating key amino acid residues in the conserved NKK motif in DBD-C could alter DNA bound conformations of RPA with potential implications in regulation of HR pathway. Each mutation in RPAzm is different i.e., NKK→NKA substitution, NKK→DRR substitution and KK→AA substitution, which could result in variations in the way the mutant protein is interacting with DNA. Using steady-state tryptophan quenching as a guide to probe conformations adopted by DBDs, we show that RPAzm-$(dT)_{35}$ binding exhibits a varying degree of tryptophan quenching, while maintaining the initial rate of binding to DNA similar to RPA-wt (Fig. 8-2, 8-3, 8-4, Table 8-2, 8-3). This change in conformation of RPAzm-ssDNA complex was further verified by proteolytic digest experiments where, RPAzm showed distinct digestion profile both in absence and presence of ssDNA (Fig. 8-5, 8-6). Using RPAzm-A^{MB543} and RPAzm-D^{MB543}, we show that both DBD-A and DBD-D have DNA binding dynamics similar to RPA-wt, except for subtle changes in the rate of trimerization core mediated

remodeling of DBD-A (Fig. 8-7, 8-8, 8-9, 8-10). While RPAzm assembly on ssDNA is similar to RPA-wt (Fig. 8-11, 8-12), RPAzm nucleoprotein filament is more easily disrupted by Srs2 helicase (Fig. 8-13). Taken together, these data suggests mutation in the NKK motif affects properties of an RPA-DNA filament, possibly due to changes in DBD-C-DNA engagement and communication between DBD-C and other DBDs. In cellular context, ease in displacement of all the RPAzm variants by other HR proteins (such as Rad51) trying to gain access to ssDNA could be enough for maintaing the balance of HR. Under these conditions, upon DNA damage, yeast lacking Srs2 would still survive as RPA can be easily displaced to allow Rad51 nucleoprotein formation and HR to continue.

APPENDIX II: SUPPLEMENTARY METHODS

9.1 Measuring concentration of protein using spectrophotometer (Agilent Technologies, Cary UV-Visible spectrophotomer)

To measure the concentration of protein, stock protein was diluted about three fold (Note: dilution depends on the expected yeild of protein and the volume of total growth that was done). Spectophotometer was set to collect an absorbance range of 240-350nm. ~400µl strorage buffer was taken in a quartz cuvette and absorption spectra (240-350nm) collected. This baseline/ reference absorption was either "zeroed" or "blanked". Then, ~400ul of diluted protein was taken in a quartz cuvette and absorption spectra collected. The following reading were noted: $Abs_{\text{protein max, nm (usually 280±4 nm)}}$ and $Abs_{350\text{ (also known as buffer correction reading)}}$. The following equation was used to calculate protein's concentration in Molar (M)

$$\text{Concentration (M)} = \frac{\text{Abs}_{280\text{ (protein max } abs)} - \text{Abs}_{350}}{\varepsilon_{protein}} * \text{dilution factor}$$

9.2 Measuring concentration of fluorescent dye using spectrophotometer (Agilent Technologies, Cary UV-Visible spectrophotomer)

Resuspend the lypholized flurophore according to the manufactor's instructions. For example, for Click chemistry tools DBCO-MB543, spin the vial for a minute using table top centrifuge, following which add 51µl of N, N Dimethylformamide (DMF) and vortex the vial for about a minute at high-speed. To measure the concentration of the resuspended dye, dilute the dye about 2000 fold (i.e. 1µl of dye was diluted in 1.999ml of protein storage buffer). Note: fold dilution might need to be adjusted depending on the

signal saturation in fluorometer. Absorption spectra from 400nm-650nm were collected and values at $Abs_{\text{fluorophore max (usually 550nm)}}$, $Abs_{\text{fluorophore correction,650nm}}$ noted.

Usually, absorption spectra consits of wavelength spanning atleast 100nm upstream and 100nm downstream of the flurophore's maximum absotption wavelength. For example, for Cy5 with maximum absorption at 650nm, absorption spectra fromm 550-750nm would be collected.

The following equation was used to calculate the concentration of stock fluorescent dye:

Concentration of fluorescent dye (M)=

$$\frac{\text{Abs}_{\text{flurophore max}} - \left(\text{Abs}_{\text{fluorophore correction}}\right)}{\varepsilon_{flurophore}} * \text{dilution factor}$$

9.3 Measuring correction factor

To measure the correction factor, stock fluorescent dye was diluted about 2000-fold in protein storage buffer (i.e. 1µl of dye was diluted in 1.999ml of protein storage buffer). Depending on the fluorophore's maximum absorption wavelength (Abs_{max}), absorption spectra spanning both the protein and fluorophore absorption range were collected. For example, for DBCO-MB543 (click chemistry tools), absorption spectra from 240nm-650nm were collected and values at Abs_{280nm}, Abs_{350}, $Abs_{\text{fluorophore max (usually 550nm)}}$, $Abs_{\text{fluorophore correction,650nm}}$ noted. Usually, proteins have Abs_{max} at 280± 5 nm with Abs_{350nm} as correction value for spectrophotometer.

Fluorophore's correction wavelength= $Abs_{\text{fluorophore max}}$ + 100nm.

Correction factor was calculated using the following equation:

$$\text{Correction factor} = \frac{\text{Abs}_{280} - Abs_{350}}{\text{Abs}_{\text{Absfluorophore max (usually 550nm)}} - \text{Abs}_{\text{fluorophore correction,650nm}}}$$

9.4 Measuring concentration of fluorescently labeled protein

Concentration fluorescent protein was diluted either 2 or 3-fold in protein storage buffer, depending on the expected yield of the protein. Absorption spectra spanning both the protein and fluorophore absorption range were collected. For example, for DBCO-MB543 (click chemistry tools), absorption spectra from 240nm-650nm were collected and values at Abs_{280nm}, Abs_{350}, $\text{Abs}_{\text{fluorophore max (usually 550nm)}}$, $\text{Abs}_{\text{fluorophore correction,650nm}}$ noted. For DBCO-Cy5(click chemistry tools), absorption spectra from 240nm-750nm were collected and values at Abs_{280nm} (the maximum absorption by protein), Abs_{350}, $\text{Abs}_{\text{fluorophore max (usually 650nm)}}$, $\text{Abs}_{\text{fluorophore correction,750nm}}$ noted.

Corrected concentration of protein in M was calculated using the following equation:

Corrected Concentration of protein (M)=

$$\frac{\text{Abs}_{280} - (\text{Abs}_{280} * \text{correction factor}) - \text{Abs}_{350}}{\varepsilon_{protein}} * \text{dilution factor}$$

Concentration of fluorophore[1] (M)= $\frac{\text{Abs}_{\text{flurophore max}} - (\text{Abs}_{\text{fluorophore correction}})}{\varepsilon_{flurophore}} * \text{dilution factor}$

Concentration in μM = concentration in Molar *10^6

Percentage labeling= $\frac{\text{Concentration of flurophore}^1(\mu M)}{\text{Corrected concentration of protein } (\mu M)} * 100\%$